CORA Cork Open Research Archive
Cartlann Taighde Oscailte Chorcaí

Title	Development of new photoluminescent sensing materials, systems and applications for cell analysis
Authors	Li, Liang
Publication date	2024
Original Citation	Li, L. 2024. Development of new photoluminescent sensing materials, systems and applications for cell analysis. PhD Thesis, University College Cork.
Type of publication	Doctoral thesis
Rights	© 2024, Liang Li. - https://creativecommons.org/licenses/by/4.0/
Download date	2026-10-31 17:00:54
Item downloaded from	https://hdl.handle.net/10468/16956

UCC
University College Cork, Ireland
Coláiste na hOllscoile Corcaigh

Ollscoil na hÉireann, Corcaigh

National University of Ireland, Cork

Development of new photoluminescent sensing materials, systems and applications for cell analysis

Thesis presented by

Liang Li

for the degree of

Doctor of Philosophy

University College Cork

School of Biochemistry and Cell Biology

Head of School/Department: Prof. Justin McCarthy

Supervisor(s): Prof. Dmitri B. Papkovsky

2024

Table of Contents

Acknowledgements 6

List of Abbreviations 7

Abstract 10

Chapter 1: Literature Review 12

1.1 Cell Metabolism and Bioenergetics 12

1.2 Optochemical Sensors 15

1.3 Phosphorescent O_2 Sensors 17

1.4. Photoluminescent pH Sensors 28

1.5 Luminescent pH and O_2 Measurement Modalities 38

1.6 Applications of Optical pH and O_2 Sensing in Bio-analysis 45

1.7 Conclusion 51

Chapter 2: Materials and Methods 51

2.1 Materials 52

2.2 Methods 52

2.2.1 Fabrication of sensor cocktails and coatings 52

2.2.2 Barometric calibration setup and procedures 53

2.2.3 Photophysical characterization of sensors 54

2.2.4 pH titration for dyes and pKa calculation 59

2.2.5 Tissue culture and animal experiments 60

2.2.6 Cell viability and toxicity assays 61

2.2.7 Cellular ECAR and OCR assays 61

Chapter 3: Barometric calibration of quenched-phosphorescence based oxygen sensors on a standard rotary evaporator system 63

3.1 Introduction 63

3.2 Results and Discussion 64
3.2.1 Rotavap system and its general suitability for calibration of O_2 sensors 64
3.2.2. Basic theory and analytical relationships 66
3.2.3. Initial testing of the Rotavap setup 67
3.2.4. Assessment of T-control of the sensors inside the Rotavap system 71
3.2.5. Detailed barometric calibrations over broad T-range 72
3.3 Conclusions **77**
Chapter 4: Phosphorescence lifetime measurements with sensor materials: comparison of different detection platforms 79
4.1. Introduction 79
4.2 Results and Discussion 80
4.2.1 General description and comparison of the different platforms 80
4.2.2 PLT measurements by the RLD method on a TRF reader Victor 2. 85
4.2.3 PLT measurements on the Cary Eclipse fluorescence spectrometer 88
4.2.4 PLT measurements on the confocal PLIM-TCSPC microscope 90
4.3 Conclusions 94
Chapter 5: New dual pH/O_2 sensing materials for cell analysis 95
5.1 Introduction 95
5.2 Results and Discussion 96
5.2.1 Screening of alternative polymeric matrices for the dual pH/O_2 sensor 96
5.2.2 Screening of PdOEP-SB analogues and indicator optimization 100
5.2.3 Introducing a reference fluor to enable the ratiometric pH sensing 102
5.2.4 Maximizing the photoluminescent signals for the dual sensor 104
5.2.5 Depositing the new sensor coatings on the substrates used in cell analysis 105
5.2.6 Cellular OCR and ECA measurements with the new pH/O_2 sensor coatings 108
5.3 Conclusions 111

Chapter 6: New pH and dual pH/O_2 sensors for cell analysis and tissue imaging 112

6.1 Introduction 112

6.2 Results and discussion 113

6.2.1 Spectral characteristics of the solid-state pH and O_2 sensors 113

6.2.2 Development and optimisation of the OEP and OEPK based pH sensors 115

6.2.3 Development of dual pH/O_2 sensors 119

6.2.4 Fluorescence lifetime-based pH sensing 122

6.2.5 ECAR and OCR analysis with the new pH and O_2 sensors 126

6.2.6. Planar calibration-free FLIM sensors for tumor pH imaging in model animals .. 128

6.3 Conclusions 132

Overall Discussion 133

Thesis outcomes 136

Reference 138

Declaration

This is to certify that the work I am submitting is my own and has not been submitted for another degree, either at University College Cork or elsewhere. All external references and sources are clearly acknowledged and identified within the contents. I have read and understood the regulations of University College Cork concerning plagiarism and intellectual property.

Signed: Liang Li

Date: 08/08/2024

Acknowledgements

I wish to give my deepest gratitude to my supervisor, Prof. Dmitri Papkovsky, who leaded me to the world of optical bioanalysis, and give me his priceless knowledge, guidance, and patients throughout my precious PhD journey.

I wish to express gratitude to Dr. Alexander Zhdanov, Dr. Rafeal Di Lazaro Gaspar and Dr. Elisa Santovito, who gave me a lot of guidance, training, and experimental skills during my PhD study. I would like to thank all my colleagues for their help and company, Dr. Chiara Zabetti, Dr. Rajannya Sen, Dr. Sophia Elisseeva, Dr. Emer Cantillon, Dominic Dollken, Lauryn, Timothy, etc.

Finally, special thanks for my parents and all my family members, who always support me and encourage me to peruse my dream with unconditional love and accompany, even it is thousands of miles away.

PhD is a strenuous journey, during which I had become more persistent, problem-solving, self-disciplined, and self-motivated. I will always stay hungry and stay foolish!

List of Abbreviations

ATP: Adenosine triphosphate

ADP: Adenosine diphosphate

Ant.A: Antimycin A

A594: Lung carcinoma cells

CoQ: Ubiquinone

Cyt c: Cytochrome c

C6: Coumarin 6 dye

2-DG: 2-Deoxy-d-glucose

DOS: Bis(2-ethylhexyl) sebacate

DLR: Dual Lifetime Referencing

DMEM: Dulbecco's Modified Eagle Medium

ECAR: Extracellular Acidification Rate

ETC: Electron Transport Chain

$FADH_2$: Flavin Adenine Dinucleotide

FITC: Fluorescein Isothiocyanate

FRET: Fluorescence Resonance Energy Transfer

FBS: Foetal Bovine Serum

FLT: Fluorescence Lifetime

FLIM: Fluorescence Lifetime Imaging

FFCP: Carbonyl cyanide-p-trifluoromethoxyphenylhydrazone

HCT 116: Human colon carcinoma

IRF: Instrument Response Function

LED: Light Emitting Diode

Li-PFPB: Lithium tetrakis(pentafluorophenyl)borate ethyl etherate

MPs: Microparticles

NADH: Nicotinamide adenine dinucleotide

NADPH: Nicotinamide adenine dinucleotide phosphate hydrogen

Na-TFMB: Sodium tetrakis[3,5-bis(trifluoromethyl)phenyl] borate (borate1)

Na-TPB: Sodium Tetraphenylborate

OxPhos: Oxidative Phosphorylation

OAA: Oxaloacetate

OCR: Oxygen Consumption Rate

OD600: Optical Density

OEP: Octaethylporphine

OEPK: Octaethylporphine-ketone

PPP: Pentose Phosphate Pathway

PtBP: Pt(II)-benzoporphyrin

PtCP: Platinum (II) Coproporphyrin

PtOEP/PdOEP: Platinum/Palladium Octaethylporphyri

PtOEP-SB: PtOEP-methyl-Schiff

PtOEPK/PdOEPK: Pt(II)/Pd(II) Octaethylporphine-ketone

PtTFPP/PdTFPP: Pt(II)/Pd(II)-tetrakis(pentafluorophenyl)porphine

PdTCPP: Pd-meso-tetra-(4-carboxyphenyl)-porphyrin dendrime

PtTPTBP/PdTPTBP: Pt(II)/Pd(II)-tetraphenyltetrabenzoporphyrin

PtTPTBPF/ PdTPTBPF: Pt(II)/Pd(II) meso-tetra(4-fluorophenyl) tetrabenzoporphyrin

PtTPTNP/ PdTPTNP: Pt(II)/Pd(II)-tetraphenyl-tetranaphthoporphyrin

PC12 cells: Rat pheochromocytoma cells

pO2: Partial oxygen pressure

PLT: Phosphorescence Lifetime

PLIM: Phosphorescence Lifetime Imaging

PLA: Poly(DL-lactide)

PLGA: Poly(DL-lactide-co-glycolide)

PMT: Photomultiplier Tube

PS: Polystyrene

PS-DVB: Poly(styrene divinylbenzene)

P/S: Penicillin-Streptomycin solution

PVC: High molecular weight poly (vinyl chloride)

PVDC: Poly(vinylidene chloride)

R5P: Ribose-5 phosphate

Ru5P: Ribulose-5-phosphate

Ru-dpp: Ruthenium tris(4,7-diphenyl-1,10-phenanthroline)

RPMI 1640: Roswell Park Memorial Institute 1640 medium

RLD: Rapid Lifetime Determination

ROI: Region of Interest

ROS: Reactive Oxygen Species

SW480: Colon adenocarcinoma cells

SDS: Sodium dodecylsulfate

S/N: Signal to noise ratio

SPAD: Single Photon Avalanche Diode

TKT: Transketolase

TALDO: Transaldolase

TCPB: Sodium tetrakis(p-chlorophynyl)borate

TCSPC: Time-Correlated Single Photon Counting

THF: Tetrahydrofuran

TFA: Trifluoroacetic acid

TCPB: Potassium tetrakis(4-chlorophenyl)borate

TR-F: Time-Resolved Fluorescence

Abstract

Cell analysis using optochemical sensors represents large and important niche in life and biomedical science. Sensor calibration and detection platforms are critical during sensor fabrication, characterization and application. However, existing calibration setups, platforms, and systems have limitations with respect to their robustness, analytical performance and capabilities. In this project, several new photoluminescent pH and oxygen (O_2) sensing materials, platforms and systems were developed, evaluated comparatively and then applied for bio-analysis particularly for samples containing cells.

The first experimental section describes a new barometric calibration setup which provides accurate, convenient and versatile O_2 calibration. Using this setup, a detailed characterization of several sensor types based on PtBP dye (sensor stickers, membrane inserts, liquid probe NanO_2-IR) was conducted in phosphorescence lifetime (PLT) mode by handheld sensor readers, and their key optional parameters (τ_0, Ksv, T-coefficients, etc) and calibration equations were determined and cross-compared.

The second experimental section evaluates comparatively the PLT measurements of several Pt-porphyrin based oxygen sensors on three different platforms: the time-revolved fluorescence reader Victor2, luminescence spectrometer Cary Eclipse, and confocal laser-scanning FLIM/PLIM-TCSPC microscope. The merits and limitations of each platform, including instrumental factors, analytical performance, lifetime calculation methods, potential sources of error were assessed.

The third experimental section presents a new photoluminescent materials for cell analysis based on the substituted phosphorescent Pt(II)- or Pd(II)-porphyrin indicator dyes bearing dual O_2 and pH sensing functionality (MePor-SB). The study includes screening of different host matrices for the sensor, synthesis and evaluation of new MePor-SB derivatives with altered protonation behaviour, development of ratiometric version of the pH sensor, photoluminescent signal enhancement options, deposition of sensor coatings on common cell analysis substrates and their demonstration in OCR/ECAR measurements with relevant cell models (PC 12 cells).

The fourth experimental section, describes novel solid-state pH sensors for cell analysis based on hydrophobic protonable metal-free porphyrins, octaethylporphine (OEP), and octaethylporphine-ketone (OEPK), as fluorescent pH indicators. The internally referenced ratiometric intensity and nanosecond lifetime-based versions of these pH sensors were

developed and also multiplexed with the O_2 sensors based on phosphorescent PtOEP dye. The key parameters of the pH sensor were optimized, including the type and concentration of proton transfer agent, working pH range and pKa, dye concentrations and cross-talk with the O_2 sensor (Pt-OEP). The optimised two-analyte sensors with stable internally referenced calibrations, convenient spectral characteristics and low cytotoxicity were coated on microplates and demonstrated with cultured cells and 3D spheroids made of HCT 116 cells, measuring their ECAR/OCR and responses to stimulation.

Finally, the planar solid-state pH sensors on polyester films (Mylar) were used to measure extracellular pH in grafted tumours produced by CT26 cells and freshly excised from animals on a portable FLIM imager. The new pH sensors and dual pH/O_2 sensors showed high stability (>1 year of storage), fast response and stable calibration, being well-suited for detailed metabolic studies of biological samples on widely available laboratory equipment.

Key words: Optochemical oxygen and pH sensors; fluorescent and phosphorescent porphyrins; barometric oxygen calibration; luminescence lifetime sensing; FLIM/PLIM; live cell analysis; ECAR and OCR measurements; tumour pH imaging

Chapter 1: Literature Review

1.1 Cell Metabolism and Bioenergetics

Cell metabolism and bioenergetics comprise a set of complex biochemical reactions that sustain the function and survival of living cells. Broadly, these reactions can be categorized into anabolism and catabolism. Catabolism involves breaking down large molecules into smaller units to produce energy, while anabolism is the biosynthesis process wherein cells utilize the energy released from catabolism to synthesize complex macromolecules, such as proteins, nucleotides, saccharides, and fatty acids [1]. The bioenergetic systems supporting energy transduction are of particular interest for biomedical research and pharmacology, due to their association with various pathologies, including diabetes, cancer, inflammation, ischemia-reperfusion, neurodegenerative diseases [2-5].

The main metabolic pathways in eukaryotic organisms include oxidative phosphorylation (OxPhos), glycolysis, tricarboxylic acid or Krebs cycle (TCA), pentose phosphate pathway (PPP), and β-oxidation, as illustrated in **Fig.1.1**. Glycolysis and OxPhos, interconnected via the TCA cycle, are considered the major ATP-generating pathways for cells to maintain optimal and constant energy levels.

Glycolysis, occurring in the cytosol, produces energy without the involvement of molecular O_2, with each glucose molecule with six carbon atoms split into two three-carbon pyruvates. It has a sequence of 10 reactions, each catalyzed by a different enzyme, producing intermediate compounds such as glucose 6-phosphate (G6P), fructose 6-phosphate (F6P), glyceraldehyde 3-phosphate (G3P), 3-phosphoglycerate, phosphoenolpyruvate and pyruvate [6]. The process requires two ATP to drive the initial steps, but in the end, it produces four ATP, two NADH molecules and two pyruvates. The pyruvates produced in the cytoplasm have several fates: 1) convert into lactate, which is then extruded resulting in (extra)cellular acidification in eukaryotic cells and O_2-deprived tissue; 2) diffuse into mitochondrial matrix to be utilized in the Krebs cycle or OxPhos with large energy generation; 3) participate in other reactions such as the synthesis of amino acids [7].

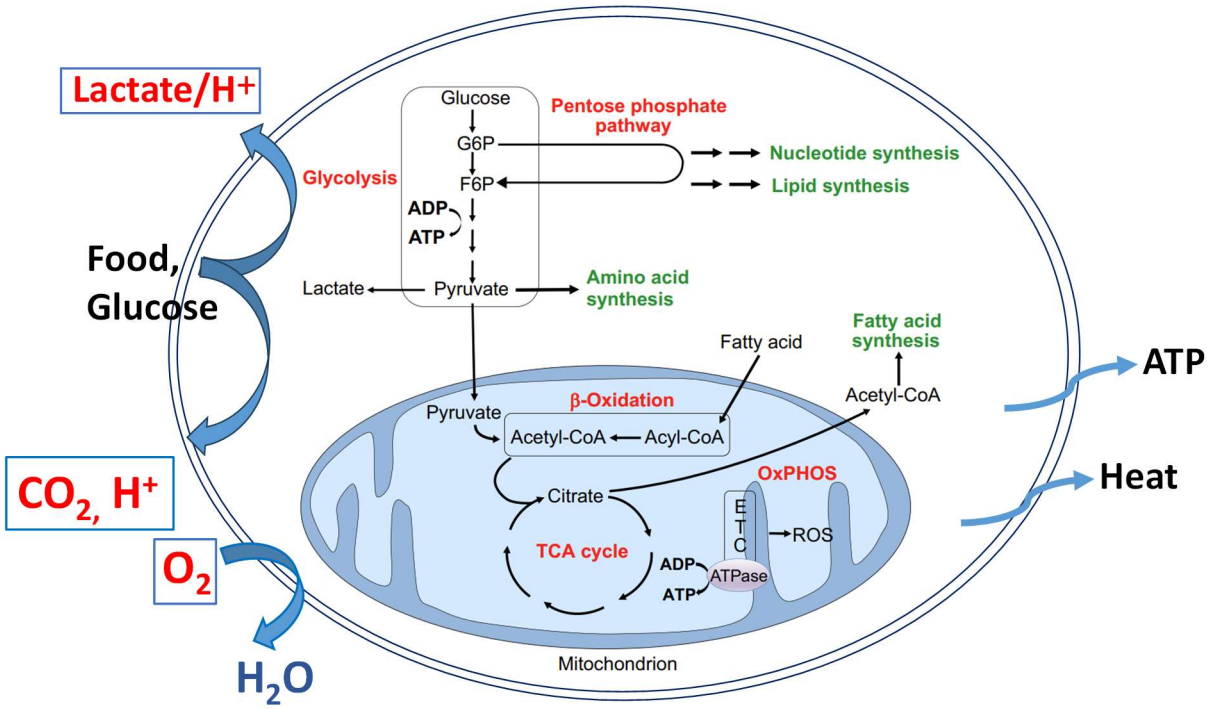

Figure 1.1. The scheme of metabolic pathways in eukaryotic cells (modified from [8]). F6P, fructose-6-phosphate; G6P, glucose-6-phosphate; ADP, adenosine diphosphate; ATP, adenosine triphosphate; ATPase, ATP synthase; TCA, tricarboxylic acid. ETC, electron transport chain; ROS, reactive oxygen species.

The TCA is a critical pathway for the inter-conversion of various metabolites including lipids, saccharides, and amino acids. Acetyl-CoA combines with oxaloacetate (OAA) to form six-carbon citrate, which is gradually oxidized in a series of enzymatic reactions and returns back to OAA. Acetyl-CoA can be obtained from various sources, including the oxidative decomposition of pyruvate, fatty acid β-oxidation, degradation of amino acids tryptophan, leucine, and isoleucine, or transport of citrate across the mitochondrial membrane via solute carrier family 25 (SLC25A1) and of conversion back into acetyl-CoA [9]. The net result of one TCA cycle are two molecules of CO_2, and energy-rich carriers: one GTP (guanosine triphosphate), three NADH, and one $FADH_2$, which are further supplied to the ETC to ultimately generate the ATP via the OxPhos.

The OxPhos is the most efficient ATP-generating pathway that occurs in the inner mitochondrial membrane, where the ETC and ATP synthase are coupled to produce the ATP. The electron carriers NADH and $FADH_2$, produced by anaerobic glycolysis, fatty acid β-oxidation, pyruvate breakdown and TCA cycle, shuttle the electrons to the ETC via the four enzyme complexes. The complexes harness the flow of electrons to pump protons across the

inner membrane forming a proton gradient, which in turn, flows back through ATP synthase and drives the phosphorylation of ADP to ATP (**Fig.1.2**). The four enzyme complexes in the ETC are: NADH dehydrogenase (Complex I), succinic-ubiquinone reductase (Complex II), cytochrome c reductase (Complex III), and cytochrome c oxidase (Complex IV). Complexes I and II are the main entry routes for electrons from NADH and $FADH_2$ into ETC. Rotenone can inhibit Complex I, and malonate - Complex II. The mobile carriers of electrons ubiquinone (CoQ) and cytochrome c (Cyt c) are coupled by Complex III. The latter can be inhibited by antibiotic antimycin A (Ant A), disrupting the ATP synthesis and resulting in the formation of superoxide radical ($\bullet O_2^-$), the main source of ROS toxic to cells [10]. Complex IV acting as a proton pump, also supplies the electrons from Cyt c to O_2. Competitive inhibitors for Complex IV include cyanide, nitric oxide and carbon monoxide. Oligomycin and FFCP are the common drugs that disturb ATP synthesis, the former inhibits ATP synthase (Complex V) and the latter is a potent uncoupler which dissipates proton gradients.

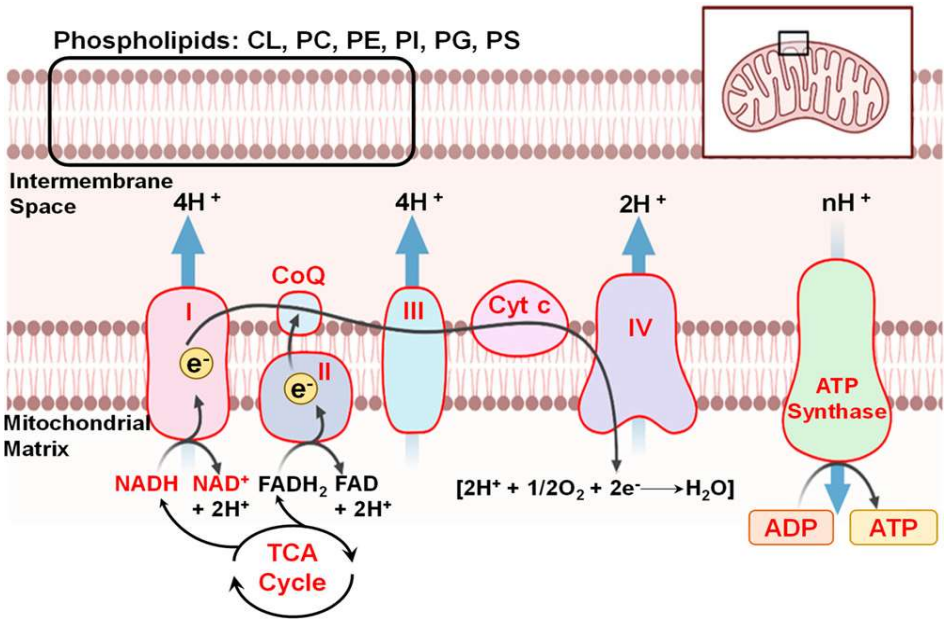

Figure 1.2. The schematic diagram of ETC in the inner mitochondrial matrix [11].

The PPP which branches from the upper part of glycolysis, is pivotal for synthesizing ribonucleotides and maintaining cellular redox homeostasis [12]. It comprises irreversible oxidative and reversible non-oxidative phases. In the oxidative phase, G6P originated from glucose is converted enzymes into ribulose-5-phosphate (Ru5P) and two NADPH molecules [13]. NADPH is used in fatty acid biosynthesis and scavenging of reactive oxygen species (ROS). In the nonoxidative phase, Ru5P is transformed into ribose-5 phosphate (R5P), which

is used for the purine and pyrimidine biosynthesis. The non-oxidative phase is controlled by the transketolase (TKT) and transaldolase (TALDO) enzymes, producing glycolytic intermediates, such as F6P and G3P, to be recruited into PPP and vice versa [14].

β-oxidation is the catabolic reaction where fatty acids (FAs) are broken down to acetyl-CoA by removing the β-carbon from the carboxylic end of long-chain acyl-CoA molecules. The overall reaction cycle can be presented as follows: C_n-acyl-CoA + FAD + NAD^+ + H_2O + CoA → C_{n-2}-acyl-CoA + $FADH_2$ + NADH + H^+ + acetyl-CoA. The negatively charged free FAs are impermeable to biological membranes, so they are transported into the mitochondrial matrix by proteins, such as the SL27, to take part in the four β-oxidation reactions [15, 16]. In each cycle, one molecule of acyl-CoA, one $FADH_2$ and NADH molecules, and a truncated acyl-CoA are generated. Then the shortened acyl-CoA re-enters the new oxidation cycle.

Overall, anaerobic glycolysis coupled with PPP converts carbohydrates to ATP, NADH, and pyruvate, and releases lactate in extracellular environment. The pyruvate is transported into the mitochondrion to produce acetyl-CoA (or from β-oxidation and other pathways), which is further oxidized via the TCA cycle to generate NADH, $FADH_2$, and CO_2 waste. When oxygen is available, the energy-rich carriers shuttle the electrons through the ETC, generating proton gradients and transmembrane potential. Then ATP synthase is driven when protons flow back into the mitochondrial matrix, generating the majority of ATP. These bioenergetic pathways are interlinked to meet cellular energy demand, maintain cellular homeostasis, and provide versatile cellular functions.

1.2 Optochemical Sensors

Optochemical sensors for environmental parameters are becoming increasingly popular in life science and biomedical research. Their advantages include simple and non-invasive measurements, portability and miniaturization potential (from cm to mm down to nanometer size), reversibility, no analyte consumption, imaging capabilities, low costs, manufacturability [17, 18]. A broad variety of different sensing materials, indicator dyes, integrated analytical platforms, and methods have been described, some of which have found use in clinical diagnostics, biotechnology, environmental monitoring, microbiology, and food safety [19-21].

Among these systems, sensors for monitoring molecular O_2 and proton ion concentration (i.e. $[H^+]$ or pH) are of major importance as they can provide detailed information of the major metabolic fluxes. One of the most popular and versatile analytical measurements for pH/O_2 sensing is based on photoluminescence technology, which has been widely used in various

complex biological samples such as live cells. In the last few decades, this technology has largely benefited from the rapid development of related disciplines, including organic and material chemistry, nanotechnology, microscopy, and semiconductor optoelectronics. Optical sensing techniques have significant advantages over the traditional glass pH electrode and Clark-type oxygen electrode, including: contact-less or minimally invasive measurements, no consumption of analytes, internal referencing and imaging capabilities, tuneable spectral characteristics, selectivity and sensitivity, versatile sensor formats including soluble probes and nanoparticles, solid-state coatings and planar films, fibre-optic probes and integrated devices [22].

The Cambridge definition of a chemical sensor is [23]: *Chemical sensors are miniaturized devices that can deliver real-time and online information on the presence of specific compounds or ions in complex samples*. Some terms frequently used in optochemical sensors and their hierarchy are presented in **Fig.1.3**. Indicator dyes are chemical structures that can respond to the analyte of interest (e.g. pH/O_2) by changing their intrinsic optical characteristics. The indicator dye can then be formulated as a liquid probe or a solid-state composite material which possesses the desired sensitivity and selectivity to the analyte. Such analyte-sensitive material can be further coupled with a suitable assay substrate and an optical detection system (standard or custom-built), to produce a self-contained sensor, sensing unit or array platform, capable of analyte detection and quantification. Finally, deep integration of the sensor unit/array with detector and ancillary components (e.g. T control, manipulations, sample/reagent addition, software) produces a sensing system tailored to a specific sensing application.

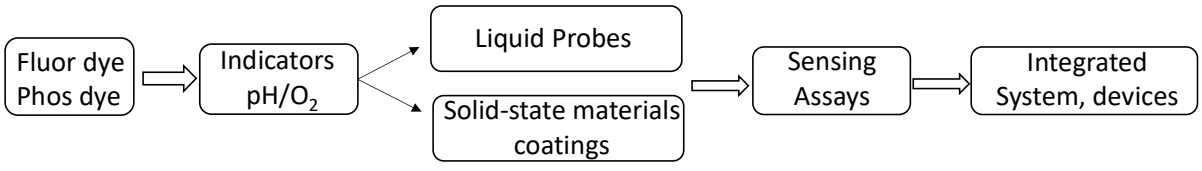

Figure 1.3. The hierarchy of the main terms used in the thesis and broadly in chemical sensors.

1.3 Phosphorescent O_2 Sensors

1.3.1 Principles of Quenched-Luminescence O_2 Detection

Optochemical O_2 sensors use dedicated phosphorescent indicator dyes with long-lived excited triplet states (T_1), quenched by O_2 molecules via the dynamic (i.e. collisional) mechanism. The energy transitions involved in the quenched-luminescence O_2 detection are illustrated in **Fig.1.4**. Upon light excitation, ground state (S_0) molecules absorb photons and get promoted to S_1 state or higher S_2 state. The subsequent relaxation by internal conversion (IC) and intersystem crossing (ISC) gives rise to photon emission, seen as fluorescence (from S_1) and phosphorescence (from T_1), respectively.

The $T_1 \rightarrow S_0$ transition involves the spin change, therefore the process is much slower than fluorescence (μs-ms vs ns ranges, respectively). As a result, the long-lived triplet states can undergo collisional interactions with O_2 molecules, which cause their rapid radiationless deactivation to the ground state. Since the energy of the long-lived excited state (T_1) is higher than the excited states of O_2 ($^1\Sigma g^+$ and $^1\Delta g$), energy transfer from the dye to O_2 is very efficient.

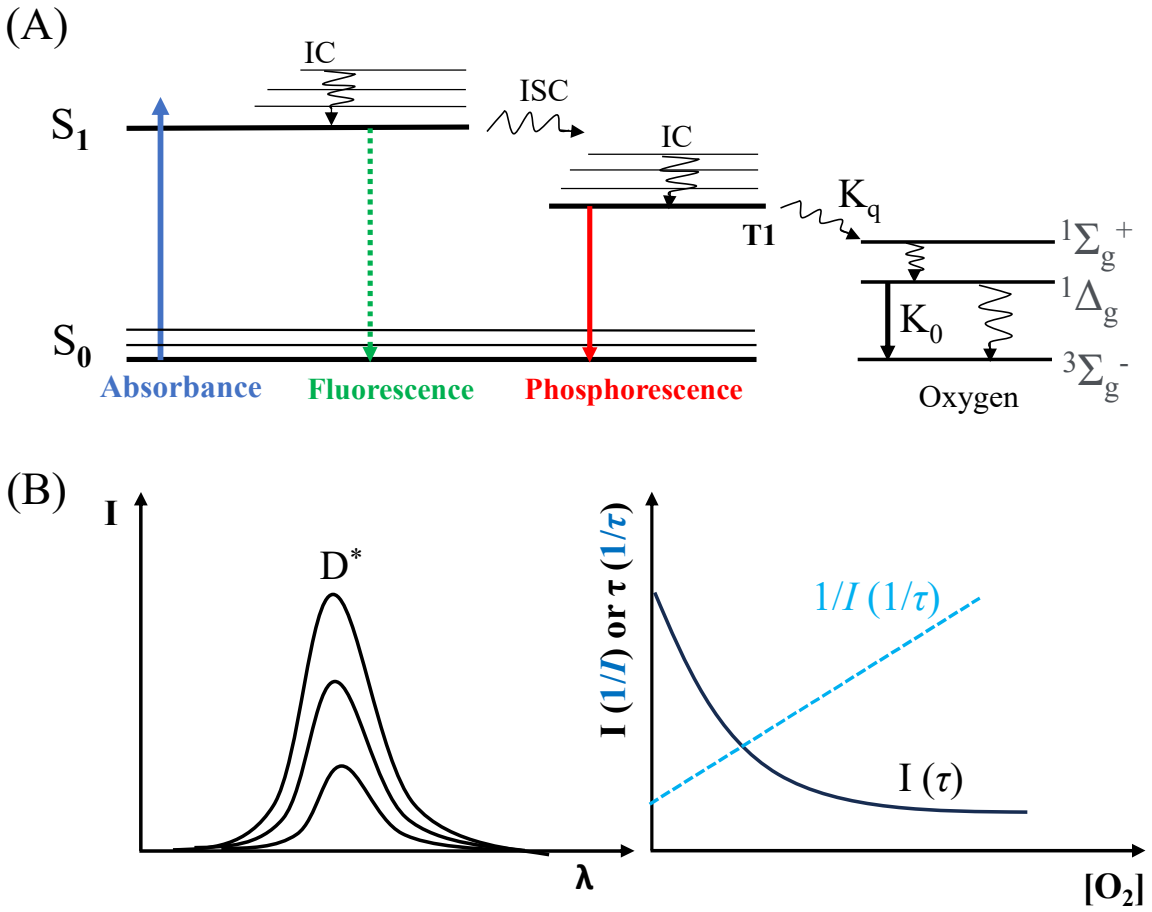

Figure 1.4. The general photophysical scheme of an optical O_2 sensor. (A) The modified Perrin-Jablonski diagram of energy transitions. (B) Quenched-phosphorescence O_2 sensing: changes in phosphorescence spectra, primary optical signals (I and τ) and reciprocal signals $1/I$ and $1/\tau$. S_0: ground state, S_1: first excited state, IC: internal conversation, ISC: intersystem crossing, T_1: excited triplet state, $^3\Sigma g^-$: paramagnetic ground state of O_2, $^1\Sigma g^+$: a short-lived state, $^1\Delta g$: singlet oxygen. D*: excited stated indicator dye, I: intensity, τ: lifetime.

During this process, the ground state paramagnetic O_2 ($^3\Sigma g^-$) causes the luminophore T_1 state to undergo ISC to the ground state S_0, while O_2 accepts the energy and gets excited to a short-lived state ($^1\Sigma g^+$), and subsequently to a low energy singlet oxygen ($^1\Delta g$ or $^1O_2$) state. Singlet oxygen, $^1\Delta g$, one of the major by-products of the phosphorescence quenching, is highly reactive, but has a short lifespan. It rapidly returns back to $^3\Sigma g^-$ state, but it can also react with adjacent molecules.

In simple terms, quenching of a luminophore by O_2 can be described by the following scheme of photochemical reactions:

$D_0 + hv_1 \rightarrow D^*$ - excitation

$D^* \rightarrow D_0 + hv_2$ - phosphorescence emission

$D^* + O_2 \rightarrow D_0 + {}^1O_2$ - quenching

According to this scheme, the last two processes compete with each other, such that the collisional interaction with O_2 decreases the phosphorescence lifetime (PLT) and intensity (I) or emission quantum yield (ϕ) of the luminophore, in a manner dependent on O_2 concentration [24]. The two primary signals, I and PLT, decay steadily towards zero levels with increasing O_2 concentration (or partial pressure, while their reciprocal values ($1/I$ and $1/\tau$) show an upward linear trend. At the same time, O_2 quenching process does not alter the shape of UV-Vis absorption ($S_0 \rightarrow S_n$), fluorescence ($S_1 \rightarrow S_0$) and phosphorescence ($T_1 \rightarrow S_0$) spectra of the indicator dye (see Fig. 1.4B).

The relationship between O_2 concentration and measured parameters of phosphorescence (I or τ) is often presented in the form of Stern-Volmer (SV) plots: I_0/I or τ_0/τ vs $[O_2]$ – see Fig. 1.4B. In the ideal case of homogeneous population of dye molecules, it is described by the following SV equation:

$$I_0/I = \tau_0/\tau = 1 + k_q * \tau_0 * [O_2] = 1 + K_{sv} * [O_2] \qquad \text{(Eqn.1.1)}$$

where I_0 and I, τ_0 and τ are the phosphorescent intensity (I) and decay times (τ) in the absence and presence of $[O_2]$, respectively; k_q is the bimolecular quenching rate constant, which depends on the environment of the luminophore, steric factors and temperature; K_{sv} is the Stern-Volmer quenching constant.

Different luminophores have different τ_0, I_0/ϕ_0, k_q and K_{SV} values, and therefore they show different O_2 quenching efficiency. Intensity-based detection, although more simple, is dependent on luminophore concentration, measurement geometry and other factors [25]. Whereas τ or PLT, the average time that luminophore molecules stay in T_1 state before emitting photon, is an intrinsic characteristic of the luminophore, independent on its concentration. Therefore, PLT is more a favourable optical readout for O_2 sensing. For different phosphors, PLT can vary from less than 1 μs to many milliseconds. Such PLTs are easy to measure, unlike the nanosecond (ns) lifetimes of fluorescent molecules which require short excitation pulses and high-speed detectors.

Based on **Eqn.1.1**, $[O_2]$ can be calculated as follows:

$$[O_2] = (I_0 - I) / (I^* K_{SV}) \qquad \text{(Eqn.1.2)}$$

$$[O_2] = (\tau_0 - \tau) / (\tau^* \tau_0^* k_q) \qquad \text{(Eqn.1.3)}$$

Note that **Eqn.1.2-1.3** are valid only for homogeneous populations of luminophores, such as solution-based systems. They correspond to linear SV plots (I_0/I vs $[O_2]$ or τ_0/τ vs $[O_2]$), which in turn, allow for convenient two-point calibrations (e.g. at zero and ambient O_2). However, many phosphorescent O_2-sensitive materials, especially solid-state composites, show significant heterogeneity (e.g. in polymers), and exhibit nonlinear SV plots. For such cases, more complex mathematical models and multi-point calibration equations and fitting algorithms are required.

Calibration usually comprises a set of measurements of sensor signals (I or τ) at different (known) $[O_2]$ standards and constant temperature, to obtain the function of $[O_2] = f(I, \tau)$. The concentration of dissolved O_2 is influenced by oxygen partial pressure (pO2) in the gas phase (Henry's law), temperature and salinity. Thus, accurate standards of dissolved $[O_2]$ can be realized by filling up the system with different gas mixtures (e.g. O_2:N_2). Some commercial O_2 sensors operate with factory calibration [26], however applying these calibrations to other sensor materials, detection settings, instruments and platforms is not possible, as this may lead to significant instrumental errors and measurement artefacts. Temperature control should also be considered for O_2 calibration, since most O_2 sensitive materials are highly sensitive to sample temperatures.

1.3.2 O_2-Sensitive Indicator Dyes

The quenching effect of O_2 on luminophores was first observed in the 1930s by Kautsky and Hirsch [27]. Since then, numerous sensing materials were reported. In 1957 Parker utilized a borate-benzo complex for monitoring gaseous O_2; In 1968 Bergman described a material based on polycyclic aromatic hydrocarbon (PAH) fluoranthene with rapid response to O_2 [28]. In 1983 a pyrene-butyric acid based system was applied for O_2 quantitation, prompting the rapid development of various sensor materials [29]. However, the short lifetime of such PAH indicator dyes (50-100 ns), low solubility in polymeric matrices, and the requirement of UV excitation limited the O_2 sensitivity and practicability of such sensors. While PAHs and other fluorescent dyes were important in early stages of sensor development, they were soon superseded by the fluorescent polypyridyl complexes of Ru (II) and Ir(III), and phosphorescent

metalloporphyrin dyes that were extensively studied in later years [30, 31]. The chemical structures and photophysical properties (e.g. spectral characteristics, brightness, luminescence decay time) of selected popular O_2 sensitive indicator dyes are given in **Fig.1.5** and **Table 1.1**.

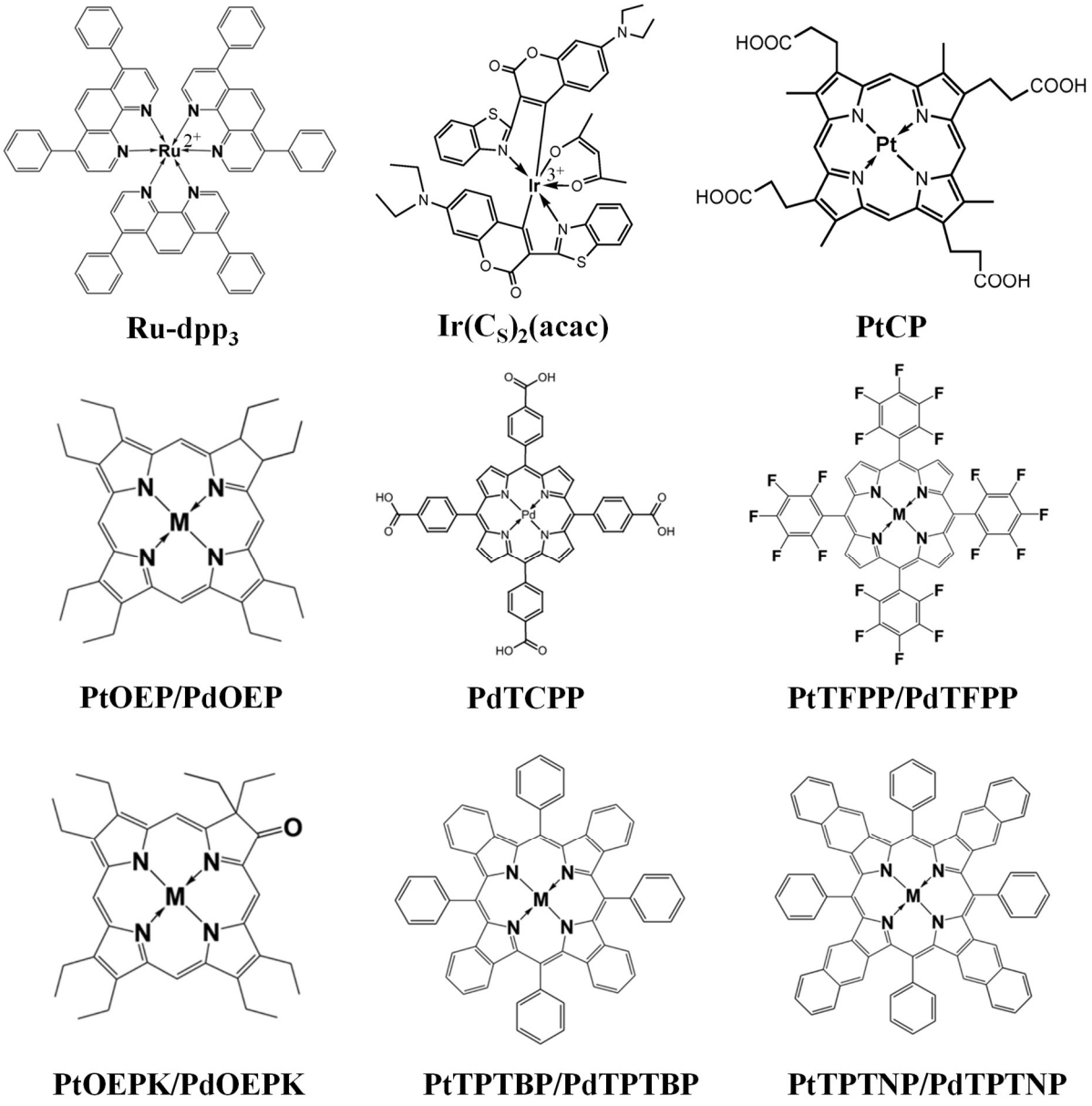

Figure 1.5 The chemical structures of common photoluminescent oxygen indicators. **Abbreviations**: Ru-dpp: ruthenium-tris(4,7-diphenyl-1,10-phenanthroline); $Ir(Cs)_2(acac)$: ruthenium(II) chloride; PtCP: Pt-coproporphyrin; PtOEP/PdOEP: Pt(II)/Pd(II)-octaethylporphyrin; PdTCPP: Pd-meso-tetra-(4-carboxyphenyl)-porphyrin-dendrimer; PtTFPP/PdTFPP: Pt(II)/Pd(II)-tetrakis(pentafluorophenyl) porphine; PtOEPK/PdOEPK: Pt(II)/Pd(II)-octaethylporphine-ketone; PtTPTBP/PdTPTBP: Pt(II)/Pd(II)-tetraphenyltetrabenzoporphyrin; PtTPTBPF/PdTPTBPF: Pt(II)/Pd(II)-6,13,20,27-terakis(4-fluorophenyl)tetrabenzoporphyrin; PtTPTNP/PdTPTNP: Pt(II)/Pd(II)-tetraphenyl-tetranaphthoporphyrin.

Table 1.1. Photophysical properties of common O_2 sensitive indicator dyes, at room temperature, in anoxic conditions (taken from [17, 22, 24, 32-35]).

Indicator dye	λ_{max} abs (nm)	λ_{max} em (nm)	τ_0 (μs)	Brightness, (ε ϕ)*($M^{-1}cm^{-1}$)	Medium
Ru-dpp_3	463	618	6.4	10582	EtOH-MeOH (4:1v/v)
Ir$(Cs)_2$(acac)	472, 444	563	11.3	50112	Chloroform
PtCP	380, 535	650	67	56000	3 mM CTAB
PdTCPP	415, 524	690	640	1900	DMF
PtOEP	382, 536	649	75	87740	Toluene
PdOEP	395, 547	669	1220	24130	Polystyrene
PtTFPP	394	648	60	28424	CH_2Cl_2
PdTFPP	407, 553	670	900	40320	CH_2Cl_2
PtOEPK	398, 592	758	60	10344	$CHCl_3$
PdOEPK	410, 603	789	445	826	$CHCl_3$
PtTPTBP	430, 614	770	47	104550	Toluene
PdTPTBP	443, 628	800	286	87360	Toluene
PtTPTBPF	430, 615	773	50	127200	Toluene
PdTPTBPF	443, 629	803	297	61640	Toluene
PtTPTNP	436, 689	883	8.5	20900	Toluene
PdTPTNP	463, 705	937	65	9360	Pyridine

ε: molar absorptivity; ϕ: phosphorescence quantum yield; τ_0: unquenched phosphorescence lifetime.

Ru(II)-tris(4,7-diphenyl-1,10-phenanthroline) (Ru-dpp_3), one of the brightest Ru(II) complexes, has unquenched lifetime up to 6.4 μs in the different matrices. Excitation of such dyes (including Ru-dpp_3) proceeds via a metal-ligand charge transfer process (MLCT), in which a metal d orbital electron is promoted to a ligand π* orbital. This results in an intense absorption band in the visible region (λ_{max}=463 nm), compatible with low-cost blue LED or diode laser (488 nm) excitation [17]. Other advantages of Ru(II) complexes, include good photostability, moderate brightness (still lower than porphyrins), inexpensive one-step synthesis, make them popular in early stage O_2 sensing systems, and even in some modern ones. On the other hand, the dyes have many limitations: the relatively short lifetimes leading to low O_2 sensitivity in common polymer matrices (e.g. polystyrene); modest molar absorption coefficients; broad excitation and emission bands. This makes them not very selective in multi-dye and multi-analyte sensing systems, requiring expensive filters and instrumentation. Also emission of Ru(II) dyes is strongly influenced by temperature since their triplet states subject to rapid thermal inactivation [36, 37].

Another group of common indicator dyes are polypyridyl complexes of Ir (III). Unlike Ru(II) complexes having a non-emitting metal-centered excited state, Ir(III) complexes are efficient triplet state emitters. Being essential functional components in organic LEDs, these dyes have good solubility in organic polymers, in which they show high quantum yields (0.2~1.0) and longer lifetimes (e.g. 11.3 μs for $Ir(C_S)_2(acac)$) than Ru(II)-complexes. However, these dyes are less photostable, which limits their long-term O_2 sensing and imaging applications [38].

Platinum (II) and palladium (II) complexes of porphyrins and some related structures (e.g. benzoporphyrins, porphyrin-ketones), are among the most popular and commonly used indicators in O_2 sensors. Pd/Pt-porphyrins possess practically no fluorescence and strong room temperature phosphorescence in the microsecond time range, which originates from the porphyrin macrocycle and is strongly quenched by O_2. Metalloporphyrins have been extensively used in solid-state O_2-sensitive materials (polymers) and in liquid probe formulations, performing well in complex biological samples and at physiological conditions (temperature, pH, salinity, additives). Their advantages include: commercial availability and well-developed synthesis; unique and convenient spectral and photophysical properties, relatively broad range of PLTs, and moderate photostability. Porphyrin structures are also easy to chemically modify and tailor to various applications.

Metalloporphyrins exhibit PLTs in the range of 40-100 μs for Pt-porphyrins (e.g. PtCP, PtOEP, PtTFPP) and 3-10 times longer for Pd-porphyrins (e.g. PdTCPP, PdOEP, PdTFPP), which translates into their O_2 sensitivity from moderate to high. Pt(II) complexes also exhibit 2-3 fold higher quantum yields than their Pd(II) analogs (e.g. PtOEP vs PdOEP). All metalloporphyrins have intense absorption band with a maximum at around 350-450 nm (called the Soret band), and also less intense absorption bands in the visible range 500-550 nm (Q-bands), and well-resolved emission bands in the range of 630-700 nm. They display high brightness upon photoexcitation at the Soret band (e.g. with a 405 nm diode laser), and allow sensitive detection on standard fluorescence spectrometers and readers (e.g. BMG, Victor 2 reader, Cary Eclipse) and on fluorescent microscopes.

Some related tetrapyrrol structures including Pt- and Pd- complexes of benzoporphyrins, porphyrin-ketones present longwave-shifted and enhanced absorption Q-bands (at > 600 nm) and near-infrared emission at 700-900 nm. Such dyes are well-suited for *in vivo* use in live animals and tissue samples, but less compatible with standard PMT detectors [39]. Popular Near-infrared (NIR) emitting dyes include PtOEPK, PdOEPK, PtTPTBP, and PtTPTBPF.

Phosphorescence of these indicators is high or moderate, except for Pd-porphyrin-ketones which show weak phosphorescence (e.g 10 times lower for PdOEPK than PtOEPK). In contrast, PtTPTBP and PdTPTBP exhibit very high molar absorption coefficients and quantum yield of phosphorescence [40]. Also some halogenated derivatives, such as PtTPTBPF and PdTPTBPF, have improved emission yield and photostability, compared to PtTPTBP/PdTPTBP [41]. Pt- and Pd- tetranaphthoporphyrins (TPTNP) have further red-shifted spectra, as compared to PtTPTBP/PdTPTBP, however their brightness and photostability are significantly lower.

1.3.3 O_2 Sensing Materials and Formats

For optimal performance, sensor chemistry must be tailored to targeted applications. Specifically, photophysical properties (brightness, photostability) of Pt-porphyrin based sensors can be fine-tuned by the macrocycle structure (e.g. TFPP, TPCTBP). For example, PtTFPP is more photostable than PtOEP, but on the other hand its brightness is several times lower [22]. The sensitivity to O_2 can be tuned via K_{SV}, k_q, τ_o, e.g. by introducing dendritic shells [38], embedding the dye in different polymeric matrices (e.g. polystyrene, sol-gel, ethyl cellulose, polyvinylchloride), or replacing the central metal ion in the macrocycle (e.g. Pd-porphyrins) [42]. For example, Pt- porphyrins are better suited for measuring ambient O_2 (0-500 µM in water or 0-100 kPa in gas), whereas for corresponding Pd-porphyrins the range is shifted down 10-fold to 0-50 µM. O_2 quenching ability is also influenced by the dye micro-environment (e.g. polymeric matrix, sensor components, and materials), and macro-environment of the dye molecules (e.g. temperature, humidity, ionic strength, pH values, other quenchers or binding reagents) [24]. Hydrophobicity of the sensor material can be adjusted by conjugating a hydrophilic carrier to the dye parent structures, or by introducing polar side substituents in dye structure (e.g. CP, TPCTBP dendrimers). For example, O_2 sensing dyes such as PtPFPP and PtBP are hydrophobic and water insoluble. However, they can be rationally re-designed by organic chemistry means to enable water solubility and their intracellular transport and sensing of intracellular O_2 [22].

Polymer chemistry also plays major roles in sensor material chemistry. A polymeric host can act as an encapsulation for the indicator dyes but also perform the function as gas diffusion barrier and physical shield for the dye molecules and selectively permeable layer for other species.

The commonly used hydrophobic polymers for O_2 sensitive indicators include silicones and ormosils (organically modified silicones), polystyrene (PS), polycarbonate (PC), fluorinated polymers, polymethyl methacrylate (PMMA), poly(vinyl chloride) (PVC). To optimize mechanical properties of the sensing layer, its adhesion to the support, O_2 solubility and diffusivity, permeability of other species (e.g. H^+ and other ions), plasticizers may be also introduced into the polymer matrix. However, the O_2 permeation rate, mechanical stability, lipophilicity, and polarity of sensor material may be also changed [43].

The hydrophilic polymers used in O_2 sensors usually contain hydrogen-bonding function groups (e.g. hydroxyl, amino or carboxamide). Polyurethane hydrogels (e.g. hydrogel D4), poly(2-hydroxyethyl methacrylate) (pHEMA), and ethyl cellulose (EC) represent hydrophilic polymers having good ion diffusion in aqueous media, but their high water uptake may result in polymer swelling, which in turn can affect sensor performance. Ionic polymers (polyelectrolytes) allow the immobilization of oppositely charged dyes. Thus, anionic Nafion and polystyrene sulfonates can immobilize cationic dyes, while cationic polyanilines are suitable for anionic dyes [44].

The different types of O_2 sensing materials and formats are shown in **Fig.1.6**. Solid-state sensors represent the largest group. Traditionally, they comprise thin film (micrometer size) polymeric coatings deposited on a suitable substrate (e.g. polyester film, microplate, microporous membrane, sticker, the tip of optical fibre). For such deposition, a precursor liquid cocktail of the sensor components in organic solvent is used, which upon drying produces solid-state sensors. Alternatively, pre-made sensor coatings, membranes, spots or stickers can be incorporated in assay or vials, pouches of microfluidic devices to enable non-invasive and reversible O_2 sensing and quantification. The polymer matrix acts as a gas diffusion barrier in the solid-state sensor which shields the indicator molecules from various interfering species or contaminations. They have been extensively used in biomedical and biological research.

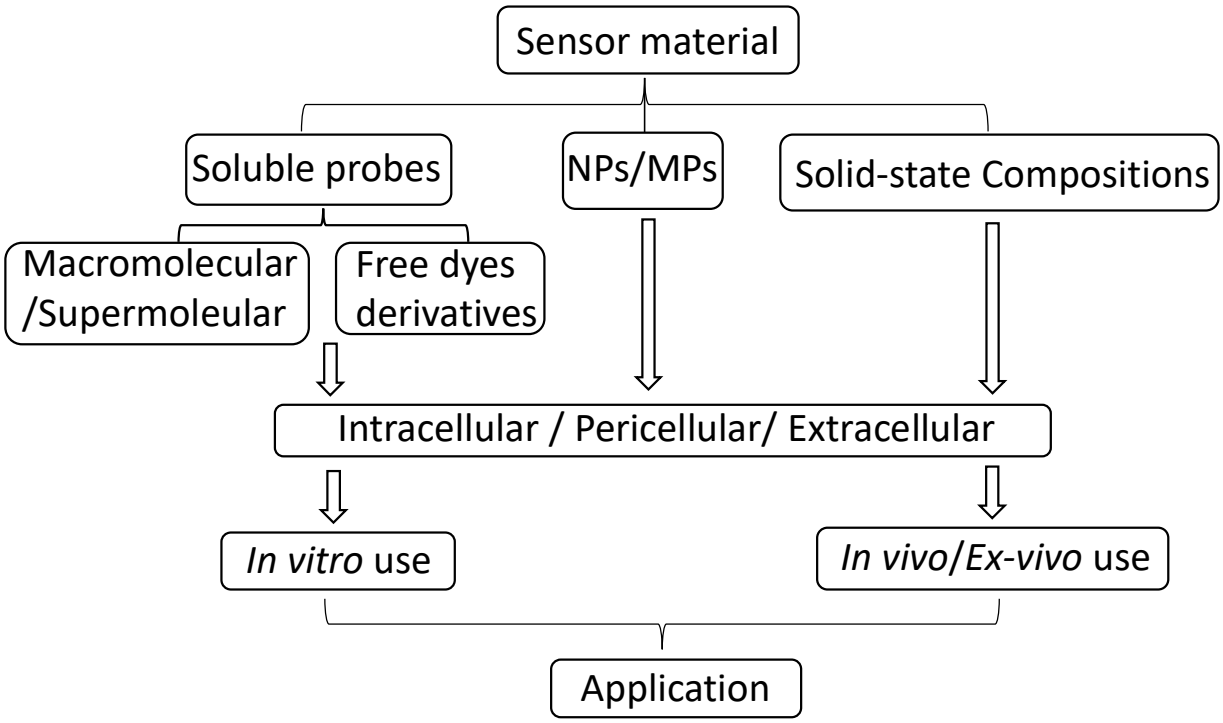

Figure 1.6 Classification of O_2 sensor system.

A range of solid-state O_2 sensors is commercially available, including the O_2 platinum OpTech sensor stickers from Mocon, the self-adhesive sensor spots (OXSP5) from Pyro science, the OXYPro® series oxygen probes from Presens, the dissolved oxygen sensors from Oxysense, and the bare-fibre O_2 sensors from Oxford Optronic [40]. The above examples prove the popularity of solid-sate sensors and their significant commercial potential in various applications and many scientific fields. However, the main drawback of solid-state sensors is the lack of flexibility.

Liquid O_2 probes can provide greater flexibility and have different structure. Examples include small molecule dyes, their conjugates, dendrimers and supramolecular structures [45, 46]. The main limitations of such probes include disposable, less convenient use and poor suitability for long-term operation and reuse. They also contaminate the samples, lack shielding and therefore are more prone to chemical and quenching interferences than solid-state sensors [40]. Despite the above, liquid O_2 probes enable a number of important sensing applications, including cell analysis, that are difficult to implement using solid-state sensors.

For example, the small molecule indicators, such as PdTPCPP, and PtCP derivates, which have moderate solubility in the aqueous samples, due to hydrophilic carboxylic and sulfonate groups present in their structures [47], can be added to cultured cells or injected in animal tissues for the subsequent *in vitro* sensing or imaging of O_2. However, the disadvantages of such probes

are their sensitivity to the sample environment (e.g. pH, ionic strength, other quenchers). Unlike solid-state sensors, they are not shielded by a gas diffusion barrier, and they can non-specific bind to surfaces, proteins and cells [38].

Supramolecular probes can partly improve this by conjugating hydrophilic macromolecular carriers (e.g. protein or PEG) to the porphyrin ring, thus making the probe cell-impermeable and keep it in solution [38, 48]. MitoXpress-Xtra is one example which uses a polypeptide carrier (BSA) covalently linked to an amino-reactive dye (PtCP-NCS). This extracellular probe was commercialized by Luxcel Biosciences (now owned by Agilent Technology), initially to assess the toxic effects of various compounds and drug candidates on mitochondrial function.

Dendrimer probes of Oxyphor R2 and Oxyphor G2 are both with 16 carboxylate groups on their Pd-porphyrin based outer layer, exhibiting high solubility in water and biological fluids. The maxima absorptions for Oxyphor R2 and Oxyphor G2 are 415 nm/524 nm and 442 nm/632 nm, with emission at 690 nm and 790 nm, respectively [49]. Both dendrimers have stable oxygen response in the physiological pH range (6.4-7.8).

Cell-penetrating supramolecular probes also exist, for example, PtCP conjugated with a 'delivery vector', such as polyarginine or proline-rich peptides, which enter the cells by passive transport and thus allow for sensing intracellular O_2 [50].

The third major group/format of O_2 sensing materials is represented by dispersed microparticles (MPs) and nanoparticle-based probes (NPs). Such materials, which combine the features of solid-state sensors and liquid probes, are under major development. Polymeric NP probes were prepared by incorporating indicator dyes during the emulsion polymerization of acrylamide or styrene [51], or by forming beads from amphiphilic polymers (e.g. RL-100, hydrogels) with core-shell nanostructure by precipitation method [52]. Thus, NanO_2 probe comprises an aqueous dispersion of cationic core-shell nanoparticles of an amphiphilic RL-100 hydrogel, with hydrophobic PtPFPP molecules physically trapped in their hydrophobic core. The polymer 'shields' the dye molecules from external environment and provides high brightness and optimal O_2 quenching ability. The NanO_2-IR probe is another O_2 sensitive probe, in which the PtPFPP dye is replaced by a long wavelength dye PtBP [41]. The probe with positive charges on the surface presents good brightness, photostability, and O_2 sensitivity with optimal excitation at 615 nm and emission at 760 nm [53]. However, they still have limitations, such as a larger size than small molecule and supramolecular probes, reproducibility of their

fabrication and sterilization, photostability during long-term storage, biocompatibility with some cells.

Of note, O_2 probes and sensors intended for use with live cells, tissues and animals also have stringent requirements with respect to their intrinsic and photo toxicity and safety, and these factors usually require thorough investigation and optimisation.

1.4. Photoluminescent pH Sensors

pH is a measure of acidity or basicity of an aqueous solution, one of the most frequently analysed parameters. pH is related to the concentration of photons $[H^+]$ in solution as: $pH = -\log([H^+])$. pH varies 0-7 in acidic solutions and 7-14 in alkalic solutions. Physiological pH values usually range between 6.0 and 8.0, spanning down to pH 4-6 for some specialized cellular compartments [54]. Accurate quantification and monitoring of pH in cells, tissue samples and biological fluids are important for biomedicine, biotechnology, food quality, and chemical sciences [55].

The gold standard for pH analysis is the glass pH electrode, which provides rapid, stable and reliable voltage readout proportional to sample pH, in a wide pH range. Basic combined pH electrodes operate on standard pH meters, they are calibrated individually and regularly with pH buffer standards, have T-compensation and are relatively easy to operate. However, the limitations of pH electrodes include their invasiveness, significant size (>1 mm, even if miniaturized), susceptibility to electrical interferences, difficulty of sterilization, and rigid design. pH electrodes are poorly suitable for biological samples containing cells due to biofouling [56]. Therefore, new approaches to pH monitoring are in high demand.

Photoluminescent pH sensors can provide a good alternative to pH electrodes, as they allow simple, non-invasive measurement of pH in multiple samples and visualisation of localized pH gradients by imaging techniques. The sensors are suitable for both *in vitro* and *in vivo* measurements, they show flexibility, robustness, accuracy, biocompatibility and multiplexing capabilities with many other sensors and probes [57, 58]. It is also possible to develop pH sensors with internal referencing, which allows for calibration-free operation, high specificity, brightness, reversible and rapid response to pH changes, and tuneable pH range. They can also operate in different detection modalities and on available instruments. All the above merits make optochemical pH sensors and sensing materials increasingly popular. However, their limitations include: narrow working range (2-3 pH units), non-linear calibration (sigmoidal), and sensitivity to ionic strength, temperature and some other species.

The following parameters should be considered when selecting and evaluating luminescent pH sensors: 1) suitable pKa values and good compatibility with matrix chemistry for the desired application; 2) robust and reversible spectral, intensity or lifetime response upon the pH change. Sensors based on far-red and NIR emitting indicators are favourable for *in vivo* applications, owing to the lower impact of light scattering and background fluorescence and deeper light penetration into tissue; 3) high brightness and photophysical signal for pH sensing and imaging; 4) large Stokes shifts to allow the collection of entire luminescence without parasitic excitation; 5) good photostability and no dye leaching during the practical applications; 6) biocompatibility.

1.4.1 Principles of Luminescence pH Detection

The photophysical scheme of a traditional optical pH sensor is shown in **Fig. 1.7A**, and of a sensor which is based on the process of photoinduced charge (proton or electron) transfer (CT or PET) is shown in **Fig.1.7B.**

In the traditional scheme, upon protonation the indicator dye D changes its aromatic electronic structure. In this ground state protonation process, the electronic levels and corresponding spectra of DH^+ are changing compared to those of D (**Fig.1.7A**, dashed lines), and the corresponding changes in absorption, fluorescence or phosphorescence are used for pH sensing **(Fig. 1.7C-E**).

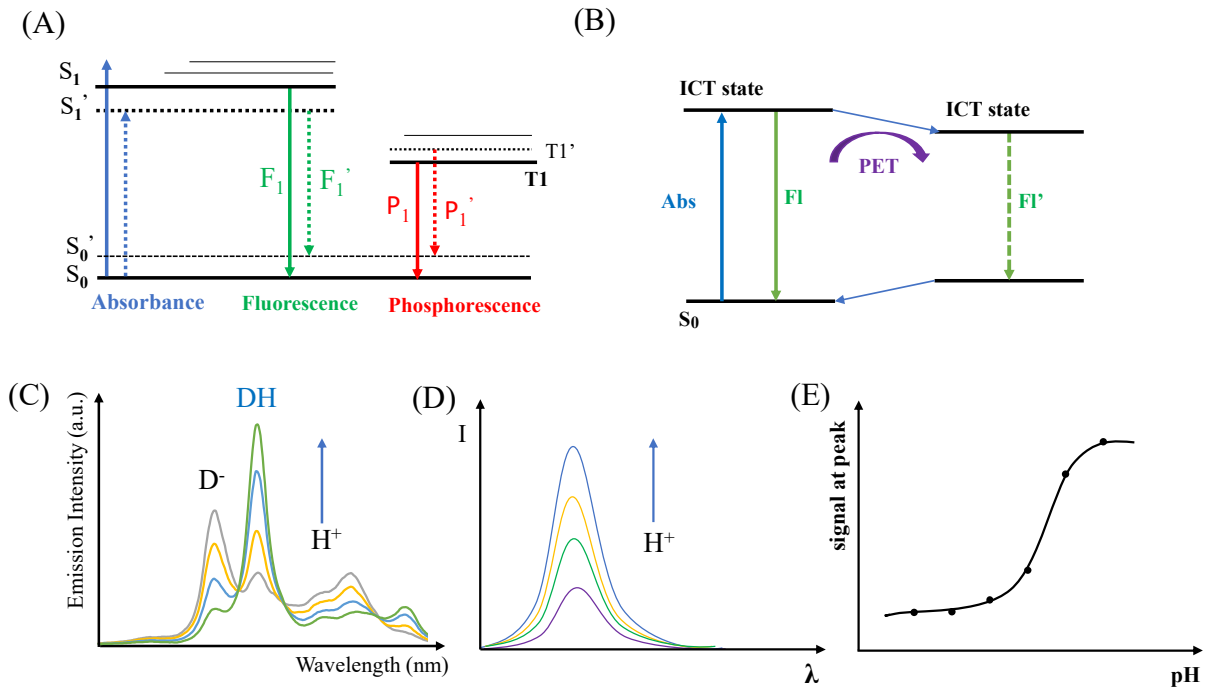

Figure 1.7. The general photophysical scheme and process of photoinduced proton transfer quenching of an optical pH sensor [33, 59] . (A) The modified Perrin-Jablonski diagram. (B) the scheme of photoinduced proton transfer. (C-E) Luminescent principle for pH sensing. S_0: ground state: S_1: first excited state; F_1: fluorescence; P_1: phosphorescence; T_1: excited triplet state; S_0', S_1', F_1', P_1' and T_1': energy transitions of protonated dye form; ICT: internal charge transfer.

If both protomeric forms D and DH^+ fluoresce, then interconversion of the two spectral forms will be seen upon dye protonation/deprotonation (Fig. 1.7C). If one protomeric form of the indicator is non-fluorescent, then sensor Abs and fluorescence intensity will change without any spectral changes in fluorescence (Fig. 1.7.D). Changes in emission lifetime may also occur, but these are more difficult to predict.

In contrast, PET is an excited state process in pH sensing, which mainly affects the fluorescence characteristics (Fig.1.7B). During PET process, a hydrogen ion (proton) or a certain group in the dye structure can be transferred to the adjacent heteroatoms (e.g. N, S, O) in the molecule, thus causing complete quenching or a change in the emission spectrum. In the PET scheme of pH sensing, absorbance spectra are usually not affected, while fluorescence of the ionised form (D or DH^+) is quenched (Fig. 1.7.D). Thus, redistribution of energy levels of the dye upon its (de)protonation, characteristic changes in its fluorescence/phosphorescence or absorption

spectra, intensity or lifetime values are observed, and these changes can be utilized for the optochemical sensing of pH (Fig.1.7C-E).

The different schemes used in pH sensing can be described with the following reactions:

$D + HB \rightleftharpoons DH^+ + B^-$ - ground state (Eqn.1.4)

$D^- + H^+ \rightleftharpoons DH$ (Eqn.1.5)

$D^* + HB \rightleftharpoons D^*H^+ + B^-$ - excited state (Eqn.1.6)

And pH quantification is based on the Hendersson-Hasselbalch scheme and the following equations 1.7 - 1.8 (derived from Eqn. 1.5):

$pH = pK_a + \log([D^-]/[DH])$ - dye concentrations (Eqn.1.7)

$pH = pK_a + \log((I-I_{DH})/(I_{D^-}-I))$ - signals (Eqn.1.8)

Where [DH] and [D^-] are the concentration of protonated and deprotonated dye form; I_{DH} and I_{D-} are the maximal and minimal emission signals (Abs, Flu or LT) at two extreme (low and high) pH values; K_a is the acidity constant of D; pK_a is the negative logarithm of K_a.

1.4.2 pH-sensitive Indicators

The commonly used photoluminescent pH indicators can be classified into two main groups: fluorescent pH indicators and metal-ligand complexes. Fluorescent pH indicators have been extensively studied; whereas metal-ligand complexes have received less attention.

Fluorescent pH indicators can exhibit a bathochromic shift in acidic solutions (e.g. quinines, acridines) or a bathochromic shift in basic solutions (e.g. phenol, sulphonamides) [60]. Metal-ligand complexes display long decay times and can be measured in time-resolved fluorescence (TRF) mode for pH sensing or imaging. However, only a small number of them present good brightness at room temperature, which mainly comprise Pt(II) or Pd(II) porphyrins, Ru(II) or Ir(III) polypyridyl complexes, and lanthanide chelates [23].

The most commonly used luminescent pH indicators include HPTS, coumarins, fluorescein and rhodamine dyes and derivatives thereof. The chemical structures of selective luminescent indicators are shown in **Fig.1.8**.

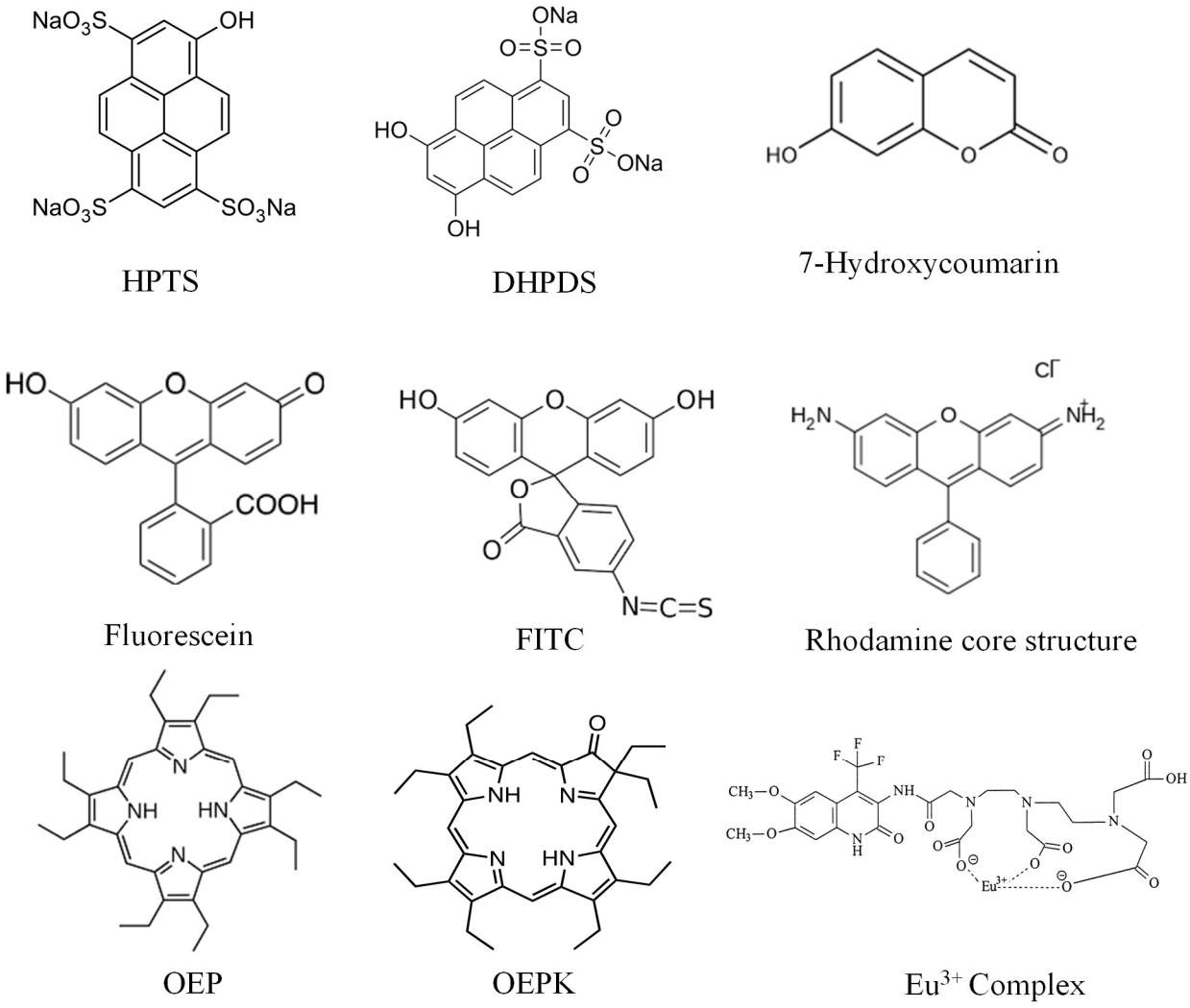

Figure 1.8. The selective luminescent pH indicators for optical sensing [17, 35, 61].

HPTS and derivatives. HPTS (8-Hydroxypyrene-1,3,6-trisulfonic acid) has been widely used as a commercial fluorescent pH indicator, which is a hydrophilic molecule with a pKa at ~7.3 (Ex=460 nm, Em= 510 nm). Since its pH response and the pKa value of its hydroxy group is close to the cell physiological range, it has been extensively used for biological pH sensing [62]. HPTS is highly charged, thus requiring covalent immobilization or chemical modification to minimize dye leaching and ionic strength interference. For example, the lipophilic derivatives of HPTS embedded in hydrogel D4, PVC, or polystyrene matrix possessed negligible leaching [63]. However, the spectral characteristics of HPTS are also affected by the derivatizations resulting in bathochromic shifts of the emission peaks. DHPDS (6,8-dihydroxypyrene-1,3-disulfonic acid) shares most of the advantages of HPTS including high quantum yield, good water solubility, and low cytotoxicity. The two hydroxy groups of its

structure (pKa of 7.33 and 8.53) can provide dual excitations and radiometric readouts for pH sensing [64].

Coumarins and derivates. 7-Hydroxycoumarin, also called hydrangine, skimmetine, or beta-umbelliferone, is a yellowish-white crystalline solid with poor solubility in water. It exhibits emission at ~455 nm under the excitation of 360 or 400 nm in the acid or basic forms. The dye shows relatively low brightness and photostability compared to HPTS. However, not all coumarin dyes and derivatives have fluorescent dependence upon protonation and deprotonation. For example, coumarin 6 (C6, Ex=450, Em=505 nm) is a yellowish pH-insensitive hydrophobic dye with a small molecular weight (350.4 g/mol) and high quantum yield (0.78), which has been widely used in drug delivery systems for the studies of cellular uptake and transport mechanisms [65].

Fluoresceins and derivatives. Fluoresceins based on the xanthene tricyclic structure, are among the most common fluorescent tracers for in biomedical applications. It is a dark orange powder with a low solubility in water. It exhibits green emission at ~515-520 nm under the excitation at 490 nm. The most common protonation/deprotonation mechanism in the aqueous solution for fluorescein is based on the deprotonation of carboxylic acid and phenolic groups (e.g. neutral species and monoanionic forms for protonation, and dianion form for deprotonation) [66]. FITC (fluorescein isothiocyanate) is an activated derivative of fluorescein, which features an isothiocyanate group (-N=C=S), has wide-ranging applications in antibody labelling, protein conjugation, and flow cytometry. It has maximum excitation at ~495 nm and emission at ~ 525 nm. These spectral properties are compatible with a standard 488 nm laser, suitable for the measurements on fluorescence microscopy or immunofluorescence. The disadvantages of fluorescein-based dyes are their relatively high photobleaching rate and broad-spectrum ranges, which limits their selective and multi-analyte labelling [67].

Rhodamine dyes also belong to the xanthene family, having high fluorescence quantum yields, molar absorption coefficients, brightness, resistance to photodegradation. They are widely available commercially (e.g. Rho B, Rho 6G, Rho19) and used in many applications [68]. The pH responsiveness of Rhodamine dyes is typically achieved by the introduction of photoinduced electron transfer (PET) groups or the opening of spirolactam structure [23]. Their pKa values can be adjusted by altering the substitution of its spirolactam structure. For example, by incorporating larger substituents which alter the xanthene ring system of the aniline-derived rhodamine spirolactams, pKa values can be shifted up by two units [69]. There are various derivatives of rhodamine dyes including Alexa 546, Alexa 633, DyLight 550 and DyLight 633,

HiLyte fluor 555 HiLyte 594, Janelia dyes JF549, and JF669, which have been customized for diverse applications, addressing the requirement such as enhanced photostability, better brightness, pronounced spectral response, and specific attachment groups.

Porphyrins. Metal-free porphyrin dyes such as OEP, OEPK and some related tetrapyrrolic structures show bright red fluorescence under excitation at ~400 nm, and a characteristic spectral response to protonation [35]. The pH sensitivity of metal-free porphyrins usually involves the addition of one or two protons to the nitrogen atoms of the tetrapyrrole macrocycle, to produce monocations and dications, respectively. The advantages of such pH indicators over the other dyes include: i) high molar absorption coefficients and large spectral shift between excitation and detection wavelengths; ii) narrow emission bands of both deprotonated and protonated forms; iii) isobestic points in absorption and fluorescence spectra which allow for normalization and internal referencing; iv) no emission between 450-600 nm, such that other lumiphores can be multiplexed with the pH sensor; v) broad choice of porphyrin dyes facilitate fine-tuning of sensor spectral characteristics and pKa. Porphyrin dyes have witnessed various biological and theranostic applications. For example, a tin-porphyrins-PEG hydrogels complex exhibits a reversible pH-responsive fluorescence in the physiological pH range, which has been applied as an implantable probe for non-invasive pH sensing *in vivo* [70].

Other traditional fluorescent pH indicators include boron-dipyrromethenes (BODIPYs), perylene diimides (PDIs), 1,8-Napthalimide dyes, BF2-chelated tetraarylazadipyrromethene dyes (aza-BODIPYs), diketropyrrolopyrroles (DPPs), cyanine dyes, and triangulenium dyes.

Metal-ligand complexes (MLCs). Luminescent MLCs usually feature long decay times and large Strokes shifts, which can efficiently minimize the background interferences arising from absorbance or scattering in the biological samples. However, several drawbacks have hindered their wider application in pH sensors: MLCs usually have lower brightness, absorption coefficients, and quantum yield (typically in the range of 0.05-0.5) compared to fluorescent organic dyes; they display cross-sensitivity with oxygen, particularly in the polymer matrixes with good oxygen probability. For those reasons, only a small number of MLCs have been used as pH-sensing materials. One of the successful examples is the hydrophilic long-decay pH-sensitive dye, which is based on the fluorescent Eu^{3+} chelate CS370-diethylenetriaminepentaacetic acid (DTPA)-hydrazide[71], which has been commercialized by Agilent as trade name pH-Xtra. The dye is chemically stable and cell impermeable with excitation at 340-410 nm and three emission peaks at 590, 615, and 690 nm, respectively. It

has a pKa value of ~6.5 and exhibits a strong lifetime response (~8-fold decrease) upon the pH change from pH 4.0 to pH 7.5 [71].

1.4.3 pH-sensing Materials

Solid state polymeric materials for pH sensing must allow proton transfer. Protons are usually hopping from H_3O^+ to a neighbouring water molecule or another acceptor. Therefore, hydrophobic polymers (e.g. polystyrene, silicones, etc.) are not advisable for dye encapsulation, apart from few exceptions, e.g. plasticized PVC [23]. The common matrices for pH sensors include uncharged hydrophilic linear polymers and cross-linked hydrophilic polymers [23], which have high hydrophilicity but are not water soluble due to their physical or chemical cross-linking networks. In nonionic polymers, such as polyurethane hydrogels (e.g. hydrogel D4) and poly(2-hydroxyethylmethacrylate) (pHEMA), the pH response is based on the charge state of the encapsulated dye. pHEMA and polyurethane hydrogels have been widely used as hosting materials for pH sensors due to their commercial availability, good biocompatibility and chemical stability [72]. On the other hand, their high-water absorption can cause the polymer to expand. This in turn may affect sensor performance including mechanical stability, pH sensitivity, calibration and response time. As for encapsulation of hydrophobic indicators in the matrix, dye aggregation should be also taken into consideration.

Some hydrophobic host materials (e.g. PVC, cellulose acetate) can be also used for the encapsulation of pH indicators, together with a plasticizer added to the matrix to facilitate the ion mobility. For such pH sensors which rely on ion exchange mechanism, incorporation of lipophilic proton transfer agents (PTAs), such as lithium, sodium or potassium salts of tetraphenylborate for positively charged indicators is essential. PTA also improves dye solubility in hydrophobic supports [73]. In this case, dye protonation usually results in a proton extraction into the host material, while the potassium or sodium ions of the lipophilic salt leave the sensor matrix, so that sensor material remains electroneutral overall (**Fig.1.9**). On the other hand, such pH sensors often show a slow response time and interferences from ions in its aqueous environment. The pH indicators covalently linked onto a cellulose polymer are also unitized in various forms such as thin coating layers on polyester films, microparticles, and nanocrystals [23].

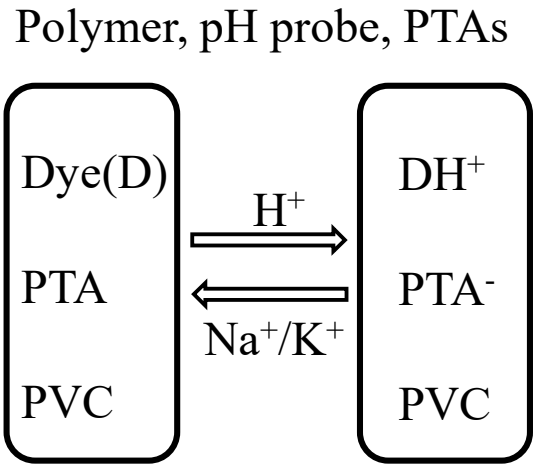

Figure 1.9. The scheme of ion exchange mechanism for solid-state pH sensors. PTAs: proton transfer agents. Plasticized PVC: Polyvinyl chloride or vinyl polymer.

Spectral and pH sensing characteristics of selected luminescent pH sensitive materials are summarized in **table 1.2**.

Table 1.2. Spectral and pH sensing characteristics of some selective luminescent pH sensitive materials.

Indicator	pKa	Ex/Em (nm)	pH range	Matrix	Response (Int, LT)	Reference
2,6-bis[(4-dimethylaminophenylimino)ethyl]pyridine	6.28	417/607	~4.0-7.0	plasticized PVC	Int	[74]
2′,7′-dichloro-5(6)-N-octadecyl-carboxamidofluorescein	6.34	448/495	5.5-7.5	hydrogel	Int	[75]
2′,7′-dihexyl-5(6)-N-octadecylcarboxamidofluorescein ethyl ester	8.3	530/570	7.3-9.3	hydrogel D4	LT	[76]
5-hexadecanoylaminofluorescein	6.62	410/500	5.0-8.0	hydrogel D4	Int	[77]
6,8-dihydroxypyrene-1,3-disulfonic acid (DHPDS) derivative	7.61	404, 457/502	6.0-9.0	poly-(ethylene glycol) diacrylate	Int (ratio)	[78]
8-hydroxy-1,3,6-pyrenetrisulfonate (HPTS)	6.4	405, 450 /520	5.4-7.4	cellulose acetate	Int (ratio)	[79]
	7.06	428, 506/540	6.0-8.0	poly(vinyl alcohol)	Int (ratio)	[80]
	6.65	328, 450/520	~ 5.5-8.0	aminoethyl cellulose	LT	[81]
	7.42	400, 460/520	~6.0-8.5	sol gel	Int (ratio)	[82]
8-hydroxy-1,3,6-pyrenetrisulfonate (HPTS) derivative	6.99	405, 460 /510	6.0-8.0	cellulose acetate	Int (ratio)	[83]
aminofluorescein derivative	6.3	430, 488/515	~5.5-7.5	polythiophene dye polymer	Int (ratio)	[84]
aza-BODPIY with PET group	7.5	695/720	6.5-8.5	hydrogel D4	Int	[85]
carboxyseminaphthofluorescein-2 (SNAFL-2) derivative	7.14	543/589 and 633	6.0-8.0	poly(acrylamide co-vinylamine) on PMMA fiber	Int (ratio)	[86]
diazaoxatriangulenium dye	7.5	560/590	6-8.5	hydrogel D4	LT	[87]
Fluorescein	6.5	484/508	5-7.5	poly(vinyl alcohol) - silica gel copolymer	Int	[88]
Fluorescein isothiocyanate (FITC)	7.61	490/525	~6.5-8.5	chitosan particles in hydrogel D4	Int	[89]
	6.4	440, 490/530	5-7.5	polyacrylamide	Int (ratio)	[90]
Hydroxy quinolinium dye	6.4	375, 425/520	5-8	polyethylene glycol dimethacrylate	Int (ratio)	[91]
naphthalenylvinylpyridine derivative	6.4	370/460, 513	~4.5-6.5	Ormosil nanoparticles	Int (ratio)	[92]
chromoionophore XIII	~7.7	605 /695	~6.5-9	hydrogel D4	LT	[93]
$Ru(Ph_2phen)_2DCbpy]Cl_2$, (DCbpy = 4,4‘-dicarboxy-2,2‘-bipyridine)	3.75	475/670, 630	2-5	Cross-linked hydrogel	LT	[94]
Eu^{3+}- thenoyltrifluoroacetone- pyridine dicarboxylic acid	~6.8	350/615	2-8	cellulose acetate	Int	[95]
Eu^{3+} chelate CS370	~6.5	340/615	4.0-7.5	PBS buffer	LT	[71]

1.5 Measurement modalities used in luminescent pH and O_2 sensor

1.5.1 Intensity and ratiometric intensity-based sensing

As shown in the Jablonski diagram (**Fig. 1.4**), response of an optical sensor to the analyte of interest, such as O_2 or H^+ concentration, can occur in the form of changes in absorbance, fluorescence, or phosphorescence of the corresponding indicator dyes. Intensity measurements are the most straightforward method in optical pH and O_2 sensing. Photoluminescence intensity signals (F) of the sensor can be conveniently measured on various widely available spectrometers and multilabel plate readers. For weakly absorbing solutions (Abs<0.05), F is related to fluorophore concentration (c) according to the Parker's Law (Eqn.1.9), which states that F is proportional to the intensity of excitation (I_0), molar absorption at the excitation wavelength (ε), dye concentration (c), optical path (l), luminescence quantum yield (ϕ), and geometrical/instrumental factor (k) [96].

$$F = I_0 * \varepsilon * c * l * \phi * k \qquad \text{(Eqn.1.9)}$$

So, sensor F is affected not only by the analyte, but also by the dye concentration, variations in instrumental geometry, the optical path, the intensity of excitation, detector sensitivity. It is also affected by photobleaching or leaching which change dye concentration.

Time-resolved fluorescence (TR-F) differs from the classical steady-state fluorescence intensity measurements under continuous excitation, in that it uses pulsed excitation and time-gated detection. In the conventional steady-state fluorescence intensity (FI) mode, the continuous excitation and emission are often influenced by high optical background due to parasitic excitation light scattering and sample autofluorescence. Whereas TR-F detection uses special luminophores with long emission lifetimes in the milliseconds range. They are excited with a pulsed light from a laser or a xenon flashlamp, and emission is measured after a short delay after the excitation pulse. In this case, a much lower optical background and better signal-to-noise ratio can be obtained compared to the standard FI assay. While the TR-F method requires special luminophores and instrumentation, it found wide uses in diagnostics (lanthanide labels and nanoparticles) and in biosensing and bioimaging [97]. Still, simple intensity-based FI and TR-F measurements have the limitations specified above.

Ratiometric intensity measurements can partly overcome these limitations. This approach operates with one main optical signal (pH or O_2 dependent) and a second reference signal (usually analyte-independent and different from the main signal) from the sensor. Some indicator dyes produce ratiometric response in their excitation (e.g. Fura-2 Ca^{2+} indicators) or

emission (e.g. many pH indicators) spectra, whereas other indicators that produce no spectral response require a second reference dye. Such ratiometric readout of the two optical signals provides more stable sensing, as it can compensate for many errors and instabilities, including dye concentration, coating thickness, instrumental factors and drifts.

Although ratiometric detection partly overcomes the drawbacks of simple intensity measurements, it cannot compensate for errors such as different photobleaching rates, autofluorescence, and light scattering at the two working wavelengths. Thus, more advanced sensing methods are required.

1.5.2 Luminescence lifetime-based sensing

Luminescence lifetime (LT) readout can also be used for the sensing and quantification of O_2 and pH. The LT represents the average time a luminescent molecule stays in the excitation state before emitting a photon and returning to the ground state. Since LT is an intrinsic characteristic of the luminophore independent on concentration, lifetime-based sensing offers advantages over traditional intensity-based measurements. The main advantages include no dependence on the dye concentration, excitation intensity, detector sensitivity, inhomogeneous dye distribution, and thickness of the sensing layer [98]. Unlike intensity-based sensing, LT measurement does not need reference signals or tedious calibrations. Thus, it is more convenient and cost-effective for the end users, however requires special dyes and sensor materials, which produce robust LT response to the analyte of interest, and dedicated instrumentation. Thanks to the rapid development of instrumentation and sensor material chemistry, LT based measurements can be made affordable and efficient, and not restricted to the excitation with ultrashort pulses and fast detectors. All this makes LT-based sensing advantageous in many applications.

Frequency domain (FD) and Time domain (TD) are the two main techniques used for LT measurement. In the FD method, sample is excited with a periodically modulated light (a sine wave or a square wave). The emission from the sample is also modulated, but shifted in phase with respect to the excitation light. The phase shift (ϕ) is used to determine the decay time according to **Eqn.1.10,** where ν is the modulation frequency of excitation light [99]. The schematic of phase-modulation LT measurement is illustrated in **Fig.1.10a**, and the ratio B/A and b/a represents the modulation (m) of the emission and the excitation.

$$\tau = \tan(\phi)/(2\pi * \nu) \qquad \text{(Eqn.1.10)}$$

Commercial sensor systems that used FD method include FireSting-GO2 oxygen meter from PyroScience, which is compact (68x120x30 mm), battery operated, has large data memory, and long-term data logging function. FireSting-GO2 uses a unique O_2-sensitive REDFLASH sensor chemistry with red excitation (~610-630 nm) and NIR emission (760-790 nm) [100], which is sensitive to pO2 and therefore enables O_2 measurements in a rapid and non-invasive manner. The REDFLASH provides low power consumption (as compared to blue light excitation), low cross-sensitivity, fast response times, reduced autofluorescence and scatting from biological samples.

An alternative LT measurement mode is the time domain (TD). In the TD mode, the sample is excited with short light pulses, and then time-dependent emission intensity decay is recorded. The pulse width is normally much shorter than measured lifetime, therefore it is more difficult and expensive to realise for short-decay lumiphores. In theory, the intensity signal I(t) is described by the following exponential decay function:

$$I(t) = I_0 \exp(-t/\tau) \qquad \text{(Eqn.1.11)}$$

where, I_0 is the initial intensity at t=0, $I(t)$ is intensity at time t after excitation pulse, τ- lifetime of the lumiphore. From the measured I(t) profile, τ is calculated as the time at which the intensity signal decreases to 1/e of its initial values. The time-dependent intensity signal is often plotted as log($I(t)$) versus time (t), and the τ value is determined as the slope ($-1/\tau$) of a trendline fitting (as shown in **Fig.1.10b**) [101]. At the same time, many sensor materials and dyes show more complex (multi-exponential) emission decays, due to their macro- and micro-heterogeneity [102].

One example of TD sensor system is OpTech-O_2 Platinum (Mocon), which utilizes a PtBP based sensor sticker to measure oxygen in gaseous and headspace. The factory calibrated disposable sensors are stable over years, and less sensitive to ambient light and temperature than other chemistries. The analyzer of OpTech-O_2 Platinum can provide non-destructive sample analysis, and has witnessed various applications in pharmaceutical industry, leak detection of packaged products, quality control of beverage and bioreactors [103].

Rapid lifetime determination (RLD) method uses a simplified algorithm for lifetime calculation. Instead of multi-point measurement of a complete decay curve with subsequent fitting and τ calculation, the RLD measures intensity signals at two different delay times and the same integration window (**Fig.1.10c)**. τ value is then calculated according to **Eqn.1.12**, where I_1 and I_2 represent the two intensities at delay times t_1 and t_2. Due to the time-gated detection, short-

lived optical background (scattering and autofluorescence from the sample) can be excluded, thus allowing for accurate lifetime readouts.

$$\tau = (t_1 - t_2)/\ln (I_1 / I_2) \qquad \text{(Eqn.1.12)}$$

Time-correlated single-photon counting (TCSPC) is also time-domain method for quantifying fluorescence/phosphorescence lifetime (FLT/PLT). TCSPC records the time of arrival (after the excitation pulse) for each detected photon. All the arrival times are iteratively collected and sorted into a histogram that represents the occurrence of photon counts at each time point of the decay. The heart of the technique is a time-to-amplitude converter (TAC), which features like a fast stopwatch for counting the arrival time of each photon. TCSPC electronics also includes a synchronization module (SYNC), a constant fraction discriminator (CFD), and a multi-channel analyser (MCA), as shown in **Fig.1.11**. The sample is repetitively excited by a pulsed light from a laser or a flashlamp. A detector monitors the emission, while SYNC detects the excitation pulse and triggers the start signal for TAC. The CFD only responds to the first emitted photon irrespective of its amplitude. Then the first photon emission triggers the stop signal for TAC. Many thousands of start-stops signals of the single-photon events from TAC are recorded and sorted by MCA to build up a cumulative probability histogram of photon counts versus time channels. The lifetime of the decay is measured from the histogram of photon arrival times.

TCSPC relies on the Poissonian statistics, so that only the first photon after each start pulse is counted in each time channel. This strategy is to avoid the time-dependent statistics distorted by the pulse pile-up effect. However, any subsequent photons after the first photon detection cannot be observed by TCSPC electronics, which makes the probability histograms skew towards these faster-arriving photons. Therefore, data-acquisition rate of TCSPC is usually limited to ~1-5% of the pulse repetition rate. In this way, the statistical probability of detecting two photons in a time channel can be neglected [104].

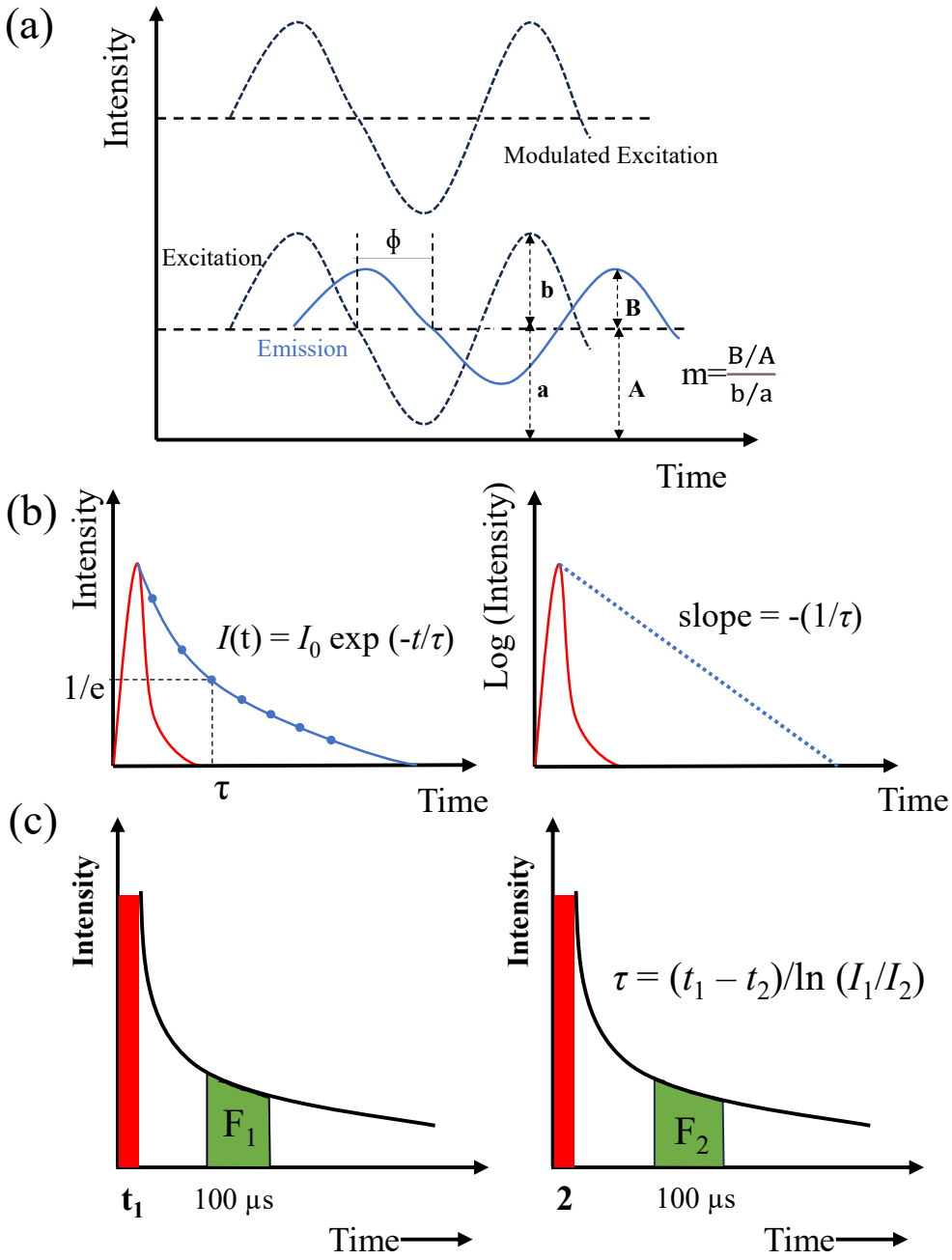

Figure 1.10. Frequency domain (FD) and time domain (TD) lifetime-based detection. **(a)** the scheme of FD measurements; excitation (black) and emission (blue) signals, illustrating the phase shift (ϕ) and modulation ratio (m). **(b)** TD measurements; excitation pulse (red) and sample emission (blue), showing exponential decay of luminescence intensity over time. **(c)** Rapid lifetime determination (RLD), I_1 and I_2 are the two measured intensity signals at delay times t_1 and t_2 (with constant gating time, e.g. 100 µs); lifetime (τ) is calculated using the formula: $\tau = (t_1\text{-}t_1)/\ln(I_1/I_2)$.

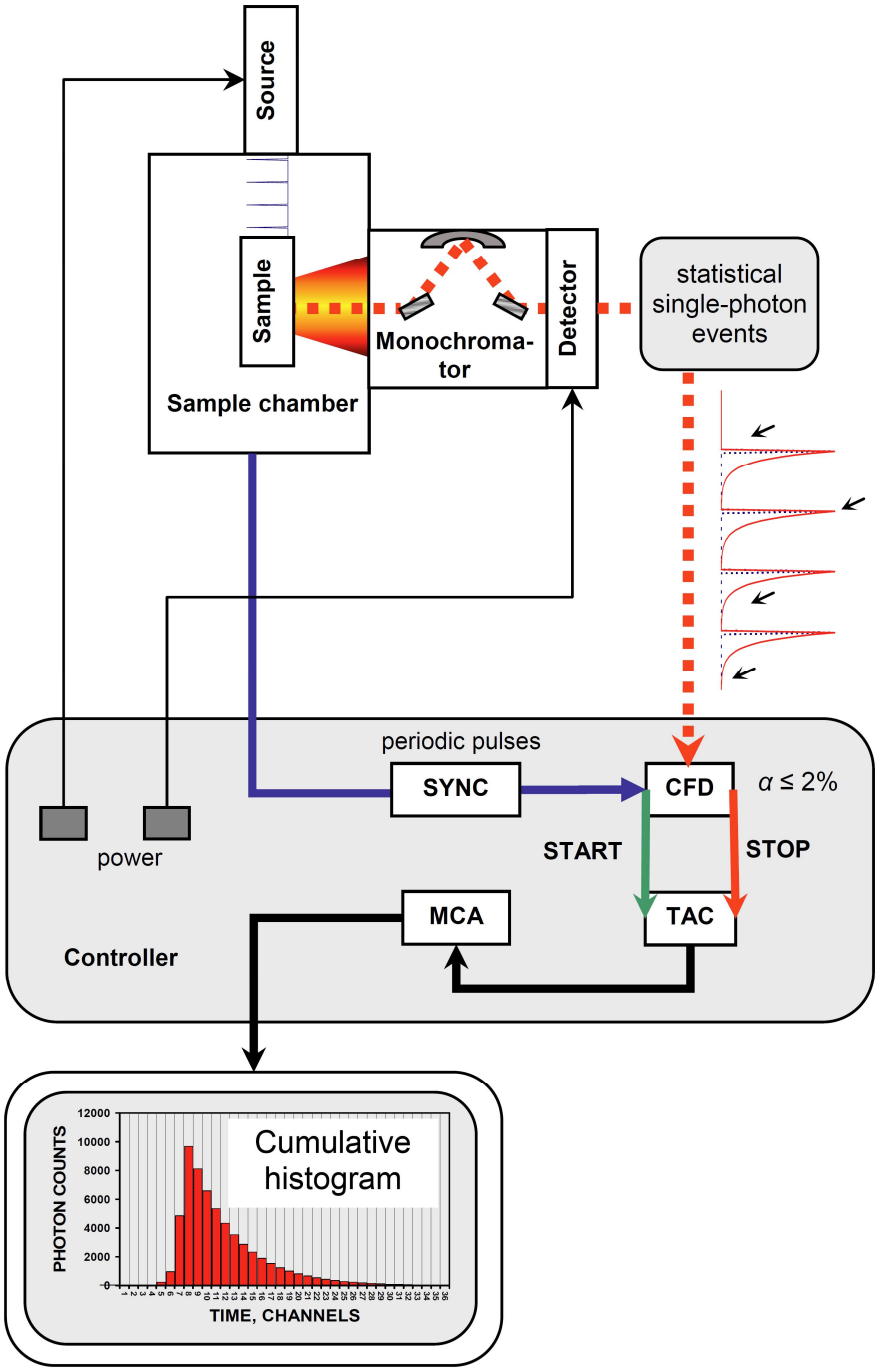

Figure 1.11. Schematic of time-correlated single-photon counting and its main electronic components [105]. SYNC: a synchronization module; CFD: a constant fraction discriminator; TAC: a time-to-amplitude converter; MCA: a multiple-channel analyser.

In principle, the TD and PD methods are equivalent and produce similar results. Each has advantages and limitations. The PD is the indirect LT measurement, which is usually faster

than TD, and it can measure LT as short as 10 ps when using a tuneable continuous excitation source ranging from UV to NIR. While TD measurement produces absolute LT values, which requires pulsed light as an excitation source. TCSPC method is favourable for samples with weak photon emission and high photobleaching, however it usually limited to dedicated and expensive pulsed light-laser diodes. Overall, LT based sensing is advantageous, and can overcome many drawbacks of intensity-based methods.

1.5.3 Luminescent pH and O_2 imaging

Luminescence imaging with pH and O_2 sensors can operate in intensity or lifetime modes. Both TD and PD methods have been reported for luminescence LT imaging [106]. The main advantages of LT imaging over intensity-based imaging include: the former can provide more stable and calibration-free imaging readouts, it is independent on the dye concentration; it enables to suppress background fluorescence of the sample and thus enhance the contrast [33]. To date, the most commonly used LT imaging is based on TCSPC technique and optical microscopy, which allows for reliable FLIM/PLIM imaging readout.

To perform FLIM/PLIM measurements, the photons need to be attributed to individual pixels on a confocal microscope, which is achieved by sorting the absolute arrival times of the photons with respect to the excitation pulse. The main components of a FLIM/PLIM setup include: pulsed excitation source (e.g. a LED, diode laser or multi-photon laser), photon sensitive detector (e.g. PMT, SPAD, SiPM), dichroic mirror (for the separation of emission and excitation), objective (for the sample focus and signal collection), TCSPC unit, X-Y scanner and detector control systems. The LT obtained from FLIM/PLIM at the pixel-level can be color-coded to generate images that provide not only the details of the spatial distribution of a luminophore, but also its "status" via lifetime sensing. The confocal laser-scanning FLIM/PLIM detects light from a thin sample layer, while for the thick sample layer, a pinhole in the upper focal plane of the microscope and a confocal laser scanning setup can be used to suppress the out-of-focus light efficiently [107].

FLIM imaging of fluorophores is getting increasingly popular in science disciplines, aiming at: 1) detection of molecular interactions (e.g. protein or DNA complex labelled with fluorophores), cellular microenvironment (e.g. ions, oxygen, pH, polarity, Ca^{2+} order/disorder phase, etc.), conformational changes in enzymes (e.g. ligand binding, chemical modification); tumour diagnostic and ophthalmology (e.g. Stargardt disease and age-related macular

degeneration); material characterization (e.g. semi-conductors, solar cells, laser diodes) [108, 109].

PLIM uses triplet state emitters such as luminescent transition metal complexes, lanthanide complex, and metalloporphyrin, which usually exhibits longer lifetime (μs to ms range) and larger strokes shift (> 100 nm) in contrast to fluorophores (single emitters with short lifetime in ns range and small stokes shifts) [110]. Therefore, PLIM can obtain a better signal-to-noise ratio by efficient separation of background fluorescence, such as autofluorescence of the endogenous emitters. Unlike FILM mode, PLIM is not influenced by pile-up effects in TCSPC, since the lifetime in the μs to ms range is much longer than the detector deadtime in the ns range [106]. PLIM is of special interest for O_2 imaging in live cell by quenched phosphorescence. Several phosphorescent probes, including the Pt-PFPP conjugates for O_2 imaging in 3D tissue models (e.g. multi-cellular spheroids) and brain tissue slices [111]; the near-infrared emitting nanoparticulate probe NanO_2-IR for tumour oxygenation analysis in model animals [52]; new PtPFPP derivatives with tunable cell-penetrating ability for O_2 imaging in mammalian cells [112].

1.6 Applications of Optical pH and O_2 Sensing in Bio-analysis

The traditional electrochemical methods for pH/O_2 sensing represented by glass pH electrodes and Clark O_2 electrodes have many limitations including their rigid design, interference with extraneous electrical potentials, analyte consumption, large size, contact measurement, etc. Optical pH and O_2 sensing technology can overcome the above drawbacks, and provide non-invasive measurements for the determination of pH/O_2, in particularly for the applications in bioanalysis, since pO2 and pH are two key parameters to reflect pathological states of perturbed cell metabolism [113]. They have been applied in many research fields such as bacterial respiration [114, 115], tumour development [116], bioprocess control [117], etc [118, 119]. The below selected sensing applications include blood and vascular system diagnostics, wound healing imaging, and mammalian cell metabolic analysis.

1.6.1. Medical diagnostics in blood and vascular system

Assessment of a patient's pH and O_2 levels in blood plasma is of high importance, particularly in critical care, surgery, various therapeutic and drug treatments, rehabilitation, etc. When O_2 saturation of blood haemoglobin goes below 95%, the state of hypoxemia develops, which may cause major health concerns, including heart disease, chronic obstructive pulmonary disease, asthma, cystic fibrosis, sleep apnoea, and acute respiratory distress syndrome. The normal blood pH levels are 7.35-7.45, which is slightly alkaline. Abnormal pH of the blood (acidosis

or alkalosis) is a sign of disorders, such as fatigue, muscle weakness, nausea and vomiting, diabetes, urinary tract infection, kidney or lung diseases, or heart dysfunction. Therefore, pH and O_2 sensors are demanding for medical diagnostics, especially the systems that provide miniaturizations, high-throughout, non-invasive and continuous monitoring *in vitro*, but also in arterial blood, vasculature, live tissue and organs.

Pulse oximeters are used routinely (even in smartphones and watches) for the monitoring of blood oxygen saturation, i.e. bound O_2. Such devices usually utilize a pair of light-emitting diodes (LEDs): red (660 nm) and infrared (910 or 940 nm), the optical signals from which reflect the concentration ratio of haemoglobin and oxyhaemoglobin, thus reporting on blood oxygen saturation [33].

Fluorescent O_2 and pH sensors were developed for blood analysis. The first multiparametric system for the intravascular monitoring of pH, O_2, and CO_2 was based solely on fluorescence. In this system, a hydrophilic hydroxypyrene trisulfonic acid with a pKa of 7.0 was immobilized in cellulose matrix on the tip of an optical fibre. The pH detection used ratiometric readout of the basic form (Ex=460, Em=520nm) and acidic form (Ex=410, Em=520nm) of the dye. A proprietary fluorescent dye was used for O_2 sensing (Ex=385 nm, Em=515 nm) [120]. A more advanced commercial system for *in vitro* blood gas analysis is a portable analyser OPTI (**Fig.1.12a**), which contained six fluorescent sensors incorporated in a disposable cartridge and measuring pH, O_2, CO_2, Na^+, K^+, and Ca^{2+}. In the OPTI system, an HPTS dye immobilized in the sensing layer is used for intensity based pH detection; and an immobilized ruthenium dye was used for intensity based O_2-sensing [121].

1.6.2. O_2 and pH sensing in wound healing

Wound healing is a complex biological process that involves four phases: haemostasis, inflammation, proliferation, and remodelling. Adequate delivery of O_2 to the tissue via microcirculation can speed up tissue recovery. The rate of surgical wound infection for patients with colorectal resection is significantly reduced by continuous supply of peripheral oxygen [122]. During wound healing, damaged tissues (e.g. epithelial cells and granulation tissue) require O_2 to be re-established ensuring resistance against pathogenic infections such as *staphylococci* and *streptococci* [123]. The production of lactate is also important during wound healing, which, together with growth factors, promotes angiogenesis and fibroblast proliferation. Typically, pH of healthy skin is slightly acidic, ranging from pH 4 to 6. For an acute wound, pH drops slightly in early stages, and then increases significantly during the

inflammation and granulation phase before returning to normal pH 4 to 6 during the re-epithelization. However, for chronic wounds, pH changes are more complex. pH drops slightly in the early stage, then increases significantly and followed by oscillations between pH 7-8 in the repeating healing process [124]. Therefore, O_2 and pH are important biomarkers in wound recovery, diagnostics and treatment.

A simple system based on a digital camera was described for simultaneous 2D imaging of pH/O_2 in wound rehabilitation, using ratiometric intensity methods [125]. The camera with a 435 nm long-pass filer was coupled with a 405 nm ring LED in the front for excitation. The O_2 sensor was based on polystyrene-co-acrylonitrile particles loaded with a Pt(II)-porphyrin, while the pH sensor used FITC dye covalently bound to cellulose particles. In the application, a thin polyurethane film containing pH and O_2 sensing particles was applied on the surface of wound samples, and then read with an RGB (red, green, blue) camera. The emission of the oxygen dye (650 nm), pH dye (530 nm), and a referenced fluorophore (diphenylanthracene, Em=440 nm) were imaged in the red, green, and blue channels, and then intensity ratio images were generated (R/B for O_2 and G/B for pH). On the distribution map of a chronic wound (**Fig.1.12b**), the upper left corner is hypoxic and also exhibits a high pH, thus indicating a possible sustained inflammatory stage.

Another low-cost, paper-based biocompatible patch for sensing O_2 supply in wound regions (**Fig.1.12c)** is based on $Ru(dpp)_3Cl_2$ dye immobilized in collagen matrix and applied on parchment paper [126]. Sprayable fluorescent sensor films for pH imaging during cutaneous wound recovery were described, based on the ratiometric readouts of FITC and $Ru(dpp)_3$ dyes (Ex=460 nm, Em=530 nm). Using these films, extensive areas were observed with high pH in the inflammatory phase of the chronic wound, and much lower pH in the areas of intact surrounding skin [127].

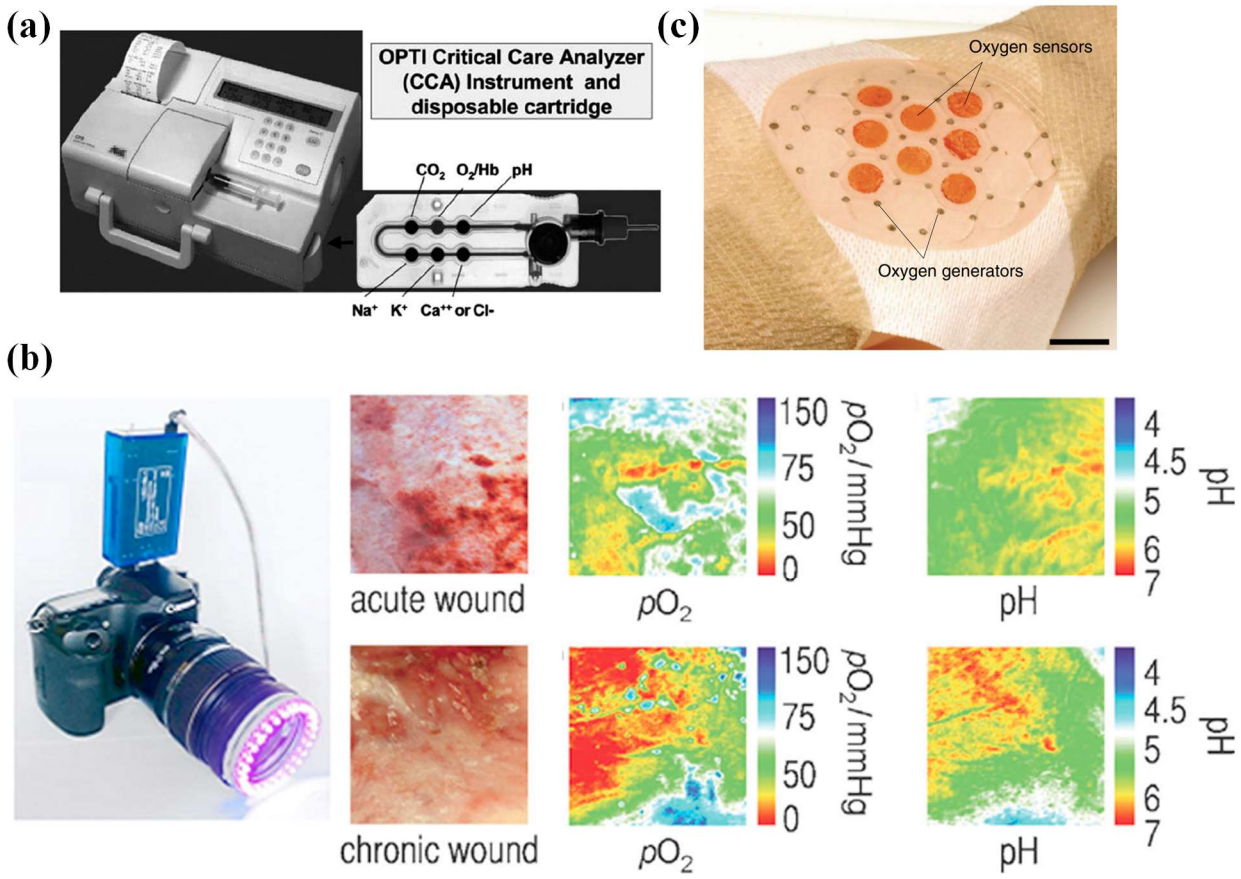

Figure 1.12. Photoluminescence based O_2 and pH sensors for blood gas analysis and wound healing monitoring. **(a)** OPTI analyzer (left) and its disposable cartridge (right). A photodiode tests the fluorescence of the sensor spots after blue LED excitation [120]. **(b)** a digital camera with a 405 nm ring LED mounted on it (left) and an optical emission filter for imaging wounds with sensor overlay film. The O_2 and pH maps compare acute and chronic wounds (right) [125]. **(c)** A close-up view of a single patch with O_2 generation and sensing sites [126].

1.6.3. Cell metabolism analysis

The main advantage of optical techniques for cell analysis is non-invasive, real-time and/or continuous monitoring. Because of the small size of cells, this is often the only available option. pH values for mammalian cells differ considerably in the different compartments and organelles: 7.1-7.2 in the cytosol, 7.5-8.0 in mitochondria, 4.5-5.5 in lysosomes, 6.3-6.5 in late endosomes, 6.0-6.7 in the Golgi network, ~7.2 in the endoplasmic reticulum and nucleus [128]. Also, O_2 levels in mammalian tissues and cells vary between 0-19 kPa. For example, in solid tumours with disturbed vasculature (0-1 kPa), in bone marrow (~6.4 kPa), intestinal tissue (~7 kPa), and immune T cells (3-19 kPa, depending on their (micro)environment) [129]. O_2 is very essential for mammalian cells, its levels tend to decrease with increasing biomass. Concurrently, lactic acid is produced by glycolysis, causing acidification of extracellular space or culture

medium [130]. Therefore, by measuring O_2 and pH, a principal picture of cell metabolism and its alterations in different disease states or stress conditions can be ascertained [131, 132], which is of high value for cell biology, clinical diagnostics, drug and medicine development.

Optical biosensors for cell analysis have been introduced by Ocean Insight [133], PreSens [134], Becton Dickinson (BD) [135], Luxcel Biosciences [136], and Seahorse Biosciences [137]. Ocean Insight applied pH/O_2 sensors on the tip of optical fibre or to peel-and-stick patch for non-invasive measurements. PreSens offers both fibre optic sensors, sensor spots (e.g. SP-PSt6-NAU), and coated sensing plates (e.g. SensorDishes®) for determination of pH/O_2 [138]. The BD oxygen biosensor system (OBS) utilizes microplates coated with a ruthenium-based fluorophore in silicone rubber matrix for real-time OCR measurement based on the intensity change of the fluorophore [139]. The Luxcel Biosciences and Seahorse Biosciences (both acquired by Agilent) are two microplate sensor-based measurements, which implemented truly quantitative two-parametric readouts for both pH/ECAR and O_2/OCR with adequate sensitivity, and compatibility with suspension/adherent cell cultures [140].

Luxcel developed and optimised a low-cost platform for real-time and calibration-free cellular OCR/ECAR measurements. The sensing systems utilizes soluble phosphorescent Pt-porphyrin based chemistry for OCR and fluorescent lanthanide chelate chemistry for ECAR. These probes feature compatible spectral characteristics, produce robust and easily separated luminescence LT responses in the microsecond time range without crosstalk. They can be measured on standard microplates and TR-F readers in RLD mode. However, the sensitivity of this platform is moderate, in particular the OCR measurement in the microplate is sealed with an oil layer. On the other hand, the pH/O_2 probes (sold under trade names MitoXpress-Xtra and pH-Xtra) are water-soluble, dispensable and non-reusable, which makes them less convenient compared to solid-state sensor coatings applied on common substrates for cell analysis. And solid-state versions of Luxel's probes have not been described [141].

The solid-state sensor approach was realised by Seahorse in their fully integrated XF (extracellular Flux) analyzer platform. The XF analyser includes a specially designed microplate with microchambers than can be sealed by moving pistons containing pH/O_2 sensor coatings, which are coupled with a detector for signal acquisition, and integrated drug delivery system for sequential addition of effector compounds [142]. This system regarded as a 'golden standard' in live cell analysis enables calibration-free OCR/ECAR readouts with excellent sensitivity and analytical performance [143]. However, its O_2 and pH sensor chemistries relying on fluorescence intensity mode are outdated, which results in significant cross-talk and

requires tedious calibration steps prior to cell analysis. Additionally, the sophisticated multi-channel detection optics adds complexity to the assay workflow, and its data processing algorithms are complicated, which leads to the high-cost of XF analytical system (~$250,000 for a basic 24-well plate version).

Cell Energy Budget (CEB) approach is one of the advanced cell analysis applications which provides a detailed picture of cell bioenergetics [140]. In the CEB, OxPhos fluxes of O_2 (i.e. OCR) and glycolytic flux of H^+ (i.e. ECAR) are measured in a microplate under a series of defined physiological conditions (supply of metabolic substrate, drug treatments) to determine their 'metabolic signatures' [144, 145]. In the CEB (**Fig.1.13**), O_2 and pH sensors are two key enabling tools for the convenient, non-destructive, and multiparametric analysis of the major energy/ATP generating pathways in mammalian cells.

The contributions of glycolysis and non-glycolytic activities (mainly the TCA) can also be devised in the CEB on standard microplates and TR-F readers, by measuring ECAR in unsealed (Lactate only, L-ECA, while CO_2 is allowed to escape) and sealed samples (total, T-ECA, i.e. lactate and mitochondria-derived CO_2 combined) together with the OCR (sealed) and total ATP (unsealed). It can be also devised on XF seahorse platform using their tailor-made microplates with specially profiled sealable chamber, moving coated pistons, detector, and integrated drug injection ports. In this case, the contribution of mitochondria-derived CO_2 from ECAR can be excluded either by moving pistons to create transient microchamber (200 μm above the cell monolayer within a microplate) or sequential addition of rotenone/Ant.A and 2-DG to the cells. Rotenone/Ant.A treatment inhibits Complex I and Complex III of the ETC, while 2-DG blocks glycolysis by inhibiting hexokinase function and G6P production.

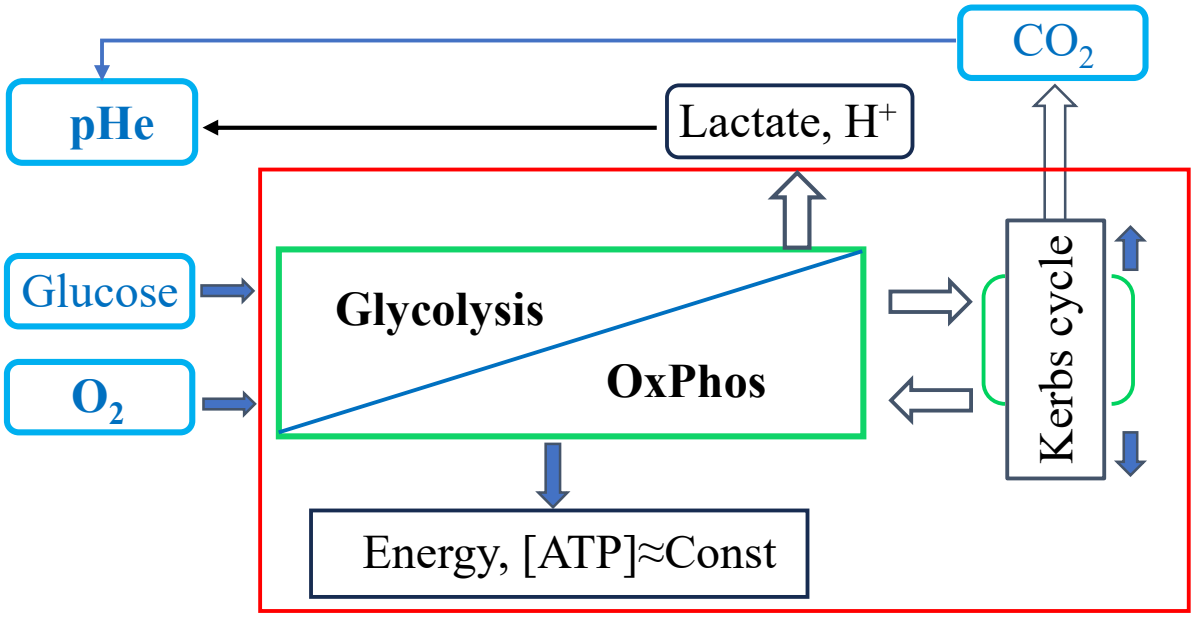

Figure 1.13. The schematic representation of Cell Energy Budget (CEB) concept.

The ideal pH/O_2 sensors for cell analysis should overcome the following potential limitations and fulfil several key requirements: 1) have optimal spectral characteristics providing real-time and accurate responses to pH and O_2 target analyte(s); 2) have stable calibration-free ECAR and OCR readouts with internal referencing capability; 3) allow low-cost solid-state sensor coatings with good stability and without complex chemistries for reuse; 4) be easy to use and compatible with available instruments (e.g. plate readers); 5) provide simultaneous pH/O_2 measurement without significant cross-talk; 6) have low cytotoxicity.

Thus, all this fuels the research for better, simpler and more efficient solid-state O_2 and pH sensing materials and detection platforms, which can provide self-referenced, quantitative, accurate, and calibration-free readouts of both ECA and OCR in biological samples containing cells.

1.7 Conclusion

This chapter outlines the typical cellular metabolic pathways in eukaryotic cells, the importance of O_2 and pH in cell analysis, the commonly used optical pH/O_2 sensing principles, indicator dyes, materials, detection modalities, and its various applications in bio-analysis. In this thesis, we will use the above optical pH/O_2 sensing knowledge and technology to develop new photoluminescent sensing materials, platforms and systems for better biological applications.

Chapter 2: Materials and Methods

2.1 Materials

PtOEP-methyl-Schiff (PtOEP-SB), PdOEP-methyl-Schiff, PdOEP-meso-formyl, PdOEP-phenyl-Schiff, PdOEP-benzyl-Schiff, PdOEP-phenyl-azine, PdOEP-ethyl-azine were synthesised by Institute of Physical Chemistry and Electrochemistry, Moscow according to the modified procedures [146, 147]. Platinum octaethylporphyrin (PtOEP), octaethylporphine (OEP), OEP-ketone (OEPK) dyes, Pt(II)-Benzoporphyrin dye (PtBP), coumarin 6 dye (C6) were from Frontier Scientific (USA). MitoXpress®-Xtra and pH-Xtra sensing probes were from Agilent (Santa Clara, CA, USA). Optech O_2 Platinum sensor stickers (PtBP-based) were from Mocon-Ametec (USA). Hydrogels D4 were from Degussa (Frankfurt, Germany). Poly(acrylate)-co-methacrylic acid, poly(DL-lactide) (PLA) and poly(DL-lactide-co-glycolide) (PLGA) were from Polysciences (Warrington, PA, USA). Eudragit RL-100 polymer was from Evonik Industries (USA). Poly(styrene) (PS), high molecular weight poly (vinyl-chloride) (PVC), ethyl cellulose, Nafion, poly(vinylidenedifluoride) (PVDF) membranes, polyester Mylar films, potassium tetrakis(4-chlorophenyl)borate (TCPB), sodium tetrakis[3,5-bis(trifluoromethyl)phenyl]borate (Na-TFMB, borate1), sodium tetraphenylborate (Na-TPB), lithium tetrakis(pentafluorophenyl) borate ethyl etherate (Li-PFPB), diphenyl phosphate,1-1'-binapthyl-2,2'-diyl hydrogen-phosphate (BNDHP), TiO_2 nanoparticles, PS-DVB microparticles, bis(2-ethylhexyl) sebacate (DOS), sodium methylate, sodium dodecylsulfate (SDS), FCCP, antimycin A, tetrahydrofuran (THF), chloroform, ethanol, trifluoroacetic acid (TFA), analytical grade acetone, ethanol, ethylacetate Na_2SO_3, HEPES buffer, McCoy's medium, Dulbecco's modified Eagle medium (DMEM), Roswell Park Memorial Institute 1640 (RPMI 1640) medium were from Millipore-Sigma (Burlington, MA, USA). Polystyrene glass coated and polypropylene microplates were from Sarstedt (Nümbrecht, Germany), Greiner Bio One (Kremsmünster, Austria) and Roche (Basel, Switzerland), respectively.

2.2 Methods

2.2.1 Fabrication of sensor cocktails and coatings

Sensor cocktail was produced by mixing stock solution of plasticized PVC, indicator dye and PTAs (borate salts) to produce the required concentrations. The stock solutions were: 120 mg of PVC and 240 mg of DOS in 3 g of THF; 2.5 mM indicator dye (OEP, OEPK, PtOEP, PtOEP-

SB) in $CHCl_3$; 0.1 M borate salt in THF; 2 mM C6 dye in THF. The resulting sensor cocktail were then deposited onto pieces of Mylar® polyester films or in wells of a standard polypropylene 96-wells plates (Greiner), and allowed to dry. The coated films and microplates were stored in the dark at room temperature for up to one year, and used as required. The other polymeric coatings were produced similarly.

The spin-coated sensor films were produced by applying 200 µL of the cocktail onto Mylar film (22×22 mm) on an SCS 6800 spin coater (Kisco, Indianapolis, IN, USA) at 1000 rpm for 60 seconds (5 sec ramp and 55 sec spin). The coated films were then fully dried at 60°C for 1 h in an incubator.

Membranes with solid-state sensor dots were prepared from the corresponding cocktails as described in [148]. Thus, 1.0 mg of PtBP dye was dissolved in 1.0 mL of 5% w/w solution of PS in ethyl acetate, and the cocktail, undiluted (UD), or diluted - 0.5 mg/ml (1:2) or 0.25 mg/ml (1:4) was applied in 5 µL aliquots with a P10 pipette (Gilson, France) onto sheets of PVDF membrane. After drying, 5-10 mm sensor dots were produced, which were cut into individual strips, 10 x 30 mm. Similarly, aqueous $NanO_2$-IR probe (see below) (UD -10 mg/mL, 1:2 - 5 mg/mL, 1:4 - 2.5 mg/mL) was spotted on PVDF membranes to produce the corresponding sensor coatings. The microparticle (MPs) based sensor coatings were produced by applying 5 µL aliquots of the precursor cocktail (kindly provided by Agilent Inc., Cork, Ireland) [19] directly on the inner surface of a vacuum flask, which after drying produced 5-10 mm sensor spots.

The liquid nanoparticle probe $NanO_2$-IR was produced according to [53]. Briefly, 250 mg of Eudragit RL-100 polymer and 4.0 mg of PtBP dye were dissolved in 125 mL of acetone and then poured in a 1 L glass beaker containing 750 mL of deionized water under rigorous stirring. The resulting solution was transferred to a 1L vacuum flask and concentrated on a rotary evaporator (~70 mbar, 40°C) to a final volume of 15 mL. This solution was centrifuged at 5000 rpm for 5 mins to remove aggregates, transferred to a 10 mL glass vial and stored at 4 °C in the dark. This stock of $NanO_2$-IR, diluted (2.5 mg/ml solution) or not with H_2O, was used in liquid form for sensor calibration at different temperatures ranging from 2°C to 40 °C.

2.2.2 Barometric calibration setup and procedures

A Rotavapor RII rotary system (Büchi, Switzerland), connected to a PC 3001 Vario Prodigital vacuum pump (Vacuubrand Germany), was used to produce series of partial oxygen pressure (pO_2) standards inside the system (called Rotavap). The solid-state sensors were attached with

an adhesive tape to the neck or bottom parts of a 100 mL vacuum flask. The sensor coatings were spotted on the inner wall of the flask, and the liquid probe (5-10 mL) was simply poured inside the flask. The flask with sensors was connected to the Rotavap system using a glass adaptor. Calibrations in humid air were conducted with water added to both the vacuum flask and solvent collecting flask (~10 mL in each).

In calibration experiments the flask was normally partly submerged in a temperature-controlled water bath (Büchi) (ranged 0-50^{o}C) and rotated for faster gas equilibration. The temperature in the bath and several different locations on the flask surface was monitored with an infrared thermometer (DT8380, Duratool). The digital vacuum pump was then primed and used to produce a series (usually 12) of calibrations points (total pressure, P_T) for the sensor/probe, going from the lowest P_T up. At each point, sensor signals (PLT or phase shift) were measured repetitively and non-invasively (i.e. through flask wall) with a handheld O_2 sensor reader Optech Platinum (Mocon-Ametec, USA) or Firesting GO2 (PyroScience, Germany). For that, rotation was stopped, flask was quickly lifted, its temperature and sensor signals were measured and then the flask was put back in the bath. Once the sensor/liquid probe started to produce stable signals (indicative of temperature and gas equilibration of the system), final readings were taken and used as calibration point. Then the measurements progressed to the next calibration point.

To generate statistically plausible data, each measurement was done in triplicate. Outliers, if any, were removed and mean values and S.D. were calculated. Phosphorescence intensity and lifetime values were analysed. Calibration curves were produced by processing sets of data points as described in the Results and Discussion. They were analysed and fitted in Excel and Origin. All calibration experiments were conducted in replicates, to ensure consistency of results.

2.2.3 Photophysical characterization of sensors

Time resolved fluorescence intensity (TR-F) signals were measured on a Victor 2 multi-label reader (Perkin-Elmer, Waltham, MA, USA) using the 340 ± 60 nm excitation and 642 ± 10 nm emission filters (**Fig. 2.1**). Sensor PLT values were measured on the plate reader using rapid lifetime determination (RLD) method [113], in air-saturated (21 kPa O_2) and deoxygenated (0 kPa) PBS buffer. Deoxygenation was achieved by the addition of 5 mg/ml Na_2SO_3 and 5 mg/ml K_2HPO_4 to PBS. Control sensors were also prepared without indicator dye(s), and blank

readings were taken to assess the influence of the sensor matrix and make necessary corrections of measured optical signals. Fluorescence of C6 dye was measured on Victor 2 reader using standard filters 485 nm excitation and 535 nm emission. The setting for the measurement of PtOEP-SB/C6, OEP/OEPK, and PtOEP on Victor 2 reader in TRF/RLD mode for O_2 and pH sensing were summarized in **Table 2.1-2.2.**

Fluorescence spectra of the sensors spotted on Mylar film and inserted in quartz cuvettes with PBS at different pH, were measured on a Cary Eclipse spectrofluorometer (Agilent, Santa Clara, CA, USA) at 390 ± 10 nm excitation. On the Cary Eclipse, PLTs were measured using phosphorescence decay mode with excitation at 390 ± 10 nm and emission 650 ± 20 nm. The delay time step was set at either 0 or 20 μs, the gate time at 10 μs, and lifetime values were calculated from mono- and bi-exponential decay fittings.

Figure 2.1. The image of Cary Eclipse spectrofluorometer (Agilent, Santa Clara, CA, USA), Victor 2 multi-label reader (Perkin-Elmer, Waltham, MA, USA), and FLIM-TCSPC microscope (Becker & Hickl, Berlin, Germany) used in the Lab.

Table 2.1 Settings for dual-mode measurement of PtOEP-SB/C6 on Victor 2 plate reader using TRF/RLD mode for O_2 sensing and ratiometric intensity mode for pH sensing.

Prompt fluorescence (**C6**)	Time-Resolved Fluorescence, TRF (**PtOEP-SB**)
Label technology..... Prompt fluorometry	Label technology..... Time resolved fluorometry
CW-lamp filter name..... F485	Emission filter name..... D642
CW-lamp filter slot..... A5	Emission filter slot..... A2
Emission filter name..... F535	Emission aperture..... Normal
Emission filter slot..... A5	Excitation filter..... D340
Measurement time ..... 0.3 s	Delay..... 30 µs
Emission aperture..... Normal	Window time..... 100 µs
CW-lamp energy..... 14024	Cycle..... 1000 µs
Second measurement CW-lamp energy….. 0	Second window delay time... 70 µs
Emission side..... Above	Second window time..... 100 µs
CW-Lamp Control..... Stabilized Energy	Light integrator capacitors..... 1
Excitation Aperture..... N/A	Light integrator ref. level..... 50
	Flash energy area..... High
	Flash energy level..... 100
	Flash absorbance measurement..... No
	Beam..... Normal

Table 2.2 Settings for the dual-mode measurement of OEP/OEPK and PtOEP on Victor 2 reader in TRF/RLD mode for O_2 sensing and ratiometric intensity mode for pH sensing.

Prompt fluorescence (**OEP/OEPK**)	Time-Resolved Fluorescence, TRF (**PtOEP**)
Label technology..... Prompt fluorometry	Label technology..... Time resolved fluorometry
CW-lamp filter name..... P405	Emission filter name..... D642
CW-lamp filter slot..... A1	Emission aperture..... Small
Second meas. CW-lamp filter name ….. P405	Excitation filter..... D340
Emission filter name..... D615	Delay..... 30 µs
Second meas. emission filter name. D642	Window time..... 100 µs
Measurement time ..... 1.0 s	Cycle..... 1000 µs
Emission aperture..... Small	Second window delay time... 70 µs
CW-lamp energy 30445	Second window time..... 100 µs
Second measurement CW-lamp energy ... 30445	Light integrator capacitors..... 1
CW-Lamp Control.....Stabilized Energy	Light integrator ref. level..... 10
Excitation Aperture..... N/A	Flash energy area..... Low
	Flash energy level..... 25
	Beam..... Narrow

Sensor FLT values (ns) were measured on a confocal FLIM-TCSPC microscope (Becker & Hickl, Germany) described in [106]. It consisted of an upright microscope AxioExaminer Z1 with a 5x/0.25 FLUAR objective, heated incubator and stage (T=37°C) with motorized Z-axis control (all from Carl Zeiss, Germany). The microscope was connected to a DCS-120 confocal scanner (B&H) coupled to a 405 nm BDL-405-SMNi picosecond diode laser (B&H), and an R10467U-40 photon counting detector, with >30% quantum efficiency at 400±700 nm (Hamamatsu Photonics, Japan). Excitation and emission light was separated with a 594 nm dichroic mirror and a 650±20 nm emission filter (both from Semrock, Rochester, NY, USA). The laser and scanner were connected to the TCSPC detection hardware (B&H), with scanning performed with 256x256 pixel resolution, and image acquisition controlled by MicroToolBox software, version 2011 (Carl Zeiss) and SPCM software, version 9.81 (B&H). The PLIM data was then processed in SPC Image software, version 8.4 (B&H) to determine PLT values. The fitting parameters for phosphorescence decays were selected by adjusting the parameters (T1, T2, shift) and binning for individual randomly selected pixels to obtain optimal χ^2 values (close to 1).

Sensors deposited a 96-well plate or Mylar film were overlaid, respectively, with 300 µl or 4 ml of PBS, and then temperature-equilibrated to 37°C. After optimization, lifetime values were calculated as follows: τ_1 and τ_2 - from the whole decay using bi-exponential fitting with T_1 = 14 µs, T_2 = 236 µs, fixed shift, binning 1, threshold 25-200, scatter 0, 'tail enhanced fit'. Alternatively, mean lifetime (τ_m) was calculated using mono-exponential fitting from the part of the decay that starts immediately after instrument response function (IRF) trace, T_1 = 55 µs, T_2 = 250 µs, fixed shift, binning 1, threshold 25-90, scatter 0, 'tail enhanced fit'. Numerical values corresponding to PLIM color images and distribution histograms of different parameters (e.g., lifetime and their fractions) were exported in Excel. The initial lifetime distribution histograms, which show frequencies of pixels with given fast-component lifetime (τ_1), slow-component lifetime (τ_2) and mean lifetime (τ_m - the amplitude weighted mean decay time per pixel), were converted to cumulative histograms and then the median τ values and the interquartile range were calculated. Spotting quality is exemplified by PtOEP/OEP sensors (**Fig.2.2A**). FLIM imaging setup and transmission spectra of the emission filters used for OEP and OEPK/PtOEP are shown in **Fig.2.2B,C**.

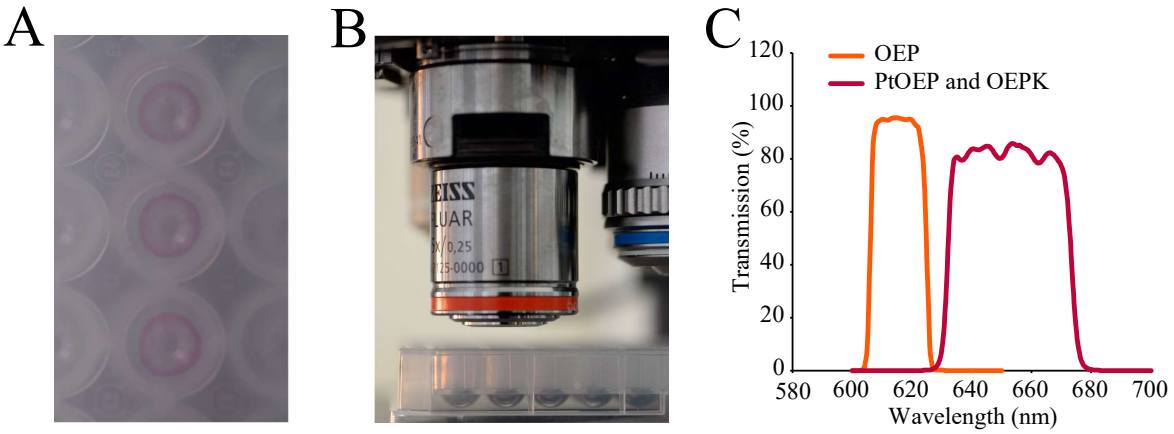

Figure 2.2 Photographs of: **A.** PtOEP/OEP sensor coating on a 96-well polypropylene plate (0.25 mM PtOEP, 0.08 mM OEP, 3 mM Na-TFMB), and, **B**. Confocal FLIM/PLIM imaging setup for pH/O_2 sensing. **C**. Transmission spectra of filter pairs (long-pass + band-pass) used for confocal FLIM/PLIM imaging of OEP and OEPK/PtOEP.

The wide-field FLIM setup with a SPAD array detector 120x140 pixel array detector (built at Tyndall National Institute by Dario Angelone, Ireland) consisted of: a) a 405 nm picosecond laser diode (Becker&Hickl) as excitation source pulsed at a repetition rate of 20 MHz; b) a 1x1.4 mm time-resolved SPAD array chip with 128x120 pixels as the imaging detector [149]; iii) collimating optics with a long-pass emission filter (>600 nm, Thorlabs FEL0600). The

optical setup had an epi-fluorescence configuration, a working distance of ~100 mm, and an imaged area of approximately 10x10 mm. The imager is controlled using custom Matlab code via an FPGA board and the data analysis is also carried out using Matlab. For fluorescence lifetime measurements, photon counts were acquired over 50-time bins, each with a width of 390 ps. Then a mono-exponential fit was performed for each pixel independently over 20 consecutive time bins starting from the time bin with the maximal photon count. A schematic of the SPAD array FLIM system for imaging live (postmortem) tissue samples with a fluorescence lifetime based planar pH sensors, and a photograph of the system, including an inset image of a tissue sample covered in the solid-state pH sensor, are shown in **Fig.2.3.**

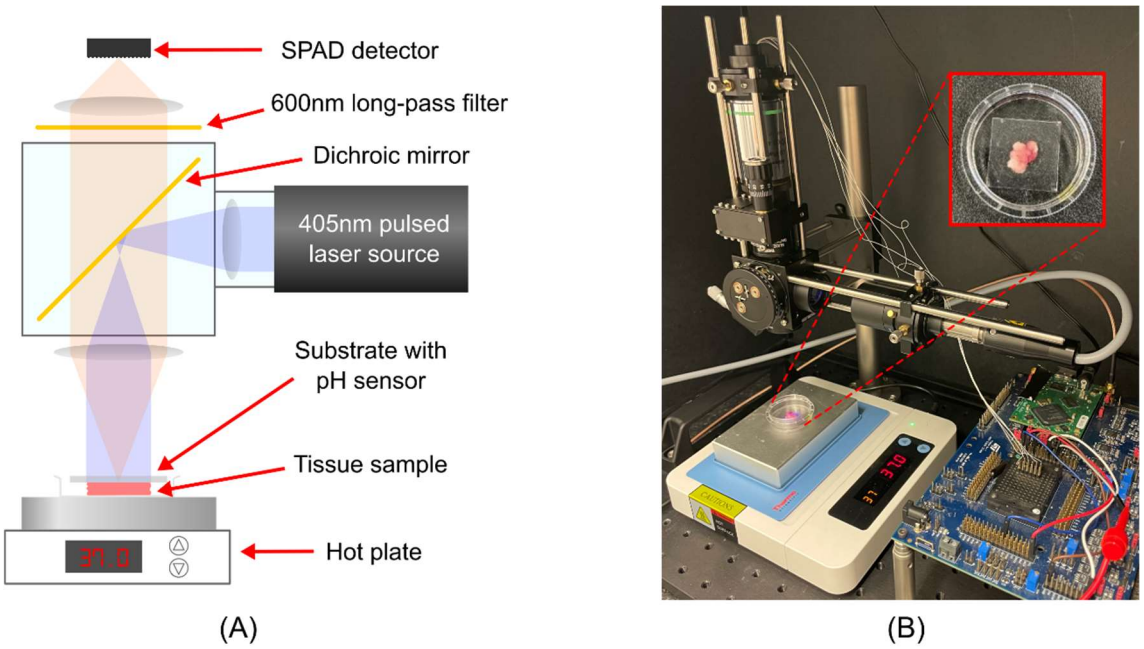

Figure 2.3: A schematic of the measurement setup including the wide-field benchtop FLIM imager, the tissue sample in a petri dish covered with the pH sensor and placed on a hot plate for temperature control **(A)** and a photograph of the measurement setup, including a vertical image of a tissue sample and pH sensor in a petri dish **(B)**.

2.2.4 pH titration for dyes and pKa calculation

UV-Vis absorption spectra of the sensor coatings and their response to pH were measured on a diode-array spectrophotometer (Agilent), using sensor films inserted diagonally in a quartz cuvette and submerged in a buffer with known pH standards. The pKa values were carried out under equilibrium conditions (with ~3 mins equilibrium time at each pH gradient), and calculated by plotting peak absorbance values vs pH, fitting the resulting sigmoidal curves and determining their inflection point which corresponds to pKa. Similarly, pKa values were determined from fluorescent titrations, measuring emission spectra or lifetime response of

sensor coatings deposited on Mylar films or microplates at different pH on a Cary Eclipse fluorescence spectrophotometer (Agilent, USA), standard TCSPC-FLIM microscopy (Becker, Germany) or compact SPAD array FLIM camera (Tyndall, Ireland).
The stability of pH sensors was evaluated by measuring pKa values each month for one year (sensors were stored at 4 °C in the dark).

2.2.5 Tissue culture and animal experiments

Rat pheochromocytoma (PC12) cells, human colon carcinoma (HCT 116), lung carcinoma (A594), colon adenocarcinoma (SW480), and murine colorectal carcinoma (CT26 cells) were from the American Collections of Cell Cultures (ATCC). PC12 cells were maintained at 37°C in humidified atmosphere of 95% air and 5% CO_2 at 37°C, as described in [150], in RPMI 1640 medium supplemented with 10% horse serum (HS), 5% fetal bovine serum (FBS), 100 U/ml penicillin and 100 µg/ml streptomycin (P/S) and 10 mM HEPES, pH 7.2. HCT116 cells were maintained in McCoy's medium supplemented with 10% foetal bovine albumin (FBS), 2 mM L-Glutamine, 100 U/ml penicillin /100 µg/ml streptomycin (P/S), and 10 mM HEPES (pH 7.2). A594, SW480, and CT26 cells were maintained in high glucose DMEM supplemented with 10% FBS, 2 mM L-glutamine, 100 U/ml penicillin /100 µg/ml streptomycin, and 10 mM HEPES, pH 7.2 (complete DMEM) in a humidified atmosphere of 95% air and 5% CO_2 at 37°C.

All animal procedures were performed according to the European Union Directive 2010/63/EU amended by Regulation (EU)2019/1010, as well as the national ethical guidelines of the Health Products Regulatory Authority (HPRA), under project authorisation AE19130/I285. Health status of all mice was monitored daily for the duration of experiments. There were no deaths outside the humane euthanasia. Mice were humanely euthanized by cervical dislocation after tumours reached the size of 1.5×1.5 cm in diameter. Female Balb/C mice (Envigo, UK) used in the experiments were in good condition, disease free, weighted 16-22 g at 6-8 weeks of age. They were kept in a conventional animal unit at constant temperature (22˚C) with natural day/night light cycle. Standard laboratory food and water were provided. Before experiments, the animals were given an adaptation period of at least 7 days.

For tumour induction, minimal tumorigenic doses of CT26 cells (1×10^5 cells in 200 µl of serum-free DMEM) were prepared and injected subcutaneously (SC) into animals, in the right flank. Following the injection, tumours were allowed to grow and develop in animals, and they were monitored daily. Tumour volume was measured and calculated according to the formula:

$V = (L \times W^2)/2$, where L is the longest diameter of the tumour (length) and W is the longest diameter perpendicular to diameter L (width).

2.2.6 Cell viability and toxicity assays

PC12, HCT116, A594 or SW480 cells were suspended in unbuffered DMEM supplemented with 10 mM glucose and 2 mM L-glutamine (ECA medium) and dispensed in wells of a 96-well plate containing sensors or appropriate controls (2.5×10^4 or 5.0×10^4 cells in 100 µl per well, respectively). After a one-hour incubation at 37°C in a CO_2 incubator, 100 µl of CellTiter-Glo® assay reagent (Promega, Madison, WI) was added to each well and mixed. Total cellular ATP content was analysed then in a white 96-well microplate on a Victor 2 reader in luminescence mode, as a measure of cell viability.

2.2.7 Cellular ECAR and OCR assays

Cultured PC 12 and HCT 116 cells were suspended in unbuffered DMEM supplemented with 10 mM glucose and 2 mM L-glutamine (ECA medium). Aliquots containing 5.0×10^5 cells in 200 µl of ECA medium were dispensed into the wells of a sensor coated 96-well plate. Control samples without cells were also prepared on the plate and used to correct sensor signals for any drifts unrelated to cellular fluxes. For system calibration, wells with pH standards (100 µl of PBS, pH 6.4, 6.9 or 7.4) were also included; they were used to generate the pH calibration equation. The plate was then inserted in a Victor2 reader and incubated at 37ºC measuring phosphorescent and fluorescent signals in each assay well every 5 min for approximately two hours. To increase the rate of glycolysis and lactate release, cells were treated with FCCP (mitochondrial uncoupler) or antimycin A (Ant A, mitochondrial complex III inhibitor). ECA analysis was also performed using pH-Xtra™ probe as described in [151]. Controls without cell were also included and used for signal drift correction.

For the ECAR imaging, HCT116 were seeded at 10^3 cells/well and cultured for 5 days McCoy's 5A medium in non-adherent Lipidure-coated 96-well U-bottom plates (AMSBIO, Abingdon, U.K.) until spheroids of 1-1.2 mm in diameter were formed [152]. Medium was refreshed every 48 hrs. Individual spheroids were gently transferred into the wells of a U-bottom microplate with sensor coatings in 200 µl of fresh DMEM supplemented with 2 mM glutamine, 1 mM pyruvate, 10 mM glucose (ECA medium) and antimycin A (Ant A, mitochondrial complex III inhibitor, 2 µM) for FLT analysis on the confocal FLIM-TCSPC microscope [153].

For OCR assay, PC12 cells and HCT 116 cells were suspended in respiration medium (ECA medium supplemented with 20 mM HEPES). Aliquots containing 5×10^5 cells in 200 µl of the medium were dispensed in the wells of a sensor coated 96-well plate. Control samples without cells were also included and used to correct sensor signals for any drifts unrelated to cellular fluxes. For comparison, cells prepared in 200 µl of respiration medium containing MitoXpress®-Xtra O_2 probe were also prepared in uncoated wells and used for signal drift correction (the corresponding 'no cells' controls were also included). Once the plate was prepared, 150 µl of mineral oil was dispensed in all assay well to seal them from ambient air. The plate was then inserted in a Victor2 reader and incubated at 37^{o}C measuring phosphorescent signals of the sensors or MitoXpress®-Xtra probe in assay wells every 5 min for approximately two hours. PLT of the probe/sensor was calculated using the RLD method and its profiles were used to assess the OCR. To increase or decrease the OCR, FCCP (mitochondrial uncoupler, 0.25 µM) and Ant A treatment were applied, accordingly.

Chapter 3: Barometric calibration of quenched-phosphorescence based oxygen sensors on a standard rotary evaporator system

3.1 Introduction

Calibration is an essential part of sensor development, characterisation and final application. It allows correct interpretation of signals generated by the sensor system and their conversion into analyte concentrations [154]. For some sensors and applications, simple measurement of two analyte standards (e.g. zero and maximal concentrations) can be used for calibration, however full-range multi-point calibrations are preferred. For small gaseous analytes, such as molecular oxygen (O_2), calibration procedure is complicated, and a number of additional factors must be taken into account. In particular, the presence of other gases in sensor environment (water vapours, CO_2, air O_2), additional liquid or solid phases, analyte partitioning and solubility in such heterogeneous systems, temperature effects and fluctuations, back-diffusion of air O_2 present in vast excess should all be factored in [33].

At the same time, O_2 is one of the most important analytes in biology, medicine, chemistry, biotechnology, drug discovery and development, food and environmental science, process control, and other areas of life sciences [155]. Various analytical techniques have been developed for the detection and quantification of O_2 in various samples. Among these, quenched-phosphorescence O_2 sensing techniques have attracted much attention, as they provide the basis for a broad range of analytical tasks and applications, many of which are unique [22]. Such sensor systems continue their active development [102], and detailed characterisation and calibration of such optical O_2 sensing systems are important.

Calibration of quenched-phosphorescence oxygen sensors involves creating a series of standard conditions with known O_2 partial pressure (pO2, kPa) or concentration ([O_2], μM), temperature and humidity, equilibrating the sensor and measuring its optical signal(s) under these conditions, and then establishing an analytical relationship (i.e. calibration equation) which can be used to convert measured sensor signals into O_2 concentration or pO2 in the sample.

Traditional O_2 calibration methods used precise titration of O_2 dissolved in the sample with glucose / glucose oxidase [156], displacement of O_2 with N_2 or Ar gas (often in the presence of a reference O_2 probe or electrode [49, 157]), use of standard gas mixtures from commercial sources or prepared on site volumetrically, with a precision mass-flow controller or a gas mixer

[158]. Such gas standards are then pumped with a gas delivery system through a thermostated flow-cell, or bubbled through a static calibration vessel containing a mounted sensor coupled with the corresponding detector. Such calibration methods are tedious and not very accurate, their main issues are slow and incomplete gas (especially in the low O_2 range) and T-equilibration of the sensor, leakage of air O_2 into the measurement chamber.

The recently suggested barometric calibration method [159] provided an attractive alternative which can overcome many of the above limitations. The setup described was specifically tailored to the calibration of valuable liquid O_2 bio-probes and consisted of high-performance commercial and home-made components: the vacuum pump, precision digital manometer, static thermostatic holder for probe vial, chamber with thermal insulation, T-probe, detector unit, gas lines, etc. While providing excellent accuracy and convenience in calibration experiments with the liquid probe, this custom-built setup looks rather bulky, inflexible and costly.

In this study, we describe a more simple, flexible and readily available setup for barometric calibration of phosphorescence based O_2 sensors, which is based on a standard rotary evaporator system equipped with a digital vacuum pump (Rotavap). We demonstrate the use of such system with different types of sensor materials and calibration conditions, highlighting its merits and limitations.

3.2 Results and Discussion

3.2.1 Rotavap system and its general suitability for calibration of O_2 sensors

We found that conventional rotary evaporator systems (**Fig. 3.1A)** are well suited for barometric calibration of various types of O_2 sensors, though with some limitations. Such systems equipped with a standard digital vacuum pump can produce, by means of a built-in mechanical regulator, precise levels of vacuum (i.e. total residual pressure, P_T in mBar, kPa or mmHg) in the system, maintain these levels over prolonged periods of time and quickly ramp them up and down.

Rotavap also possesses other features useful for O_2 sensor calibration. Firstly, it can accommodate various sensor materials, by mounting them appropriately in the evaporation flask or sample vial. Thus, solid-state sensor inserts can be attached at the neck or bottom of a standard flask (**Fig. 3.1B**), sensor coatings deposited to the bottom of the flask from a liquid 'cocktail', and liquid probes - simply poured into a 100 mL flask (**Fig. 3.1C**). When the flask

is connected to the Rotavap system, such sensors can be optically interrogated with sensor readers, measuring their optical signals from the outside, in a contactless manner.

Figure 3.1. Images of the Rotavap system for barometric calibration of phosphorescent O_2 sensors. **A.** Main system components: 1-digital vacuum pump (with absorber of organic vapours); 2-condenser unit; 3-rotation motor assembly; 4-water/solvent collecting flask; 5-water bath; 6- sensor flask; 7-Optech and Firesting readers. **B**. Vacuum flask with different types of PtBP based sensors: O_2 Platinum sensor stickers (Mocon) attached to the neck (top), membrane with a solid-state sensor dot mounted in the bottom left part, and microparticle sensor (MPs) coating applied on the inner wall of the flask (right side); **C**. 100 mL flask with liquid $NanO_2$-IR probe**.**

Rotavap system can also provide active temperature control during sensor calibration, by means of a heating/cooling bath in which the sensor flask is immersed. Since O_2 sensors have high cross-sensitivity to temperature, precise control and knowledge of sensor temperature during calibration procedure are critical [160]. Surface *T* of the flask can be verified with a handheld IR-thermometer (DT8380, Duratool) and then extrapolated as the sensor temperature. However, for some settings of the calibration system, the anticipated sensor temperature is not always achieved (see below).

The Rotavap system allows sensor calibrations to be performed in: i) dry gas environment (no water and water vapour in the system); ii) humid gas environment (saturating *Pw* conditions), or iii) aqueous phase. Potentially, the range of usable conditions and O_2 sensors can be extended

by substituting water phase in the sensor flask with an appropriate organic solvent [161]. So, Rotavap system can model the main types of environments and samples in which O_2 sensors currently operate.

Immersing the sensor flask in a bath and rotating it facilitate rapid gas and *T* equilibration of the sensor, whereas equilibration under static conditions, especially for large liquid samples, can be slow [162]. However, rotation mode complicates the measurement of sensor signals, which now includes: i) stopping flask rotation, ii) lifting it from the bath; iii) measuring sensor signal and T with an optical reader and IR-T probe; iv) moving the flask back into the bath; v) resuming rotation. For a skilled operator, such measurement cycle takes ~10 s, during which sensor *T* does not change much.

During the calibration experiment in a closed Rotavap system, sensor optical signals, namely phosphorescence intensity (RFU), lifetime (µs) and/or phase shift ($dphi^o$), are measured non-invasively and under ambient light. For this, we used two commercial handheld readers - Optech Platinum (Mocon-Ametec, USA) and Firesting-GO2 (PyroScience, Germany). Both are designed to operate with detached PtBP based sensors (615 nm excitation and 760 nm emission bands). These instruments allow flexible optical alignment and measurement distance between the sensor and detector of up to 5-10 mm [163]. The Optech reader directly measures phosphorescence decay and lifetime values, while the Firesting reader measures phase shift ($dphi^o$) signals, under periodically modulated LED excitation (4 kHz in our case). For homogeneous samples, $dphi^o$ signals can be converted into τ_p (µs) values as described in Eqn.1.10 [101]:

3.2.2. Basic theory and analytical relationships

According to the Dalton's law, total residual pressure in the gas phase of the Rotavap system, P_T can be expressed as follows:

$$P_T = P_W + \text{pO2}/0.2095 \tag{3.1}$$

where P_W is partial pressure of water, and 0.2095 is the O_2 fraction in dry air. So, for each P_T value set up by the vacuum pump, pO2 can be calculated as:

$$\text{pO2} = 0.2095*(P_T - P_W) \tag{3.2}$$

For the sensor environment, such calculations require knowledge of *in situ Pw* and *T* (ºC), i.e. inside the flask. In this study, temperatures of 2ºC, 23ºC, 30ºC and 40ºC were set in the Rotavap

water bath and monitored in the sensor flask with an IR-thermometer. The corresponding P_W values were taken from (https://www.wiredchemist.com/chemistry/data/vapor-pressure).

If the sensor is liquid (e.g. NanO_2-IR probe) or operates in aqueous samples, pO2 calibrations (in kPa or Torr values) may need to be converted into O_2 concentrations, e.g. µM. Such conversions are done using O_2 solubility data calculated using the Henry's law equation. Specific conditions and parameters used in this study are given in **Table 3.1.** The corresponding values of O_2 solubility in water and seawater at different temperatures were taken from the (https://www.engineeringtoolbox.com/oxygen-solubility-water-d_841.html).

Table 3.1: Parameters of the gases under the conditions used in this study.

Temperature, °C	Pw, kPa	Pw, torr	O_2 Solubility in Water, mM	O_2 Solubility in Seawater, mM
0	0.611	4.59	457	349
10	1.23	9.21	353	275
20	2.39	17.54	284	225
30	4.25	31.84	236	190
40	7.38	55.37	202	165
50	12.34	92.5	177	146

Sets of calibration data points (τ; pO2) or (τ; [O_2]) produced in the calibration procedure are then analysed to determine the corresponding quenching constants and assess the linearity in Stern-Volmer plots and sensor homogeneity [164]. Then the calibration plots are inverted, i.e. (pO2; τ) or ([O_2]; τ) and fitted with a suitable physical model or mathematical function, to give a calibration equation that can be used to convert measured PLT values into pO2 (kPa) or [O_2] (µM). For the Firesting reader, the same data processing algorithm can be applied to the primary signal readings (phase shift, $dphi^o$), or calculated PLT values.

3.2.3. Initial testing of the Rotavap setup

General usability of the Rotavap system was initially assessed with solid-state sensor inserts attached inside the flask. Different types of sensors were measured under ambient air environment (i.e. 21 kPa pO2, vacuum pump off) and room temperature (23°C): the commercial sensor sticker (Mocon), PtBP-PS coatings on PVDF membrane, PtBP-dyed microparticles in hydrogel D4 binder (MPs), and NanO_2-IR probe spotted and dried on PVDF

membrane (**Fig. 3.2**). Two sensor types were also produced from the cocktails diluted 1:2 and 1:4.

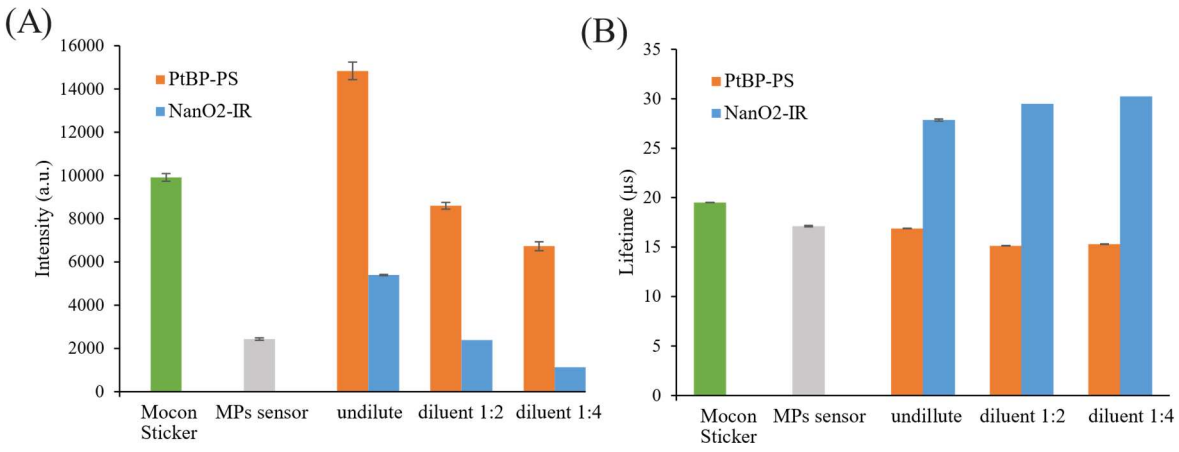

Figure 3.2. Phosphorescence intensity (A) and lifetime (B) signals for the different solid-state sensors, placed inside the Rotavap flask and measured with an Optech reader in dry air environment (21 kPa pO2, vacuum pump OFF) at ambient temperature (23°C). N = 3.

From **Fig. 3.2A** one can see that highest *I* signals were obtained from standard (UD) PtBP-PS coatings on PVDF support (~15,000 FU), followed by the Mocon sensor (~10,000 FU), the $NanO_2$-IR coating (UD, ~5,500 FU) and the MP sensor (~2,500 cps). As expected, the sensors from diluted cocktails produced gradually decreasing *I* signals. The *I* signals from all the sensors were above the acceptable threshold of 1000 cps for the Optech reader (except for 1:4 diluted $NanO_2$-IR), resulting in stable and accurate τ signals (**Fig. 3.2B**). The close τ signals from the Mocon, solid-state and MP based sensors (17-19 µs) suggest their similar chemical composition and O_2 quenching micro-environment in PS and PS-DVB polymers. In contrast, the $NanO_2$-IR sensors produced significantly higher τ values (28 µs), due to the different encapsulation medium for PtBP dye. These τ readings are in agreement with previously reported τ_q values for these sensors [19, 165]. Thus, for these settings of the Rotavac system, the sensors are deemed usable for calibration over the pO2 range 0-21 kPa.

Next, using Optech and Firesting readers, we measured the signals from a sensor sticker placed in a 100 mL vacuum flask and exposed to a dry and humid gas environment with variable pO_2 levels (0 - 21 kPa, produced by the Rotavap system) at 23 °C. The results presented in **Fig. 3.3**, led us to the following conclusions:

- Humidity (*Pw*) of the gaseous atmosphere has practically no effect on sensor calibration. This is in agreement with vendor's specifications, which states no cross-sensitivity with relative humidity (RH) for this sensor type.
- The shape of calibration curves and the magnitude of lifetime response to pO_2 look normal and optimal for O_2 sensing. The non-linearity of the Stern-Volmer plots is minor ($R^2 = 0.9942$) so sensor homogeneity is high, whereas many existing O_2 sensors and polymeric matrices show prominent heterogeneity [102, 161].
- The results produced by the two instruments do not match, particularly in the high and low *pO2* ranges. This is likely due to the different lifetime measurement methodologies: direct time-domain method for the Optech and indirect phase fluorometry for the Firesting, with τ calculation according to **Eqn.1.10**, which strictly speaking is not applicable for sensors with non-linear Stern-Volmer plots [101]. Although with this systematic error, the sensitivity, repeatability and stability of the measurements on Firesting were comparable to Optech, the latter instrument was selected by us in further experiments.

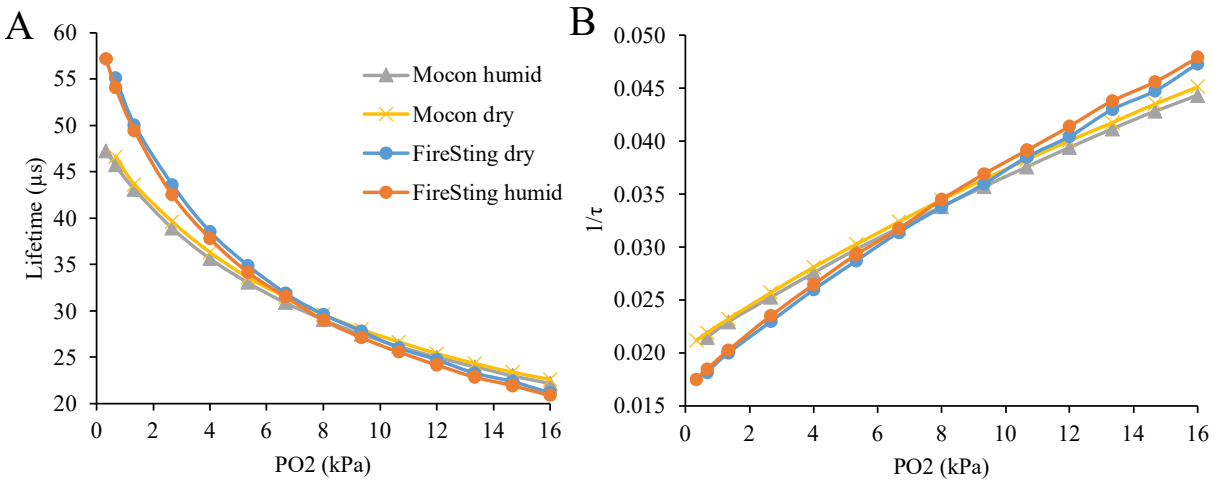

Figure 3.3. Calibrations of a Mocon sensor sticker inside the flask (bottom part), generated on the Rotavap system in dry and humid gaseous atmosphere at 23 °C, using Optech and Firesting readers. **A:** τ *vs* pO2 plots; **B:** and 1/τ *vs* pO2 plots. N = 3.

Similarly, we carried out barometric calibrations in the dry and wet gaseous environment, at 23°C for the solid-state MP sensors and spotted RL100 polymer-based coatings. The first sensor type comprises a rigid polymer material (crosslinked PS-DVB), while the second - nanoparticles of an amphiphilic polymer that can swell in humid environment.

Indeed, **Fig. 3.4A-B** shows practically no difference between the dry and humid air calibrations for the MP sensor, i.e. no cross-sensitivity with humidity. Conversely, the RL-100 coatings showed prominent sensitivity to humidity with significant differences in pO2 calibrations. In the dry environment, τ values were consistently higher than for the humid sensor (by 2-5 µs - **Fig. 3.4C-D**), while its K_{SV} was lower.

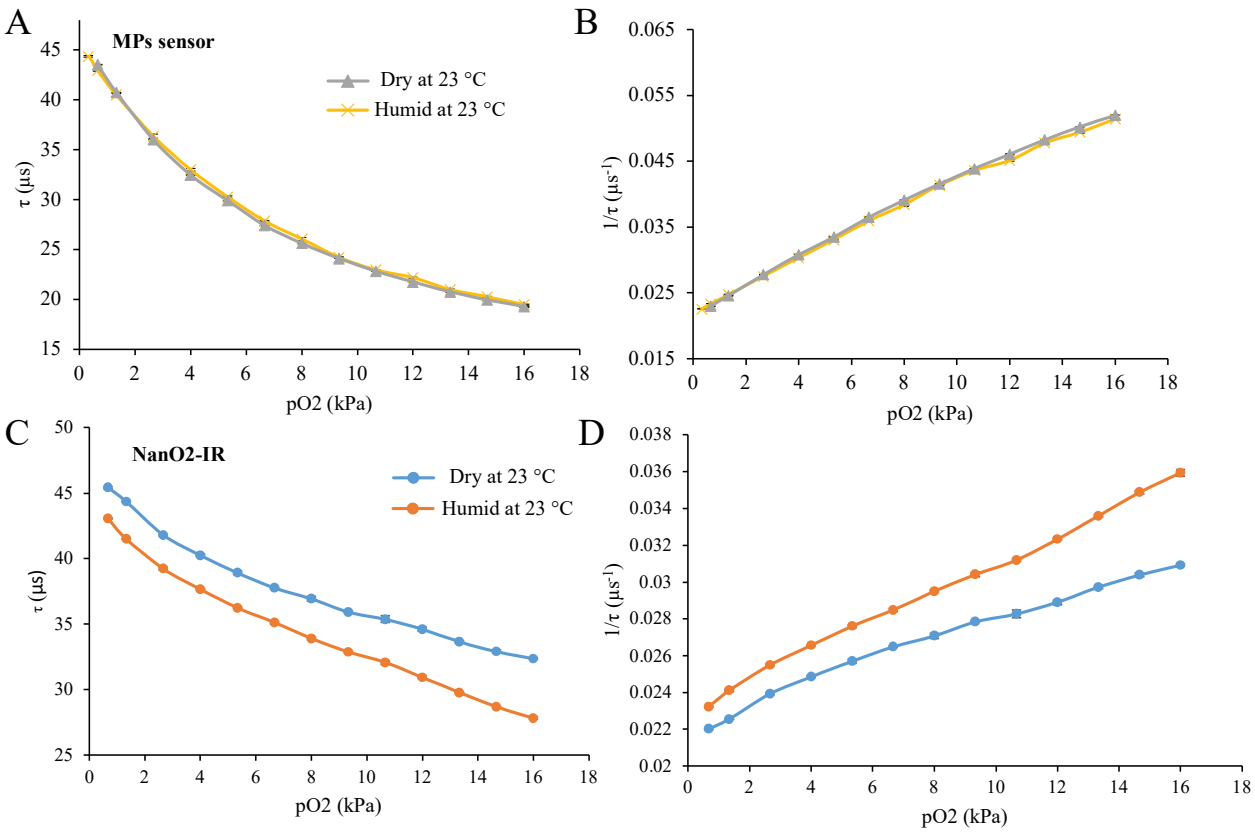

Figure 3.4. Lifetime calibrations and Stern-Volmer plots for the solid-state MP sensors **(A-B)** and RL-100 polymer-based NanO$_2$-IR coatings **(C-D)**, generated on the Rotavap system in dry and wet atmosphere at RT 23°C using Optech reader. N =3. The NanO$_2$-IR coatings were made by spotting 5 µL of 5 mg/mL stock on the PVDF membrane. Note: the standard deviations for replicates are within data point margins.

3.2.4. Assessment of T-control of the sensors inside the Rotavap system

Following the initial evaluation of the Rotavap system at ambient temperature, we attempted to calibrate the solid-state sensors and coatings at other temperatures: 4ºC, 30ºC, 40ºC and 50ºC, in humid gaseous environment. We found that when the sensors were mounted near the flask neck, with an adhesive tape (membrane inserts) or in-built adhesive pad (Optech sticker), they showed unexpectedly small changes in O_2 calibration when the bath *T* changed stepwise from 4ºC to 50ºC (**Fig. 3.5A-C**). This pointed to poor T-control for such sensors, working part of which was not closely adhered to the area of the flask which was subjected to heating or cooling. Indeed, reference measurements with an IR-thermometer (**Fig. 3.5B**) confirmed the significant differences between the set *T* in the bath and sensor *T in situ*. And when the sensors were placed further away from the bath inside the glass adapter, ramping the bath *T* only marginally changed sensor *T* and O_2 calibration (**Fig. 3.5C-D**).

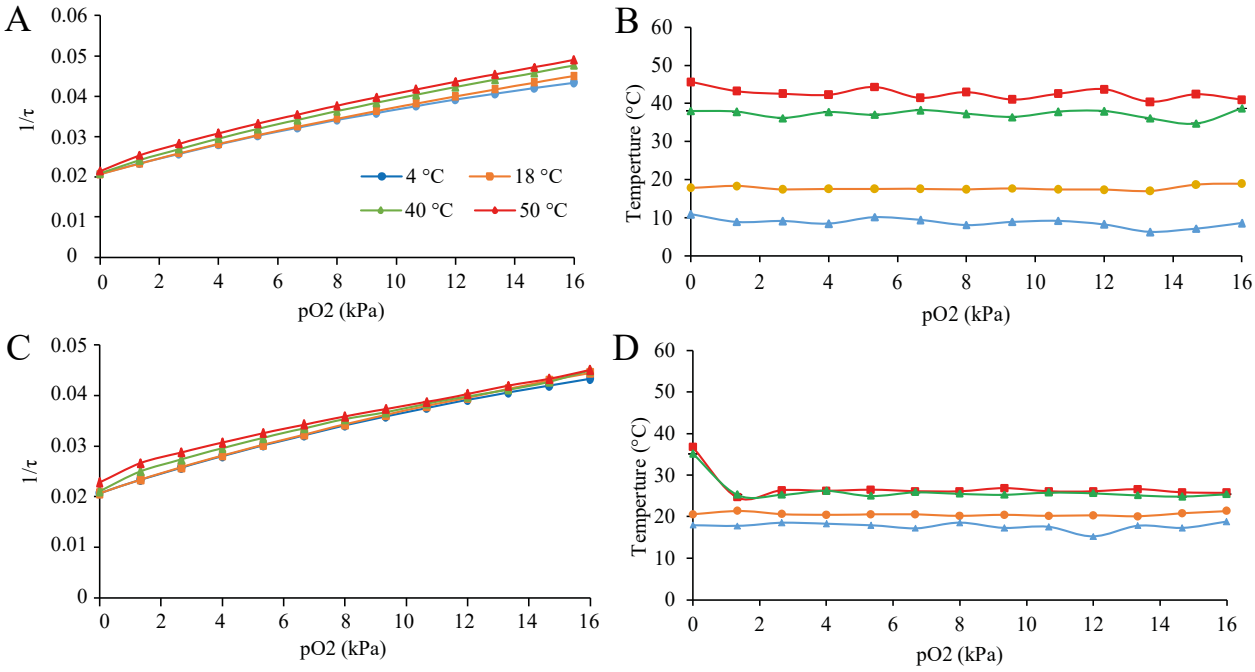

Figure 3.5. O_2 calibrations in humid gas atmosphere for the sensor membranes mounted inside the flask neck **(A)** or near the glass adaptor **(C)**, at different temperatures set in the bath, measured with Optech reader. Corresponding profiles of actual temperature, measured with IR-thermometer, are shown in **(B)** and **(D)**. N = 3.

From these experiments, we concluded that detailed characterisation of solid-state sensors by barometric calibrations on the Rotavap system, mounted as in **Fig. 3.1B** and measured in

gaseous environment at different temperatures, requires care. The critical part of this setup is heating transfer between the water bath, flask wall and sensor substrate, which is inefficient in the absence of close contact between the sensor and the thermostated/bathing part of the flask wall.

3.2.5. Detailed barometric calibrations over broad T-range

The issues with T control of the sensor material, highlighted above and in **Fig. 3.5**, can be overcome by depositing solid-state sensor coatings directly on the inner wall of the bottom part of the flask (**Fig. 3.1B**), or using liquid sensors poured into the flask (**Fig. 3.1C**). Such calibration settings provide more efficient heat transfer along the sensor/flask/bath axis of the Rotavap system. As a result, they ensure stable and accurate O_2 calibrations over wide ranges of T and pO2 values.

Thus, **Fig. 3.6A** illustrates that temperature of the liquid probe, NanO$_2$-IR (10 mL of 5 mg/mL aqueous solution) was stable and accurate, resulting in smooth and well resolved O_2 calibrations (in τ scale) and corresponding Stern-Volmer plots (in $1/\tau$ scale) at the different T settings in the water bath (**Fig. 3.6B-C**). The prominent reductions in τ_q and increases in K_{SV} at higher temperatures are in agreement with basic theory, unlike the results in **Fig. 3.5**, while the minor decreases in τ_o values at higher T are due to more efficient non-radiative deactivation of excited triplet states [101]. The structural changes in the dye-polymer assembly of the sensor nanoparticles [53] may release internal quenching at higher temperature.

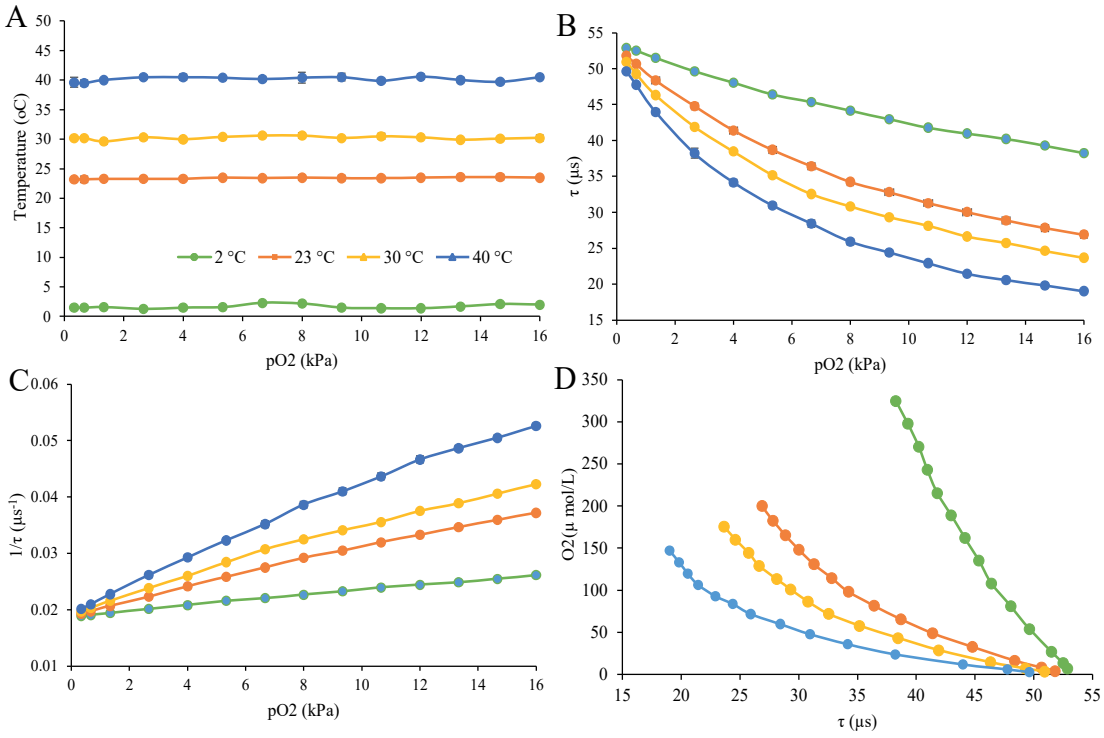

Figure 3.6 Calibrations of the liquid probe, $NanO_2$-IR (10 mL of 2.5 mg/mL solution) at different temperatures, obtained using Optech reader. **A.** *T* profiles at the flask surface and sensor were measured with an IR T-gun. **B, C.** Calibrations in τ and $1/\tau$ scale at different *T*. **D.** The final O_2 calibration: dissolved [O_2] vs τ. N=3. Note: the standard deviation for replicates are within data point margins.

From **Fig. 3.6** data, a number of key operational parameters of the sensor material can be determined. Thus, τ_0 values, which are difficult to measure experimentally in barometric calibrations, can be accurately quantified by extrapolating the corresponding plots in **Fig. 3.6C,** with the Y-axis intercepts corresponding to $1/\tau_0$ values. *Ksv* values can be calculated from the trendline fitting of **Fig. 3.6C** plots, as the product of the calculated τ_0 value and the slope of $1/\tau$ plot. The heterogeneity of sensor material and *Ksv* can also be assessed using more complex approximations of **Fig. 3.6C** data, such as the two-site model [102, 166]. And the ultimate O_2 calibration equations for each *T* can be obtained from **Fig. 3.6D** plots, by fitting individual curves with appropriate functions with mathematical equations. A summary of these parameters for the different calibration conditions and sensor materials is given in **Table 3.2**.

Of note, in each individual calibration experiment with $NanO_2$-IR probe, which lasted 1-2 hours, about 1.0-1.5 mL, or 10-15% of the sample volume were lost as a result of water evaporation under vacuum. Nevertheless, since Rotavap barometric calibrations do not consume or contaminate the probe, it can be effectively recovered and reused. We did this by weighing the recovered probe sample and adding pure water to it to the original volume/weight. The recovery and reuse of liquid probes is particularly important for valuable sensing materials.

To further prove the performance of the Rotavac setup, we compared the calibrations of $NanO_2$-IR probe at 1:2 and 1:4 dilutions, and in the presence of salt (5 g/L NaCl), at 30 ^oC. **Fig. 3.7** demonstrates the stability and accuracy of such calibrations.

Table 3.2. The key operational parameters of the different sensors determined from barometric O_2 calibrations on the Rotavac system at different temperatures.

Sensor type	Condition	Linearisation equation 1/τ vs pO2	τ_0, ms	Ksv, kPa^{-1}	O_2 Calibration Equation [O_2], μM *vs* τ, μs
$NanO_2$-IR	H_2O, 2°C	y = 0.0005x + 0.0189 (R^2 = 0.9973)	52.91	0.0265	y = 0.7368x^2 - 88.873x + 2648.3 (R^2 = 0.9993)
	H_2O, 23°C	y = 0.0012x + 0.0194 (R^2 = 0.9962)	51.55	0.0619	y = 0.2719x^2 - 28.787x + 770.36 (R^2 = 0.996)
	H_2O, 30 °C	y = 0.0014x + 0.020 (R^2 = 0.9928)	50.00	0.0700	y = 0.2404x^2 - 23.761x + 595.46 (R^2 = 0.993); y = -0.0101x^3 + 1.3615x^2 - 63.768x + 1055.2, (R^2=0.9994)
	H_2O, 40 °C	y = 0.0021x + 0.0208 (R^2 = 0.994)	48.08	0.1024	y = 0.1733x^2 - 16.024x + 376.86 (R^2 = 0.9845); y = -0.0081x^3 + 0.994x^2 - 42.305x + 642.03, (R^2 = 0.9956)
	NaCl, 5g/l 30°C	y = 0.0013x + 0.0202 R^2 = 0.9948	49.50	0.0644	y = 0.2497x^2 - 24.88x + 627.32 (R^2 = 0.9962)
MP	H_2O, 2°C	y = 0.0016x + 0.0227 R^2 = 0.9896	44.05	0.0705	y* = 0.2422x^2 - 19.939x + 417.46 (R^2 = 0.9875)
	H_2O, 23°C	y = 0.0019x + 0.0227 R^2 = 0.9947	44.05	0.0837	y* = 0.6069x^2 - 52.336x + 1150.1 (R^2 = 0.9930)
	H_2O,40°C	y = 0.0021x + 0.0234 (R^2 = 0.993)	42.74	0.0897	y* = 0.3173x^2 - 27.407x + 601.69 (R^2 = 0.9904)
Optech Sticker	Dry gas, 23 °C	y = 0.0015x + 0.0214 (R^2 = 0.9956)	46.73	0.0701	y* = 0.0249x^2 - 2.3233x + 55.194 (R^2 = 0.9965)
	Humid gas, 23 °C	y = 0.0015x + 0.0215 R^2 = 0.995	46.51	0.0698	y* = 0.0244x^2 - 2.2821x + 53.996 (R^2 = 0.9961)
PtBP-PS	Dry gas, 23 °C	y = 0.0017x + 0.023 R^2 = 0.9964	43.48	0.0739	y* = 0.0285x^2 - 2.3812x + 51.498 (R^2 = 0.9954)
	Humid gas, 23 °C	y = 0.0017x + 0.023 R^2 = 0.9964	43.48	0.0739	y* = 0.0302x^2 - 2.4992x + 53.446 (R^2 = 0.9963)

* - Calibration equation is in kPa scale.

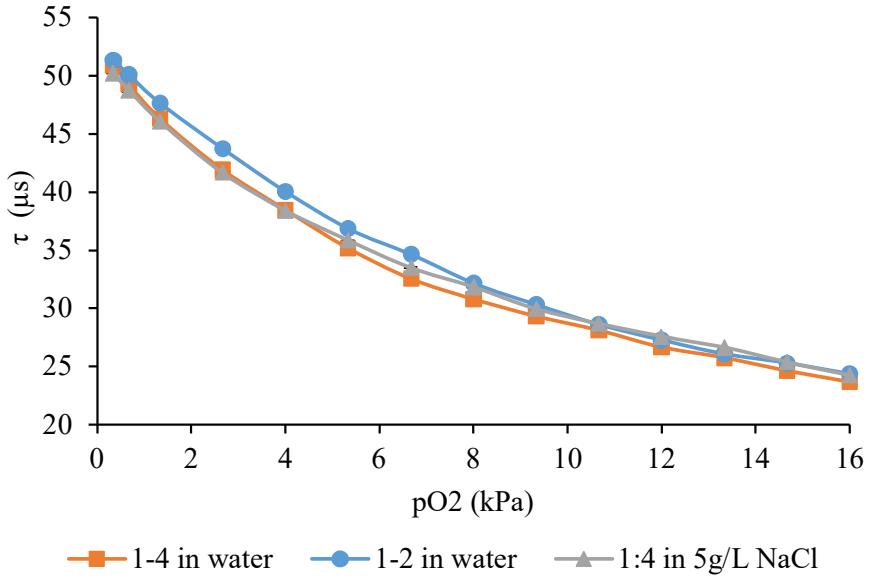

Figure 3.7 The effects of probe concentrations and media salinity on the calibrations of $NanO_2$-IR probe, generated with Optech reader at 30ºC (n=3).

Similar to the above experiments with $NanO_2$-IR, we also calibrated the MP sensors spotted on the inner wall of the flask. From **Fig. 3.8** and **Table 3.2** data, the following observations and comparisons can be made: i) T-sensitivity of the MP sensor is lower, seen as narrower span of the calibration curves; ii) the τ_o values for the MP sensor are significantly lower (<45 µs *vs* >48 µs); iii) the span of the τ values is lower at 40 ºC (45-20 µs *vs* 50–20 µs), but higher at 2 ºC (45–22 µs *vs* 52-45 µs); iv) the K_{SV} values of the MP sensor at 2 ºC are >2.5-times higher than those of the $NanO_2$-IR, so as the sensor sensitivity to O_2; v) all O_2 calibrations are fitted well with second or third power polynomial functions with good correlation (**Table 3.2**).

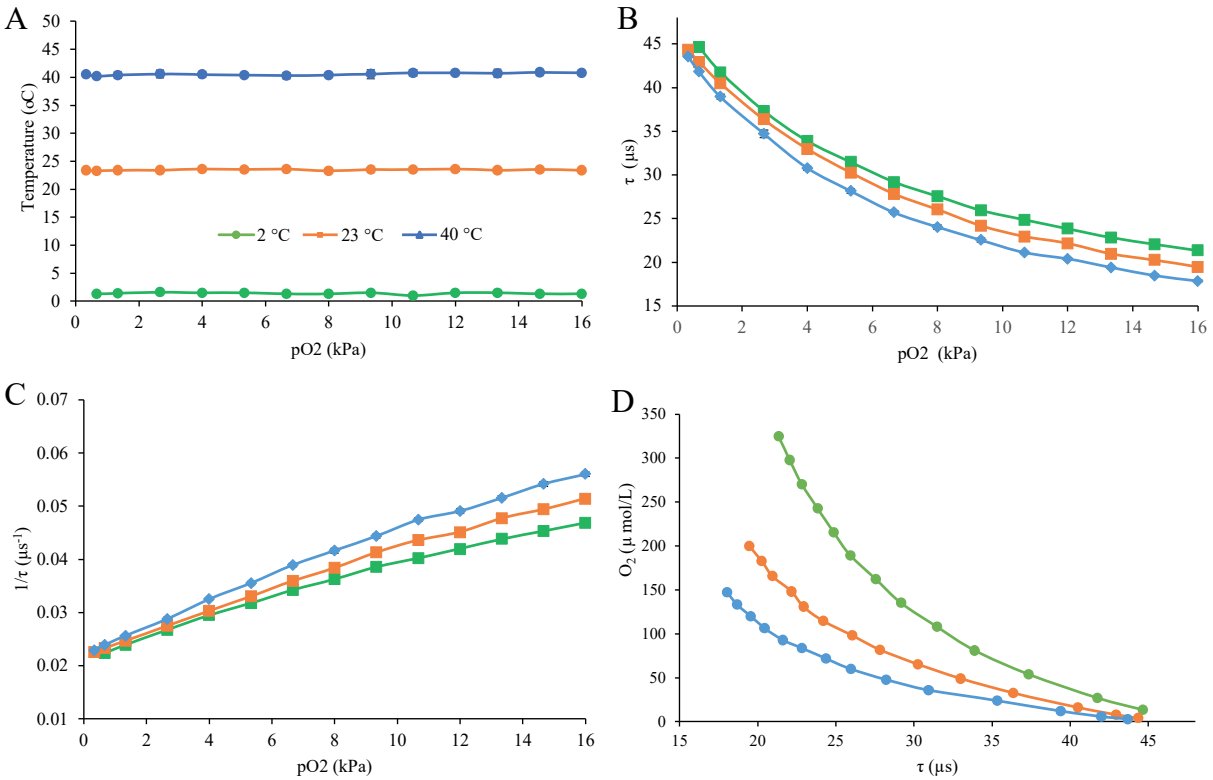

Figure 3.8. MPs sensor (5 µL of the cocktail spotted inside the glass flask) calibrated at different temperatures in aqueous environment (10 mL of water) using Optech reader (n=3). **A.** Profiles of sensor *T in situ* measured with an IR T-gun. **B-C.** Calibration curves in τ and $1/\tau$ scale. **D.** The calibration curve of dissolved [O_2] *vs* τ.

By plotting the calculated K_{SV} *vs* T data points, an analytical function can be obtained for calculating K_{SV} for any temperature within the studied range (**Fig. 3.9**). From these dependences, correction coefficients (kPa^{-1} / ºC or % / ºC) can be worked out for compensating sensor readings for T fluctuations [102].

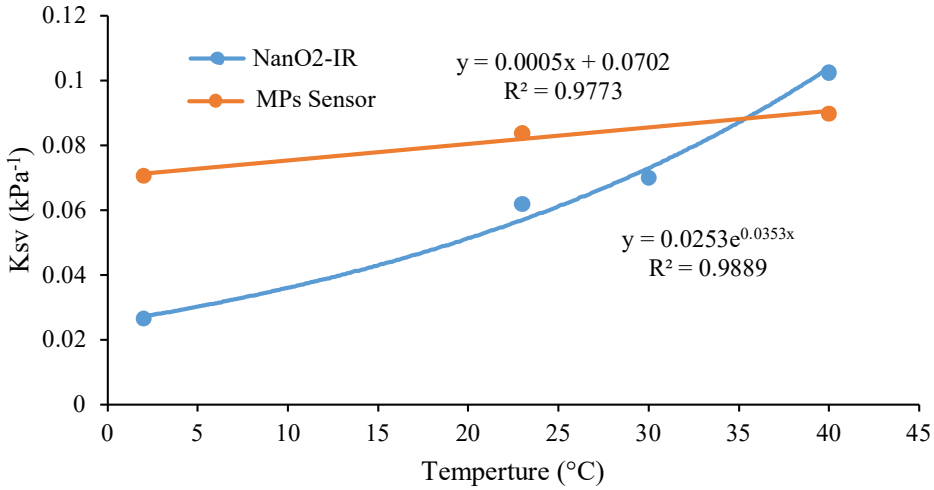

Figure 3.9. Temperature dependences of K_{SV} and analytical equations, obtained from barometric calibrations of the MP sensor and NanO$_2$-IR probe.

Lastly, we compared barometric calibration of NanO$_2$-IR probe at 30 ºC with conventional O$_2$ calibration performed using standard N$_2$:O$_2$ gas mixtures generated by a gas mixer/tonometer (LNI, Switzerland), bubbling them through a vial with the probe [148, 158]. We found that conventional O$_2$ displacement method significantly underestimated τ values in the low O$_2$ range (τ_o = 46 µs *vs* 50 µs), due to incomplete gas equilibration of the liquid sample. As a result, it produced inaccurate O$_2$ calibration equation: [O$_2$, µM] = 770.35*exp(-0.049*τ) - 86.16. So, since barometric calibrations show better accuracy and precision, the corresponding calibration equations were adopted for use in biological experiments with NanO$_2$-IR probe [52].

3.3 Conclusions

The new barometric O$_2$ calibration setup, based on a standard Rotavap system equipped with a digital vacuum pump, was demonstrated with a panel of different sensor materials based on the common PtBP O$_2$-sensitive phosphorescent dye. The range of sensors, including the commercial sensor stickers, membrane inserts with solid-state sensor coatings, coatings applied directly inside the vacuum flask and liquid O$_2$ probe NanO$_2$-IR, were measured in a contact-less manner with handheld readers Firesting and Optech operating in PLT-based sensing mode.

The system was seen to produce smooth and accurate multi-point calibrations in dry and humid gas atmosphere or in aqueous media, at different temperatures and with different sensor types.

However, care is required when calibrating detachable solid-state sensors in the gas phase at different temperatures, ensuring efficient control of their *T* inside the Rotavap.

Having optimised the measurement settings and calibration procedures on the Rotavac system, detailed calibrations and characterisation of several sensor materials were carried out and sensors' main operational parameters were determined and compared. The results prove that the new barometric calibration setup provides a convenient and versatile alternative to traditional O_2 calibration methods, and it is also more accurate and simpler.

Chapter 4: Phosphorescence lifetime measurements with sensor materials: comparison of different detection platforms

4.1. Introduction

Platforms for (bio)analytical applications utilizing phosphorescence are increasingly popular, thanks to their convenient spectral properties, large stokes shifts, longwave emission, and straightforward lifetime-based measurements in the µs range [17]. PLT based detection is particularly advantageous for quenched-phosphorescence sensing of O_2, where it allows for the simple and robust analytical systems with internal referencing, stable once-off calibration and accurate quantitative readout of O_2 concentration [167, 168]. Nowadays, PLT based detection is regarded as superior to the traditional intensity-based sensing [169].

To date, a diverse array of such systems facilitate the rapid O_2 determination in both liquid and gaseous specimens as well as intricate biological samples containing respiring cells and tissues [22]. Some of these applications have been developed into comprehensive bio-analytical platforms [170], gaining widespread use particularly in live cell analysis and multi-analyte sensing [111]. Other applications have been performed on existing detection platforms with PLT detection functions, for example, TR-F readers [171] and PLIM microscopy [172].

PLT based detection can be achieved by various methods, including phase shift measurements, decay time measurements using binning method, by simplified time-gated RLD or advanced TCSPC technique [110, 173]. A few other specialized schemes for PLT measurements have also been described [170]. Besides the different detection methods, PLT can be also realized as point measurement or in an imaging format. The latter is further sub-divided into 2D (wide-field or confocal) and 3D (laser scanning), one-photon and two-photon imaging [174].

Phase shift measurements typically utilize an LED (pulsed at kHz frequency) as modulated excitation, and a silicon photodiode for detection. Such platforms offer many advantages including being compact, stable and convenient. For instance, they can be designed as handheld readers for contactless and non-invasive measurements [175], providing cost-effective, reliable, and accurate readouts. Nevertheless, such platforms usually necessitate strong phosphorescence intensity signals, a high signal-to-noise ratio (S:N) and/or integrated optics. In the cases where samples utilizing dim sensors, or exhibit high light scattering or

autofluorescence, phase-based PLT systems may encounter inaccuracies and interfere by light scattering or sample auto-fluorescence.

From this prospective, time domain based PLT methods are favored, particularly for analyzing complex biological samples containing mammalian cells, at high levels of parasitic light (scattering and sample autofluorescence), or using 'dim' sensors with low S:N ratio. Despite their generally better stability than intensity-based measurements, PLT based platforms still suffer from measurement artefacts, and they can also generate inaccurate PLT values. Thus, it is essential to carry out cross-comparative measurements of each PLT detection platforms for ordinary users and large-scale applications.

In this study, we conducted a head-to-head comparison of different PLT measurement platforms operating in the time domain, to evaluate and validate them against one another. We aimed to disclose the main sources of errors and work out strategies for optimizing such measurements. To achieve this, different types of solid-state phosphorescent materials were measured on the three different detection platforms under several environmental conditions (e.g. air-saturation and deoxygenation) and different experimental settings. Based on this, we provide practical recommendations for potential users on these platforms and O_2 sensing applications.

4.2 Results and Discussion

4.2.1 General description and comparison of the different platforms

The different detection platforms compatible with Pt-porphyrin based sensors that were evaluated in this study utilize different measurement principles and optoelectronic components/hardware to quantify PLTs in the µs range. Victor 2 reader and Cary Eclipse spectrofluorometer both use Xe-flash lamp excitation and provide point measurement of mean PLT values. The confocal PLIM/FLIM TCSPC microscope [176] utilizes 405 nm picosecond diode laser excitation and imaging readout. The fourth PLT detection platforms (Tpx3Cam PLIM imager) equipped with a time-stamping Tpx3Cam optical camera (Amsterdam Scientific Instruments) and an LED excitation source (50-500 ns wide plus), was also used for comparison of PLT readouts. However, this was done by another researcher (Dr. Rajannya Sen) and is therefore not presented in this chapter and thesis. More details regarding this PLT based platform can be found in [107].

PerkinElmer Victor 2 is a filter-based multi-label plate reader for diagnostic applications. It enables absorbance, prompt fluorescence and TR-F detection functions. Specifically, its TR-F

module is devised to deliver ultimate detection sensitivity for fluorescent lanthanide labels such as Eu^{3+}, Tb^{3+}, and Sm^{3+} chelates. This is achieved through high-energy UV excitation with a 15 W Xe-flash lamp, efficient epi-fluorescence optics, and a photon-counting time-gated PMT detector. Coupled with an active temperature control of the microplate compartment, the instrument is well-suited for detecting phosphorescent Pt-porphyrin labels and O_2 sensors on their basis [34]. Facile PLT measurements on this platform by the RLD method allows for quantitative quenched-phosphorescence O_2 sensing and high-throughput O_2 respirometry, along with related cell-based assays [177]. These instruments offer stable and reproducible PLT readouts, smooth and accurate kinetic profiles, with PLT calibrations that can be transferred between different devices [151]. Similar TRF plate readers such as Biotek, Tecan and BMG, are also commercially available in the market.

Cary Eclipse represents a classical cuvette spectrofluorometer, featuring a 75W Xe-flashlamp excitation source, 90-degree optics with two diffraction grating monochromators in the excitation and emission channels, and a PMT detector. These monochromators offer flexibility in selecting optimal excitation, emission and sensitivity settings (utilizing two wavelengths and slits). It can be tailored for diverse phosphorescent samples, which may vary in their spectral characteristics and brightness. Both specific and parasitic light components in the system can be assessed by spectral scanning, in prompt fluorescence or TR-F mode. Compared to the Victor, Cary Eclipse has limitations in detection sensitivity and temperature control, and similar detections in Xenon based flashlamp excitation. Nevertheless, its PLT decay mode is more robust and powerful than the RLD based methods, which enables both mono- and bi-exponential fittings of the multi-point phosphorescence decay curves.

The confocal FLIM-TCSPC microscope developed by Becker& Hickl is specially designed for 3D FLIM measurements of ns/ps fluors in biological samples. It is equipped with a picosecond or femtosecond laser operating at 20-80 MHz frequency range for excitation, laser-scanning confocal optics, and fast TCSPC electronics. Subsequently, it was upgraded to support the PLIM mode, wherein emitted photons are recorded after the ps laser delivers a train of excitation pluses and switched into OFF mode. PLIM mode enables more rapid generation of ms decays compared to direct TCSPC-FLIM mode, but still, it requires rather long time to collect sufficient number of photons for the fitting. PLIM acquisition time typically ranges from ~2 min for 2D images and 20-40 min for 3D images or ~18 ms per pixel. Note that phosphors with lifetimes around 20-50 μs necessitate a ~200 μs time range (laser-on plus laser-off time). The confocal FLIM/PLIM system is more sensitive and accurate as its ps/fs laser

does not contribute parasitic photons to the decay. The generated decays contain a substantial amount of data points (hundreds and thousands of photons and time bins), thus facilitating straightforward fitting and extraction of PLT details. The main features of the three platforms are summarized and compared in **Table 4.1**.

In this chapter, we evaluated these instruments by measuring PLT values of three solid-state phosphorescent sensors based on red-emitting Pt-porphyrin dyes (**Table 4.2**). These phosphors share similar excitation and emission characteristics as illustrated in **Fig. 4.1**, but differ in brightness, levels of optical background and PLT values. In addition, their similar chemical structure results in similar dye-polymer interaction of the sensor's films, decreasing this effect on the photophysical properties. PLT measurements were carried out in deoxygenated and air-saturated conditions at 37°C. Non-phosphorescent materials with low or high optical background were also used as Blank samples (**Table 4.2**). Note that for Sensor 2, high spectral overlap between OEPK absorption and Pt-OEP emission allows FRET to occur (**Fig.4.2**) which can alter PLT values of the latter dye.

Table 4.1. Comparison of the different PLT measurement platforms.

Platform/Parameter	**Victor TRF Reader**	**Cary Eclipse spectrofluorometer**	**Confocal FLIM/PLIM microscope**
PLT Measurement Method	RLD	Phos Decay /binning	Multi-channel Scaler
Measurement Mode	Point measurements	Point measurements	2D/3D Imaging
Excitation source	15W Xe-flashlamp (pulse >20 µs)	75W Xe-flashlamp (pulse >20 µs)	10 mW Picosecond laser
Excitation wavelength	340 ± 60 nm (filter)	390 ± 10 nm (grating)	405 nm
Emission	642 ± 10 nm	650 ± 20 nm (grating)	650±30 nm (filter)
Detector type	Photon counting PMT	Analog PMT	Photon counting PMT and TCSPC
No of points on decay (time bins)	2	10-20	1024
Decay fitting	Pseudo 1-exponential	1/2-exponential	1/2-exponential
Measured LT range	>10 µs	>10 µs	>100 ns
Sensitivity	High	Medium	Medium
Measurement & sample geometry	Sensor coatings in 96-well plate	Planar sensor in a cuvette	Flat sensor coating
Signal acquisition time	~1s	~5s	>2 min
Measurement mode	Single shots and kinetics	Single shots	Single shots
Volume of data for PLT processing	Low	Medium	High
Price range, $	>$30k	>$30k	>$400k
Main optimisation parameters	Delay, t_1 and t_2 Lamp energy	Delay time t_d Gate time, t_g	Delay, t Laser-on time

Table 4.2. Description of the tested solid-state phosphorescent materials.

Material	Chemical composition	Photoluminescence properties
Sensor 1	4.3 mM PtOEP in PVC	Strong phosphorescence
Sensor 2	4.3 mM PtOEP & 1.37 mM OEPK in PVC	Strong/moderate phosphorescence and strong fluorescence
Sensor 3	4.3 mM PtOEP-SB in PVC	Moderate/weak phosphorescence
Blank 1	Plasticised PVC	Low background (scattering)
Blank 2	1.37 mM OEPK in PVC	High background (fluorescence)

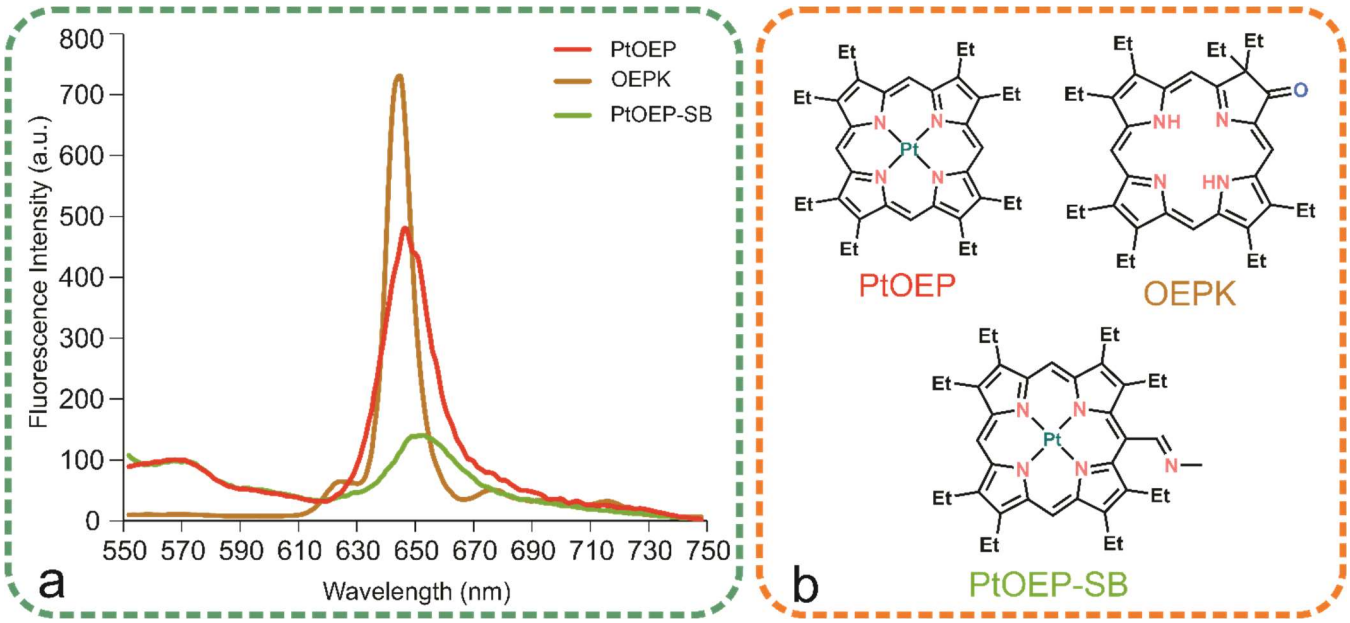

Figure 4.1. Emission spectra (**a**) and chemical structures of the dyes (**b**) used for the sensors 1-3 measured on a Cary Eclipse spectrofluorometer**.**

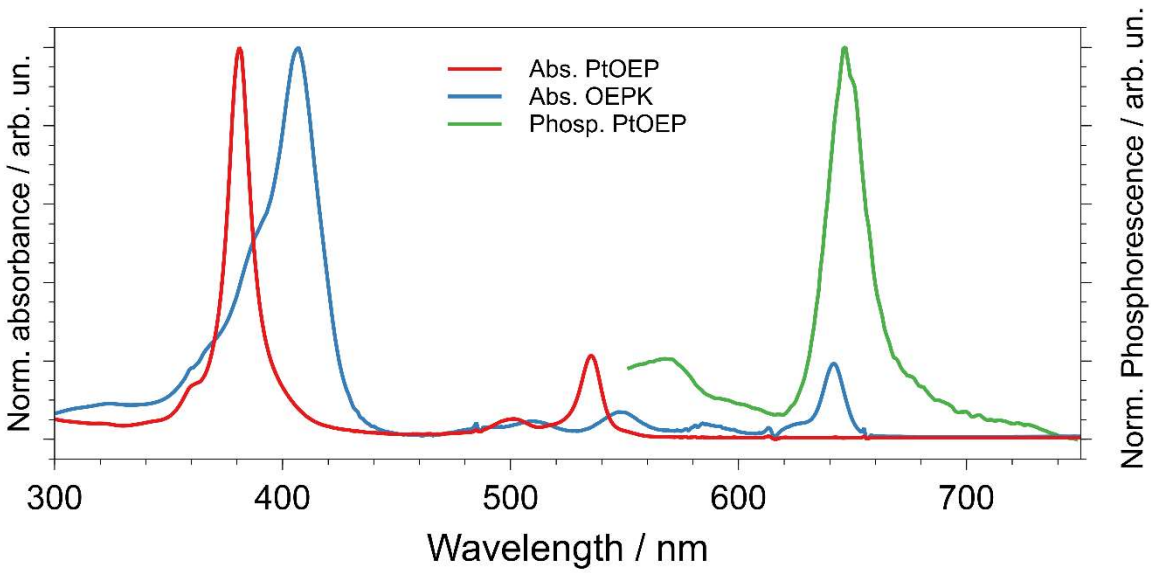

Figure 4.2. UV-Vis spectra of the PtOEP and OEPK solutions ($CHCl_3$, 8 µmol L^{-1}) and phosphorescence emission spectra of the PtOEP solid-state sensor. The overlap between OEPK absorption band at 642 nm and PtOEP emission at 650 nm points to the FRET effect seen in the emission lifetime decays of OEPK-PtOEP based sensors.

4.2.2 PLT measurements by the RLD method on a TRF reader Victor 2.

Victor readers and alike are by far the most widely used platform for O_2 sensing experiments and OCR measurements using Pt-porphyrin based probes and PLT readout. They are simple, efficient and robust, particularly for use with biological samples containing live cells. At the same time, this platform has some features that can lead to experimental errors and skewed PLT data, in particular:

1) Excitation pulse duration of 10-20 µs limits the range of reliably measured PLTs to >10 µs, or even higher. As a consequence, such instruments are unsuitable for many alternative sensor materials, such as those based on Ru^{2+}, Ir^{2+}, Os^{2+} complexes having PLT values <10 µs [151].
2) The RLD method of PLT quantification assumes mono-exponential emission decay [178], which is not valid for many solid-state phosphorescent materials [17].
3) PLT values produced by the RLD can be influenced by high blank signals or low S:N ratio. This requires blank correction of the measured TR-F intensity values and complicates the measurements (see below).
4) High detection sensitivity can lead to detector saturation by strongly emitting samples (e.g. many O_2 sensors), and this also leads to erroneous PLT values.
5) Strong fluorescence in the detection range of phosphorescent samples can also affect PLT measurements on this platform.

These limitations can be illustrated schematically in **Fig.4.3** and by experimental data in **Fig.4.4-4.5**. Thus, **Fig.4.4** shows high sensitivity and selectivity of TRF measurements: intensity signals (first window) for Sensors 1-3 were in the range of 10^4-10^6 cps, greatly exceeding Blank 1 signals and giving S:N ratio of >50. These conditions allow precise determination of PLT values for the sensors, which in air-saturated conditions ranged between 11-25 µs (**Fig.4.5**). However, those air-saturated short PLT values by RLD method are not accurate (**Table 4.3**) and show prominent dependence on the measurement settings, particularly the delay times t_1 and t_2 (**Fig.4.5A-B**). These effects are attributed to sensor heterogeneity, poly-exponential decays, and flash lamp afterglow (**Fig.4.3B**). Nonetheless, due to the high-performance optics and simple calculation algorithm, the PLT measurements by RLD method are precise and reproducible (**Fig. 4.5C, Table 4.3**).

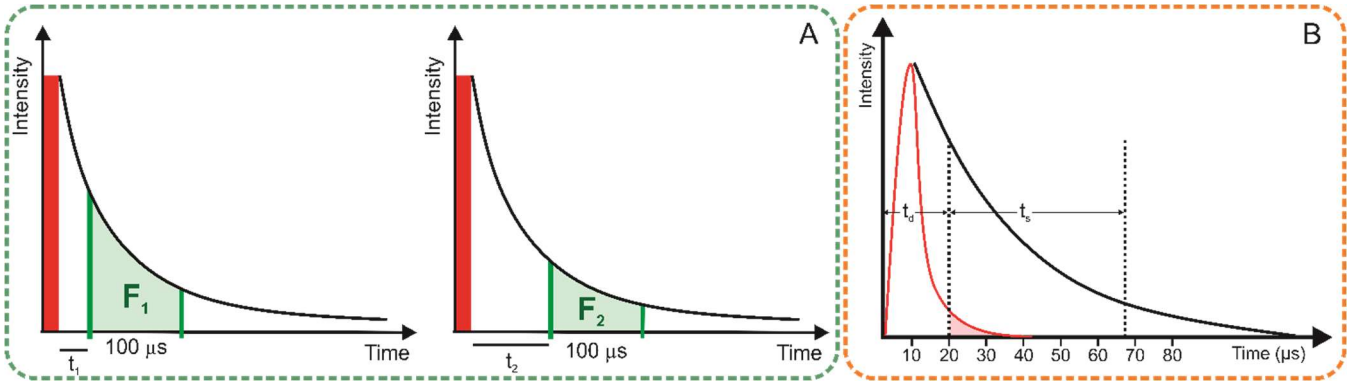

Figure 4.3. Schematic representation of: **A.** PLT measurements by the RLD method; **B.** the shape of the excitation flash at 400 nm (red curve) and sensor emission decay at 650 nm (black curve).

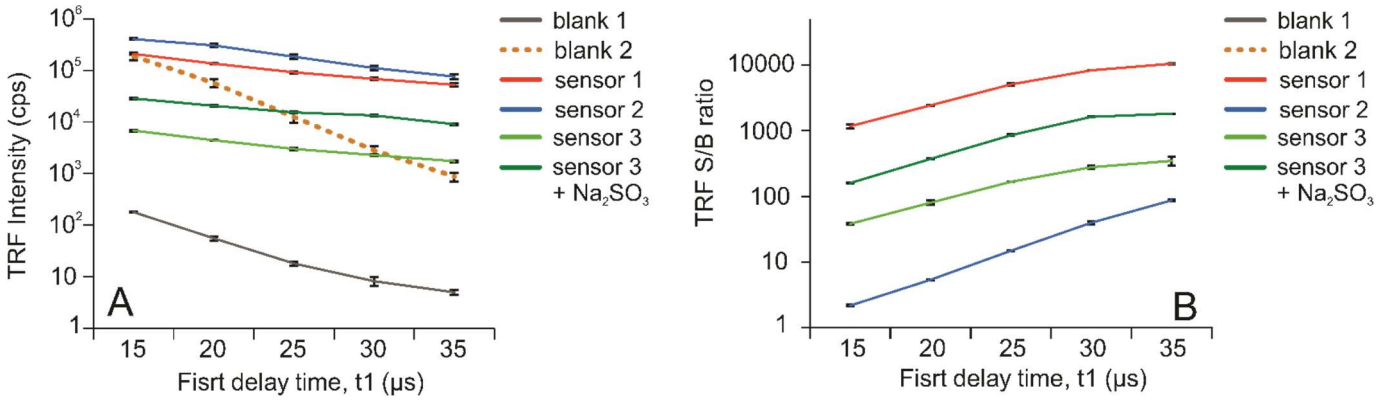

Figure 4.4. PLT measurement of the different sensor materials on Victor 2 reader. **A.** TRF intensity signals and (**B**) S:N ratio at different delay times t_1 (as indicated) and constant t_2=40 µs. Blank 1 was used for sensors 1 and 3, Blank 2 - for sensor 2.

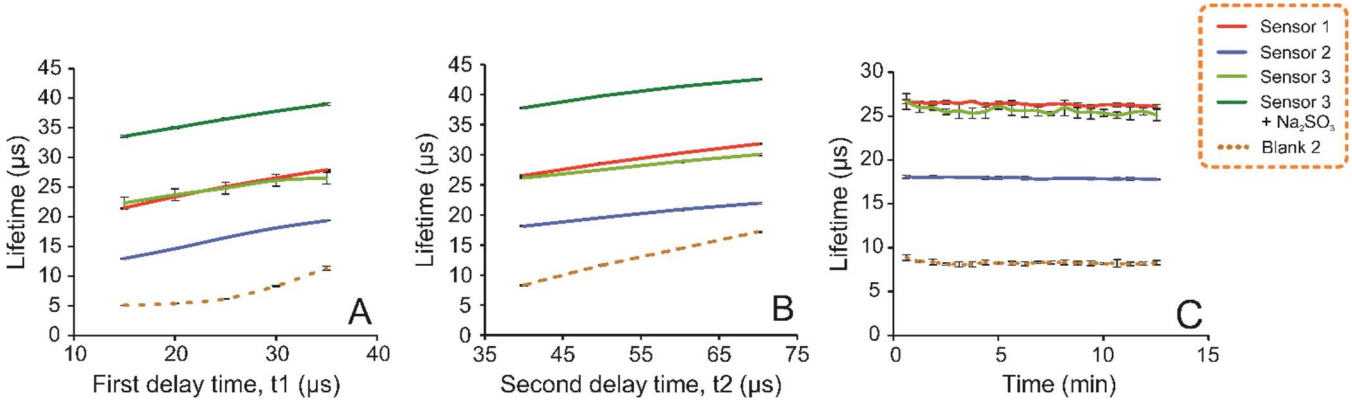

Figure 4.5. PLT measurements of the different sensor materials on a Victor 2 reader under different settings. PLT values calculated from TRF intensity signals at (**A**) variable t1 (as indicated) and constant t_2=40 µs; (**B**) variable t_2 and constant t_1=30 µs. Blank 1 was used for sensors 1 and 3, Blank 2 for sensor 2. **C**. Kinetic analysis of PLT stability at t_1=30 µs and t_2=40 µs. Error bars show standard deviations (N=3).

At the same time, the presence of a short-lived red-emitting fluor in sensor material can affect the RLD and resulting PLT values. Thus, OEPK dye having strong red emission produces decay profiles that follow the flash-lamp afterglow profile. In essence, OEPK converts the parasitic UV excitation light, which is normally rejected by the pair of optical filters, into red emission that passes freely through the emission filter. The resulting 'fake' long-decay emission of OEPK reduces the S:N ratio and skews the PLT values produced by the target phosphor, PtOEP (**Fig.4.5**). Furthermore, high OEPK concentration in sensor material leads to solution FRET, with OEPK acting as FRET acceptor which shortens the PLT values of PtOEP donor (**Fig.4.2** and **Table 4.3**).

It is worth noting that the above effects and measurement artefacts become pronounced when sensor PLT values are close to temporal resolution of the system, i.e. <15 µs. For PLT values >20 µs, which usually correspond to deoxygenated conditions, PLT measurements by the RLD method become more accurate and less dependent on the measurement settings. The corresponding decays also become close to mono-exponential, since one of the key heterogeneity factors - O_2 quenching efficiency - is eliminated in deoxygenated conditions.

Table 4.3. PLT values for the different sensor materials measured* on the Victor reader and Cary Eclipse.

Sensors and O_2 levels		RLD, Victor (μs) t1=30 μs, t2=40 μs	Phosphorescence Decay, Cary		
			Start point (Delay, μs)	Mean PLT (μs) **	
				Mono-exponential	Bi-exponential
Sensor 1	21%	25.56 ± 0.06	0	8 ± 1.63	9.94 ± 0.15
			20	**21 ± 0.17**	**22.9 ± 0.16**
	~0%	NM	0	**51 ± 2.19**	**53.94 ± 2.13**
			20	**51 ± 1.83**	**51.23 ± 1.01**
Sensor 2	21%	18.13 ± 0.08	0	6 ± 2.71	6.06 ± 0.21
			20	**11 ± 0.28**	**10.99 ± 0.32**
	~0%	NM	0	12 ± 4.32	15.46 ± 0.53
			20	**21 ± 0.94**	**18.31 ± 0.28**
Sensor 3	21%	26.14 ± 0.01	0	8 ± 3.2	10.22 ± 0.48
			20	**22 ± 0.35**	**20.97 ± 0.48**
	~0%	37.08 ± 0.12	0	15 ± 6.4	23.5 ± 1.2
			20	**32 ± 1.35**	**32.79 ± 0.57**

* Measured at 37°C in PBS (21% O_2) or PBS with added sulphite (~0% O_2); NM – not measurable (detector saturation); ** Bold shows most reliable values.

4.2.3 PLT measurements on the Cary Eclipse fluorescence spectrometer

This platform generates multi-point phosphorescence decay curves with a temporal resolution (minimal step of the decay) of 8 μs (**Fig.4.6A**). For Pt-porphyrin based sensors, this usually gives 5-20 reliable experimental data points, which can be analyzed visually and fitted mathematically. Visually, one can assess the impact of the excitation flash (initial 1-3 points) and offset value of the decay, which can then be considered in the fitting (e.g. 20 μs delay). Instrument Xe flash lamp pulse is longer due to higher power output, and can increase parasitic light interference compared to the Victor 2 reader. **Fig. 4.6A-D** show how the quality of fits for PtOEP and Pt-SB sensors in oxygenated state can be improved by optimizing the conditions for decay analysis. Even with simple mono-exponential function one can achieve good fitting of experimental data (**Fig. 4.6B, D).** And without such initial optimization, even the more powerful bi-exponential fitting can produce inaccurate results (**Fig.4.6A, C** and **Table 4.3**). Conversely, the contribution of excitation flash in the PLT calculations can be neglected for deoxygenated Sensors 1 and 3, for which bi-exponential (Sensor 3) and even

mono-exponential (Sensor 1) fits produce good results (**Fig. 4.6E**). The corresponding mean PLT values are given in **Table 4.3**, and compared with those generated on a Victor 2 by the RLD method.

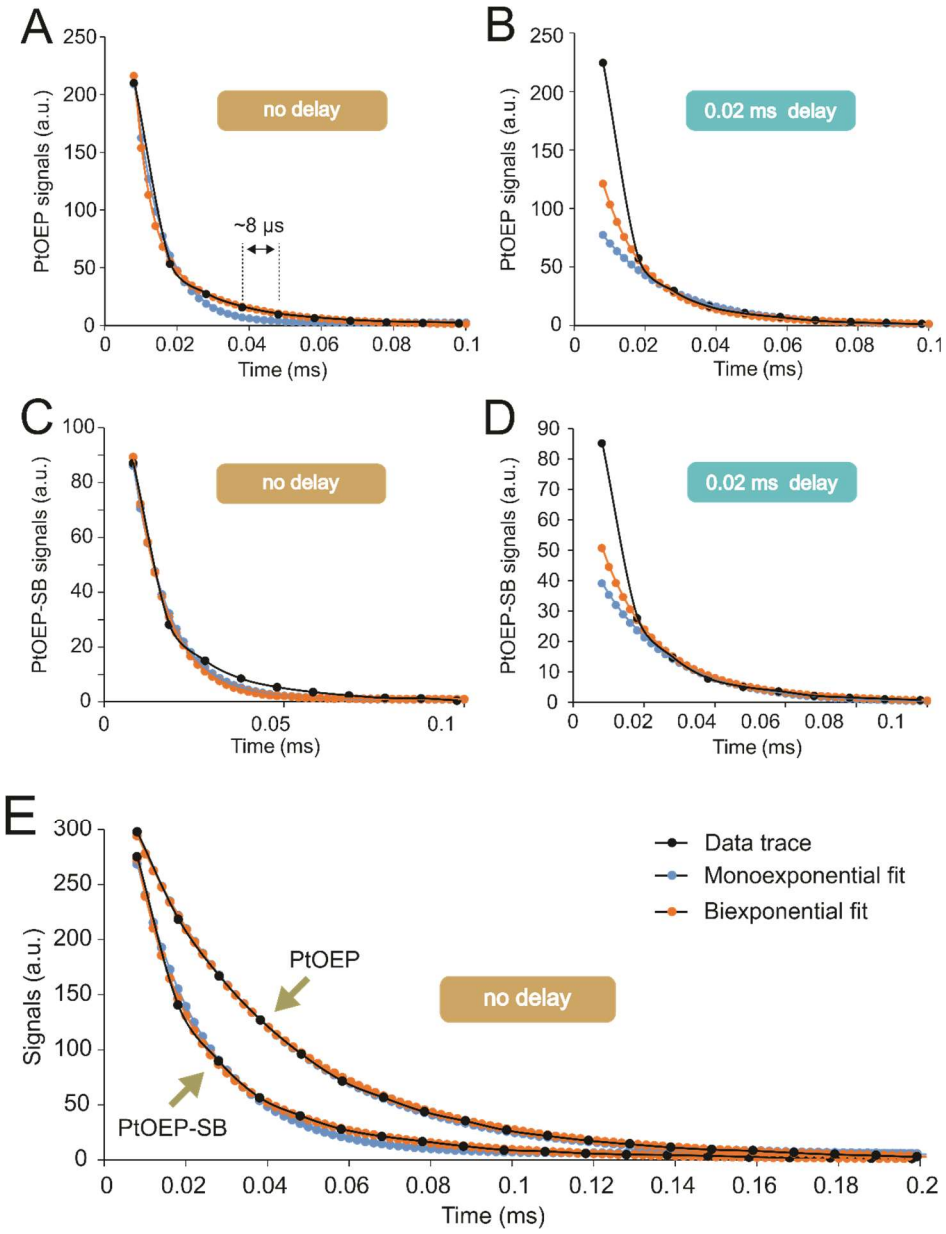

Figure 4.6 Typical phosphorescence decays of the PtOEP based sensors 1, 2 (**A**, **B**) and PtOEP-SB based Sensor 3 (**C**, **D**) measured on Cary Eclipse, and their mono- and biexponential fitting without or with removal of the flash zone by introducing a 20 µs delay (offset 0.02 ms) after excitation pulse. Decay curves of Sensors 1 and 3 with added sulphite and no delay are shown in (**E**).

Compared to the RLD-based Victor platform, the Cary platform provides better separation of parasitic light (e.g. tail of excitation pulse) from the phosphorescence and more accurate determination of individual PLT components and mean PLT values for heterogeneous phosphorescent materials. On the other hand, measurements on Cary are more laborious and less suited for kinetic PLT measurements. The data produced by the two methods do not match exactly and cannot be used for platforms cross-

verification. However, when a platform-specific calibration of particular sensors is done, both platforms provide accurate analysis of sample oxygenation.

4.2.4 PLT measurements on the confocal PLIM-TCSPC microscope

The following imaging parameters were optimised: laser power, pinhole aperture, image collection time, the number of imaging cycles for each pixel, time range for decay recording and laser-on time for generating the phosphorescence signal (% of the total time range). We found that for all sensors a 2 mm pinhole and 30-50% laser power provided high-resolution PLIM images with 0.5-1×10^4 counts per pixel. Only minor photobleaching of the dyes was observed at these conditions, as shown in **Fig.4.7** for Sensor 1. Fitting accuracy of decay tails having different length was compared and the 250 μs time range was found optimal. By taking PLIM images of pure Mylar film and with fluorescent OEPK sensor, we also generated IRFs for different laser-on times, which revealed a ~1.8 μs-long parasitic decay component for BDL-405-SMNi lasers (**Fig.4.8**). IRF was considered in PLT calculations: 1) bi-exponential fitting of entire data traces and 2) mono-exponential fitting of fragments that exclude the IRF area.

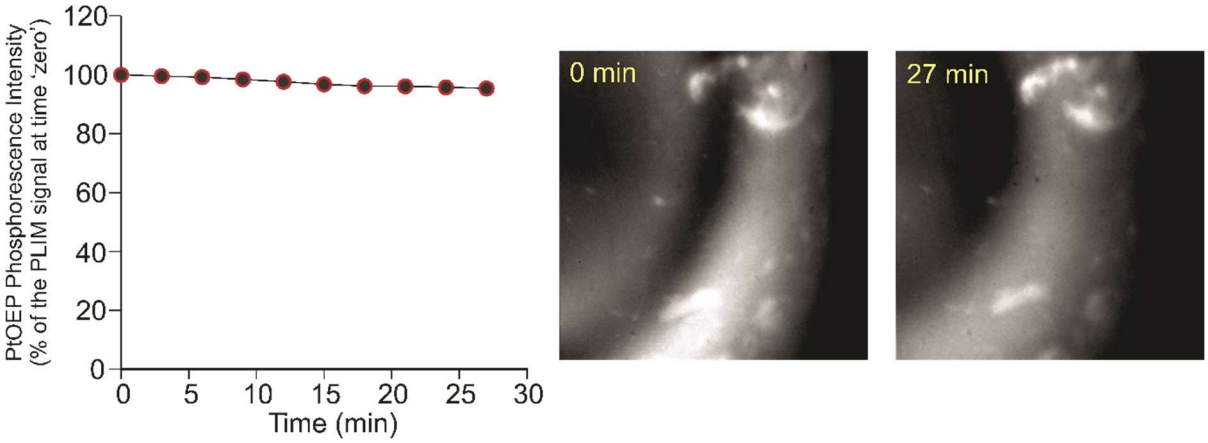

Figure 4.7. Analysis of PtOEP intensity signal stability during confocal PLIM imaging. Images were taken every 3 minutes (2 minutes per image).

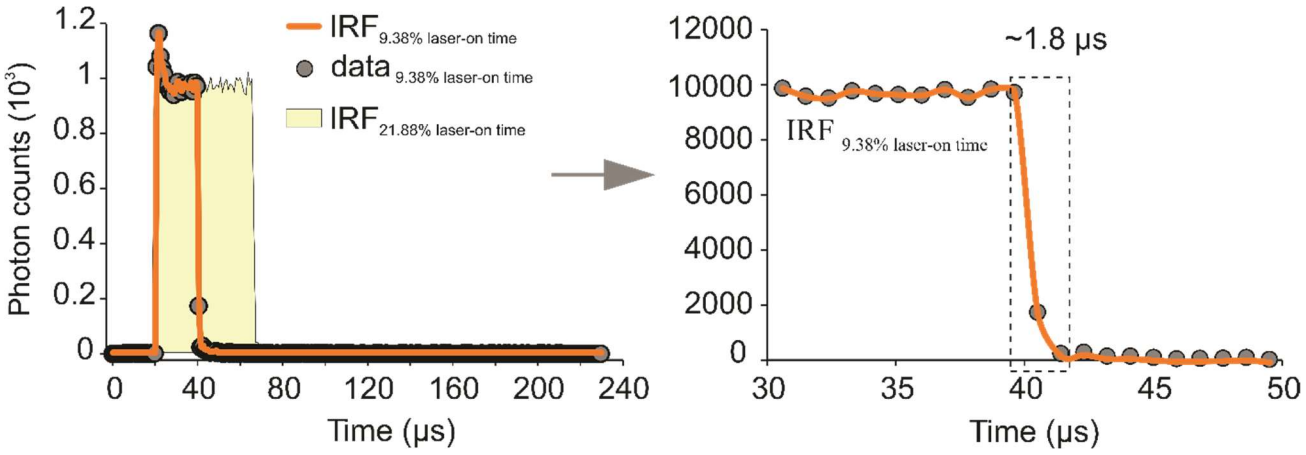

Figure 4.8. Instrument response function (IRF) for confocal PLIM imaging of the OEPK sensor using the 405 nm BDL-405-SMNi picosecond diode laser. Right panel zooms into the area of the laser-on/off transition (9.38% laser-on time), showing the 'parasitic' ~1.8 µs decay component.

While optimising the data processing, we found that mean lifetime (τ_m) and the slow component (τ_2) produced by mono- and bi-exponential fitting (20.6 µs and 20.4 µs, respectively for Sensor 1 in oxygenated state) and the corresponding χ^2 values were almost identical. And the fast component (τ_1) component was not observed for Sensor 1 at 0% oxygen. Therefore, we simplified data processing to mono-exponential fitting for all the sensors and conditions.

Using the algorithm described in [179], we found that at 21% of O_2, the PLT medians were 20.4 µs and 10.8 µs for the PtOEP-based Sensor 1 and Sensor 2, respectively, suggesting efficient quenching of PtOEP phosphorescence by OEPK **(Fig.4.9-4.10)**. In the presence of OEPK, the interquartile range of PLT shifted from 18.8-21.9 µs (Sensor 1) to 10.1-11.6 µs (Sensor 2). Importantly, for Sensor 2 we were able to collect only limited number of the phosphorescence photons, due to the overflow of the photons emitted by OEPK during laser-on time. At ~0% oxygen, the median PLT value for Sensor 1 was 57.2 µs with the 51.3-61.9 µs interquartile range (**Fig.4.10A, Table 4.4**). For deoxygenated Sensor 2, the PLT (21.1 µs) and interquartile range (19.9-22.8 µs) were strongly reduced relative to Sensor 1 (**Fig.4.10B, Table 4.4)**. For Sensor 3, the median PLT values increased from 23.7 µs to 35.6 µs upon deoxygenation, and the interquartile range changed proportionally **(Fig. 4.10C, Table 4.4)**.

The limitations of the platform with respect to the imaging of phosphorescent sensors included: micro-heterogeneity of sensor coating can produce variable PLT values, not seen on low magnification imaging and point measurement platforms; strong fluorescence in the same range as phosphorescence may 'blind' the detector and decrease the sensitivity of PLT measurements.

In summary, the imaging platform has revealed the bi-exponential nature of PtOEP decay, but only the slow component τ_2, showed the typical sensitivity to O_2. τ_2 was almost identical to τ_m produced by the

mono-exponential fittings. Although the different hardware, software and fitting algorithms, the PLT values produced by the FLIM microscope still have a good match with Cary spec, and the comparable readout with Victor 2 reader for Sensor 1-3 (**Tables 4.3** and **4.4**).

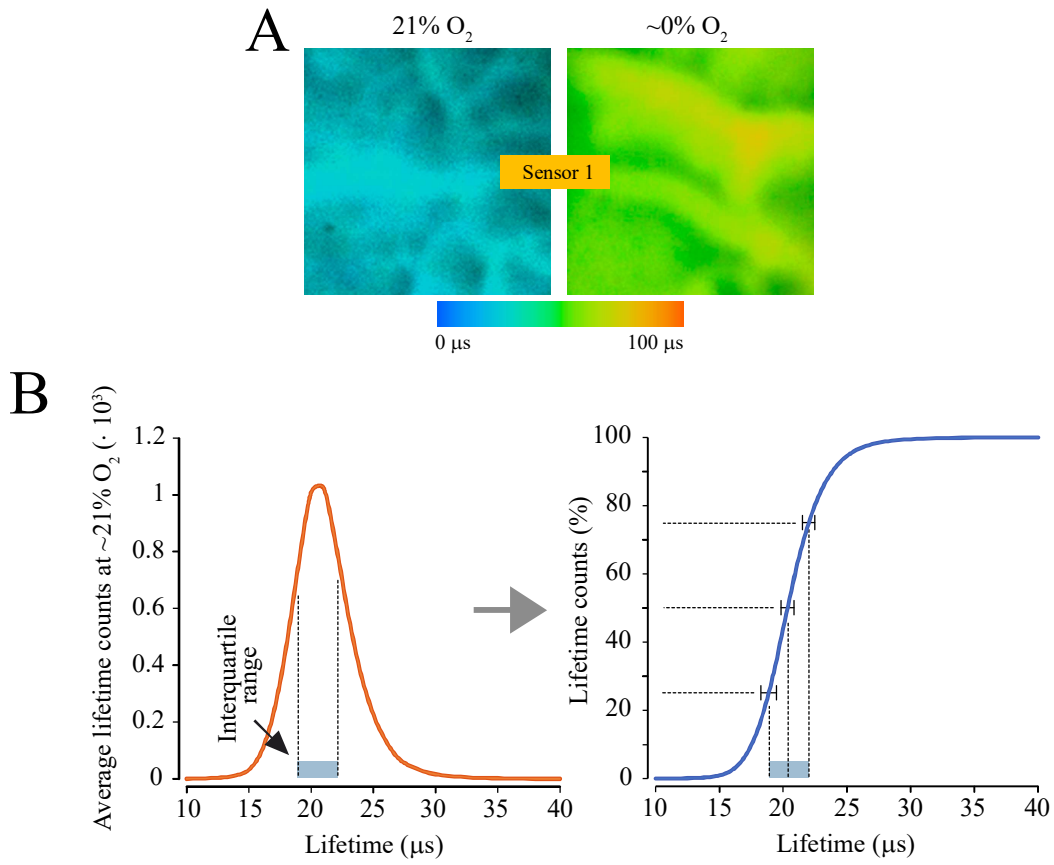

Figure 4.9. PLT distribution analysis of the confocal PLIM data. **A.** Representative PLT changes for Sensor 1 upon deoxygenation (false rainbow colour palette). **B.** Distribution and cumulative distribution histograms of Sensor 1 τ_m in the oxygenated state demonstrate the principle of interquartile range calculations that include monoexponential fitting of photon data trace, extraction of lifetime distribution histogram, its conversion into a relative cumulative lifetime distribution histogram and calculation of 25th, 50th and 75th quartile values. Error bars show standard deviations for 25th, 50th (median) and 75th quartiles (N=3); interquartile range (grey box) is indicated by an arrow.

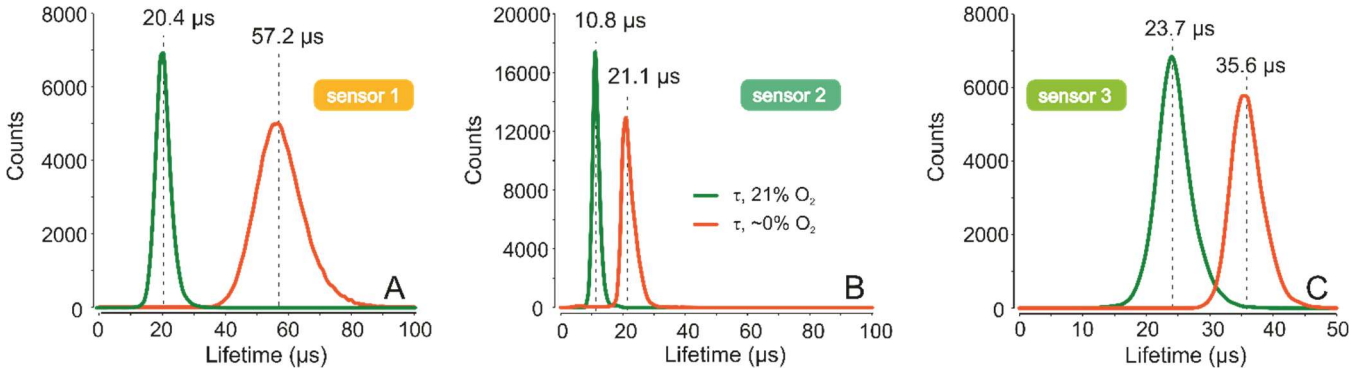

Figure 4.10. Distribution histograms of PLT values for Sensors 1 (**A**), 2 (**B**) and 3 (**C**) in oxygenated and deoxygenated state produce by confocal PLIM microscopy. Y axes show the number of pixels with given τ_m values. Median τ_m values are indicated; N=3.

Table 4.4. PLT values (µs) measured* on the confocal PLIM imaging platforms.

Sensors and O_2 levels		**PLIM Confocal**		
		25th quartile	**Median**	75th quartile
Sensor 1	21%	18.8±0.3	20.4±0.0	21.9±0.3
	~0%	51.3±2.2	57.2±1.7	61.9±2.1
Sensor 2	21%	10.1±0.30	10.8±0.2	11.6±0.2
	~0%	19.9±0.2	21.1±0.4	22.8±0.9
Sensor 3	21%	22.0±0.3	23.7±0.2	25.6±0.6
	~0%	33.4±0.3	35.6±0.4	37.0±0.8

* Measured at 37°C in PBS (21% O_2) or PBS with added sulphite (~0% O_2).

4.3 Conclusions

This study and its results have demonstrated the merits and limitations of the different PLT measurement platforms. They also reveal a significant number of factors and that may lead to measurement artefacts and inaccuracies in the determination of PLT values. Based on their origin, these sources of experimental error in PLT determination can be categorized into the following groups:

1) ***Instrument hardware*** including excitation source (flash lamp/ns LED/ps laser), optical filtration (filters, monochromators), detector type (analog or photon counting PMT or TCSPC optoelectronics), point measurements/imaging;

2) ***PLT calculation method*** ranging from simple but inaccurate RLD vs absolute TCSPC method, multi-point decays with mono- or double exponential fitting, offset and blank correction;

3) ***Sensor material*** including the type of phosphor, its micro- and macro-heterogeneity, the magnitude and span of PLT values;

4) ***Background signals*** including support material afterglow, autofluorescence, solution FRET with other fluorophores presents in the sensor or tested sample;

5) ***Sample and its environment*** including uniform and known oxygenation state, precise T-control, sample to sample variability/reproducibility, cuvette/vessel type.

By carefully considering these critical factors, one can ensure stable and reproducible measurements and generation of accurate PLT values for different phosphorescent samples.

Chapter 5: New dual pH/O_2 sensing materials for cell analysis

5.1 Introduction

Optochemical sensors based on luminescent indicator dyes have been rapidly developing in recent decades. Various sensing materials, detection modalities, applications and integrated analytical systems have been studied for use in biomedical research, pharmaceutical quality control, clinical, and food industry [23]. Among these systems, biosensors for tracking of molecular oxygen (O_2) and proton ion concentration (i.e. [H^+] or pH) are relatively well developed, diversified and utilized for cell analysis. The two major 'metabolic signature' of the cell, i.e. the activity of cellular glycolysis and OxPhos, can be assessed by detailed ECAR/OCR analysis using suitable pH and O_2 sensors [151, 180]. Such information is of high importance for cell biology, biotechnology, clinical diagnostics, pharmacologic research, evaluation of disease mechanisms and drug toxicity [181].

However, when it comes to optical biosensors for cell analysis with simultaneous pH and O_2 readout, the existing sensors have significant limitations. Their main drawbacks include, but are not limited to: non-optimal spectral characteristics and response to target analyte(s); unstable and tedious calibrations and the need for frequent recalibrations due to the lack of internal referencing capability; complex signal acquisition and data analysis algorithms; pronounced cross-talk between the current O_2 and pH sensors, low multiplexing potential; cytotoxicity and high costs [22] .

Optochemical (bio)sensors with internally referenced detection capabilities have the potential to overcome many of the above limitations of traditional photoluminescence intensity-based sensors, and also minimize the impact of key interfering factors such as variations of dye concentration, photobleaching, measurement geometry, fluctuation of the light source and photodetector, etc. The common approaches for internally referenced detection include: i) phosphorescence/fluorescence lifetime (PLT/FLT) measurements; ii) ratiometric intensity measurements using indicator dyes with characteristic spectral response (protonated and deprotonated emission bands); iii) pairs of dyes with spectrally distinct analyte-responsive and analyte-irresponsive emission; iv) dual lifetime referencing (DLR) technique using pairs of short and long-decay emitting dyes [182, 183].

Furthermore, development of dual pH/O_2 sensors for cell analysis, including the systems with internal referencing, brings a number of additional practical requirements and complications, such as: compatible spectral characteristics and/or distinct lifetime characteristics for pairs of indicator dyes; selection of universal encapsulation medium (polymeric matrix) which ensures optimal functionally for both pH and O_2 sensing dyes, compatibility with conventional substrates (plastic microplates) and detection instruments used in cell analysis, and low toxic action on cells. All this largely limits the

selection of indicator dyes and sensor systems, and ignites researchers to innovate new 'hybrid' platforms for multiplexed detection of cellular OCR/ECAR.

Recently, our lab reported a dual pH/O_2 sensing system utilizing one phosphorescent Pt(II)- or Pd(II)-porphyrin dye with a protonable Schiff base group in *meso*-position (MeOEP-SB) [184]. This sensor chemistry displays O_2 and pH sensitivity across physiological ranges. It enables a self-referenced PLT readout for O_2 sensing, and operates under straightforward detection settings with just one excitation (~400 nm) and emission (~650 nm) wavelengths. However, its downsides include the non-referenced intensity readout for pH sensing and the utilization of plasticised PVC matrix for the sensor. Thus far, such sensors have not been demonstrated in live cell analysis applications, using standard detection platforms and relevant cell models.

This study was aimed to address the drawbacks of the existing dual pH/O_2 sensor system and demonstrating its practical applications in the quantitative analysis of ECAR/OCR. For that, we adopted a holistic approach and evaluated the key factors of this sensor performance, including its indicator dyes, encapsulation matrices, additives and reference dyes for ratiometric pH sensing. We also applied this sensor system on available detectors with physiologically relevant cell models.

5.2 Results and Discussion

5.2.1 Screening of alternative polymeric matrices for the dual pH/O_2 sensor

Structures of the indicators MeOEP-SB dyes and their abbreviations are shown in **Fig. 5.1.** The original dual pH/O_2 sensing approach utilised plasticized PVC matrix to immobilise PtOEP-SB (Dye **1**) in the presence of proton transfer agent (PTA) TCPB [184]. While providing usable sensing performance, this solid-state sensor system had number of shortcomings, including complex chemical composition (four components: dye, polymer, DOS plasticizer, TCPB) and the use of non-friendly solvents (chloroform-THF mixture) for coating deposition.

Tring to improve this, we studied a number of alternative polymeric matrices, benchmarking them against the original PVC matrix. Selection criteria for such polymers were: i) amphiphilic nature facilitating proton permeability; ii) proton donating properties that can potentially eliminate the need for PTA; iii) good solubility for the hydrophobic MePor-SB indicator dyes; iv) use of more friendly solvents (e.g. alcohols) in sensor cocktail; v) ability to form stable coatings without dissolution or leakage of sensor components in aqueous biological media; vi) previous demonstration in pH sensing with other indicator dyes [102]. Since the mechanism of spectral response to MePor-SB dyes to pH is based on the protonation of the peripheral SB group in *meso*-position [184] (**Fig. 5.1**), we mainly focused on amphiphilic neutral, weakly acidic and strongly acidic polymers, with or without PTA additives. The results of this screening are summarised in **Table 5.1.**

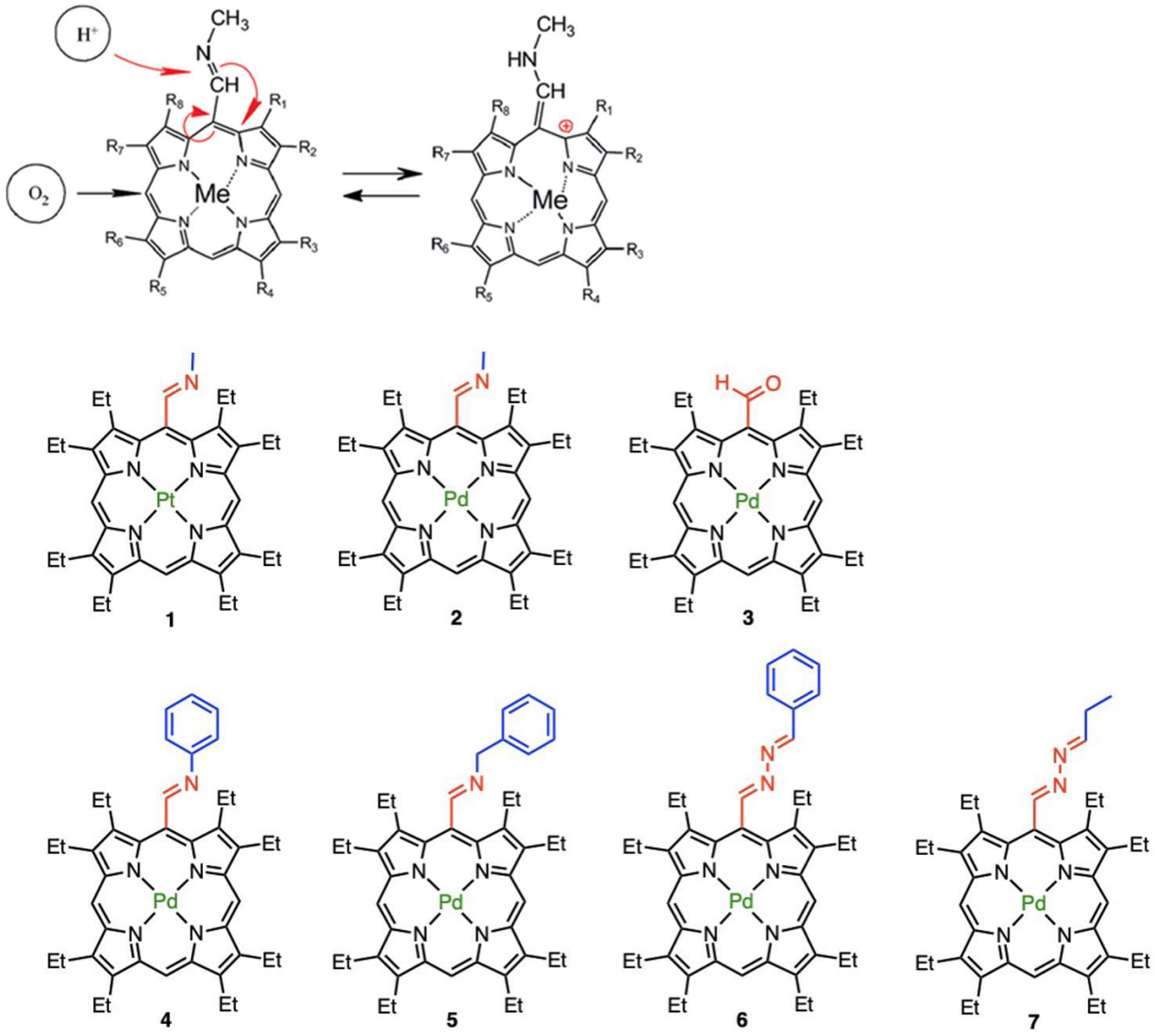

Figure 5.1 Mechanism of spectral response to MePor-SB dyes (top) and chemical structures of dyes (bottom) used in the study: **1**-PtOEP-methyl-Schiff (PtOEP-SB); **2** - PdOEP-methyl-Schiff; **3** - PdOEP-*meso*-formyl; **4** - PdOEP-phenyl-Schiff; **5** - PdOEP-benzyl-Schiff; **6** - PdOEP-phenyl-azine; **7** - PdOEP-ethyl-azine.

Table 5.1 The properties and protonation behaviour of the polymer matrices with PtOEP-SB indicator.

No.	Polymeric matrix	Solvent	Properties	PtOEP-SB Protonation
I.	PVC-DOS-TPCB	THF	Neutral plasticised polymer with PTA additive	Efficient protonation in the physiological pH range
II.	Hydrogel D4	Ethanol	Neutral-amphiphilic polymer, friendly solvent	No protonation at pH>4.0
IIa.	D4-SDS	Ethanol-H_2O (2:1)	Hydrogel with PTA additive (10 mM)	No protonation at pH>4.0, rapid dye and SDS leakage
IIb.	D4-TCBP	Ethanol	Hydrogel with PTA additive (1-10 mM)	No protonation at pH>4.0
III.	Ethyl cellulose	THF	Neutral more hydrophobic polymer	No protonation at pH>4.0
IV.	Poly(acrylate)-co-methacrylic acid	THF	Weakly anionic co-polymer with carboxy groups	No protonation at pH>4.0
V.	Poly(DL-lactide) (PLA)	THF	Weakly anionic polymer	No spectral changes between pH 8.5-4.0
VI.	Poly(DL-lactide-coglycolide)PLGA	THF	Weakly anionic polymer	No spectral changes between pH 8.5-4.0
VII.	Nafion	Alcohols-H_2O	Strongly anionic polymer with sulfo-groups, friendly solvent	Protonation upon drying, rapid dye decomposition (colorless next day)
VIIa.	Nafion-$NaOCH_3$	Alcohols-H_2O	Nafion partly neutalised (0-60 mM methylate)	Spectral changes ($NaOCH_3$), but pKa is 5-6

We found that all the selected neutral (**II**, **III**) and weakly anionic (**IV-VI**) polymers did not provide protonation of PtOEP-SB in the desired pH range: no spectral changes in the pH range 9.0-4.0. PTA additives (see sensors **IIa, IIb**) did not improve sensor behaviour. Only the original plasticized PVC (**I**) and strongly acidic Nafion polymer (**VII, Fig.5.2**) produced prominent colour changes indicative of the dye protonation already in the cocktail. However, spotting the cocktail containing acid Nafion polymer on substrates (Mylar film) with overnight drying produced practically colourless coatings. This suggests that in the strongly acidic Nafion matrix, the complete and sustained protonation into carbocation form [185] destabilised the PtOEP-SB and led to its rapid chemical degradation. Such a behaviour of MePor-SB dyes has not been reported previously, while it could be critical for sensing applications and should be considered carefully.

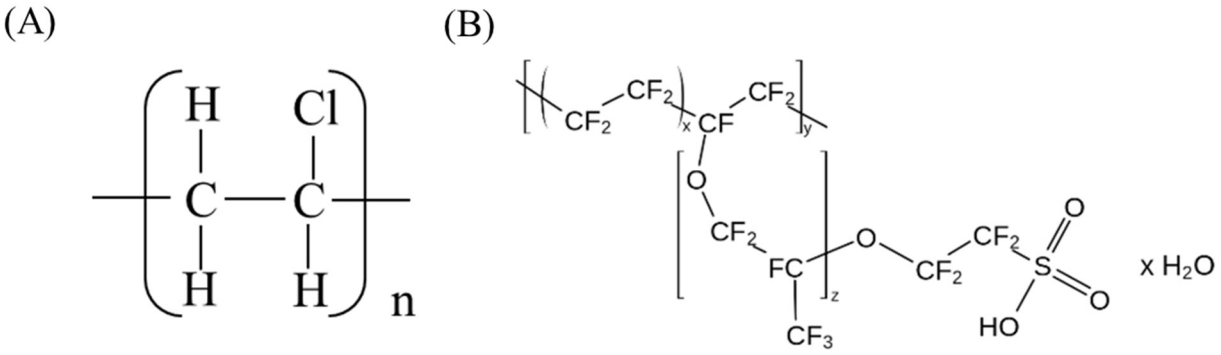

Figure 5.2. The molecular structures for polymers. (A) polyvinyl chloride (PVC). (B) Nafion polymer [186].

Trying to overcome the dye degradation effects, we examined partial neutralisation of Nafion sulfo-groups with sodium methylate (**VIIa**). Indeed, the strong base $NaOCH_3$ at 10 mM concentration was seen to inhibit dye degradation and produce coloured (pink) sensor coatings, which were stable upon storage in dry state and which produced a distinct absorbance response to pH in aqueous buffers (**Fig. 5.3**). However, the pKa below 6.0 was too acidic and degradation of the dye during sensor operation was still evident. Furthermore, Nafion matrix was poorly suited for O_2 sensing [102]: dye **1** was quenched >10-fold in air-saturated conditions, producing dim phosphorescent signals and weak response to O_2 changes in this range.

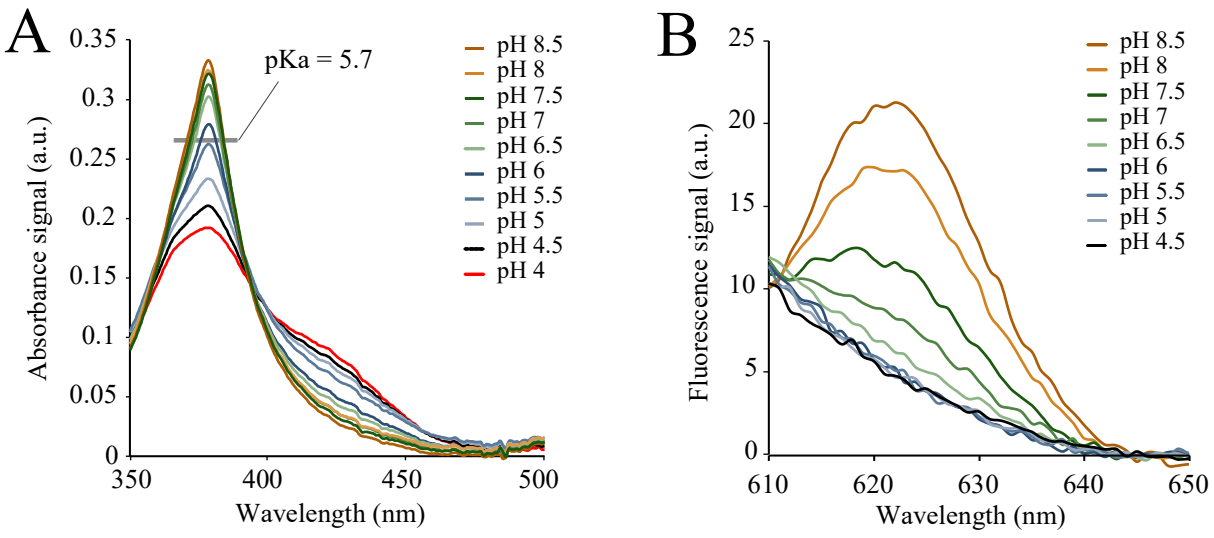

Figure 5.3 Spectral responses to pH for the PtOEP-SB-Nafion sensor coatings (45 mM Nafion, 10 mM $NaOCH_3$) in air-saturated solution, at 25°C: changes in UV-Vis absorption (A) and phosphorescence intensity (B). In (A), pKa is an average of pKa values (5.65, 5.75) measured in two independent experiments (N=2)

Collectively, none of the tested polymers showed marked improvements over the original plasticized PVC-TCPB matrix, that would justify their use as alternative matrices in the dual pH/O_2 sensors based on PtOEP-SB dye. Performance-wise, the PVC based sensors still look superior over these polymers. Rapid decomposition of the dye was observed in the Nafion matrix; however, this process was not so prominent in the new sensors (see below). Therefore, we decided to proceed further with plasticised PVC as sensor matrix. However, search will be continued for other polymers, particularly those having a lower acidity than Nafion but higher than acrylic polymers.

5.2.2 Screening of PdOEP-SB analogues and indicator optimization

While the initial dual sensors based on MePor-SB dyes showed favourable pH sensing characteristics, structure-activity relationships (SAR) for such materials remain poorly studied. Development of indicator dyes and pH sensors that are more basic than the current ones would also be beneficial, especially if they can operate without PTA additive.

In this context, we studied a series of structural analogues of the original dye **1 (see Fig. 5.1)**, that were synthesised and characterised by our collaborators at the Institute of Physical Chemistry and Electrochemistry, Moscow, Russian Federation [146]. In particular, the following Pd-complexes, which are much easier to synthesize than the corresponding Pt-complexes, were studied: PdOEP-phenyl-Schiff (**4**) and PdOEP-benzyl-Schiff (**5**) that bear more electron-withdrawing peripheral substituents than the parent methyl-Schiff (**1),** as well as PdOEP-phenyl-azine (**6**) and PdOEP-ethyl-azine (**7**) with more electron-donating substituents. PdOEP-*meso*-formyl (**3**) was also included in the study, as this precursor dye was noticed to produce colour changes in weakly acidic solvents (unpublished data). Chemical structures of the dyes, which were expected to produce sensors with altered pK_a (**Fig. 5.1)**.

First, we titrated solutions of the different dyes in THF with TFA, while monitoring their visible absorption spectra. All the dyes showed the characteristic spectral response to protonation (**Fig. 5.4A**), which was indicative of the carbocation formation [185]. However, none of the MePor-SB analogues showed a higher basicity than the parent dye **2**. For the new derivatives, spectral changes mostly occurred at higher TFA concentrations (**Fig. 5.4B**), thus indicating their reduced basicity. Only dye 5 showed the basicity similar to 2. Since 5 is also easier to make [146], this dye, or the corresponding Pt-complex, can potentially replace the methyl-Schiff dyes 1 and 2 in the dual pH/O_2 sensors.

We then incorporated the new dyes in the plasticized PVC matrix and studied their pH-sensing properties by absorption measurements. As expected, sensor coatings based on dyes 2 and 5, in the presence of TCPB additive (proton transfer agent, PTA), produced robust and reversible response to pH with apparent pKa of 7.45 ± 0.20 and 7.14 ± 0.07, respectively (**Fig. 5.4C**). These sensors cover

the most useful pH range for cell analysis, while the dye 4 sensors showed a more acidic pKa of 5.68 ± 0.24, and dyes 6 and 7 sensors - no detectable protonation even at pH 3.0. Unlike the Nafion sensors, in the plasticized PVC matrix all the new dyes showed no significant degradation.

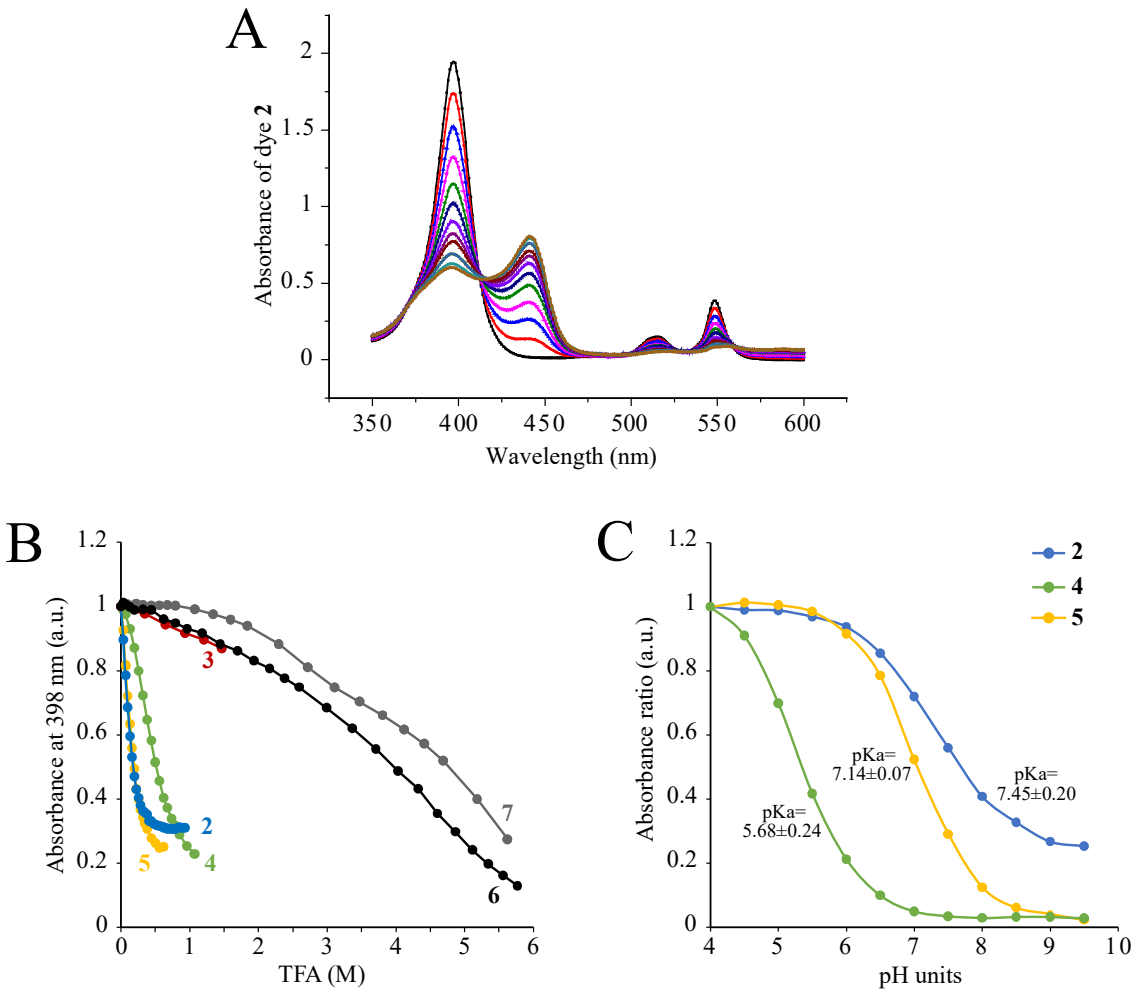

Figure 5.4 Absorbance based responses to protonation for dyes **2**-**7**. **A**. UV-Vis spectra of dye **2** in THF titrated with TFA. **B**. TFA concentration dependences for the different dyes. **C**. Absorbance ratio for the solid-state sensor coatings based on dyes **2** (448/399nm), **4** (473/401 nm) and **5** (450/399 nm) (0.25 mM in plasticised PVC-PTA matrix) at different pH. Calculated pKa values are shown as mean ± SD (N=4).

Next, we measured phosphorescent signals from the sensors in air-saturated buffers and observed pH responses similar to the absorbance-based responses. At the same time, we noted that sensor coatings based on dyes **2**-**7** displayed rather weak emission, which could not be explained just by O_2 quenching. To elaborate these effects, we measured absorbance, phosphorescence intensity in time-resolved mode and lifetime signals from the different sensors in air-saturated and deoxygenated buffer, pH 8.0. For comparison, similar sensors were produced from standard PdOEP dye, which has no *meso*-substituents

and has a phosphorescence quantum yield of 0.2 in the unquenched state [187]. The results are summarised in **Table 5.2**.

Table 5.2 Phosphorescence intensity* and lifetime signals for the different sensor dyes.

Sensor Dye	Air-saturated / deoxygenated	A_{405} (CORR)	I_1 (CORR)	I_2 (CORR)	I_1/A_{405}	Relative Brightness (%)	LT (μs)
2	PBS, pH8	0.105	3,527	1,635	33,708	0.035	52.0
	PBS pH8 + sulfite**	0.074	47,940	29,970	646,187	0.667	85.2
4	PBS, pH8	0.076	6,548	3,449	85,680	0.088	62.4
	PBS pH8 + sulfite**	0.041	126,411	83,767	3,118,599	3.22	97.2
5	PBS, pH8	0.075	4,583	2,225	61,095	0.063	55.4
	PBS pH8 + sulfite**	0.048	87,084	53,838	1,827,278	1.885	83.2
PdOEP (Reference)	PBS, pH8	0.051	32,136	14,531	624,088	0.644	50.4
	PBS pH8 + sulfite**	0.024	2,319,563	1,888,911	96,926,790	100	194.8
Blank	PBS, pH8	0.130	672	346			
	PBS pH8 +sulfite**	0.121	3,477	2,140			

*Measured in TRF mode at delay times 30 μs and 70 μs, gate time 100 μs for I_1 and I_2, respectively.

**Sample actual pH was 6.7-6.8.

Indeed, all the *meso*-substituted PdOEP-SB derivatives showed largely reduced brightness of emission, as compared to the unsubstituted PdOEP. At 21 kPa O_2 (in PBS, pH 8.0), their TRF intensity signals were quenched >20-fold compared to deoxygenated conditions (PBS with sulphite). However, this quenching of intensity signals is artificially amplified by the TRF detection mode and by absorbance changes and pH shifts induced by sulphite addition (**Table 5.2**). On the other hand, quenching of the lifetime signals at 21 kPa O_2 was smaller (~30%), being optimal for sensing applications [168] and greater than for the Pt-complex **1** (see below).

All in all, these SARs are useful and should be considered in the design of new pH/O_2 sensors.

5.2.3 Introducing a reference fluor to enable the ratiometric pH sensing

The original dual-sensing approach using MePor-SB utilised the self-referenced phosphorescence lifetime-based sensing of O_2, while pH sensing was intensity based without self-referencing. On the other hand, such sensing materials require just one spectral channel (395 nm excitation and 650 nm emission). This feature facilitates the integration of additional photoluminescence functionalities in the unused spectral window 450-600 nm. We explored this by incorporating in the MeOEP-SB dual-analyte sensor an additional reference fluor C6, which is excitable at the same wavelength (~400 nm)

and has a distinct emission band at ~560 nm. Thus, the fluorescence intensity signal of C6 was coupled with PtOEP-SB phosphorescence at 650 nm to produce a ratiometric (i.e. self-referenced) readout for pH (**Fig.5.5A**). By optimising the C6 (0.1 mM) and PtOEP-SB (0.25 mM) concentrations, a new sensor material was produced which shows a robust ratiometric response to pH and sensitivity similar to the original sensor. While C6 fluor has an ionisable group, which starts to protonate at pH ≤4.5 producing a spectral response (see **Fig. 5.5A** and [188]), this does not influence much sensor behaviour in the neutral pH range used in cell analysis (6.0 - 7.5 pH units) .

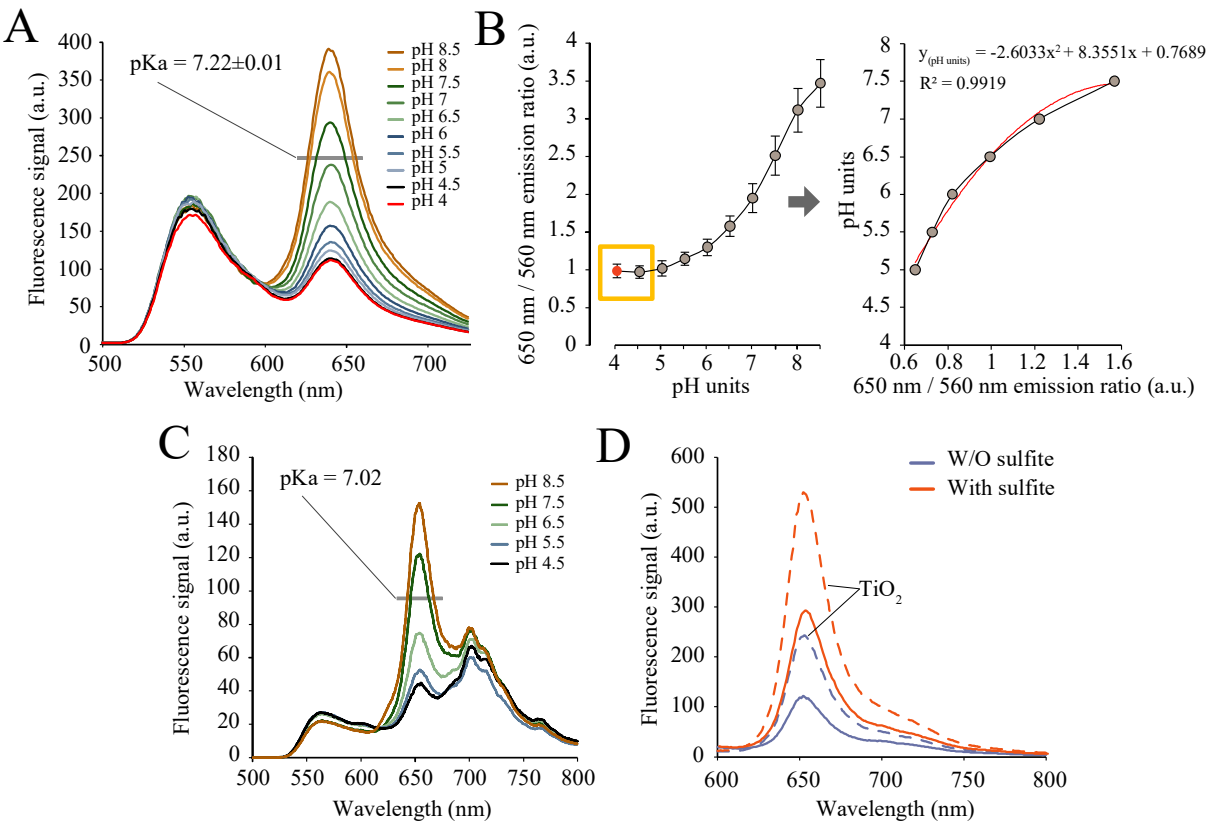

Figure 5.5 Responses to pH and O_2 of the PtOEP-SB sensors in the presence of C6 dye and the light scattering particles. **A.** Fluorescence spectra of PtOEP-SB sensor containing C6 reference dye; pKa is shown as mean ± SD (N=3). **B.** The ratio of intensity signals at 650 nm and 560 nm shows linear response to pH in the range 6.5-7.5 (left panel). For a broader pH range (5-7.5), a quadratic equation can be used (right panel, R^2 of the fit > 0.99). Data are normalised to the 650 nm/560 nm emission ratio at pH=4.5 (1 a.u.). Error bars show standard deviations (N=3). Note that C6 starts to protonate at pH ≤4.5, as highlighted by the red colour (A, B) and yellow rectangle (B). **C.** TiO_2 additive (< 100 nm particles, 5% w/w) has practically no effect on the response of the PtOEP-SB-C6 sensor to pH and the resulting pKa, which represents an average of pKa values (6.96, 7.08) measured in two independent experiments (N=2). **D.** TiO_2 additive (5% w/w) increases signals of PtOEP-SB in both oxygenated (21 kPa O_2) and deoxygenated state, measured at pH 7.5. The measurements were conducted on Cary Eclipse spectrometer using planar sensors on Mylar strips.

Like the original sensor [184], the new ratiometric pH sensor still shows cross-sensitivity to O_2, and thus requires compensation of PtOEP-SB intensity signal for O_2 quenching. On the other hand, this sensor also enables O_2 sensing in the ratiometric intensity mode which is useful for basic microplate readers that do not support the TRF/RLD sensing mode. In this case, sensor cross-sensitivity to pH can be suppressed by the use of buffered media (low molarity media is normally used in ECA measurements [136]), or by excluding the PTA additive from the sensor formulation. Since the pH and O_2 sensing capabilities of the dual sensor are both embedded in MePor-SB indicator dye, substitution of C6 with another reference dye is also possible and relatively straightforward.

5.2.4 Maximizing the photoluminescent signals for the dual sensor

High intensity signals and S:N ratio obtainable from the sensor are pre-requisites of its good analytical performance in complex sensing schemes and applications such as cell analysis. High intensity signals also facilitate accurate tracing of minor changes in luminescence decay or phase shift in lifetime-based sensing, and of the ratio signal in ratiometric intensity sensing. Sensor basal intensity signals can be maximized by: a) optimising dye concentration and thickness of the coating; b) luminescence enhancement by means of plasmonic enhancers [189, 190] or light-scattering additives [191, 192] integrated in the sensor material; c) optimising detection optics and mode. However, with the new sensors described above, strategy a) was already exhausted with the dye concentration(s) and coating thickness (5-15 micron) being close to optimal values. Strategy c) is usually targeted when building a dedicated new instrument for already optimised sensor materials. The use of plasmonic enhancers of luminescence was deemed problematic for our multi-component and heterogeneous sensor material with two dyes, polymer, plasticizer, PTA. Trying to optimise the sensors for use on existing detection instrumentation, we therefore focused on strategy b), incorporating inert light-scattering nano- and microparticulate additives in our dual sensors. This approach was earlier seen to produce >10-fold enhancement of photoluminescence intensity signals [191], though for the other sensors and sensor substrates.

We evaluated the effects of solvent-resistant PS-DVB microparticles and TiO_2 nanoparticles, added to the sensor cocktails at different concentrations, on the resulting intensity signals of PtOEP-SB dye. We found that TiO_2 nanoparticles (<100 nm) were more efficient providing at highest concentration 5% w/w up to 2-fold enhancement of the phosphorescence intensity (**Fig. 5.5C, D**). Further increase of the additive content in the sensor was not practical as it increased cocktail viscosity, led to phase separation, complicated the coating process, and reduced sensor reproducibility.

5.2.5 Depositing the new sensor coatings on the substrates used in cell analysis

High throughput OCR and ECA analyses are normally conducted in multi-well plates [140], specialised microplate assemblies [142, 193] or microfluidic chips [194, 195], made from common plastics and optimised for cell growth. Having completed the initial optimisation of the dual pH/O_2 sensors on planar supports (strips of Mylar film - see above), we deposited such PtOEP-SB based sensor coatings on several different substrates used in cell analysis and tested them.

First, we manually applied the different sensor cocktails on the pistons of uncoated Seahorse XF cartridge lids (Agilent). This procedure produced arrays of relatively uniform coatings (**Fig.5.5A**). The sensors were then measured on a Fibox4 sensor reader (PreSens) equipped with a fibre-optic probe (**Fig.5.6B**). Fibox4 was originally designed for Pt(II)-pentafluorophenylporphyrin (PtPFPP)-based O_2 sensors (exc/em 505/650 nm), but it is also compatible with PtOEP-SB dye. We measured phosphorescence intensity and phase shift signals from the different PtOEP-SB based sensors and compared them with the signals of commercial PtPFPP-based O_2 sensor (Type PS3, PreSens) and sensor-coated XF cartridge (Type V3-PS, Agilent).

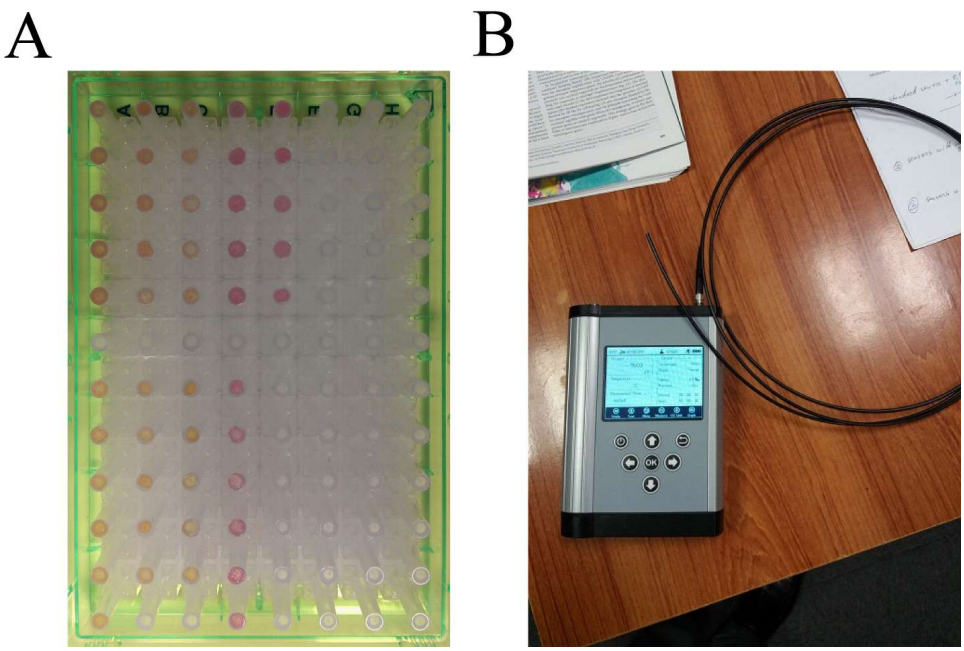

Figure 5.6. Photographs of Agilent's XF plate cartridge (lid with piston tips) containing the different pH/O_2 sensor coatings (A), and Fibox4 reader (PreSens) equipped with a fibre-optic probe (B).

Table 5.3 Phosphorescence intensity and phase shift signals for the different PtOEP-SB based sensors, with and without enhancers, and the two reference sensors, measured on a Fibox4 reader in air at 22°C.

No	Sensor Type	Intensity signal, mV		Phase signal, degrees		Relative Intensity Signal
		average	SD (RSD)	average	SD	
Ref.1	Type PS3 O_2 sensor (PreSens)	~70,000		29.9		8.5
Ref.2	Type V3-PS pH/O_2 sensor cartridge for XF Analyser (Agilent)	8,200	731 (8.9%)	28.3	0.12 (0.4%)	1
1	Sensor 1 0.25 mM PtOEP-SB, 3 mM TCPB, 6% PVC	1,586	295 (18.6%)	26.49	0.64 (2.4%)	0.19
2	Sensor 2 0.25 mM PtOEP-SB, 3 mM TCPB, 6% PVC, 0.15% TiO_2	1,853	395 (21.3%)	28.2	0.59 (2.1%)	0.23
3	Sensor 3 0.25 mM PtOEP-SB, 3 mM TCPB, 6% PVC, 1% PS-DVB	1,990	590 (29.7%)	26.35	0.19 (0.7%)	0.24
4	Sensor 4 0.25 mM, PtOEP-SB, 3 mM TCPB, 6% PVC, 0.1 mM C6, 0.15% TiO_2	2,333	94 (4%)	22.5	0.4 (1.8%)	0.28
5	Sensor 4a 0.25 mM PtOEP-SB, 3 mM TCPB, 6% PVC, 0.25 mM C6, 0.15% TiO2	2,500	644 (25.8%)	17.7	0.46 (2.6%)	0.3
6	Sensor 5 0.25 mM PtOEP-SB, 3 mM TCPB, 6% PVC, 0.1 mM C6, 1% PS-DVB	1,987	138 (7%)	20.5	0.69 (3.4%)	0.24
7	Sensor 5a 0.25 mM PtOEP-SB, 3 mM TCPB, 6% PVC, 0.1 mM C6, 0.5% PS-DVB	1,900	367 (19.3%)	20.95	1.66 (7.9%)	0.23
8	Sensor 4/5 0.25 mM PtOEP-SB, 3 mM TCPB, 6% PVC, 0.1 mM C6, 1% PS-DVB, 0.15% TiO2	1,994	99 (4.9%)	11.2	0.66 (5.9%)	0.24

The results of such testing are summarised in **Table 5.3.** One can see that PreSens PS3 sensor, designed and fully optimised for general O_2 sensing, showed maximal intensity readings (70,000 mV) and phase shift of 29.9 degrees. Seahorse sensors, which use a similar PtPFPP-based O_2 sensing material, blended with a pH-sensitive material and deposited on the plastic substrate, produced markedly

reduced intensity signals (8.5 times lower). The phase shift signals for XF sensors were also slightly lower (by 1.6 degrees), most likely due to minor crosstalk with the fluorescent sensor component. These results reflect the trade-offs between sensor performance and application requirements.

The PtOEP-SB based sensor coatings deposited on the same substrate showed 4-5 times lower intensity signals than the XF sensors. The sensors with light-scattering additives were generally brighter than neat sensors, but only by 5-40%. The variability of intensity signals for the new sensor coatings deposited manually was comparable to the XF sensors (RSDs 29% and 8.9%, respectively), which were produced by an automated deposition process. Phase shift signals from the sensors without C6 reference were also close to the reference PtPFPP based sensors, thus reflecting their similar lifetime values, while in the presence of C6 phase signals were markedly reduced. We attribute this to non-optimal filtration of the two emission signals from the sensor, bleeding of the short-lived fluorescence of C6 (phase shift close to zero) into the detector and decreasing the total phase signal. Such adverse effects are common for phase fluorometry [168], however they are less pronounced in time-resolved and ratiometric intensity detection that were targeted in this study.

Next, we applied the new sensor coatings into wells of a glass-coated 96-well plate (Plate+™, Greiner). Subsequently, the wells were filled with DMEM medium adjusted to the different pH values (6.0, 6.5, 7.0, 7.5) and measured at 37°C on a ClarioStar multi-label reader (BMG Labtech, Aylesbury, UK) equipped with an Atmospheric Control Unit (ACU) providing O_2, CO_2 and T control. The instrument was programmed to ramp the O_2 concentration in the plate compartment, while measuring sensor TRF intensity signals and converting them into PLT values [196]. **Fig.5.7** shows that the new sensors produced robust and reversible phosphorescent response to changing O_2 in the medium. When moving from the air-saturated (20 kPa) to depleted O_2 levels (2 kPa) and back to 20 kPa, the changes in sensor lifetime values were not very large (6-7 μs), but sufficient for accurate O_2 and OCR measurements. They were also rather uniform across the measured range and consistent with the previously reported values [184] . The changes in TRF intensity were much greater (7-fold between 2 and 20 kPa O_2), as a consequence of the time-gated detection, in which the short-lived fractions of the intensity signal were excluded from the integration. The lifetime values obtained on BMG reader (25.6 μs at 20 kPa O_2) were close to those measured on Victor 2 reader (~23.5 μs at 21 kPa O_2). Again, the new sensors showed no significant degradation of the dyes over the measurement period, which lasted several hours.

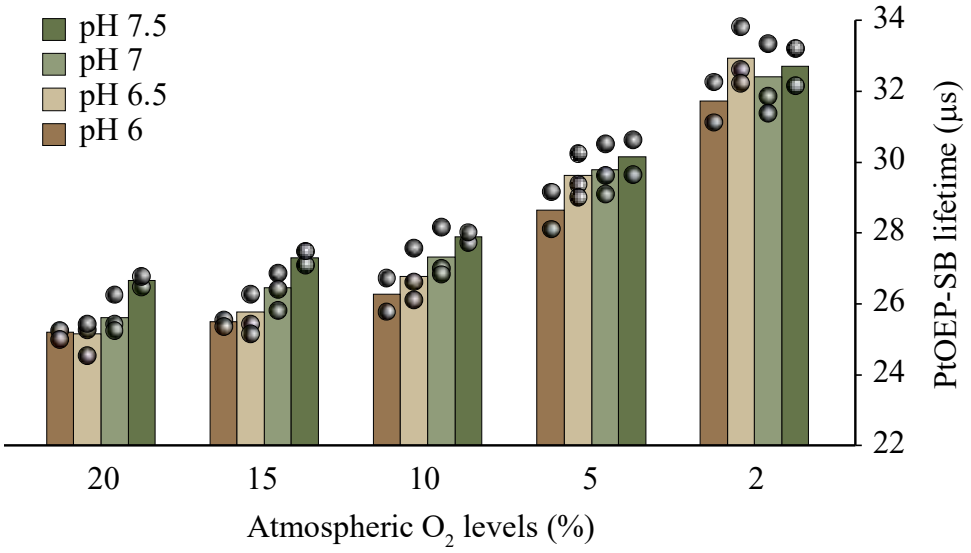

Figure 5.7 Response to O_2 of the PtOEP-SB based sensors deposited on Plate+™ Glass-Coated Microplate and measured on a BMG-ACU reader in TRF mode at different pH. PLT is shown as mean values and individual data points obtained (N = 2 for pH 6 and 7.5; N = 3 for pH 6.5 and 7) during continuous monitoring at the corresponding O_2 levels.

Thus, we concluded that the new pH/O_2 sensor formulations are suitable for the deposition on plastic substrates and subsequent use in cell analysis. Their brightness is satisfactory, even though PtOEP-SB dye is less bright than normal Pt(II)-porphyrins. The light-scattering enhancers in sensor coatings produced little benefit: the resulting signal gains were small, so they were omitted. On the other hand, correction of variability of intensity signals, enabled by C6 reference dye, is expected to improve performance of the new sensors in cell analysis. Collectively, the sensor-coated plastic substrates look adequate for targeted applications.

5.2.6 Cellular OCR and ECA measurements with the new pH/O_2 sensor coatings

Having succeeded with sensor optimisation and deposition on the different substrates, we then performed O_2 and pH sensing experiments with samples containing mammalian cells. We used the highly respiring and glycolytic PC12 cell model to perform cellular ECA and OCR on a standard multi-label reader. Of note, the PtOEP-SB/C6 sensors (0.25 mM PtOEP-SB, 0.1 mM C6, 3 mM TCPB in PVC) coated on Agilent XF cartridge exerted negligible effect on cell viability (P=0.27. t-test, **Fig.5.8**).

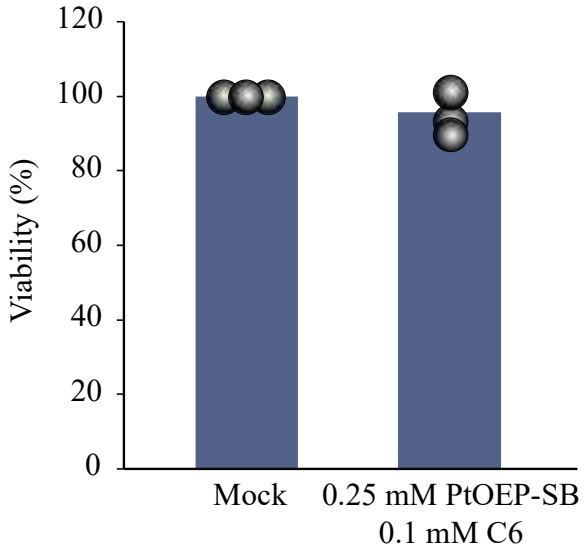

Figure 5.8 Sensor cytotoxicity analysis: suspensions of PC12 cells were exposed for 1 h to PtOEP-SB/C6 sensors deposited on the Agilent XF cartridge (submerged), and then cell viability was measured using CellTiter-Glo® Luminescent cell viability kit (Promega). The effect of the sensor on cells was analysed using t-test (p=0.26, N=3, mean values and individual data points are shown).

First, a three-point pH calibration of the sensors (pH = 6.4, 6.9 and 7.4) was performed on the same plate, which revealed the following linear relationship between sample pH and ratio of the C6 and PtOEP-SB intensity signals (**Fig.5.9A**): $pH = (I_{560}/I_{642} + 0.746)/0.126$.

Next, suspensions of PC12 cells, treated for 90 min with DMSO (mock, resting cells) or with FCCP and Ant A drugs, were analysed and seen to acidify the medium from pH 7.4 to pH 7.1, 6.95 and 6.4, respectively (**Fig. 5.9B, C**). The observed increases in ECA by FCCP and even more so by Ant A treatment were in agreement with expectations, reflecting activated glycolysis and lactate release in cells with inhibited oxidative phosphorylation.

Similarly, the analysis of OCR revealed a slow increase in PtOEP-SB lifetime signals of for the resting cells, a more rapid increase (up to 32 μs) for the FCCP uncoupled cells and no increase for the cells treated with Ant A (**Fig. 5.9D**). A comparison of these results with the O_2 calibration data (**Fig.5.7**) showed that O_2 levels in PC12 cell suspension decreased below 5 kPa upon the FCCP treatment. Since in the respiration medium buffered with 20 mM HEPES, pH remained practically unchanged. PtOEP-SB/C6 signal ratio can be used for direct estimation of the OCR. Indeed, this ratio revealed (**Fig. 5.9E**) that deoxygenation profiles were almost identical to those shown in **Fig. 5.9D**, with a better signal span (0.2 and 2.4 ratio units) for the Ant A and FCCP treated samples, respectively. The lifetime based and ratiometric OCR results generated with the PtOEP-SB-C6 sensors also correlated well with those produced with commercial O_2 probe MitoXpress®-Xtra (**Fig. 5.9 F**).

It should be noted though that quantitative OCR and ECA analysis in the ratiometric mode still requires sensor calibration on each instrument [24]. In contrast to this, lifetime based O_2 calibrations are usually stable and transferrable between different instruments (see [168]).

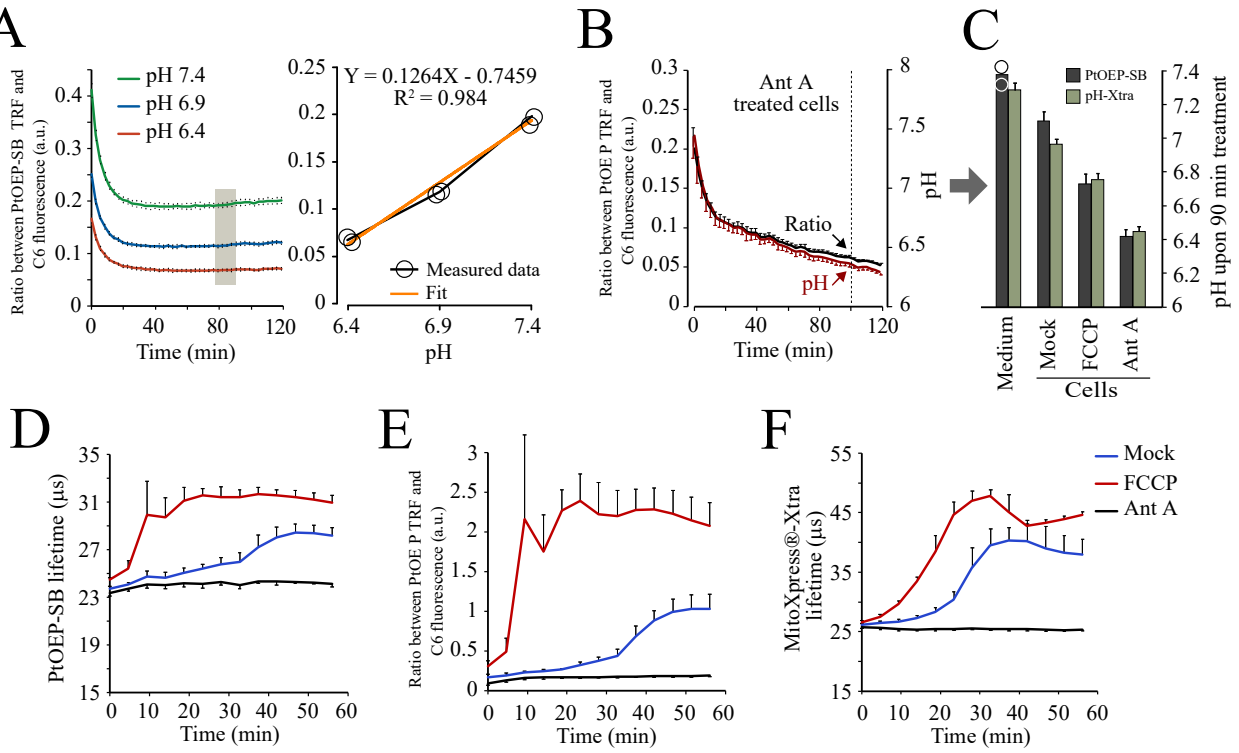

Figure 5.9. Monitoring of ECA **(A-C)** and OCR **(D-F)** in a suspension of PC12 cells on Victor 2 reader in standard 96-well plates coated with PtOEP-SB-C6 sensors. **A.** Sensor pH calibration in PBS using pH standards 6.4, 6.9 and 7.4. The right panel shows the linear dependence between the ratio signal (TRF at 642 nm and prompt fluorescence at 535 nm) and pH, calculated for the 80-90 min time slot (highlighted by grey rectangle). The calibration equation: $pH = (I_{560}/I_{642} + 0.746)/0.126$ allows the calculation of pH in biological samples, as exemplified in (B) by the ECA profile of PC12 cell suspension upon inhibition of mitochondrial complex III (2 µM Ant A) or end point pH analysis in cell suspension at rest (mock) and upon inhibition of the OxPhos flux with Ant A or FCCP (0.25 µM). **D-F.** The lifetime (D) and intensity ratio (E) of the PtOEP-SB-C6 sensors reflect the respiratory activity of the cells. MitoXpress®-Xtra probe (F) was used as a benchmark for the new OCR assays. Small black dots in (A) and empty circles in (A, C) show individual data points (N=2). Error bars show standard deviation (N=3).

5.3 Conclusions

In summary, we presented and optimised a panel of advanced multi-modal, multi-analyte optochemical sensing materials for live cell analysis. The sensors employ the substituted PtOEP-SB or PdOEP-SB indicator dyes that possess dual pH and O_2 functionality, formulated with a host polymer, a reference fluor and a proton transfer agent. The sensor precursor cocktail is applied on standard plastic substrates used in cell analysis, producing stable solid-state sensor coatings with robust photoluminescent responses to both pH and O_2 in self-referenced detection modes.

The study also included: 1) the screening of extended panel of polymeric host matrices for the sensor; 2) synthesis and evaluation of the new MePor-SB derivatives with altered protonation behaviour; 3) development of the ratiometric version of the sensor; 4) photoluminescence signal enhancement schemes; 5) sensor deposition on common cell analysis substrates and their demonstration in OCR and ECA measurements with relevant cell models.

The main outcomes include the elaboration of the structure-function relationships for this multi-mode, multi-analyte sensing platform, the development of tandem pH/O_2 sensors for OCR/ECA measurements that are fully self-referenced and thus enable calibration-free operation (or once-off calibration). The new sensors were demonstrated on standard plastic substrates used in cell analysis, and benchmarked against the existing platforms in the experiments with cells. The dual sensing platform was seen to provide detailed ‘metabolic signature’ and energy budget breakdown for tested cells similarly to the existing platforms, but with more efficient and stable detection modes. Thus, it has potential for wide practical use and can successfully compete with existing sensors in biological applications.

Chapter 6: New pH and dual pH/O_2 sensors for cell analysis and tissue imaging

6.1 Introduction

The maintenance of physiological homeostasis is crucial for cell survival and proper functioning. The major metabolic pathways of human and animal cells include OxPhos, glycolysis and TCA cycle, which are supplemented by the pentose phosphate, β-oxidation, and glutaminolysis [197, 198]. These metabolic pathways are interlinked and cross-regulated, so they can respond to altered energy demand (e.g. muscle exertion), substrate availability (e.g. tumour hypoxia), or stress condition (e.g. drug exposure) [151, 199]. This feature enables the cell to compensate for dysfunctional pathway or imposed stress. As a consequence, the characteristic metabolic profiles and adaptive or mal-adaptive responses of cells under disease or stress state can be obtained for effective therapeutic diagnostics and pharmacological treatments [6, 9].

Optochemical pH and O_2 sensors are well suited for probing cell metabolism [1]. Thus, OxPhos and glycolysis fluxes can be assessed by measuring OCR and ECAR of host cells with appropriate O_2 and pH sensors. Sensor-based imaging systems for key markers of tissue metabolism are also important, particularly for the monitoring of tissue oxygenation state and acid-base homeostasis of tumours, where hypoxia, enhanced glucose catabolism and lactate acid accumulation are common [200]. While tumour cells are usually able to maintain normal slightly alkaline intracellular pH (pHi), their extracellular pH (pHe) is lower due to Warburg effect [201]. This is a result of poor perfusion and disorganised vasculature, causing the major acid load to be transported outside the cells to tumour tissue where cannot be removed efficiently resulting in tumour acidosis [202]. The reduced pHe in solid tumours facilitate cell proliferation (maximized at pHe 6.8 vs 7.3 for normal cells) and metastases, which contributes to cancer aggressiveness and the effectiveness of anti-cancer therapy [203].

Currently the PLT based sensing approach is common and successful in cell and tissue O_2 sensing, and exists in many commercial systems and tunable platforms. Conversely, self-referenced pH sensors remain relatively under-developed [204, 205]. Thus, a fluorescent sensor based on diazaoxotriangulenium dyes which gives a prominent FLT response (3-12 ns) to pH was described [206]. However, this sensing scheme relies on homo-FRET mechanism, resulting in the sensor being not fully referenced and stable (depends on dye concentration). The broad spectra of the dye also make the resulting pH difficult to multiplex with common O_2 sensors and with other fluors emitting around 400-600 nm. The pH sensors based on acridinium dye and FLT measurements have sub-optimal pKa and other characteristics (wavelength dependence of the FLT and cross-sensitivity to O_2) for cell

analysis, while those based on the other common pH indicator dyes have very narrow span of FLT changes [23, 204]. Intracellular and extracellular O_2 probes based on the lipophilic and hydrophilic Iridium (III) complex were described for Hela cells analysis [207] which have low toxic action on cells and allow self-referencing by PLIM. However, there was no further description of similar lifetime-based pH and dual pH/O_2 sensors on their basis.

Among the few sensor based systems developed and optimised for real-time measurement of cellular OCR and ECA, is the one that uses the phosphorescent Pt-porphyrin based O_2 sensing probe and the pH-sensitive fluorescent lanthanide probe [136]. This pH and O_2 sensing probes have favourable spectral characteristics (one excitation wavelength and well resolved emission bands), robust and easily separated PLT/FLT responses in the μs range, optimal O_2 and pH sensitivity, and no crosstalk. However, these commercial probes (pH-Xtra and MitoXpress-Xtra from Agilent) comprise water-soluble reagents used on a disposable basis, which are less efficient and less user-friendly than traditional solid-state sensor coatings for cell analysis.

The current 'golden standard' in the field is the Seahorse Biosciences XF platform, which comprises solid-state O_2 and pH sensor coatings deposited on a specially designed microplate with moving pistons, coupled with the detector for signal acquisition and injection ports for the addition of effector compounds [142]. This platform provides simultaneous measurement of ECAR/OCR with high sensitivity and performance. However, its sensors operated in in fluorescence intensity mode are not self-referenced, thereby requiring calibration for each sensor prior to measurement. This in turn complicates both the assay workflow and data processing algorithms.

In this study, we have developed a novel solid-state pH and dual pH/O_2 sensor-based systems for simpler, rapid and more stable measurement of cellular OCR/ECAR in biological samples. Such system (in several modifications) utilizes internally referenced pH sensors based on fluorescent porphyrin dyes, and an O_2-sensitive phosphorescent Pt-porphyrin dye. We demonstrated how the optimised sensor materials applied on microplates substrates for biological applications including OCR/ECAR analysis in relevant cell models and 3D spheroids cultures. We also demonstrated how the new planner FLIM sensors (coatings deposited on polyester films) used for tumour pH imaging in the model animals.

6.2 Results and discussion

6.2.1 Spectral characteristics of the solid-state pH and O_2 sensors

The hydrophobic metal-free porphyrin dyes, OEP and OEPK, were selected as fluorescent pH indicators for development of solid-state pH sensors and dual pH/O_2 sensors. Both dyes have intense

excitation bands at ~400 nm (Soret band) and sharp well-resolved emission bands of the neutral and protonated forms at >600 nm (**Fig.6.1**).

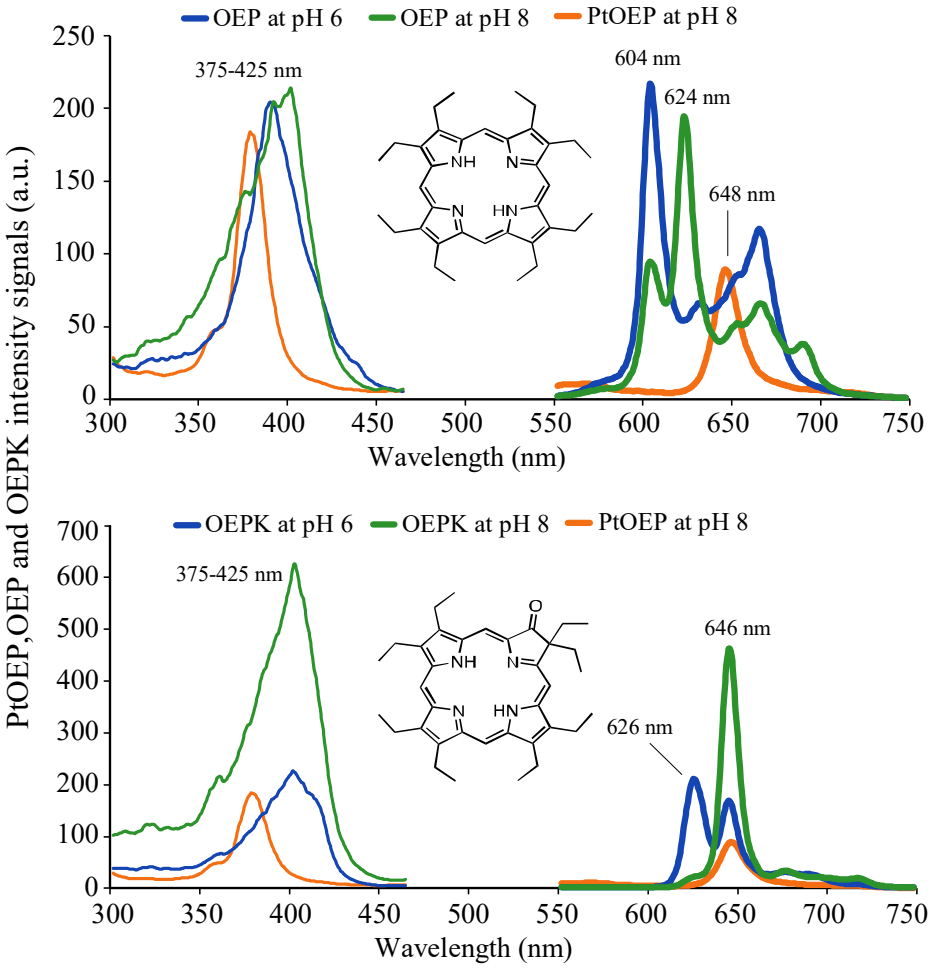

Figure 6.1. Photoluminescence spectral characteristics of OEP/PtOEP (top) and OEPK/PtOEP (bottom) dye pairs, and chemical structures of OEP and OEPK (neutral forms). Fluorescence spectra of sensor coatings (0.08 mM OEP or OEPK and 0.25 mM PtOEP) spotted on Mylar films were measured on a Cary Eclipse at 390 ± 10 nm excitation.

Furthermore, both OEP and OEPK dyes show excellent spectral compatibility with Pt-porphyrin dyes (e.g., PtOEP or PtPFPP) commonly used in O_2 sensors, which allows the realisation of simple dual pH/O_2 sensing systems. Specifically, one light source can be used to excite both O_2 and pH-sensitive dyes at ~400 nm, with red phosphorescence of PtOEP at 648 nm, fluorescence of OEP neutral form at 624 nm and of OEP protonated form at 604 nm. This facilitates effective photoluminescence detection of these dyes, either selectively or combined. And for the second pair, the protonated form of OEPK fluoresces at 626 nm, with its neutral form fluorescing at 646 nm, which is almost identical to PtOEP phosphorescence. Considering the intense absorption Q-band and high emission yield of OEPK, its basic form can potentially act as efficient FRET acceptor for PtOEP and/or interfere with PtOEP detection.

Another useful feature of the OEP, OEPK and PtOEP based sensors is that they emit in the red spectral range (600-750 nm) without blocking the visible range. So, these sensor dyes can be used in conjunction with other fluorescence probes, such as the genetically encoded fluorescent protein tags (e.g., GFP, CFP, YFP), nuclear stains (e.g., DAPI, Hoechst 2332), mitochondrial membrane potentials probes (e.g., TMRM, JC-1), and fluorescent Ca^{2+} probes (e.g., Fura-2, Fluo-4) [208, 209]. Such fluorescent probes, which emit in the 400-600 nm range, can be detected in the presence of the sensor dyes without much interference. This is very useful for cell analysis.

Thus, the porphyrin dyes look promising for development of efficient pH and dual pH/O_2 sensors for cell analysis. In addition to the existing PLT based O_2 sensors with internal referencing capabilities, there is also a potential to develop complementary solid-state pH sensors with internal referencing, based on either ratiometric intensity measurements in steady-state fluorescence mode, and potentially using the nanosecond FLT readout in time-resolved fluorescence mode.

6.2.2 Development and optimisation of the OEP and OEPK based pH sensors

OEP and OEPK dyes were previously tested in general pH sensing using plasticised PVC matrix and lipophilic borate salt (TCPB) as proton-transfer agent (PTA) [185], however these sensors were not fully developed and optimised for cell analysis and/or multi-parametric readout. Their specific imperfections included: the low solubility of TCPB in polymer matrix, which resulted in dye and TCPB aggregation upon cocktail drying and spatially inhomogeneous sensor; no internally referenced readout(s) of pH, pKa was not fully tuned for cell analysis and ECA measurements; sensor safety and toxic action on cells were not assessed.

It is also worth noting, that ionisation mechanism for pH-sensitive porphyrin dyes usually involves the addition of a proton or two protons to the nitrogen atoms of the tetrapyrrole macrocycle [210, 211]. As a result, for solid-state pH sensors based on lipophilic porphyrin dyes and lipophilic polymers, a lipophilic PTA such as a tetraphenylborate salt, must be present in the sensor material, to drive the protonation process. Without a PTA, ionisation will not proceed, unlike the dyes with proton donor properties which do not require PTA[205]. However, in this study we have shown that the previously described TCPB based pH sensors [184] have prominent toxic action on cells. Thus, when samples containing cultured mammalian cells were exposed to TCPB based sensors for ~1h, cell viability decrease drastically (**Table 6.1**).

Table 6.1: Effects of different PTA additives (lipophilic borate salts) on the viability of mammalian cells.

Borate type	Cell line	Dyes*	Borate concentrations (mM)				Mock (%)
			1 mM	2 mM	3 mM	5 mM	
TCPB	HCT 116	a	56.4 ± 1.43	64.8 ± 5.63	67.1 ± 2.58	67.0 ± 4.98	100 ± 1.03
		b	58.5 ± 0.67	66.6 ± 4.92	64.3 ± 4.27	69.3 ± 3.3	
Lithium-PFPB	HCT 116	a	69.6 ± 1.78	73.4 ± 1.93	83.8 ± 0.41	88.7 ± 1.91	100 ± 1.03
		b	74.6 ± 0.49	75.7 ± 1.21	79.4 ± 3.51	87.5 ± 0.89	
Na-TFMB (borate1)	HCT 116	a	75.0 ± 3.02	83.4 ± 2.07	90.6 ± 0.61	92.2 ± 1.08	100 ± 1.51
		b	67.8 ± 0.28	77.3 ± 0.58	82.1 ± 2.38	88.3 ± 0.8	
	A594	a	88.7 ± 0.27	92.9 ± 0.05	96.1 ± 0.92	94.6 ± 1.25	100 ± 1.07
		b	81.0 ± 2.29	89.6 ±1.36	93.7 ±1.84	95.5 ± 1.59	
	SW480	a	72.1 ± 0.12	83.7 ± 1.31	88.0 ± 3.78	91.8 ± 2.31	100 ± 1.06
		b	70.1 ± 1.74	83.8 ± 0.99	87.5 ± 1.49	90.8 ± 0.03	

*a. 0.08 mM OEP/0.25 mM PtOEP; b. 0.08 mM OEPK/0.25 mM PtOEP

To reduce the cytotoxicity TCPB, we tried the following: i) soaked the sensors overnight in 0.01 mg/ml collagen IV solution (to form a protective layer), or in cultured medium (a pre-wash); ii) applied a barrier layer of D4 hydrogel on top of the TCPB sensor (physical separation from cells). Although these additional steps partly reduced the cytotoxicity of the TCPB based sensors (**Fig. 6.2A**), they also decreased or even eliminated the response to pH (**Fig. 6.2B**). Therefore, they have been ruled out.

To solve the sensor toxicity problem, we screened a small panel of alternative PTAs, which included three borate (Na-TFMB, Li-PFPB, and Na-TPB) and two organic phosphates (diphenyl phosphate and BNDHP) salts. Form this panel, the pH sensors based on Li-PFPB and Na-TFMB PTA showed greatly reduced cytotoxicity (**Table 6.1**) and excellent pH-sensing performance.

In particular, the superiority of the new Na-TFMB based pH sensors over the current TCPB based sensors includes: a) low cytotoxicity (**Fig.6.2C-D**); b) better solubility in sensor cocktails and in plasticised PVC matrix and better quality of the resulting sensor coatings (uniform colour, low heterogeneity and dye aggregation); c) excellent spectral response (**Fig.6.3A-C**) and good compatibility with OEP and OEPK dyes (and PtOEP – see below); d) good span of the usable pH values covering the most important physiological range, with the possibility to fine-tune sensor pKa across >1.3 pH units (5.86-7.21) by adjusting the PTA concentration (**Fig.6.3D**); e) practically linear pH response for the OEP based sensors in the internally referenced ratiometric intensity mode (**Fig. 6.3E**).

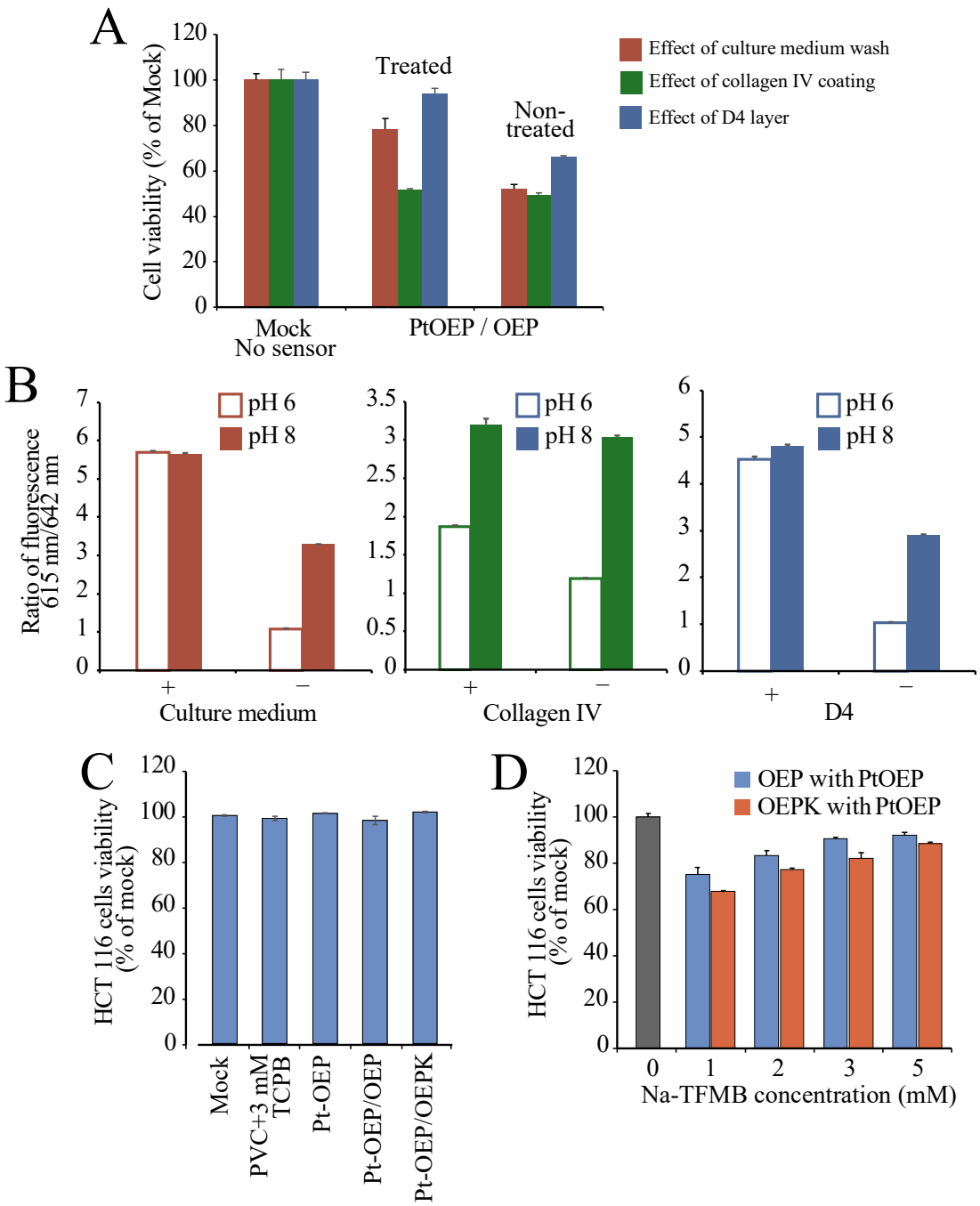

Figure 6.2. Optimisation of the pH/O_2 sensors. **A**. Cell viability tests with PC12 (effects of medium prewash and collagen) and HCT116 cells (effect of D4 protective layer). **B**. Effects of sensor pre-treatment on the 615/642 nm ratio. **C**. Effect of 3 mM TCPB on cell viability (sensors coated on Agilent Seahorse cartridges then inserted from the top to cells suspension for 1 hr). **D**. Effect of Na-TFMB on cell viability (sensors coated at the bottom of 96 wells plates). N=3.

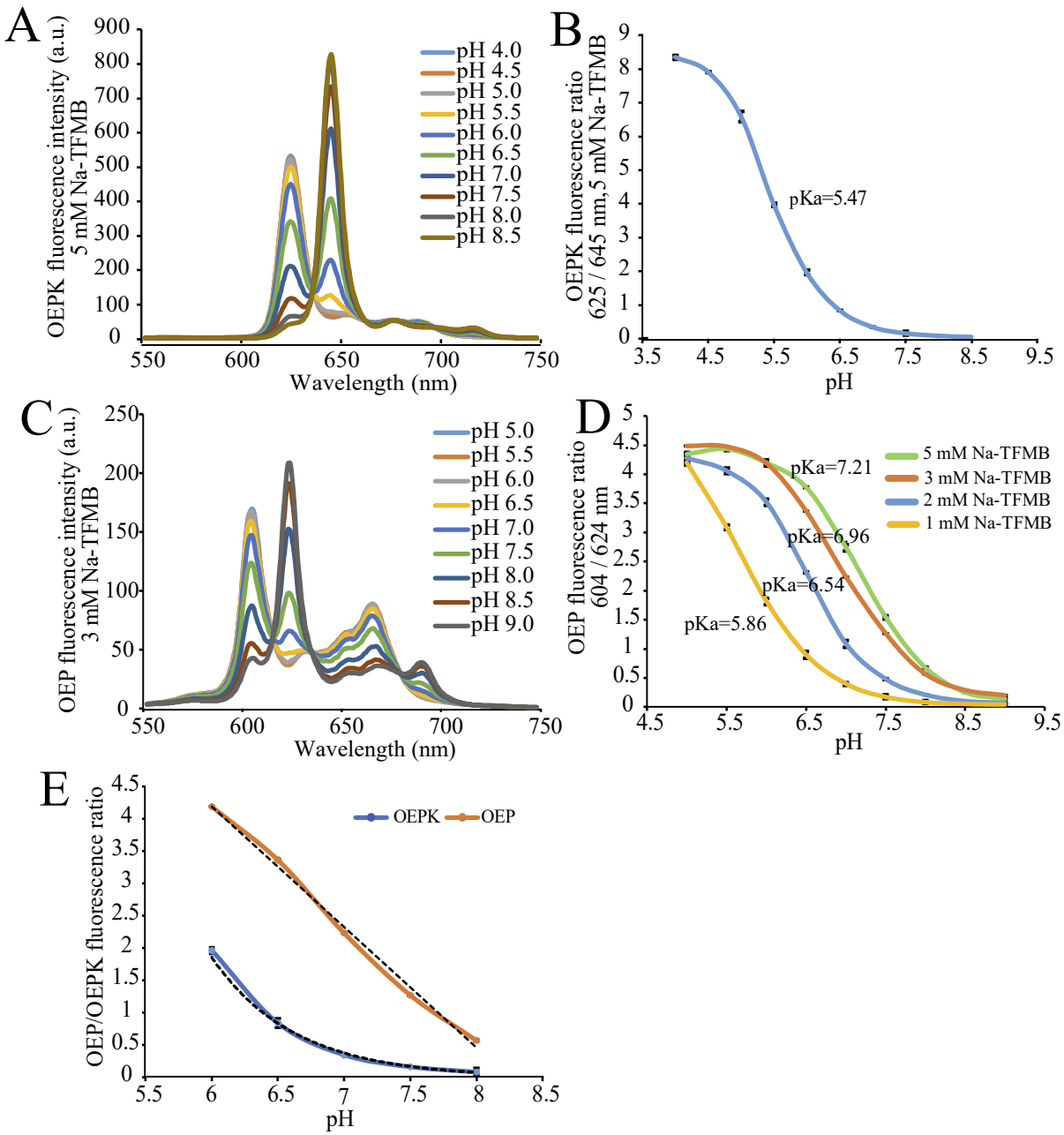

Figure 6.3. Tunability of pKa values for the OEP/OEPK sensors. **A-B**. Spectral response of OEPK to pH and fluorescence intensity ratio calibration. **C-D**. Spectral responses of OEP sensors to pH and calibrations at different Na-TFMB concentrations. **E.** Dependence of the 604/624 nm signal ratio on pH for OEP (3 mM Na-TFMB) and of the 625/645 ratio for OEPK (5 mM Na-TFMB), and corresponding equations: $pH_{(OEP)} = (15.392-y)/1.867$ ($R^2 = 0.995$); $pH_{(OEPK)} = -\ln(y/26459)/1.594$ ($R^2 = 0.999$). The sensor coatings were analysed at 37℃ on Cary Eclipse. Note: Optical measurements were carried out under equilibrium conditions with around 3 mins response time at each pH point.

Based on the above results, we have selected the OEP-based sensors with 3 mM Na-TFMB, deposited as thin film coatings (thickness <10 μm) at the bottom of polypropylene 96-well plates, for further use. Such freshly made pH sensors, upon their exposure to cell containing samples, reduce cell viability by ≤10%. They cover the most useful physiological range of pH 6-8, with a linear response (R^2=0.9949)

in the ratiometric intensity (615nm/642 nm) mode. For comparison, similar pH sensor based on OEPK dye showed more acidic pKa (5.47 at 5 mM Na-TFMB, **Fig.6.3B**), which makes them complementary to the OEP based sensors and allows further tuning of sensor response. Interestingly, when the new OEP and OEPK based pH sensors were deposited not on the bottom of the wells of a 96WP, but on the Seahorse cartridges and then inserted in biological samples from the top, such sensors showed no detectable cytotoxicity but similar analytical performance. The new pH sensors show fast response to pH changes. Unlike the Seahorse sensors, they do not require lengthy pre-conditioning and calibration, and can be used with biological samples straight away, after ~15 min of soaking in PBS.

6.2.3 Development of dual pH/O_2 sensors

For efficient optochemical sensing of pH and O_2, working concentrations of both indicator dyes in sensor matrix (plasticized PVC) need to be maximised, while at the same time minimizing the undesirable effects such as the cross-talk between the two optical signals, dye aggregation, concentration quenching or solution FRET. This will ensure high and stable photoluminescence signals from the sensor, robust and reliable pH and O_2 sensing and ECA and OCR measurements.

6.2.3.1 OEP/PtOEP sensor

For the OEP/PtOEP sensor, the concentration of 0.25 mM for both dyes in the cocktail was found optimal. The resulting coatings deposited in wells of 96-wells plates produced high, reproducible and well-resolved emission signals on the TRF reader Victor 2 which uses a 340 ± 40 nm excitation filter. The two signals at 615 ± 10 nm and 642 ± 10 nm (standard emission filters) increased linearly with OEP concentration at pH 6 and pH 8 (**Fig.6.4**). At these sub-optimal wavelengths (see **Fig. 6.1**), the 615/642 nm intensity ratio produced robust and reversible ~3.5-fold change when pH changed from 6 to 8, with a close to linear relationship and pKa of 7.5 (**Fig. 6.5A**). At the same time, the 615/642 nm ratio was increasing with an increase of OEP concentration.

The phosphorescent signals of PtOEP, measured from oxygenated dual sensors in TRF mode, were also very high and not influenced by OEP concentration and pH changes. At the highest OEP concentration a minor quenching of the PLT signal was observed, but it was absent at and below 0.08 mM of OEP (**Fig. 6.5C**). In deoxygenated state the effects of OEP on the PLT signals from PtOEP were more significant (**Fig. 6.8A**). Based on these results, optimal concentrations of OEP and PtOEP dyes in the dual pH/O_2 sensors were found to be 0.08 mM and 0.25 mM, respectively.

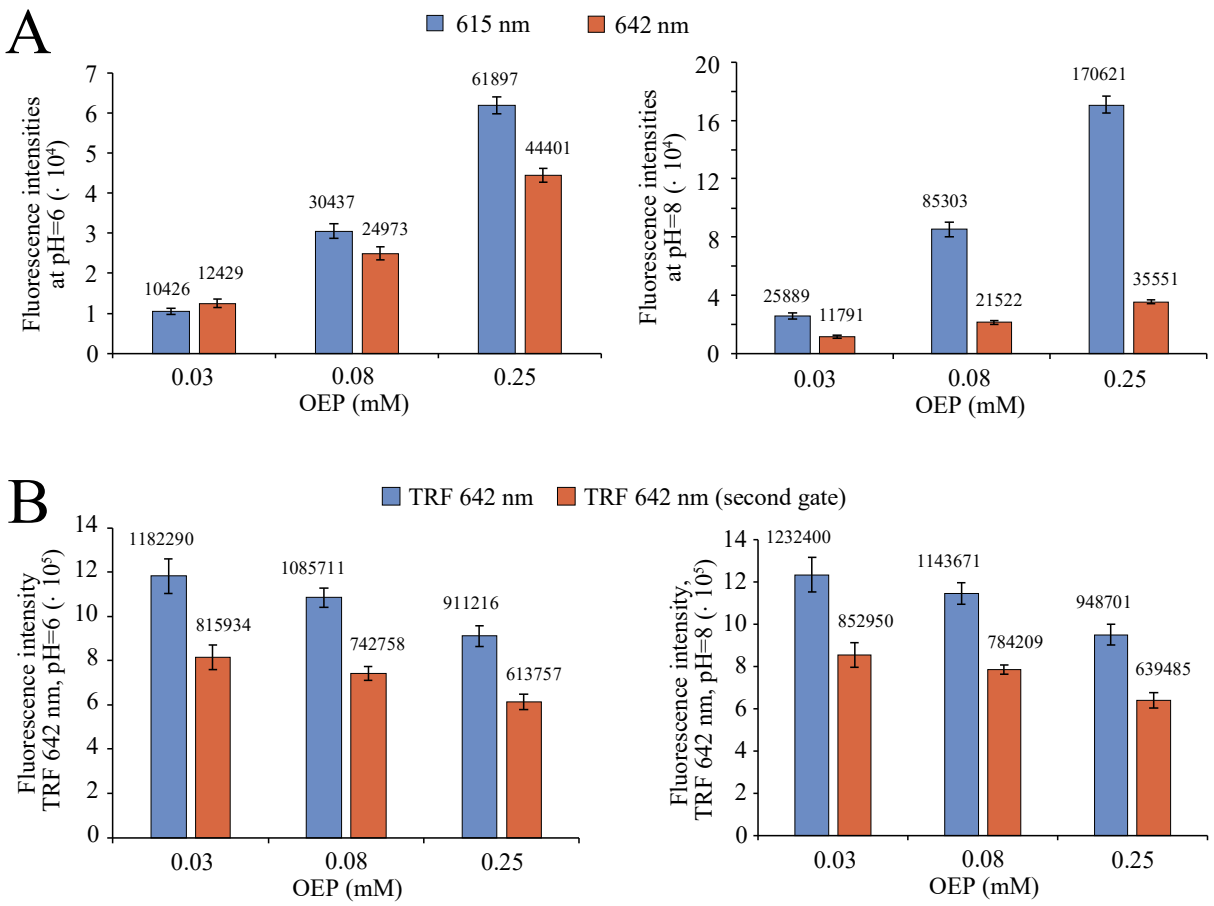

Figure 6.4 Signals from OEP/PtOEP sensors spotted on a 96-well polypropylene plate and measured on Victor 2 reader. **A.** Prompt fluorescence intensity at 615 nm and 642 nm in PBS at pH 6 (left) and pH 8 (right panel). **B.** TRF intensity at 642 nm in the first and second TRF window (at pH 6, left, and pH 8, right panel). Sensors contained 3 mM Na-TFMB, 0.25 mM PtOEP, and OEP at specified concentrations (0.03 mM, 0.08 mM, 0.25 mM) (Mean ± SD values are shown, N=3).

6.2.3.2 OEPK/PtOEP sensor

The performance of OEPK and PtOEP based sensors was tested on Victor 2 and Cary Eclipse specs. In the range of pH 6-8, the span of fluorescence ratio signal (615/642 nm) was much greater than for the OEP/PtOEP based sensors (**Fig. 6.5B, Fig.6.6A**). Also, at high OEPK concentrations TRF signals and PLT values for PtOEP dye decreased profoundly (**Fig. 6.5D, Fig.6.6B**). This was because fluorescence of the basic form of OEPK largely overlaps with PtOEP phosphorescence, unlike for the OEP. OEPK has more intense Q-band and higher emission yield, which make OEPK a good FRET acceptor for PtOEP. Such solution FRET quenching can be minimised by using low OEPK concentrations or a two-layer structure for the sensor dyes. Such experiments were outside the scope of the current study, and we proceeded with testing the OEP/PtOEP sensors deposited on 96-well plates, using them in OCR/ECAR analysis of cells on Victor 2 reader (see below). It should also note that there was a dye aggregation for OEPK in the mM range, which can be seen from the intensity image with clear patterns (**Fig.6.14 A-B**).

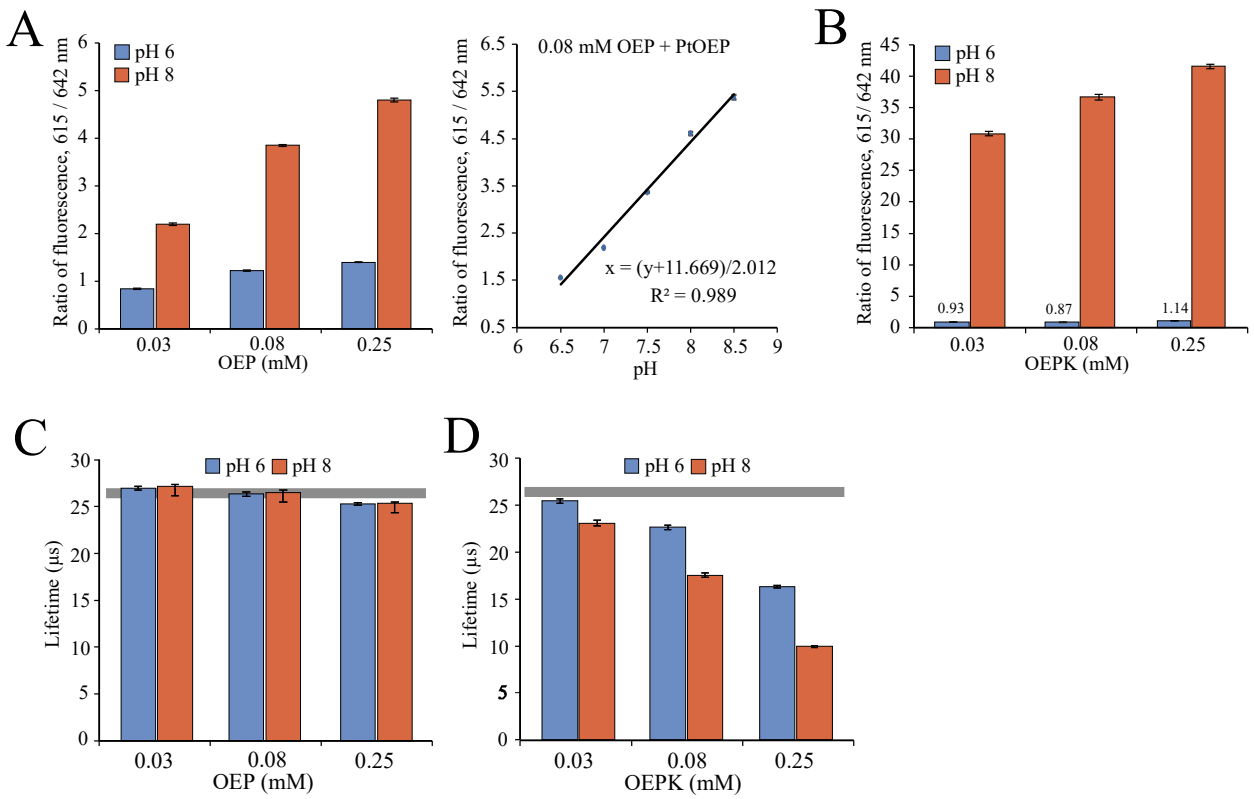

Figure 6.5. Optical signals of the OEP/PtOEP and OEPK/PtOEP sensors measured on a TRF reader Victor 2. **A**. 615/642 nm fluorescence intensity ratio at pH 6 and pH 8 (left panel) and the linear pH response to pH (right panel) for the OEP/PtOEP sensors; **B.** 615/642 nm fluorescence intensity ratio at pH 6 and pH 8 for the OEPK/PtOEP sensors. **C, D.** Effects of OEP and OEPK on the PtOEP lifetime. Grey line shows the PLT of the PtOEP sensor (without pH-sensitive dyes). N=3. All the sensors contained 3 mM of Na-TFMB.

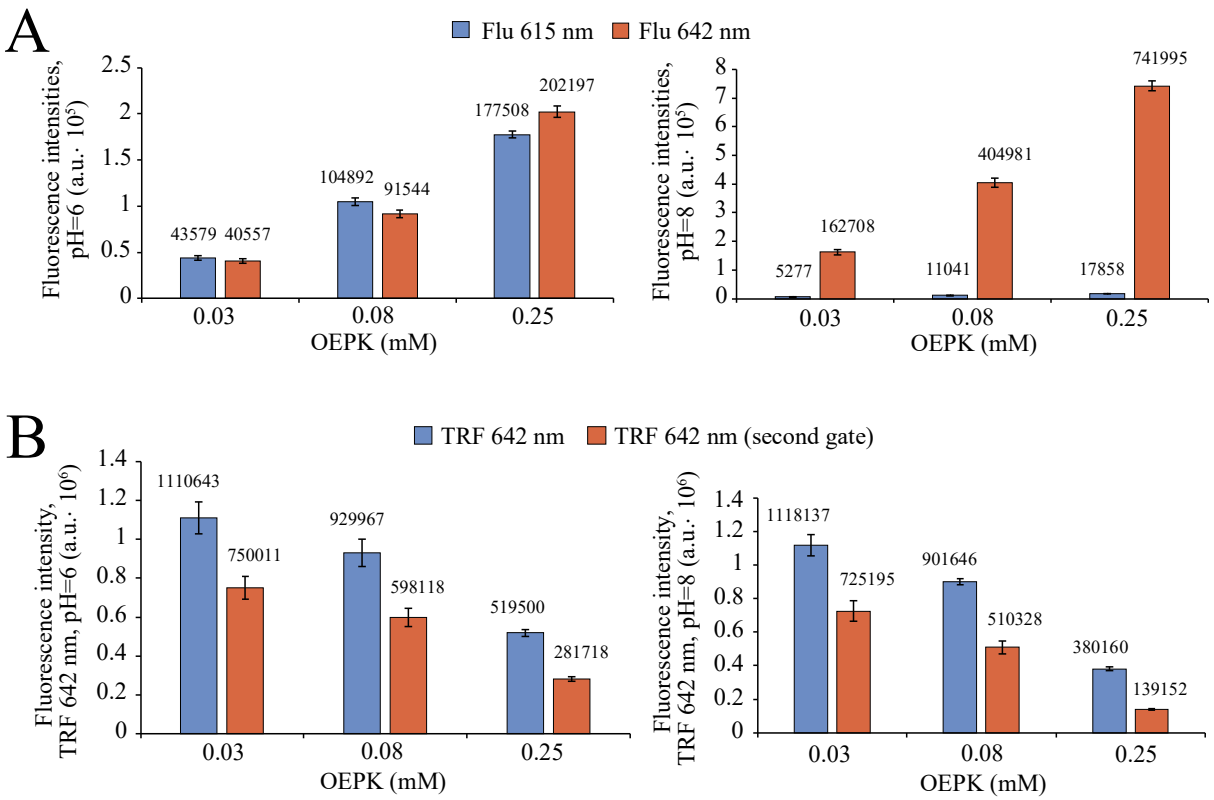

Figure 6.6. Signals of the OEPK/PtOEP sensors spotted on a 96-well polypropylene plate, measured on Victor 2 reader. **A** Prompt fluorescence intensity at 615 nm and 642 nm in PBS, pH 6 (left) and pH 8 (right). **B.** TR-F intensity at 642 nm in the first and second window at pH 6 (left) and pH 8 (right). Sensors contained 3 mM Na-TFMB, 0.25 mM PtOEP, and OEPK at specified concentrations (0.03 mM, 0.08 mM, 0.25 mM) (Mean ± SD values are shown, N=3).

6.2.4 Fluorescence lifetime-based pH sensing

FLT values for free porphyrin dyes typically lay in the region of 5-10 ns, and they depend on the fluor's electronic structure (free base, mono- and dication) [211]. We therefore reasoned that FLT values of our new pH sensors should change upon the protonation of the porphyrin dye. Notably, fluorescence of the different protomeric forms can be captured with the same excitation and emission filters: e.g. 400 nm excitation and 630 ± 30 nm bandpass emission filters (see **Fig. 6.1**).

Indeed, we found that protonation of the OEP and OEPK based pH sensors was accompanied by significant and reversible changes in their FLT values (**Fig. 6.7**). Measured on the confocal TCSPC-FLIM microscope, the span of FLT values was surprisingly large: 6.9-12.3 ns for the OEP and 3-5.7 ns for the OEPK sensors. The FLT values and their changes were much greater than for the existing pH sensors based on other fluorescent dyes: 1-3 ns and 5-20% change, respectively [204, 212] . As expected, the FLT-based pH sensing with OEP/PtOEP and OEPK/PtOEP dye pairs was unaffected by the solution FRET (**Fig. 6.8B**). These features make the FLT based detection superior over the intensity-based and ratiometric pH sensing. We performed pH calibration of the OEP and OEPK based sensors with 3 mM Na-TFMB, their pKa values were 7.4 and 6.0, respectively (**Fig. 6.7**). Bearing in

mind the tunability of the pKa by PTA concentration (**Fig. 6.3D**), we calibrated the OEP sensors with 1 mM Na-TFMB and observed the anticipated decrease of pKa from 7.4 to 6.6 (**Fig. 6.8C**) with a slight increase in the span of FLT values. While the pKa values determined by the ratiometric and FLT measurements did not match perfectly (**Fig. 6.3D**, **6.5A** and **6.8C**), both methods showed good reproducibility of results for the same batches of sensors. Batch-to-batch variability of PLT values was higher, likely due to minor variations of sensor cocktail composition (borate and dye concentrations) prepared manually.

We also examined the effects of dye concentration on the FLT values and response to pH. The FLT values of the dual sensors at 0.08 mM and 0.02 mM of OEP perfectly matched at pH 6, while at pH 7.5 they differed slightly at the low OEP concentration (**Fig. 6.8D**). And for the OEPK-based sensors no concentration-dependent effects were observed (**Fig.6.8E**). In all the above FLT calculations, we used the default mono-exponential data fitting with χ^2 test as 'goodness of fit' criterion.

Compared to the nanosecond FLT values of the pH sensors, the PLT values of PtOEP lay in the microsecond range, thus allowing for selective time-gated detection in the dual pH/O_2 sensing. The cross-talk between pH and O_2 was also studied for optimised dual sensors (**Fig.6.9**). The low and high pH has no effects on Pt-OEP lifetime (μs) in oxygenated medium, and negligible change was observed in the anoxic state. However, the OEP lifetime (ns) for pH sensing saw a slight increase at a higher pH value in deoxygenated indicating the small crosstalk between the two analytes.

Overall, dual pH/O_2 sensing with full internal referencing can be realised with the chosen dyes and sensor chemistries by: a) nanosecond FLT for pH and microsecond PLT for O_2 sensing, or b) ratiometric intensity-based pH sensing and microsecond PLT based O_2 sensing. Either of these detection methods provide simple separation of the key environmental parameters of tested samples (pH and O_2), and stable and simultaneous readout of the ECAR and OCR fluxes.

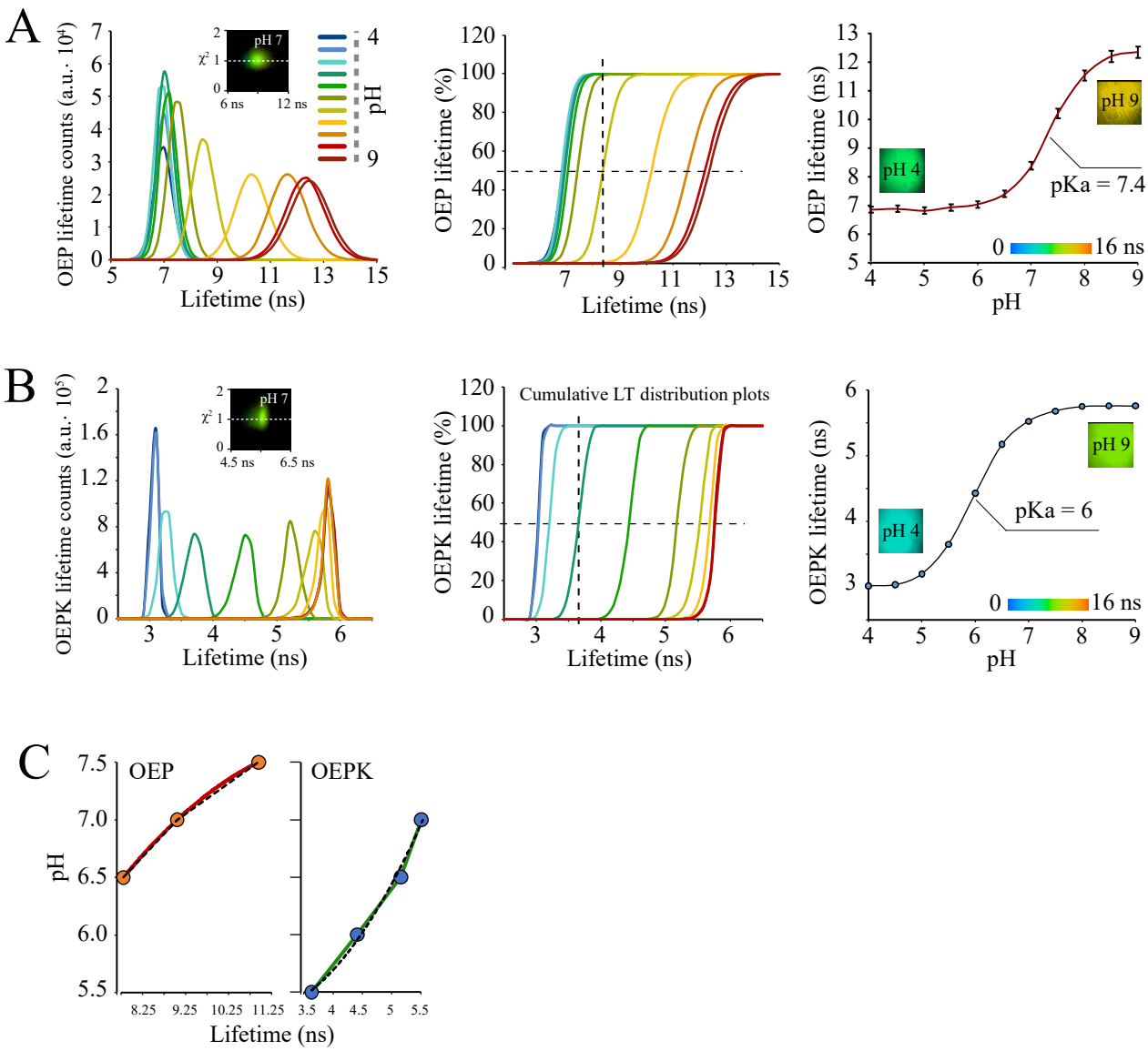

Figure 6.7. Results of FLT measurements for the dual pH/O_2 sensor using confocal FLIM microscopy. **A, B.** pH calibrations for the OEP (**A**) and OEPK-based (**B**) sensors; median PLT values were used to calculate pKa values, which are indicated. **C**. Parts of the sensor calibration curves that have a good fit in the physiological pH range according to the equations: $pH_{(OEP)} = -0.0431\tau^2 + 1.1269\tau + 0.335$ ($R^2 = 1$, 6.5-7.5 pH range); $pH_{(OEPK)} = 0.1933\tau^2 - 1.006\tau + 6.611$ ($R^2 = 0.991$, 5.5-7 pH range). N=3. Note: Measurements at each pH standard were performed under equilibrium conditions with around 3 mins response time.

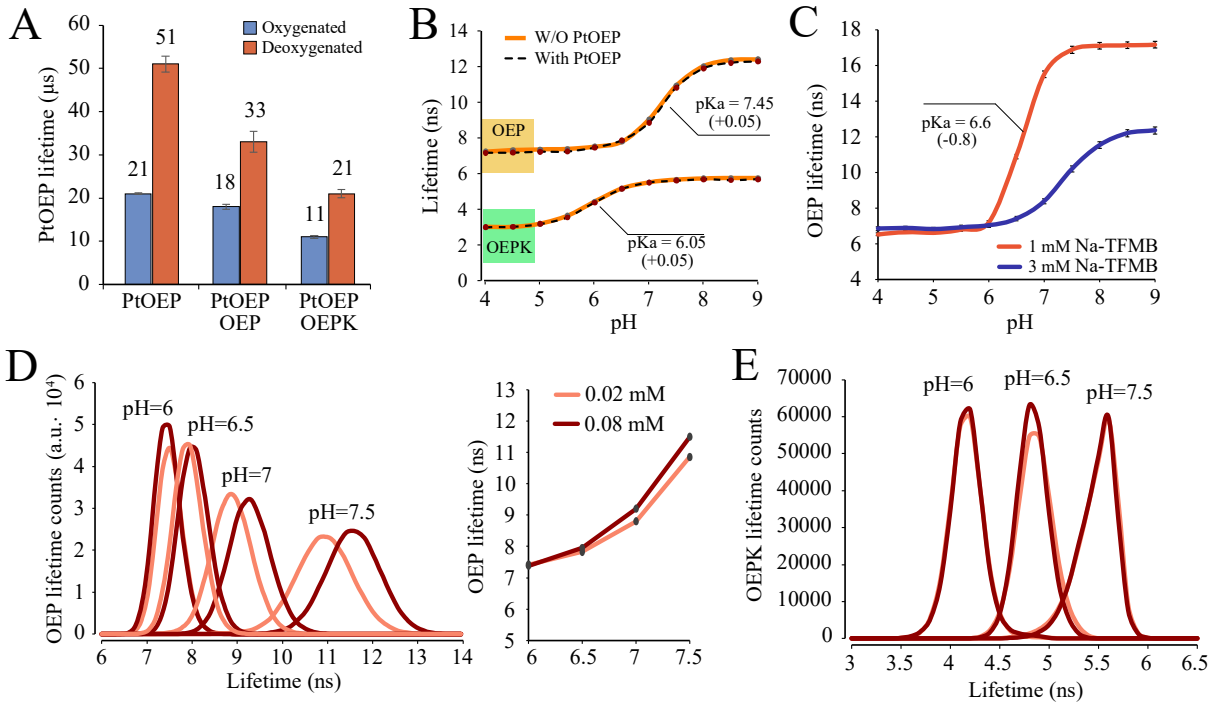

Figure 6.8 Reciprocal effects of PtOEP and OEP/OEPK dyes and Na-TFMB concentration on sensor lifetime and pKa values. **A.** The effect of OEP on PtOEP lifetime. **B.** The effect of PtOEP on FLT values of OEP and OEPK. **C.** pH calibrations for OEP at 1 mM and 3 mM of Na-TFMB. **D-E.** FLT response to pH at two concentrations (0.08 mM and 0.02 mM) of OEP (D) and OEPK (E). Cary Eclipse (A) and confocal FLIM (B-E) analyses (N=3).

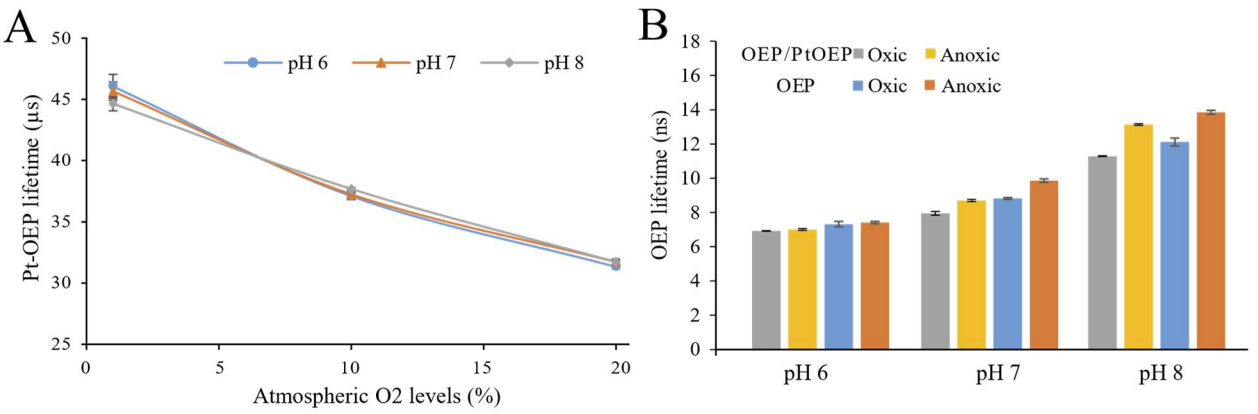

Figure 6.9. The pH and O_2 cross-talk of OEP/PtOEP sensors. **A.** The effect of pH on the PtOEP lifetime (µs). **B.** The effect of O_2 concentrations on the OEP lifetime (ns). The lifetime values were measured on the TRF reader Victor 2 (µs) and on the confocal microscope (ns), respectively (N=3).

6.2.5 ECAR and OCR analysis with the new pH and O_2 sensors

Prior to the experiments with live cells, we examined response time of the pH sensors to pH transitions 7.5 → 6.0 → 7.5. For that, a dual sensor spotted on Mylar film was inserted in a cuvette, conditioned in PBS with specified pH, then quickly changed to another buffer. Sensor emission was monitored at 644 nm emission on a Cary Eclipse spectrofluorometer. The results, exemplified with the OEP/PtOEP sensor, indicate that complete and reversible sensor response occurs within ~2 min (**Fig. 6.10A**).

Next, we spotted the OEP/PtOEP and OEPK/PtOEP sensors (0.08 mM pH dyes, 0.25 mM PtOEP, 3 mM Na-TFMB) on a polypropylene 96-well plate and conducted pH and O_2 sensing experiments with cells on Victor 2 reader. The ECAR and OCR traces generated in repeating measurement cycles under optimised settings are shown in the material and methods **(Table 2.2)**. In the ECA experiments, HCT116 cells in suspension were treated with FCCP and Ant A (effector compounds), or DMSO (mock, negative control). In all the samples with cells strong pH responses were observed. Compared to mock, the drop of pH was more pronounced in the FCCP-treated and particularly in the Ant A-treated samples (**Fig. 6.10B**), indicating the activated glycolysis and lactate release by HCT116 cells with inhibited oxidative phosphorylation [151]. The OCR results (**Fig. 6.10C**) show that the maximal OCR was attained by adding FCCP, which uncouples electron transport from ATP synthesis and thus accelerates O_2 consumption [213]. The PLT signal increased relatively slow in the mock and remained flat in the samples treated with Ant A, which is known to strongly inhibit mitochondrial respiration.

Finally, ECAR analysis in a 3D tissue model of multicellular spheroid structures formed by HCT116 cells was performed on a confocal FLIM microscope. The imaging experiments showed that both OEP- and OEPK-based pH sensors were able to detect pH changes caused by the glycolytic activity of cells within the spheroid. The results obtained using the OEP and OEPK sensors agree with each other (**Fig. 6.10D**). Collectively, the above results indicate that the new sensors perform well in the analysis of ATP-producing pathways in cultured cells and in 3D tissue models.

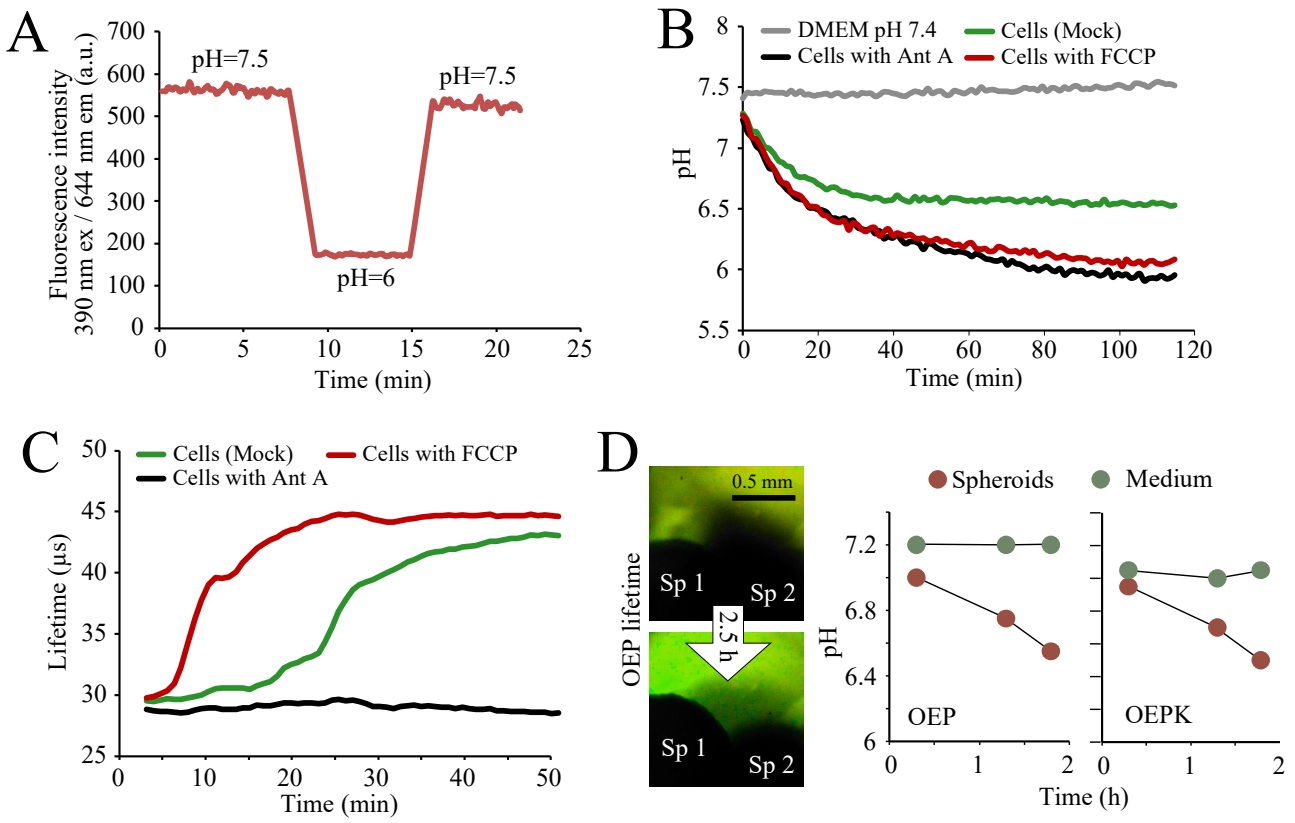

Figure 6.10. Biological application of the OEP/PtOEP and OEPK/PtOEP sensors. **A**. Analysis of response time required to pH changes for the OEP/PtOEP sensor on a Cary Eclipse spectrofluorometer. **B**. ECAR and (**C**) OCR analyses for HCT116 cells treated with Ant A (2 µM), FCCP (0.25 µM) and DMSO (mock); measured with the OEP/PtOEP dual sensor in a 96-well microplate on Victor 2 reader. **D**. ECAR analysis of spheroids formed by HCT116 cells, measured on a confocal FLIM microscope; spheroids treated with Ant A (2 µM) in wells of a 96-well plate, with the ECA medium as negative control.

The OEP and OEPK based sensors also showed good storage stability (**Fig.6.11**), with pKa values remaining unchanged and no dye degradation over one year of storage. Thus, they are well suited for wide practical use and commercialisation.

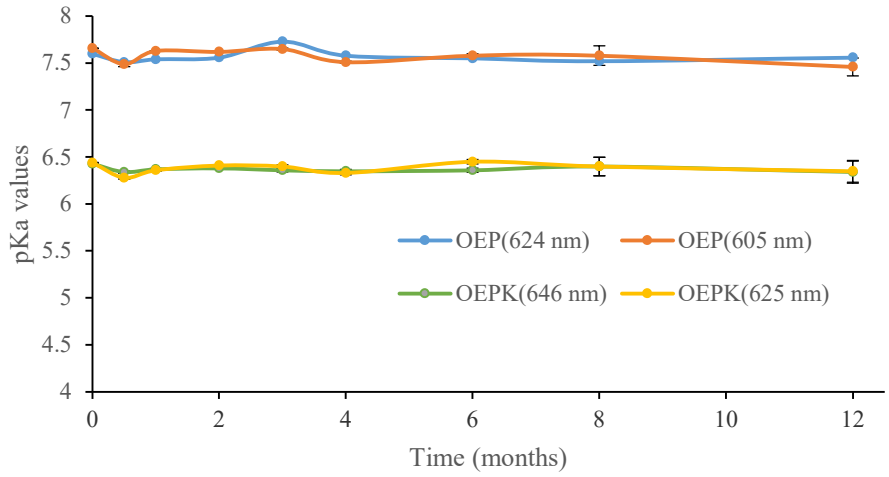

Figure 6.11. The storage stability of OEP and OEPK based sensor. The pKa values were calculated based on protonation and deprotonation peaks of OEP and OEPK on Cary Eclipse (N=3).

6.2.6. Planar calibration-free FLIM sensors for tumor pH imaging in model animals

To operate with freshly excised animal tissue samples, disposable planar fluorescent OEPK sensors were prepared by applying sensor cocktail on 22x22 mm pieces of Mylar film on a spin coater SCS 6800 (Kisco, Indianapolis, USA). The CT26 tumour cells suspended in DMEM medium were injected subcutaneously into animal's right flank and allowed to develop solid tumours. Groups of five animals were sacrificed at different stages of tumour development (**Fig.6.12**), samples of tissue were freshly excised and measured on a wide-filed FLIM imager (see methods in **Fig.2.3**). Normal muscle tissue samples from five untreated animals were also measured as blank controls. This animal trial is aimed to address two questions: 1) How pHe in tumour tissues compares with the normal muscle tissue? 2) Is there a change in pHe during the CT26 tumour development?

Prior to the final application to the animal tissue, operational stability and response to pH for the sizeable planar sensors were investigated on the FLIM imager. We compared pH calibrations of the unused pH sensors, used pH sensors (after physical contact with animal tissues for 20 mins then rinsed with Milli-Q® water), and the sensors pre-soaked in 100% foetal bovine serum (FBS) for 5 mins. The results indicate that the pH response is fully reversible and remains stable after direct contact with tissue samples and biological fluids (**Fig. 6.13**). Hence, the sensors can be used in the animal trial without re-calibrations.

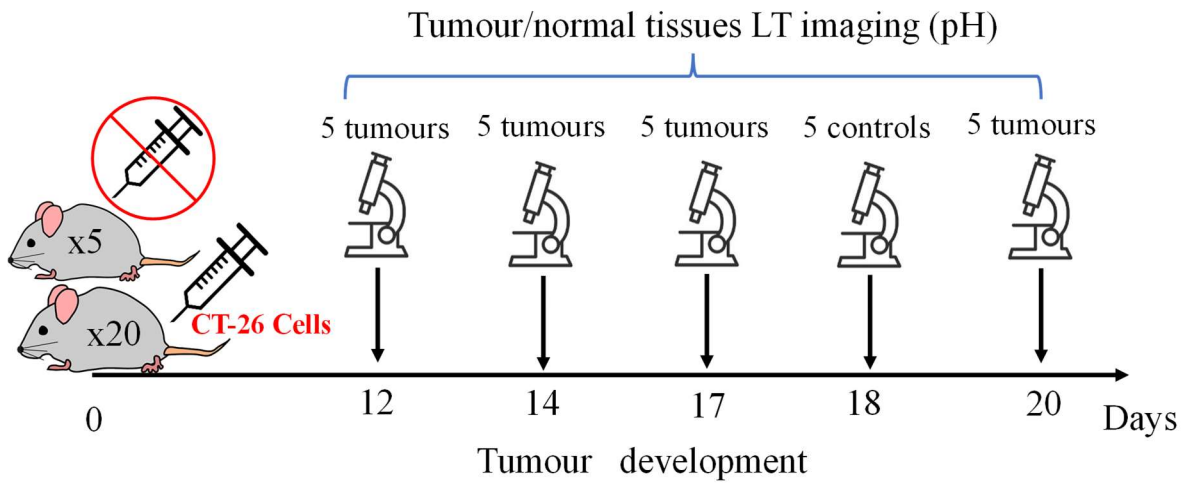

Figure 6.12: Scheme of the animal trial with sensor-based imaging of pHe in ex-vivo tissue samples by a SPAD based wide-field FLIM imager.

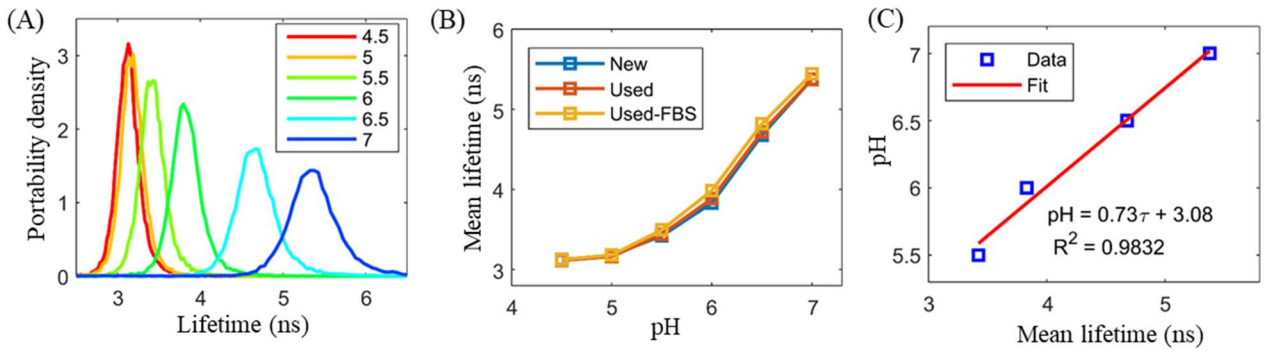

Figure 6.13: The operational stability and pH response of OEPK based planar sensors. **(A)** The FLT distributions at different pH standards. **(B)** The lifetime calibrations of the unused and used disposable sensors. (C). The linear fitting part of graph (B) with inverted axes and four calibration points (pH 5.5-7.0) of the unused sensors. The fitting equation for pHe measurement is also shown: pHe = 0.73 τ + 3.08. Note: Time response for each pH standard is around 3 mins.

Since temperature is important for the sensor performance and also the cell/tissue metabolism [23], we used a non-invasive IR thermometer to monitor the temperature profile of tissues samples. The tissue samples were in a petri-dish covered with pH sensor, and placed on a heating block for temperature control (see methods in **Fig.2.3)**. The result shows after the initial equilibration period of <2 min, sample temperature remains constant over the time (**Fig.6.14**). Based on this data, the FLIM system was set to acquire five repeating images for each tissue sample, starting from 3 mins.

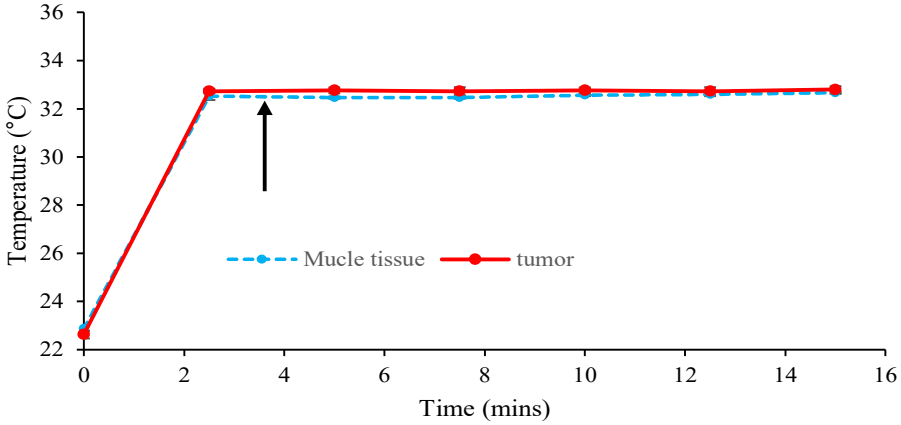

Fig. 6.14. T-profiles of tissue imaging samples and the time starting point of FLIM images acquisitions (n=3).

Following the above optimisations, the OEPK planar sensors were applied for tissue pH imaging by FLIM (**Fig. 6.14**). The intensity signals are indistinguishable between muscle and tumour samples, while there is a significant difference in lifetime imaging. The patterns observed on the intensity images are not seen on the lifetime images, indicating the inhomogeneous dye concentration (dye aggregation) and/or measurement geometry such as topography of sensor coatings, tissue sample, and petri dish, rather than pH gradients. From the cross-section plots and images, the lifetime readouts, compared to intensity ones, are more uniform and stable across sample area.

The mean FLT values (N=5) at each different stage of tumour growth were also measured, which revealed only a minor difference in their pH: 5.68 ± 0.16 ns (day 12), 5.72 ± 0.17 ns (day 14), 5.52 ± 0.17 ns (day 17), and 5.48 ± 0.17 ns (day 20). They correspond to mean pH values of 7.22 ± 0.12 (day 12), 7.25 ± 0.12 (day 14), 7.11 ± 0.12 (day 17) and 7.08 ± 0.12 (day 20) respectively. While for muscle controls, the mean sensor FLT is 5.07 ± 0.20 ns and the corresponding pH value is 6.78 ± 0.15.

Surprisingly, the pHe values of tumour tissue samples were consistently higher than for the normal muscle tissue, and they also differ significantly from the values widely accepted by clinicians [201]: 6.5-7.0 in various tumours and ~ 7.3 in normal tissue. Such discrepancies in pHe values may stem from several factors: i) the extensive invasiveness of tissue excision and preparation: cutting through the tumour may release the more alkaline intracellular fluid, which then mixes with extracellular fluid and shifts the measured pHe; ii) normal muscle tissue may prove inadequate control, or real lack of acidification in grafted tumours produced by CT26 cells. However, there is a more physiological explanation for our results. The literature data refer to *in vivo* settings, where tumour tissue is perfused with blood which continuously supplies the essential nutrients such as glucose and O_2, and removes biological waste (e.g. CO_2 and lactate) to maintain the natural physiological homeostasis.

On the contrary, in our experiments *ex-vivo*, post-mortem samples were freshly harvested from sacrificed animals for analysis. Such samples lacked natural blood perfusion and metabolic homeostasis, while the cells still remained alive, and consumed available nutrients (e.g. glucose) and accumulated waste (e.g. lactate and CO_2). While tumour tissue was originally hypoxic and had more active metabolism, normal tissue retained a higher capacity for both glucose and O_2. Thus, upon cessation of the blood supply, normal tissue was able to produce more acidic waste (lactate and H^+), creating more acidic environment than the excised tumour tissue. This physiological theory can explain the 'inversion' of pHe values for the grafted tumour and normal tissue in such *ex-vivo* condition. This theory is compatible with the *in vivo*- tumour acidification attributed to enhanced anabolic respiration of the cells.

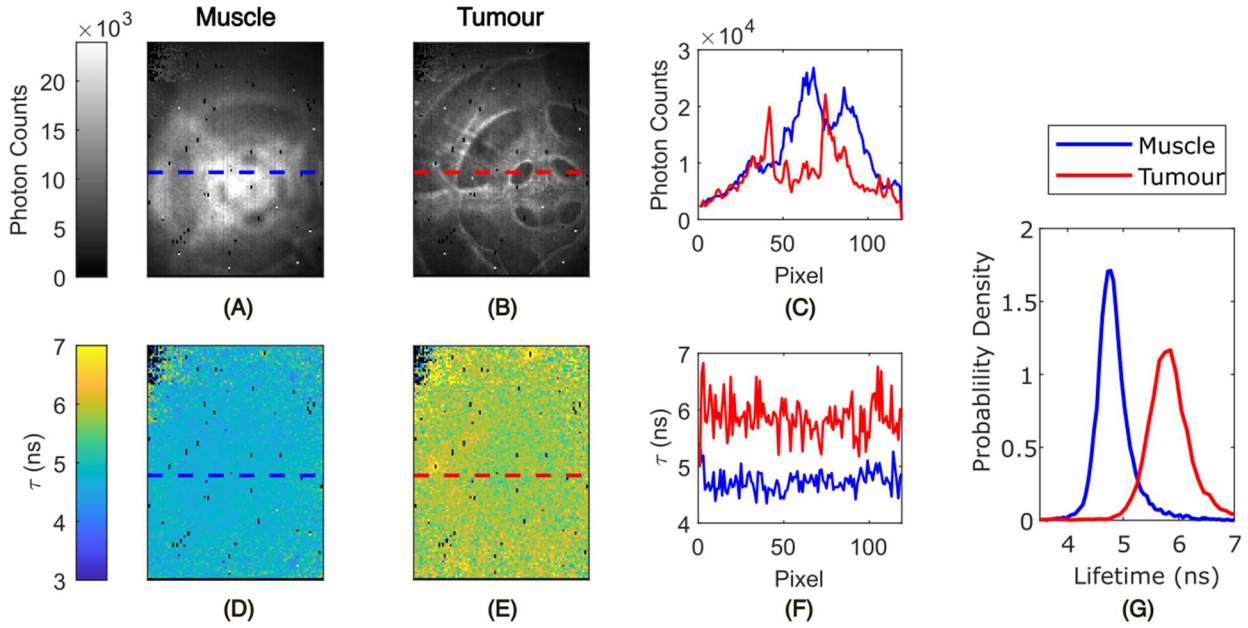

Figure 6.14: Tissue pH imaging on a FLIM imager equipped with SPAD array detector. Example fluorescence intensity (**A-C**) and lifetime (**D-F**) images of a muscle sample and tumour sample taken from the mice on day 14. Cross-section plots along pixel column 76 for both intensity and lifetime images of the samples (as indicated with the blue and red dash line). (**G**). The lifetime distributions for both samples. (*Note: This tumour pH imaging work was done in collaboration with Dario Angelone, MSc from Tyndall National Institute, who set up the SPAD based lifetime imager and performed the initial FLIM data analysis, and with Ciaran Devoy from Cancer Research Centre @UCC, who worked with live animals.)

6.3 Conclusions

We have described, characterised and demonstrated a new family of solid-state optochemical pH sensors and dual pH/O_2 sensors for cell analysis, which utilise fluorescent pH-sensitive OEP or OEPK dyes, and phosphorescent O_2 sensitive PtOEP dye. These dye pairs are spectrally compatible and provide internally referenced readouts in the ratiometric intensity, FLT and PLT modes and combinations thereof. The study included: spectral characterization of the main optical and sensing properties and lifetime characteristics of the sensing materials; screening and optimisation of PTA additives to achieve best sensing performance and low cytotoxicity; optimization of sensor composition and dye concentrations to reduce cross-sensitivity and improve performance; sensor calibration on the different detection platforms. The new dual pH/O_2 sensors were applied to relevant cell models and 3D spheroids, for the real-time measurement their pH and O_2, ECA and OCR. The OEPK based planar FLIM sensors have been applied for *ex-vivo* analysis of pHe in grafted tumour tissue samples. The results indicate that the advanced pH and dual pH/O_2 sensors can provide multi-parametric, multimodal, non-destructive and real-time analysis of biological samples containing live mammalian cells/tissues, in common assay substrates (coated microwell plates or polyester mylar films), and detection equipment (plate readers, confocal FLIM microscopes, and FLIM imagers with SPAD array detector). These sensing platforms have the potential for wide use with biological samples and development of new integrated platforms for cell and tissue metabolic analysis. Such high-performance sensor systems have not been reported so far.

Overall Discussion

With consideration of the existing gaps and challenges in the areas of optochemical sensors and metabolic assessment of mammalian cells and tissue samples highlighted in the literature review, the focus of this research project has been on the following:

- Development of new solid-state optochemical sensors, particularly quenched-phosphorescence O_2 sensors, fluorescence-based pH sensors and/or dual photoluminescence-based pH/O_2 sensors, with internal referencing capabilities, improved analytical performance and applicability;
- Adaptation and fine-tuning of these sensor materials for use in cell analysis on existing and newly emerging detection platforms, including the TRF plate reader and PLIM/FLIM imaging systems;
- Demonstration of the new O_2 and pH sensing systems with relevant cell and tissue models, including animal trials with grafted tumour models;
- Development of new O_2 and pH sensing platforms and ancillary tools for sensor characterisation and application;
- Validation, comparison and ranking of the existing and new O_2 and pH sensing materials and photoluminescence lifetime-based detection and imaging platforms, from the viewpoint of cell analysis.

Thus, Chapter 3 describes a new barometric setup for calibration of quenched phosphorescence O_2 sensors, based on a standard Rotovap system equipped with a digital vacuum pump. The system is easy to operate, convenient and accurate for O_2 calibration of different sensing materials (e.g. solid-state sensor coatings on various substrates, liquid sensor formulations) at different conditions (e.g. dry or humid air, water, temperatures ranging 2ºC-50ºC, residual total pressure). The system was used for a detailed characterisation of sensor's key operation parameters (e.g. τ_o, K_{SV} and its heterogeneity, T-coefficients, etc.). The results prove the barometric calibration setup is convenient accurate, and it can replace traditional methods such as gas mixture and glucose/glucose oxidase titrations.

Chapter 4 describes the evaluation and cross-comparison of the three common PLT measurement platforms, which utilise different PLT calculation modes (RLD, TCSPC, muti-point decays with mono- or double exponential), instrumental factors (detector types, excitation sources, point measurements/imaging, devices cost), and analytical performance (e.g. signal acquisition time, sensitivity, data processing). The TR-F reader Victor2, which uses RLD method and Xe-flash lamp excitation, yielded stable but inaccurate PLT redouts <15 μs, affected by flash-lamp afterglow and sensor heterogeneity. The Cary Eclipse spectrometer, which measures muti-point phosphorescence

decays, can partially correct these interfering factors, and deliver more accurate PLT values by mono- and bi-exponential fittings. Nevertheless, its short PLT readings remained affected by parasitic afterglow. The imaging platform (confocal FLIM/PLIM microscope) provided stable and accurate measurement of short PLT values, using ps diode laser pulsed excitation at 405nm and TCSPC detection technique, revealing the short-lived components in the samples decay, but its limitations included the large volume of data processing and storage, hight cost, and slow image acquisition time. Overall, each PLT platform has its advantages and disadvantages, it can be used for PLT detection, but potential sources of errors should be considered and minimized by careful optimization of their main settings.

Having studied the sensor calibration and detection platforms, several new pH and O_2 sensing materials were developed. The first sensing concept and materials based on PtOEP-SB and coumarine C6 dyes incorporated in plasticized PVC matrix, are described in Chapter 5. Theses sensors possessed dual pH/O_2 functionality with internal referencing capability. The calibration-free pH and O_2 readouts operated in ratio-metric fluorescence and PLT mode, respectively. In this study, a panel of polymeric hosting materials for this pair of dyes were screened, the new MePor-SB derivatives with altered protonation were synthesized and evaluated. As a result of this work, the ratio-metric version of the pH sensor and optical signal enhancement approaches were developed. Then, optimised sensor coatings were deposited on the microplates and benchmarked against the existing platforms. They were demonstrated to be usable in real-time cellular OCR/ECAR analysis, but drawbacks of this system included low brightness of PtOEP-SB dye, limited PLT range for O_2 sensing, cross-sensitivity between O_2 and pH, and non-optimised proton transfer agent (TCPB).

In another sensing concept (described in Chapter 6), we conceived novel solid-state pH sensors based on hydrophobic protonable metal-free porphyrins (OEP and OEPK) as fluorescent pH indicators. The self-referenced ratio-metric fluorescence and FLT (ns) based pH sensors were designed and multiplexed with phosphorescent O_2 sensors (PtOEP). We optimised key parameters of the sensors, including their spectral characteristics, dye encapsulation matrix, the concentrations and types of proton transfer agents, measurement pH range and pKa, dye concentrations. pH sensor cross-talk with the O_2 sensor and its FLT response were studied by confocal FLIM microscopy. The optimised pH and dual pH/O_2 sensors were used to coat the 96-well microplates and to produce planar sensor coatings on polyester films (Mylar). The sensor microplates were then used to measure ECAR/OCR in cell cultures and in 3D spheroids made of HCT116 cells. Subsequently, these planar OEPK and FLIM based pH sensors were used on disposable, calibration-free basis, for the analysis on a portable lifetime imager of pHe in grafted tumour tissue samples (produced using CT26 cells), freshly excised from model animals. Overall, the new pH and dual pH/O_2 sensors exhibited high storage (>1 year) and operational stability, high optical signals, wide PLT/FLT sensing range, low cross-sensitivity and

cytotoxicity, stable pH and O_2 calibrations, fast and reversible pH or pH/O_2 response. Therefore, the new sensors are well-suited for metabolic analysis of biological samples on commonly available and also new detection platforms.

Thesis outcomes

Journal Publications:

[1] **Li, L.,** Gaspar, R.D., Papkovsky, D.B. (2024). Faicile barometric calibration of photoluminescence-base oxygen sensors on a standard rotary evaporator system with a digital vacuum pump. *Sensors & Actuators B. Chemical*, 418, 136286.

[2] **Li, L.,** Zhdanov, A.V., Papkovsky, D.B. (2022). Advanced multimodal solid-state optochemical pH and dual pH/O_2 sensors for cell analysis. *Sensors and Actuators B: Chemical*, 371,132486.

[3] Sen, R., **Li, L.,** Zhdanov, A.V., Gaspar, R. D., Papkovsky, D. B. (2022). Phosphorescence lifetime measurements with sensor materials: comparison of the four different detection platforms. *Sensors and Actuators B: Chemical*, 132496. **(Co-first author)**

[4] Zhdanov, A.V., **Li, L.,** Yang, P., Shkirdova, A.O., ... & Papkovsky, D.B. (2022). Advanced multi-modal, multi-analyte optochemical sensing platform for cell analysis. *Sensors and Actuators B: Chemical*, 355, 131116.

[5] Zhdanov, A.V., Sen, R., Devoy, C., **Li, L.,** Tangney M., Papkovsky, D.B. (2023) Analysis of tumour oxygenation in model animals on a phosphorescence lifetime based macro-imager. *Scientific Reports,* 13(1), 18732.

[6] Zanetti, C., **Li, L.,** Gaspar, R. D. L,Santovito E, Elisseeva S, Collins S. G, Maguire A.R, Papkovsky, D.B. (2024) Susceptibility of the different oxygen-sensing probes to interferences in respirometric bacterial assays with complex media. *Sensors*. 2024; 24(1):267.

[7] Angelone, D., **Li, L.,** Devoy, C., … & Papkovsky, D.B. (2024) Metabolic imaging of tumour tissue samples using planar fluorescence lifetime-based pH sensors and a SPAD array imager. *ACS Sensors*. (Under review)

[8] **Li L.,** Zhdanov, A.V., Dmitri B. Papkovsky (2024), Sensor based system for the analysis of cell metabolism and bioenergetics (Under Review).

Conference proceedings

Li, L., Zhdanov, A.V., Papkovsky, D.B. (2023). New solid-state optochemical pH sensors for the analysis of cell bioenergetics. *Optical Sensors 2023* (Vol. 12572, pp. 268-274). SPIE

Patent Applications:

D.B. Papkovsky, **L. Li,** A.V. Zhdanov, AN OPTOCHEMICAL SENSOR, AND USES THEREOF. European Patent Application, No. 22157103 (2022)

Conference Presentations:

International

1. **Li, L**., Zhdanov, A.V., & Papkovsky, D.B. Advanced new pH and pH/O_2 sensors for live mammalian cells analysis [Poster].*7th International Conference on Molecular Sensors & Molecular Logic Gates (MSMLG)*, Radisson Blu Hotel, Dublin, Ireland. (12-15th July, 2022)

2. **Li, L**., Zhdanov, A.V., & Papkovsky, D.B. Multimodal solid-state fluorescent pH/Oxygen sensors for cell analysis [Poster]. *17th Conference on Methods and Applications in Fluorescence (MAF)*, Charmers University of Technology, Gothenburg, Sweden. (11-14th September, 2022)

3. **Li, L.,** Zhdanov, A.V., & Papkovsky, D.B. Advanced multimodal photoluminescence-based pH/O_2 sensing and imaging platforms for cell analysis [Poster]. *The Annual Microscopy Society Ireland Symposium (MSI)*, Tyndall National Institute, University College Cork. (18-20th January, 2023)

4. **Li, L.,** Zhdanov, A. V., & Papkovsky, D. B. New solid-state optochemical pH sensors for the analysis of cell bioenergetics [Poster]. *2023 SPIE Optics + Optoelectronics conferences*, Prague, Czech Republic. (24-27th April, 2023)

5. **Li, L.,** Angelone, D., Devoy, C., Papkovsky, D. B. Fluorescence lifetime-based pH sensing materials and imaging platforms for use with tissue models [Poster]. *The Annual Microscopy Society Ireland Symposium (MSI)*, University of Limerick, Ireland. (17-19th January, 2024)

6. **Li, L.,** Gaspar, R.D.L., Papkovsky, D.B. Facile barometric calibration of quenched-phosphorescence oxygen sensors on a standard rotary evaporator system [Poster]. *2024 XVI Europt(r)ode conference*. University of Birmingham, UK. (24-28th March, 2024)

National

1. **Li, L.,** Zhdanov, A.V., Shkirdova, A.O., & Papkovsky, D.B. Exploring the capabilities of the phosphorescent multi-analyte sensors for cell analysis [Poster]. IPIC Industry Workshop 2021, Tyndall National Institute, Cork, Ireland. (2nd March, 2021)

2. **Li, L**., Zhdanov, A.V., & Papkovsky, D.B. New pH/O_2 sensing materials for analysis of cells bioenergetics [Poster]. IPIC Industry Workshop 2023, University College Cork, Ireland. (2nd March, 2023)

3. **Li, L**., Angelone, D., Devoy, C., … &Papkovsky, D. B. New fluorescence lifetime-based pH sensing materials tailored for cell analysis and tissue imaging [Poster]. IPIC Industry Workshop 2024, University College Cork, Ireland [Poster]. (19th April, 2024)

Study Courses

Advanced Study Course on Optical Chemical Sensors (ASCOS Series), Obergurgl, Tyrol, Austria. (15-22 October, 2022)

Reference

[1] C.A. Schmidt, K.H. Fisher-Wellman, P.D. Neufer, From OCR and ECAR to energy: Perspectives on the design and interpretation of bioenergetics studies, Journal of Biological Chemistry, 297(2021).
[2] A. Somogyi, E.D. Kirkham, E. Lloyd-Evans, et al., The synthetic TRPML1 agonist ML-SA1 rescues Alzheimer-related alterations of the endosomal-autophagic-lysosomal system, Journal of Cell Science, 136(2023).
[3] W. Ji, X. Tang, W. Du, et al., Optical/electrochemical methods for detecting mitochondrial energy metabolism, Chemical Society Reviews, 51(2022) 71-127.
[4] L. Puspita, S.Y. Chung, J.-w. Shim, Oxidative stress and cellular pathologies in Parkinson's disease, Journal of Molelular Brain, 10(2017).
[5] G. Soto-Heredero, M.M. Gomez de las Heras, E. Gabandé-Rodríguez, et al., Glycolysis a key player in the inflammatory response, The FEBS Journal, 287(2020) 3350-3369.
[6] S. Paul, S. Ghosh, S. Kumar, Tumor glycolysis, an essential sweet tooth of tumor cells, Seminars in Cancer Biology, 86(2022) 1216-1230.
[7] K.S. McCommis, B.N. Finck, Mitochondrial pyruvate transport: a historical perspective and future research directions, Biochemical Journal, 466(2015) 443-454.
[8] J. Mathieu, H. Ruohola-Baker, Metabolic remodeling during the loss and acquisition of pluripotency, Journal of Development, 144(2017) 541-551.
[9] I. Martínez-Reyes, N. Chandel, Mitochondrial TCA cycle metabolites control physiology and disease, Nature Communications, 11(2020) 102.
[10] N. Dairaku, K. Kato, K. Honda, et al., Oligomycin and antimycin A prevent nitric oxide induced apoptosis by blocking cytochrome C leakage, Journal of Laboratory, 143(2004) 143-151.
[11] E.F. Bayne, A.D. Simmons, D.S. Roberts, et al., Multiomics method enabled by sequential metabolomics and proteomics for human pluripotent stem-cell-derived cardiomyocytes, Journal of Proteome Research, 20(2021) 4646-4654.
[12] T. TeSlaa, M. Ralser, J. Fan, et al., The pentose phosphate pathway in health and disease, Nature Metabolism, 5(2023) 1275-1289.
[13] K.O. Alfarouk, S.B. Ahmed, R.L. Elliott, et al., The pentose phosphate pathway dynamics in cancer and its dependency on intracellular pH, Metabolites, 10(2020) 285.
[14] K.C. Patra, N. Hay, The pentose phosphate pathway and cancer, Trends in Biochemical Sciences, 39(2014) 347-354.
[15] H. Zhang, Z. Shen, Z. Yang, et al., Abundance of solute carrier family 27 member 6 (SLC27A6) in the bovine mammary gland alters fatty acid metabolism, Food Function, 12(2021) 4909-4920.
[16] M.M. Adeva-Andany, N. Carneiro-Freire, M. Seco-Filgueira, et al., Mitochondrial β-oxidation of saturated fatty acids in humans, Mitochondrion, 46(2019) 73-90.
[17] X.-d. Wang, O.S. Wolfbeis, Optical methods for sensing and imaging oxygen: materials, spectroscopies and applications, Chemical Society Reviews, 43(2014) 3666-3761.
[18] B. Müller, P. Sulzer, M. Walch, et al., Measurement of respiration and acidification rates of mammalian cells in thermoplastic microfluidic devices, Sensors and Actuators B: Chemical, 334(2021) 129664.
[19] E. Santovito, S. Elisseeva, A. Bukulin, et al., Facile biosensor-based system for on-site quantification of total viable counts in food and environmental swabs, Biosensors and Bioelectronics, 176(2021) 112938.

[20] D. Hassan, H. Bakhsh, A.M. Khurram, et al., Fluorescent nanotechnology: an evolution in optical sensors, Current Analytical Chemistry, 18(2022) 176-185.
[21] L. Jin, L. Shi, W. Shi, et al., Fluorescence lifetime-based pH sensing by platinum nanoclusters, Analyst, 144(2019) 3533-3538.
[22] R.I. Dmitriev, D.B. Papkovsky, Quenched-phosphorescence detection of molecular oxygen: applications in life sciences, Royal Society of Chemistry, 2018.
[23] A. Steinegger, O.S. Wolfbeis, S.M. Borisov, Optical sensing and imaging of pH values: spectroscopies, materials, and applications, Chemical Society Reviews, 120(2020) 12357-12489.
[24] D.B. Papkovsky, R.I. Dmitriev, Biological detection by optical oxygen sensing, Chemical Society Reviews, 42(2013) 8700-8732.
[25] J. Jan, N. Jan, F. Marcel, et al., Measurement of spectral characteristics and CCT mixture of PDMS and the luminophore depending on the geometric parameters and the concentration of the samples of the special optical fibers, In Micro-structured and Specialty Optical Fibres SPIE2017, pp. 131-136.
[26] C. Kelly, E. Santovito, M. Cruz-Romero, et al., Application of O_2 sensor technology to monitor performance of industrial beef samples packaged on three different vacuum packaging machines, Sensors Actuators B: Chemical, 304(2020) 127338.
[27] H. Kautsky, A. Hirsch, Interactions of excited dye molecules and oxygen, Ber Dtsch Chem Ges, 64(1931) 2677-2686.
[28] I. Bergman, Rapid-response atmospheric oxygen monitor based on fluorescence quenching, Nature, 218(1968) 396-396.
[29] D. Lübbers, N. Opitz, Opticl fluorescence sensors for continuous measurement of chemical concentrations in biological systems, Sensors and Actuators, 4(1983) 641-654.
[30] O.S. Wolfbeis, M.J. Leiner, H.E. Posch, A new sensing material for optical oxygen measurement, with the indicator embedded in an aqueous phase, Microchimica Acta, 90(1986) 359-366.
[31] D.B. Papkovsky, J. Olah, I.V. Troyanovsky, et al., Phosphorescent polymer films for optical oxygen sensors, Biosensors and Bioelectronics, 7(1992) 199-206.
[32] S.M. Borisov, I. Klimant, Ultrabright oxygen optodes based on cyclometalated iridium (III) coumarin complexes, Analytical Chemistry, 79(2007) 7501-7509.
[33] M. Quaranta, S.M. Borisov, I. Klimant, Indicators for optical oxygen sensors, Bioanalytical Reviews, 4(2012) 115-157.
[34] T.C. O'Riordan, A.E. Soini, J.T. Soini, et al., Performance evaluation of the phosphorescent porphyrin label: solid-phase immunoassay of α-fetoprotein, Analytical Chemistry, 74(2002) 5845-5850.
[35] D.B. Papkovsky, G.V. Ponomarev, O.S. Wolfbeis, Longwave luminescent porphyrin probes, Spectrochimica Acta Part A: Molecular Biomolecular Spectroscopy, 52(1996) 1629-1638.
[36] G. Liebsch, I. Klimant, O.S. Wolfbeis, Luminescence lifetime temperature sensing based on sol-gels and poly (acrylonitrile)s dyed with ruthenium metal ligand complexes, Advanced Materials, 11(1999) 1296-1299.
[37] P. Hartmann, M.J. Leiner, M.E. Lippitsch, Luminescence quenching behavior of an oxygen sensor based on a Ru (II) complex dissolved in polystyrene, Analytical Chemistry, 67(1995) 88-93.
[38] R.I. Dmitriev, D.B. Papkovsky, Optical probes and techniques for O_2 measurement in live cells and tissue, Cellular Molecular Life Sciences, 69(2012) 2025-2039.

[39] T.s.C. O'Riordan, K. Fitzgerald, G.V. Ponomarev, et al., Sensing intracellular oxygen using near-infrared phosphorescent probes and live-cell fluorescence imaging, American Journal of Physiology-Regulatory, Integrative Comparative Physiology, 292(2007) 1613-1620.
[40] D. Papkovsky, A.V. Zhdanov, A. Fercher, et al., Phosphorescent oxygen-sensitive probes, Springer, 2012.
[41] S. Borisov, G. Nuss, I. Klimant, Red light-excitable oxygen sensing materials based on platinum (II) and palladium (II) benzoporphyrins, Analytical Chemistry, 80(2008) 9435-9442.
[42] J. Hynes, S. Floyd, A.E. Soini, et al., Fluorescence based cell viability screening assays using water-soluble oxygen probes, SLAS Discovery, 8(2003) 264-272.
[43] K. C, Investigation of optical properties and sensing potentials of some organic dyes in polymeric matrices, Fen Bilimleri Enstitüsü, 2018.
[44] J.R. Marland, F. Moore, C. Dunare, et al., Optimization of Nafion polymer electrolyte membrane design and microfabrication, IEEE Transactions on Semiconductor Manufacturing, 33(2020) 196-201.
[45] S.M. Borisov, C. Krause, S. Arain, et al., Composite material for simultaneous and contactless luminescent sensing and imaging of oxygen and carbon dioxide, Advanced Materials, 18(2006) 1511-1516.
[46] P. Melnikov, A. Bobrov, Y. Marfin, On the use of polymer-based composites for the creation of optical sensors: a review, Polymers, 14(2022) 4448.
[47] A. Fercher, G.V. Ponomarev, D. Yashunski, et al., Evaluation of the derivates of phosphorescent Pt-coproporphyrin as intracellular oxygen-sensitive probes, Analytical Bioanalytical Chemistry, 396(2010) 1793-1803.
[48] S. Zhang, M. Hosaka, T. Yoshihara, et al., Phosphorescent light–emitting iridium complexes serve as a hypoxia-sensing probe for tumor imaging in living animals, Cancer Research, 70(2010) 4490-4498.
[49] I. Dunphy, S.A. Vinogradov, D.F. Wilson, Oxyphor R2 and G2: phosphors for measuring oxygen by oxygen-dependent quenching of phosphorescence, Analytical Biochemistry, 310(2002) 191-198.
[50] C. Foerg, H.P. Merkle, On the biomedical promise of cell penetrating peptides: limits versus prospects, Journal of Pharmaceutical Sciences, 97(2008) 144-162.
[51] A. Reisch, A.S. Klymchenko, Fluorescent polymer nanoparticles based on dyes: seeking brighter tools for bioimaging, Small, 12(2016) 1968-1992.
[52] A.V. Zhdanov, R. Sen, C. Devoy, et al., Analysis of tumour oxygenation in model animals on a phosphorescence lifetime based macro-imager, Scientific Reports, 13(2023) 18732.
[53] A. Fercher, S.M. Borisov, A.V. Zhdanov, et al., Intracellular O_2 sensing probe based on cell-penetrating phosphorescent nanoparticles, ACS Nano, 5(2011) 5499-5508.
[54] S. Burgstaller, H. Bischof, T. Gensch, et al., pH-Lemon, a fluorescent protein-based pH reporter for acidic compartments, ACS Sensors, 4(2019) 883-891.
[55] S.-H. Lee, J.R. Griffiths, How and why are cancers acidic? Carbonic anhydrase IX and the homeostatic control of tumour extracellular pH, Cancers, 12(2020) 1616.
[56] B. Pedras, G. Orellana, M.N. Berberan-Santos, Luminescence-based sensors for aeronautical applications, Springer, 2019.
[57] R. Sen, L. Li, A.V. Zhdanov, et al., Phosphorescence lifetime measurements with sensor materials: Comparison of the four different detection platforms, Sensors and Actuators B: Chemical, 371(2022) 132496.
[58] T. Arakawa, D.V. Dao, K. Mitsubayashi, Biosensors and chemical sensors for healthcare monitoring: a review, IEEJ Transactions on Electrical Electronic Engineering, 17(2022) 626.

[59] Z. Tang, T. Bai, P. Zhou, Sensing mechanism of a fluorescent probe for cysteine: photoinduced electron transfer and invalidity of excited-state intramolecular proton transfer, The Journal of Physical Chemistry A, 124(2020) 6920-6927.
[60] O. Wolfbeis, E. Furlinger, H. Kroneis, et al., A study on fluorescent indicators for measuring near neutral pH-values, Analytical Chemistry, 314(1983) 119-124.
[61] A. Lobnik, N. Majcen, K. Niederreiter, et al., Optical pH sensor based on the absorption of antenna generated europium luminescence by bromothymolblue in a sol–gel membrane, Sensors and Actuators B: Chemical, 74(2001) 200-206.
[62] A. Scarciglia, E. Di Gregorio, S. Aime, et al., Effects of cations on HPTS fluorescence and quantification of free gadolinium ions in solution; assessment of intracellular release of Gd^{3+} from Gd-based MRI contrast agents, Molecules, 27(2022) 2490.
[63] M. Larsen, S.M. Borisov, B. Grunwald, et al., A simple and inexpensive high resolution color ratiometric planar optode imaging approach: application to oxygen and pH sensing, Limnology Oceanography: Methods, 9(2011) 348-360.
[64] A. Hakonen, S. Hulth, A high-performance fluorosensor for pH measurements between 6 and 9, Talanta, 80(2010) 1964-1969.
[65] C. Wang, Reconstituted lipid nanoparticles from cells/tissues for drug delivery in cancer, Molecular Pharmaceutics, 20(2023) 2891-2898.
[66] N. Klonis, W.H. Sawyer, Spectral properties of the prototropic forms of fluorescein in aqueous solution, Journal of Fluorescence, 6(1996) 147-157.
[67] F. Le Guern, V. Mussard, A. Gaucher, et al., Fluorescein derivatives as fluorescent probes for pH monitoring along recent biological applications, International Journal of Molecular Sciences, 21(2020) 9217.
[68] M. Beija, C.A. Afonso, J.M. Martinho, Synthesis and applications of Rhodamine derivatives as fluorescent probes, Chemical Society Reviews, 38(2009) 2410-2433.
[69] S.G. Stratton, G.H. Taumoefolau, G.E. Purnell, et al., Tuning the pKa of fluorescent rhodamine pH probes through substituent effects, Chemistry A European Journal, 23(2017) 14064-14072.
[70] H. Huang, S. Chauhan, J. Geng, et al., Implantable tin porphyrin-PEG hydrogels with pH-responsive fluorescence, Biomacromolecules, 18(2017) 562-567.
[71] J. Hynes, T.C. O'Riordan, A.V. Zhdanov, et al., In vitro analysis of cell metabolism using a long-decay pH-sensitive lanthanide probe and extracellular acidification assay, Analytical Biochemistry, 390(2009) 21-28.
[72] P. Petrini, S. Fare, A. Piva, et al., Design, synthesis and properties of polyurethane hydrogels for tissue engineering, Journal of Materials Science, 14(2003) 683-686.
[73] E. Bakker, P. Bühlmann, E. Pretsch, Carrier based Ion-selective electrodes and bulk optodes: general characteristics, Chemical Reviews, 97(1997) 3083-3132.
[74] C. Hazneci, K. Ertekin, B. Yenigul, et al., Optical pH sensor based on spectral response of newly synthesized schiff bases, Dyes Pigments, 62(2004) 35-41.
[75] C. Hoefer, J. Santner, S.M. Borisov, et al., Integrating chemical imaging of cationic trace metal solutes and pH into a single hydrogel layer, Analytica Chimica Acta, 950(2017) 88-97.
[76] H. Stahl, A. Glud, C.R. Schröder, et al., Time-resolved pH imaging in marine sediments with a luminescent planar optode, Limnology Oceanography: Methods, 4(2006) 336-345.
[77] N. Rudolph, S. Voss, A.B. Moradi, et al., Spatio-temporal mapping of local soil pH changes induced by roots of lupin and soft-rush, Plant Soil, 369(2013) 669-680.
[78] H.R. Kermis, Y. Kostov, G. Rao, Rapid method for the preparation of a robust optical pH sensor, Analyst, 128(2003) 1181-1186.
[79] S. Hulth, R.C. Aller, P. Engström, et al., A pH plate fluorosensor (optode) for early diagenetic studies of marine sediments, Limnology Oceanography, 47(2002) 212-220.

[80] Q. Zhu, R.C. Aller, Y. Fan, High-performance planar pH fluorosensor for two-dimensional pH measurements in marine sediment and water, Environmental Science Technology, 39(2005) 8906-8911.
[81] S.G. Schulman, S. Chen, F. Bai, et al., Dependence of the fluorescence of immobilized 1-hydroxypyrene-3, 6, 8-trisulfonate on solution pH: extension of the range of applicability of a pH fluorosensor, Analytica Chimica Acta, 304(1995) 165-170.
[82] D.A. Nivens, M.V. Schiza, S.M. Angel, Multilayer sol-gel membranes for optical sensing applications: single layer pH and dual layer CO_2 and NH_3 sensors, Talanta, 58(2002) 543-550.
[83] N. Strömberg, E. Mattsson, A. Hakonen, An imaging pH optode for cell studies based on covalent attachment of 8-hydroxypyrene-1, 3, 6-trisulfonate to amino cellulose acetate films, Analytica Chimica Acta, 636(2009) 89-94.
[84] D. Millar, R. Henderson, A. Keeper, Electrochemical immobilization of a pH sensitive fluorescein derivative: synthesis and characterization of a fluorescein-derivatised polythiophene, Chemical Communications, (1998) 477-478.
[85] C. Staudinger, J. Breininger, I. Klimant, et al., Near-infrared fluorescent aza-BODIPY dyes for sensing and imaging of pH from the neutral to highly alkaline range, Analyst, 144(2019) 2393-2402.
[86] Z. Xu, A. Rollins, R. Alcala, et al., A novel fiber-optic pH sensor incorporating carboxy SNAFL-2 and fluorescent wavelength-ratiometric detection, Journal of Biomedical Materials Research, 39(1998) 9-15.
[87] I. Dalfen, R. Dmitriev, G. Holst, et al., Background free fluorescence decay time sensing and imaging of pH with highly photostable diazaoxotriangulenium dyes, Analytical Chemistry, 91(2018) 808-816.
[88] M. Cajlakovic, A. Lobnik, T. Werner, Stability of new optical pH sensing material based on cross-linked poly (vinyl alcohol) copolymer, Analytica Chimica Acta, 455(2002) 207-213.
[89] R.M. Kenney, M.W. Boyce, N.A. Whitman, et al., A pH-sensing optode for mapping spatiotemporal gradients in 3D paper-based cell cultures, Analytical Chemistry, 90(2018) 2376-2383.
[90] A.A. Panova, P. Pantano, D.R. Walt, In situ fluorescence imaging of localized corrosion with a pH-sensitive imaging fiber, Analytical Chemistry, 69(1997) 1635-1641.
[91] R. Badugu, Y. Kostov, G. Rao, et al., Development and application of an excitation ratiometric optical pH sensor for bioprocess monitoring, Biotechnology Progress, 24(2008) 1393-1401.
[92] S. Kim, H.E. Pudavar, P.N. Prasad, Dye-concentrated organically modified silica nanoparticles as a ratiometric fluorescent pH probe by one-and two-photon excitation, Chemical Communications, (2006) 2071-2073.
[93] S.M. Borisov, K. Gatterer, I. Klimant, Red light-excitable dual lifetime referenced optical pH sensors with intrinsic temperature compensation, Analyst, 135(2010) 1711-1717.
[94] Y. Clarke, W. Xu, J. Demas, et al., Lifetime-based pH sensor system based on a polymer-supported ruthenium (II) complex, Analytical Chemistry, 72(2000) 3468-3475.
[95] W.W. Al-Qaysi, A. Duerkop, Sensor and sensor microtiterplate with expanded pH detection range and their use in real samples, Sensors and Actuators B: Chemical, 298(2019) 126848.
[96] Y.-C. Zhu, L.-P. Mei, Y.-F. Ruan, et al., Enzyme-based biosensors and their applications, Elsevier, 2019.
[97] Q. Ma, J. Wang, Z. Li, et al., Recent progress in time-resolved biosensing and bioimaging based on lanthanide-doped nanoparticles, Small, 15(2019) 1-22.

[98] M.E. Lippitsch, S. Draxler, D. Kieslinger, Luminescence lifetime-based sensing: new materials, new devices, Sensors Actuators B: Chemical, 38(1997) 96-102.
[99] C.M. McGraw, G. Khalil, J.B. Callis, Comparison of time and frequency domain methods for luminescence lifetime measurements, The Journal of Physical Chemistry C, 112(2008) 8079-8084.
[100] C. Staudinger, M. Strobl, J.P. Fischer, et al., A versatile optode system for oxygen, carbon dioxide, and pH measurements in seawater with integrated battery and logger, Limnology Oceanography: Methods, 16(2018) 459-473.
[101] J.R. Lakowicz, B.R. Masters, Principles of fluorescence spectroscopy, Journal of Biomedical Optics, 13(2008) 29901.
[102] S.M. Borisov, Chapter 1 Fundamentals of quenched phosphorescence O_2 sensing and rational design of sensor materials, Quenched-phosphorescence detection of molecular oxygen: applications in life sciences, The Royal Society of Chemistry2018, pp. 1-18.
[103] C.A. Kelly, M. Cruz-Romero, J.P. Kerry, et al., Assessment of performance of the industrial process of bulk vacuum packaging of raw meat with nondestructive optical oxygen sensing systems, Sensors, 18(2018) 1395.
[104] B. Valeur, M.N. Berberan-Santos, Molecular fluorescence: principles and applications, Wiley, 2012.
[105] J. Yvon, Which fluorescence lifetime system is best for you?, HORIBA Fluorescence Group,2004.
[106] W. Becker, V. Shcheslavskiy, A. Rück, Multi-parametric live cell microscopy of 3D tissue model, Springer, 2017.
[107] R. Sen, New photonic imaging systems for biomedical applications, University Colloge Cork, 2023.
[108] K. Nie, X. Peng, W. Yan, et al., Luminescent probes for luminescence lifetime sensing and imaging in live cells: a narrative review, Journal of Bio-X Research, 3(2020) 174-182.
[109] L.M. Hirvonen, K. Suhling, Fast timing techniques in FLIM applications, Frontiers in Physics, 8(2020) 161.
[110] P.S. Chelushkin, S. Tunik, Phosphorescence lifetime imaging (PLIM): State of the art and perspectives, Progress in Photon Science, (2019) 109-128.
[111] R.I. Dmitriev, A.V. Kondrashina, K. Koren, et al., Small molecule phosphorescent probes for O_2 imaging in 3D tissue models, Biomaterials Science, 2(2014) 853-866.
[112] C. Zanetti, R.D.L. Gaspar, A.V. Zhdanov, et al., Heterosubstituted derivatives of PtPFPP for O_2 sensing and cell analysis: structure activity relationships, Bioconjugate Chemistry, 33(2022) 2161-2169.
[113] A.V. Zhdanov, L. Li, P. Yang, et al., Advanced multi-modal, multi-analyte optochemical sensing platform for cell analysis, Sensors and Actuators B: Chemical, 355(2022) 131116.
[114] S. Elisseeva, E. Santovito, E. Linehan, et al., Performance assessment of the two oxygen sensor based respirometric platforms with complex media and in selective bacterial assays, Sensors Actuators B: Chemical, 383(2023) 133582.
[115] X. Zou, T. Pan, L. Chen, et al., Luminescence materials for pH and oxygen sensing in microbial cells–structures, optical properties, and biological applications, Critical Reviews in Biotechnology, 37(2017) 723-738.
[116] G. Hao, Z.P. Xu, L. Li, Manipulating extracellular tumour pH: An effective target for cancer therapy, RSC advances, 8(2018) 22182-22192.
[117] I. Urriza-Arsuaga, G. Ielasi, M. Bedoya, et al., Luminescence-based sensors for bioprocess applications, Fluorescence in Industry, (2019) 1-38.

[118] S. Elisseeva, C. Kelly, M. Cruz-Romero, et al., The use of optical oxygen sensing and respirometry to quantify the effects of antimicrobials on common food spoilage bacteria and food samples, Sensors and Actuators B: Chemical, 322(2020) 128572.
[119] C. Zanetti, L. Li, R.D. Gaspar, et al., Susceptibility of the different oxygen-sensing probes to interferences in respirometric bacterial assays with complex media, Sensors, 24(2024) 267.
[120] J.L. Gehrich, D.W. Lubbers, N. Opitz, et al., Optical fluorescence and its application to an intravascular blood gas monitoring system, IEEE Transactions on Biomedical Engineering, (1986) 117-132.
[121] J.K. Tusa, H. He, Critical care analyzer with fluorescent optical chemosensors for blood analytes, Journal of Materials Chemistry, 15(2005) 2640-2647.
[122] F. Gottrup, Oxygen in wound healing and infection, World Journal of Surgery, 28(2004) 312-315.
[123] P.G. Rodriguez, F.N. Felix, D.T. Woodley, et al., The role of oxygen in wound healing: a review of the literature, Dermatologic Surgery, 34(2008) 1159-1169.
[124] T.R. Dargaville, B.L. Farrugia, J.A. Broadbent, et al., Sensors and imaging for wound healing: a review, Biosensors Bioelectronics, 41(2013) 30-42.
[125] R.J. Meier, S. Schreml, X.d. Wang, et al., Simultaneous photographing of oxygen and pH in vivo using sensor films, Angewandte Chemie International Edition, 50(2011) 10893-10896.
[126] M. Ochoa, R. Rahimi, J. Zhou, et al., Integrated sensing and delivery of oxygen for next-generation smart wound dressings, Microsystems Nanoengineering, 6(2020) 46.
[127] S. Schreml, R.J. Meier, O.S. Wolfbeis, et al., 2D luminescence imaging of pH in vivo, Proceedings of the National Academy of Sciences, 108(2011) 2432-2437.
[128] J.R. Casey, S. Grinstein, J. Orlowski, Sensors and regulators of intracellular pH, Nature Rviews Molecular Cell Biology, 11(2010) 50-61.
[129] L.A. Zenewicz, Oxygen levels and immunological studies, Frontiers in Immunology, 8(2017) 324.
[130] M.A. Hanson, X. Ge, Y. Kostov, et al., Comparisons of optical pH and dissolved oxygen sensors with traditional electrochemical probes during mammalian cell culture, Biotechnology Bioengineering, 97(2007) 833-841.
[131] S. Tada, M.E. Choudhury, M. Kubo, et al., Zonisamide Ameliorates Microglial Mitochondriopathy in Parkinson's Disease Models, Brain Sciences, 12(2022) 268.
[132] Z. Javed, B.L. Worley, C. Stump, et al., Optimization of extracellular flux assay to measure respiration of anchorage-independent tumor cells spheroids, Bio-protocol, 12(2022) 4321.
[133] J. Werner, M. Belz, K.-F. Klein, et al., Fiber optic sensor designs and luminescence-based methods for the detection of oxygen and pH measurement, Measurement, 178(2021) 109323.
[134] P. Keil, G. Liebsch, L. Borisjuk, et al., Multisense: a multimodal sensor tool enabling the high-throughput analysis of respiration, Plant Respiration and Internal Oxygen, 1670(2017) 47-56.
[135] C. Fraker, M.R. Timmins, R.D. Guarino, et al., The use of the BD oxygen biosensor system to assess isolated human islets of langerhans: oxygen consumption as a potential measure of islet potency, Cell Transplant, 15(2006) 745-758.
[136] J. Hynes, E. Natoli Jr, Y. Will, Fluorescent pH and oxygen probes of the assessment of mitochondrial toxicity in isolated mitochondria and whole cells, Current Protocols in Toxicology, 40(2009) 2-16.

[137] A.A. Gerencser, A. Neilson, S.W. Choi, et al., Quantitative microplate-based respirometry with correction for oxygen diffusion, Analytical Chemistry, 81(2009) 6868-6878.
[138] C. Demuth, J. Varonier, V. Jossen, et al., Novel probes for pH and dissolved oxygen measurements in cultivations from millilitre to benchtop scale, Applied Microbiology Biotechnology, 100(2016) 3853-3863.
[139] C. Fraker, M.R. Timmins, R.D. Guarino, et al., The use of the BD oxygen biosensor system to assess isolated human islets of langerhans: oxygen consumption as a potential measure of islet potency, Cell Transplantation, 15(2006) 745-758.
[140] A. Zhdanov, C. Favre, L. O'Flaherty, et al., Comparative bioenergetic assessment of transformed cells using a cell energy budget platform, Integrative Biology, 3(2011) 1135-1142.
[141] L. Li, A.V. Zhdanov, D.B. Papkovsky, Advanced multimodal solid-state optochemical pH and dual pH/O2 sensors for cell analysis, Sensors and Actuators B: Chemical, 371(2022) 132486.
[142] D.A. Ferrick, A. Neilson, C. Beeson, Advances in measuring cellular bioenergetics using extracellular flux, Drug Discovery Today, 13(2008) 268-274.
[143] G.J.W. van der Windt, C.H. Chang, E.L. Pearce, Measuring bioenergetics in T cells using a seahorse extracellular flux analyzer, Current Protocols in Immunology, 113(2016) 3-16.
[144] K. Olesen, N. Moruzzi, I. Bulatovic, et al., Diversity of respiratory parameters and metabolic adaptation to low oxygen tension in mesenchymal stromal cells, Metabolism Open, 13(2022) 100167.
[145] I.A. Okkelman, N. Neto, D.B. Papkovsky, et al., A deeper understanding of intestinal organoid metabolism revealed by combining fluorescence lifetime imaging microscopy (FLIM) and extracellular flux analyses, Redox Biology, 30(2020) 101420.
[146] D.R. Erzina, I.A. Zamilatskov, N.M. Stanetskaya, et al., Transformations of meso-Iminofunctionalized Pd(II) and Ni(II)-complexes of β-alkylsubstituted porphyrins, European Journal of Organic Chemistry, 2019(2019) 1508-1522.
[147] E.S. Belyaev, A.O. Shkirdova, G.L. Kozhemyakin, et al., Azines of porphyrinoids. Does azine provide conjugation between chromophores?, Dyes and Pigments, 191(2021) 109354.
[148] C.A. Kelly, C. Toncelli, J.P. Kerry, et al., Discrete O_2 sensors produced by a spotting method on polyolefin fabric substrates, Sensors and Actuators B: Chemical, 203(2014) 935.
[149] A.T. Erdogan, T. Al Abbas, N. Finlayson, et al., A high dynamic range 128x120 3-D stacked CMOS SPAD image sensor SoC for fluorescence microendoscopy, IEEE Journal of Solid-State Circuits, 57(2022) 1649-1660.
[150] A.V. Zhdanov, M.W. Ward, C.T. Taylor, et al., Extracellular calcium depletion transiently elevates oxygen consumption in neurosecretory PC12 cells through activation of mitochondrial Na^+/Ca^{2+} exchange, Biophysica Acta Bioenergetics, 1797(2010) 1627-1637.
[151] D.B. Papkovsky, A.V. Zhdanov, Cell energy budget platform for multiparametric assessment of cell and tissue metabolism, Humana Press, 2021.
[152] S. Tanaka, K. Takizawa, F. Nakamura, One-step visualization of natural cell activities in non-labeled living spheroids, Scientific Reports, 12(2022) 1-11.
[153] A.V. Zhdanov, I.A. Okkelman, F.W.J. Collins, et al., A novel effect of DMOG on cell metabolism: direct inhibition of mitochondrial function precedes HIF target gene expression, Biochimica et Biophysica Acta (BBA)-Bioenergetics, 1847(2015) 1254-1266.
[154] S.M. Borisov, O.S. Wolfbeis, Optical biosensors, Chemical Reviews, 108(2008) 423.
[155] D.B. Papkovsky, J.P. Kerry, Oxygen sensor-based respirometry and the landscape of microbial testing methods as applicable to food and beverage matrices, Sensors, 23(2023) 4519.
[156] J.M. Vanderkooi, G. Maniara, T.J. Green, et al., An optical method for measurement of dioxygen concentration based upon quenching of phosphorescence, Journal of Biological Chemistry, 262(1987) 5476-5482.

[157] H. Kerger, G. Groth, A. Kalenka, et al., pO2 measurements by phosphorescence quenching: characteristics and applications of an automated system, Microvascular Research, 65(2003) 32-38.
[158] C. Kelly, D. Yusufu, I. Okkelman, et al., Extruded phosphorescence based oxygen sensors for large-scale packaging applications, Sensors and Actuators B: Chemical, 304(2020) 127357.
[159] A.S. Golub, R.N. Pittman, Barometric calibration of a luminescent oxygen probe, Journal of Applied Physiology, 120(2016) 809-816.
[160] D.B. Papkovsky, N. Papkovskaia, A. Smyth, et al., Phosphorescent sensor approach for non-destructive measurement of oxygen in packaged foods: optimisation of disposable oxygen sensors and their characterization over a wide temperature range, Analytical Letters, 33(2000).
[161] M. Quaranta, M. Murkovic, I. Klimant, A new method to measure oxygen solubility in organic solvents through optical oxygen sensing, Analyst, 138(2013) 6243-6245.
[162] S. Matthiesen, R. Jahnke, M.R. Knittler, A straightforward hypoxic cell culture method suitable for standard incubators, Methods and Protocols, 4(2021) 25.
[163] S. Banerjee, C. Kelly, J.P. Kerry, et al., High throughput non-destructive assessment of quality and safety of packaged food products using phosphorescent oxygen sensors, Trends in Food Science & Technology, 50(2016) 85-102.
[164] A.S. Gentleman, T. Lawson, M.G. Ellis, et al., Stern–Volmer analysis of photocatalyst fluorescence quenching within hollow-core photonic crystal fibre microreactors, Chemical Communications, 58(2022) 10548-10551.
[165] E. Santovito, S. Elisseeva, J.P. Kerry, et al., Rapid detection of bacterial load in food samples using disposable respirometric sensor sachets, Sensors and Actuators B: Chemical, 390(2023) 134016.
[166] E.R. Carraway, J.N. Demas, B.A. DeGraff, et al., Photophysics and photochemistry of oxygen sensors based on luminescent transition-metal complexes, Analytical Chemistry, 63(1991) 337-342.
[167] A.S. Golub, R.N. Pittman, PO2 measurements in the microcirculation using phosphorescence quenching microscopy at high magnification, American Journal of Physiology-Heart Circulatory Physiology, 294(2008) 2905-2916.
[168] D.B. Papkovsky, A.V. Zhdanov, Phosphorescence based O_2 sensors – Essential tools for monitoring cell and tissue oxygenation and its impact on metabolism, Free Radical Biology and Medicine, 101(2016) 202-210.
[169] D.B. Papkovsky, R.I. Dmitriev, Imaging of oxygen and hypoxia in cell and tissue samples, Cellular Molecular Life Sciences, 75(2018) 2963-2980.
[170] W. Becker, Fluorescence lifetime imaging–techniques and applications, Journal of Microscopy, 247(2012) 119-136.
[171] D.J. O'Shea, T.C. O'Riordan, P.J. O'Sullivan, et al., Homogeneous time-resolved fluorescence assays for the detection of activity and inhibition of phosphatase enzymes employing phosphorescently labeled peptide substrates, Analytica Chimica Acta, 583(2007) 349-356.
[172] C. Dysli, S. Wolf, M.Y. Berezin, et al., Fluorescence lifetime imaging ophthalmoscopy, Progress in Retinal Eye Research, 60(2017) 120-143.
[173] M. Valledor, J.C. Campo, I. Sánchez-Barragán, et al., Determination of phosphorescence lifetimes in the presence of high background signals using phase-shift measurements, Sensors Actuators B: Chemical, 113(2006) 249-258.
[174] L.M. Hirvonen, K. Suhling, Wide-field TCSPC: methods and applications, Measurement Science Technology, 28(2016) 012003.

[175] M.Y. Berezin, S. Achilefu, Fluorescence lifetime measurements and biological imaging, Chemical Reviews, 110(2010) 2641-2684.
[176] W. Becker, 3 Advanced TCSPC-FLIM techniques, Multiphoton microscopy and fluorescence lifetime imaging, De Gruyter2018, pp. 23-52.
[177] J. Hynes, S. Nadanaciva, R. Swiss, et al., A high-throughput dual parameter assay for assessing drug-induced mitochondrial dysfunction provides additional predictivity over two established mitochondrial toxicity assays, Toxicology in Vitro, 27(2013) 560-569.
[178] K.K. Sharman, A. Periasamy, H. Ashworth, et al., Error analysis of the rapid lifetime determination method for double-exponential decays and new windowing schemes, Analytical Chemistry, 71(1999) 947-952.
[179] A.V. Zhdanov, I.A. Okkelman, A.V. Golubeva, et al., Quantitative analysis of mucosal oxygenation using ex vivo imaging of healthy and inflamed mammalian colon tissue, Cellular Molecular Life Sciences, 74(2017) 141-151.
[180] J.P. Cascales, E. Roussakis, L. Witthauer, et al., Wearable device for remote monitoring of transcutaneous tissue oxygenation, Biomedical Optics Express, 11(2020) 6989-7002.
[181] K. Youssef, A. Ullah, P. Rezai, et al., Recent advances in biosensors for real time monitoring of pH, temperature, and oxygen in chronic wounds, Materials Today Bio, (2023) 100764.
[182] R.I. Dmitriev, X. Intes, M.M. Barroso, Luminescence lifetime imaging of three-dimensional biological objects, Journal of Cell Science, 134(2021) 1-17.
[183] I. Klimant, C. Huber, G. Liebsch, et al., Dual lifetime referencing (DLR)-a new scheme for converting fluorescence intensity into a frequency-domain or time-domain information, New Trends in Fluorescence Spectroscopy, Springer2001, pp. 257-274.
[184] N.B. Borchert, G.V. Ponomarev, J.P. Kerry, et al., O_2/pH multisensor based on one phosphorescent dye, Analytical Chemistry, 83(2011) 18-22.
[185] D.B. Papkovsky, G.V. Ponomarev, O.S. Wolfbeis, Protonation of porphyrins in liquid PVC membranes: Effects of anionic additives and application to pH-sensing, Journal of Photochemistry and Photobiology A: Chemistry, 104(1997) 151-158.
[186] N. Bellomo, M. Michel, B.R. Pistillo, et al., Chemical Vapor Deposition for Advanced Polymer Electrolyte Fuel Cell Membranes, Chem Electro Chem, 9(2022) e202101019.
[187] T.C. O'Riordan, A.E. Soini, D.B. Papkovsky, Monofunctional derivatives of coproporphyrins for phosphorescent labeling of proteins and binding assays, Analytical Biochemistry, 290(2001) 366-375.
[188] M.V. Mina, I.P. Puzyk, M.V. Puzyk, The effect of acids on fluorescence of coumarin-6 in organic solvents, Optics and Spectroscopy, 114(2013) 244-246.
[189] M. Mitsuishi, H. Tanaka, M. Obata, et al., Plasmon-Enhanced Luminescence from Ultrathin Hybrid Polymer Nanoassemblies for Microscopic Oxygen Sensor Application, Langmuir, 26(2010) 15117-15120.
[190] O. Stranik, H.M. McEvoy, C. McDonagh, et al., Plasmonic enhancement of fluorescence for sensor applications, Sensors and Actuators B: Chemical, 107(2005) 148-153.
[191] D.B. Papkovsky, A.N. Ovchinnikov, V.I. Ogurtsov, et al., Biosensors on the basis of luminescent oxygen sensor: the use of microporous light-scattering support materials, Sensors and Actuators B: Chemical, 51(1998) 137-145.
[192] I. Klimant, O.S. Wolfbeis, Oxygen-Sensitive Luminescent Materials Based on Silicone-Soluble Ruthenium Diimine Complexes, Analytical Chemistry, 67(1995) 3160-3166.
[193] S. Nadanaciva, P. Rana, G. Beeson, et al., Assessment of drug-induced mitochondrial dysfunction via altered cellular respiration and acidification measured in a 96-well platform, Journal of Bioenergetics and Biomembranes, 44(2012) 421-437.

[194] S. Lladó Maldonado, P. Panjan, S. Sun, et al., A fully online sensor-equipped, disposable multiphase microbioreactor as a screening platform for biotechnological applications, Biotechnology and Bioengineering, 116(2019) 65-75.
[195] P. Gruber, M.P.C. Marques, N. Szita, et al., Integration and application of optical chemical sensors in microbioreactors, Lab on a Chip, 17(2017) 2693-2712.
[196] T.C. O'Riordan, A.V. Zhdanov, G.V. Ponomarev, et al., Analysis of intracellular oxygen and metabolic responses of mammalian cells by time-resolved fluorometry, Analytical Chemistry, 79(2007) 9414-9419.
[197] R. Chaudhry, M. Varacallo, Biochemistry, Glycolysis., Treasure Island: StatPearls Publishing, (2020).
[198] M. Fisher, Lehninger principles of biochemistry, The Chemical Educator, 6(2001) 69-70.
[199] B. Alberts, D. Bray, K. Hopkin, et al., Essential cell biology, Garland Science, 2015.
[200] R.A. Gatenby, R.J. Gillies, Why do cancers have high aerobic glycolysis?, Nature Reviews Cancer, 4(2004) 891-899.
[201] A. Anemone, L. Consolino, F. Arena, et al., Imaging tumor acidosis: a survey of the available techniques for mapping in vivo tumor pH, Cancer Metastasis Reviews, 38(2019) 25-49.
[202] X. Zhang, Y. Lin, R.J. Gillies, Tumor pH and its measurement, Journal of Nuclear Medicine, 51(2010) 1167-1170.
[203] A. Anemone, L. Consolino, L. Conti, et al., Tumour acidosis evaluated in vivo by MRI-CEST pH imaging reveals breast cancer metastatic potential, British Journal of Cancer, 124(2021) 207-216.
[204] A. Ryder, S. Power, T. Glynn, et al., Time-domain measurement of fluorescence lifetime variation with pH, SPIE, 2001.
[205] D. Aigner, B. Ungerböck, T. Mayr, et al., Fluorescent materials for pH sensing and imaging based on novel 1, 4-diketopyrrolo-[3, 4-c] pyrrole dyes, Journal of Materials Chemistry C, 1(2013) 5685-5693.
[206] I. Dalfen, R.I. Dmitriev, G. Holst, et al., Background-free fluorescence-decay-time sensing and imaging of pH with highly photostable diazaoxotriangulenium dyes, Analytical Chemistry, 91(2018) 808-816.
[207] T. Yoshihara, N. Matsumura, T. Tamura, et al., Intracellular and intravascular oxygen sensing of pncreatic tissues based on phosphorescence lifetime imaging microscopy using lipophilic and hydrophilic Iridium(III) complexes, ACS Sensors, 7(2022) 545-554.
[208] I.A. Okkelman, R. McGarrigle, S. O'Carroll, et al., Extracellular Ca^{2+}-sensing fluorescent protein biosensor based on a collagen-binding domain, ACS Applied Bio Materials, 3(2020) 5310-5321.
[209] J. Keyes, S. Mehta, J. Zhang, Multiplexed imaging of signaling networks by genetically encoded, fluorescent protein-based biosensors, Methods in Molecular Biology, 2350(2021) 1.
[210] M. Gouterman, 1-Optical spectra and electronic structure of porphyrins and related rings, The Porphyrins V3: Physical Chemistry, Part A, Part 1, (1978).
[211] K. Smith, Porphyrins and metalloporphyrins. their general, physical and coordination chemistry and laboratory methods, Elsevie, 1965.
[212] P. Sarder, D. Maji, S. Achilefu, Molecular probes for fluorescence lifetime imaging, Bioconjugate Chemistry, 26(2015) 963-974.
[213] S. Demine, P. Renard, T. Arnould, Mitochondrial uncoupling: a key controller of biological processes in physiology and diseases, Cells, 8(2019) 795.